# DESIGN OF POROUS GEL AND AEROGEL MEDIA FOR OIL-WATER SEPARATION AND SMALL ORGANIC MOLECULE ADSORPTION

A Dissertation

Presented to

The Graduate Faculty of the University of Akron

In Partial Fulfilment

Of the Requirements for the Degree

Doctor of Philosophy

Pratik S. Gotad

August 2024

DESIGN OF POROUS GEL AND AEROGEL MEDIA FOR OIL-WATER SEPARATION AND SMALL ORGANIC MOLECULE ADSORPTION

Pratik S. Gotad

Dissertation

Approved:

Advisor
Dr. Sadhan C. Jana

Committee Member
Dr. Kevin Cavicchi

Committee Member
Dr. Fardin Khabaz

Committee Member
Dr. Toshikazu Miyoshi

Committee Member
Dr. George Chase

Accepted:

Interim Director, SPSPE
Dr. Mark Soucek

Dean, College of Engineering and Polymer Science
Dr. Craig Menzemer

Interim Dean, Graduate School
Dr. Gwyneth Price

Date :

# ABSTRACT

In this research, several separation problems were investigated with the aid of porous gel and aerogel media. Oil-water emulsion separation is relevant for several industries and processes such as filtration of automotive engine fuel, crude oil recovery processes, water purification, etc. The difficulty in separation of oil-water emulsions is attributed to the presence of surface active molecules, such as surfactants that stabilize the dispersed phase droplets. The first part of this work focused on the development of novel polymer-based filter media offering high specific surface area and coexisting meso- and macropores in the form of polymer aerogels and their applications in separation of oil-water emulsions. The central hypothesis was the ability of nanoscale polymer strands in the aerogel adsorbing large quantities of surfactant molecules thus depleting water-oil interfaces, destabilizing the emulsion, and promoting coalescence of droplets. The first two projects investigated the surfactant adsorption abilities of different surface energy polymer gels. It was found that the surfactant adsorption and in turn, the emulsion separation performance of the gels were greatly influenced by the polymer gel surface energy, its pore sizes, surfactant size and the structural organization of the surfactant molecules on the polymer surface. The third project evaluated several mechanisms of separation of surfactant-stabilized emulsified water droplets from diesel fuel using high surface area (50-370 m2/g) and high porosity ( >90%) filter media fabricated by combining aerogels and glass fiber mats in a continuous flow system. The final project focused on designing an effective adsorbent media for quick removal of environmentally persistent, bioaccumulative, and noxious contaminant called perfluorooctanoic acid (PFOA) from water. This

research, therefore, aimed at understanding and exploiting the potential of porous polymer gel and aerogel media for addressing two pressing purification and separation challenges.

DEDICATION

This dissertation is dedicated to

*My grandparents, my parents, my elder brother Nitesh, and my younger brother Pranit*

*for being my teachers, constant motivators, and my strongest support system*

ACKNOWLEDGEMENT

I would like to express my heartfelt gratitude to my advisor Dr. Sadhan Jana, who has been my mentor, my motivator, my critique, and my strongest support in Akron. It is because of his guidance and encouragement that I was able to immensely enjoy the 5 years of my Ph.D. journey and have been able to make a significant contribution towards the field of polymers. I have been an admirer of his intent to always push the boundaries of science, his focus on solving problems which create an impact on society and his strong ethical value system. I have knowingly and unknowingly learnt so much from him. Just being with him and seeing the way he leads his professional life, the way he handles different situations, his polite and kind nature towards every person around, have all left a lasting impression on me and have made me a better person today. His mentoring style has made me a researcher who can work well independently, who is not afraid to ask difficult questions, and who is always looking to contribute innovatively to solve problems. He has always made sure to put me outside my comfort zone and allowed me to grow as an individual, scientist, engineer but at the same time gave me the assurance that he is standing right behind me. I am eternally thankful to him for this, and I would not have enjoyed my Ph.D. journey if it wasn't for him.

Secondly, I would like to thank my committee members Dr. Kevin Cavicchi, Dr. George Chase, Dr. Toshikazu Miyoshi, Dr. Fardin Khabaz and Dr. Hunter King for contributing towards my Ph.D. in one way or the other. Dr. Miyoshi and Dr. Chase have been our key collaborators for several of the projects I have worked on during my Ph.D. Thanks to both for being extremely kind, motivating and providing me guidance for the questions I went to them with. Our work on filtration wouldn't have been possible without the help and expertise of Dr. George Chase, who is a pioneer in this

field. I would also like to thank Dr. Cavicchi, Dr. Khabaz and Dr. King for their valuable suggestions and comments which led me to explore more in my research work. In addition, I would like to thank Dr. Mesfin Tsige for being one of our key collaborators and extending our experimental work to simulations and modelling. The technical discussions we had were valuable and I appreciate all the time and effort you gave us. Furthermore, I would like to thank Dr. Chrys Wesdemiotis for helping us with the analytical techniques to quantify the PFAS molecules and collaborating with us to solve the PFAS problem. My heartfelt thanks to my collaborators Akshata Kulkarni, Navin Kafle, Abdol Hadi Mokarizadeh and Calum Bochenek for being great teammates, providing your expertise and helping me solve the questions I had, with the same passion and determination. I would also like to extend my gratitude towards Mr. Will Imes, and Mr. Edward Laughlin for helping me build and fix equipments and to Mr. Jack Gillespie for helping me prepare my samples for NMR analysis. I would like to thank Sarah, Deb, Jacqui, Jon, Dr. Lingyan Li for making the last 5 years a smooth ride. I also want to take this opportunity to thank all my professors at the University of Akron and at the Institute of Chemical technology for building a strong foundation about polymers and chemical engineering.

There are so many other people I have to thank for being a part of my life and playing important roles at different stages of it. I will start by thanking my oldest and closest friend Darshan for being a pillar of support and my constant cheerleader throughout our 15 year friendship. I would like to thank Saili, Abhishek, and Aishwarya for again being an important part of my life, especially Saili for being my cheerleader and for always believing in me. I would also like to thank two of my closest friends from my undergraduate days, Varun, and Aditya. We three have stuck to each other throughout our undergraduate days and have made sure to support each other whenever one needs it. Thank you for making my undergraduate journey memorable and something which I will always look back at and smile. Apoorva, thank you for motivating me to pursue a Ph.D. in the US. Also, a

big thanks to my other friends Sampanna, Rishi, Ashlesha, and Akanksha at ICT. The feeling of Akron being a home is because of the lovely people I have met here and it's imperative I thank each of them for making this place a home for me. Thank you Luffy for being there for me throughout these 5 years. Having you around to talk about anything made me feel extremely positive and I knew you were always a call away whenever I needed you, thank you so much my man for making my stay at Akron easy and comfortable. Thank you Frenk, my favorite cricket partner and friend, our cricket memories together and all the time we have spent will always be cherished by me. Thank you to my friend Murali who I can easily call my brother, for always being there for me. We have known each other for just a year but our bond is very special to me, and I am grateful for everything you have done for me. Thank you to Sravya for being with me through the most difficult phase of my Ph.D., for believing in me, for making me calm and grounded, for being one of my pillar of strength and for always lending an ear when I need to talk. Thank you Chellamma (Lahari).Thank you to Suresh, Akshata, Aparna, Nilay, Sainath, Renuka and Anvay for being great seniors and for your guidance every step of the way. The time we all spent together will always be a happy memory to me. Thank you to my entire AYB cricket team for all the memorable moments that we all have shared together. Big shoutout to my research group members: Erin, Moni, Amani, Abdul, Abbas who have played an important role in completion of my Ph.D. I would also like to thank my friends and fellow batchmates Utkarsh, Chaitanya, Jomin, Veni, Udayan for being wonderful friends and great company. A big thank you to all my friends and family who have been a part of this beautiful journey.

I would also like to send out thanks to my alma mater St. Anthony's High School and the Institute of Chemical Technology, for being instrumental in my career and personality development. My heartfelt thanks to the University of Akron and several funding agencies for providing the resources and infrastructure vital for the successful completion of my PhD thesis.

Lastly, I owe my biggest thank you and gratitude to my family back in India. My mother, father and younger brother are the reason for everything that I am today. Thank you Mumma, Papa and Pranit for being my three strongest pillars of support, my best friends, my teachers, and my motivators. It is the values you have instilled in me; it is the love you have given me; it is the education you have provided me; it is the belief you have in me, that has made me achieve this today. Staying away five years from each other has been the most difficult thing we have done, but we have stood with each other as a team every step of the way. Thank you Mumma for sacrificing your career ambitions for us and for taking care of our needs, and those of everyone around you. You are the strongest woman I know and there is so much I admire about you and learn from you every day. Papa you know you are my biggest strength and my role model. Even though everybody says I look like you, what I actually want to be is what you are as a person. You both have navigated through extremely hard times and sacrificed so many of your desires ambitions to make sure we both were provided everything we needed. Thank you! Pranit, although you are younger to me, you know that you are one of my biggest strength too. Every decision I have taken till today is only after knowing your opinion because you are the one I trust the most to provide me with the right perspective. I consider myself lucky to have you as my brother. Thank you to my extended family, mama, mami, Shubham, kaka, kaki and all my cousins for being with us throughout this journey.

TABLE OF CONTENTS

Page

LIST OF FIGURES

Figure Page

LIST OF TABLES

LIST OF SCHEMES

Scheme Page

# CHAPTER I

# INTRODUCTION

Porous high surface area materials have been used extensively for applications such as adsorption, filtration, catalysis, drug delivery, thermal insulation, energy storage, etc. The unique properties of these porous materials such as low bulk density, high surface areas, high porosity and interconnected open pore architecture make them highly desirable for several applications listed above. It was S. Kistler in 1931 who discovered the process to create porous aerogels[1]. Silica aerogel was the first aerogel which Kistler worked with. Since then, several other organic and inorganic aerogel systems have been developed ranging from polyimide, polyurea, syndiotactic polystyrene, polyurethane, polybenzoxazine, graphene, carbon, cellulose, chitosan, polyethylene, etc. The polymer gels are formed by either a chemical or a physical crosslinking mechanism. For example, the polyimide gel system is formed by a step-growth condensation reaction of two difunctional monomers namely a diamine and a dianhydride, representing a chemically crosslinked system, whereas systems such as syndiotactic polystyrene or high density polyethylene are formed by a thermoreversible gelation mechanism, representing a physically crosslinked system. The physical properties of the aerogels depend greatly on the type of monomers or polymers, solids

concentration, and the solvent type. The polymer gels are converted into aerogels using a process called 'supercritical drying'. The aerogels produced have a combination of pores with sizes in the micro-(< 2 nm), meso- (2-50 nm), and macro-(> 50 nm) pore range. The specific surface area of the polymer aerogels ranges from 300-900 $m^2/g$[2–5]. The extremely high surface areas provided by these materials make them ideal choices for applications in adsorption of small molecules thus facilitating their use in filtration and separation applications. The thesis is made up of several chapters, with each chapter aimed at advancing the understanding and applications of these materials in separation of harmful, toxic substances from liquids. The thesis is divided into 6 chapters: chapter II gives a comprehensive overview about the polymer aerogel technology, the polymer aerogel systems used, their applications and the potential to use these materials for applications in oil-water emulsion separation, surfactant removal and separation of per-and polyfluoroalkyl substances also known as PFAS for purification of water along with the current state of art to solve these pressing filtration and separation problems. The original work conducted in the thesis is presented in chapters III, IV, V, and VI. Chapter VII presents a summary along with recommendations for future work.

Chapter III deals with building a fundamental understanding in regard to use of polymer gel and aerogel systems for removal of small organic molecules from liquids. This chapter forms the foundation of the thesis by answering the primary hypothesis of this work that polymer aerogels due to their high specific surface areas, high pore volume and interconnected pore architecture would adsorb large amounts of organic molecules from liquids compared to conventional porous or fibrous materials. In this chapter, we studied the adsorption of non-ionic surfactants namely polyethylene oxide-polypropylene oxide-polyethylene oxide (PEO-PPO-PEO), by three polymer gel systems such as syndiotactic polystyrene (sPS), polyimide (PI), and polyurea (PUA), offering different levels of surface energy. All three polymer gel systems were predominantly meso- and

macro-porous in nature. The adsorption of the surfactant was evaluated for two different structurally different regimes of the surfactant namely below the critical micelle concentration (CMC) and above the CMC. The first surfactant studied was a Pluronic L35 (molecular weight ~1900 g/mol) surfactant. It was found that the syndiotactic polystyrene gels adsorbed the highest amount of this surfactant followed by the polyimide and polyurea gels and this feature was explained in terms of the surface energies provided by the three polymer gels. Subsequently, the effective concentration of the adsorbed surfactant within the gel was calculated and it was found that this concentration was ~10, 6 and 2 times higher for the sPS, PI and PUA gels suggesting an energetically favorable large driving force for the adsorption of the surfactant within the gel. The next question that we answered was whether the surfactant interacts with the nanofibrous surface of the polymer or was merely confined within the pores of the polymer gels. This information was obtained using solution $^{1}$H NMR analysis of the surfactant adsorbed polymer gels. It was found that the surfactant interacted with the sPS surface most strongly followed by the PI and finally by the PUA gel, as implied from the extent of the surfactant $^{1}$H peak broadening effect. Another important information provided by the NMR analysis was that the adsorbed surfactant interacts strongly with the polymer gel at concentrations below the CMC whereas above the CMC the surfactant starts to lose its interaction ability with the polymer gel and is possibly trapped as micelles within the pores of the gel. To further strengthen the hypothesis regarding the confinement and entrapment of surfactant micelles above the CMC, two other PEO-PPO-PEO surfactants namely Pluronic P123 (molecular wt.~ 5,800 g/mol) and Pluronic F127 (molecular wt.~ 12,600 g/mol) along with Pluronic L35 with different micelle sizes of ~ 36.8, 14.5 and 2.7 nm were evaluated for their adsorption performance. It was found that the micelle size played a significant role in deciding the adsorption performance of the surfactant with the smallest micelle size surfactant (Pluronic L35 ) being adsorbed in higher amount compared to Pluronic P1233 followed by the Pluronic F127 surfactant. The results of this study presented an important first step toward

understanding of demulsification of surfactant stabilized oil−water emulsion systems using high surface area polymer gels which was studied in Chapter IV.

Chapter IV documents results on translating the surfactant adsorption abilities of the polymer gels studied in chapter III for demulsifying surfactant stabilized oil-water emulsions. Four different polymer gels namely sPS, PI, PUA and silica were evaluated for their oil-in water emulsion separation performance. The emulsions were prepared with a non-ionic PEO-PPO-PEO block copolymer surfactant i.e. Pluronic L35. The polymer gels were dipped in the emulsion for 24 h and optical microscopy were taken to count the number of oil droplets and measure their sizes before and after the polymer gels were bought in contact with the emulsion. The emulsions which were bought in contact with a sPS, and PI gel showed significant reduction in the number of oil droplets whereas the PUA and silica gels did not show a significant change in the oil droplet count or sizes. The sPS gel showed a higher emulsion separation efficiency compared to the PI gels. It was expected that the depletion of the surfactant molecules from the emulsion would result in coalescence of oil droplets and hence, larger oil droplets would be observed in the emulsion but that was not the case. Instead, the number of oil droplets in the emulsion decreased. This suggested absorption of oil droplets by sPS and PI gels once the surfactant molecules were removed from the emulsion. The replacement of water present originally within the polymer gels upon contact with oil studied. It was observed that oil preferentially wetted the surfaces of sPS and PI gels. It was also observed that the emulsion separation performance scaled directly with the surfactant adsorption ability of the polymer gel. This was established using an emulsion stabilized by Pluronic F127 surfactant. The sPS gel did not adsorb the Pluronic F-127 surfactant as efficiently as it adsorbed the Pluronic L35 surfactant. Thus, poor emulsion separation was observed for the former. Atomistic simulations were performed to understand why the short chain Pluronic L35 surfactant adsorbed more effectively on the Pluronic F127 surfactant in terms of their structural configuration

at the sPS-water interface, their interaction energy, their hydrogen bonding, their occupied surface area and the possibility of forming higher order structures.

The results from surfactant adsorption and emulsion separation by polymer gels were exploited by fabricating functional polymer aerogel coated glass fiber media and using these for separation of emulsified water-in ultralow sulphur diesel fuel (ULSD) emulsion. Such results are discussed in Chapter V. The presence of emulsified water droplets in diesel fuel is a long standing problem which has proven to be detrimental for fuel ignition performance and the engine components. The aim of this work was to fabricate a high quality factor filter media which has a high water droplet separation efficiency along with a low pressure drop. This was achieved by means of several cooperative filtration mechanisms such as size exclusion, coalescence filtration, surfactant adsorption, and water absorption working in tandem to separate the emulsified water droplets from diesel fuel. A dual wettability filter media was fabricated by dip coating a silica-syndiotactic polystyrene aerogel onto a glass fiber mat, which acts as a mechanical support for the aerogel. The high surface area and high pore volume composite media separated the water droplets with an efficiency of ~ 92% whereas the control glass fiber media (conventionally used for this purpose) showed a separation efficiency of mere 30%. The mechanism by which the water droplets were separated so efficiently by the aerogel coated glass fiber composite media was illustrated in this work. Size exclusion of water droplets by the abundant meso- and macro-pores of the filter media and surface coalescence of water droplets into large sizes facilitated by the presence of the high surface energy silica aerogel, were found to be dominant filtration mechanisms. In addition, the presence of the high surface area, high interfacial energy silica aerogel on the fiber media allowed removal of the surfactant from the system which possibly eased the process of droplet coalescence. However, surfactant adsorption and water absorption were found to be time-

dependent processes and therefore, may have played a minor role in the separation of the water droplets.

Chapter VI aimed at addressing another emerging and pressing challenge in front of the filtration and separation industry today, i.e., separation of PFAS molecules from water. For over 9 decades, the PFAS molecules have been widely used in several applications ranging from production of fluoropolymers, as surfactants, for manufacturing water and oil-repellant coatings, heat resistant coatings, firefighting foams, etc. Therefore, these molecules have been all around us for a long time and over a period of these 9 decades have leached into our water sources and severely contaminated it. The negative impacts of drinking PFAS contaminated water on human health have been discovered and it was in 2022 that the U.S. environmental protection agency released health advisory limits for permissible amounts of four PFAS molecules namely perfluorooctanoic acid (PFOA), perfluorooctane sulphonic acid (PFOS), perfluorobutanoic (PFBA)/ perfluorobutane sulphonic acid (PFBS) and the Chemours produced GenX chemicals in drinking water. The limits set for the two primary PFAS molecules namely PFOA and PFOS are extremely stringent at 4 ng/L. To address this issue, in this work, we used meso-macroporous sPS polymer wet gels for removal of PFOA from water. The evaluation of the adsorption performance of sPS was done at environmentally relevant concentrations of PFOA in water i.e. < 1 µg/L. The adsorption experiments were carried out in a batch mode setup where the sPS gels were dipped in different concentrations of PFOA in water for a specified period. Mass spectrometry was used as the analytical technique to quantify the amount of PFOA in water. It was found that the sPS gels were highly effective in removal of the PFOA molecules from water. Specifically, the sPS gels showed a 99.98 % separation efficiency of PFOA when present at a concentration of 1 µg/L in water. In addition, the adsorption kinetics of PFOA was studied along with the effect of sPS pore size and pore volume for PFOA adsorption. Further, benchmarking experiments were carried out

to compare the performance of conventional adsorbent media such as activated carbon and ion-exchange resin. This work provided solid groundwork for qualifying meso-macroporous polymer gels as promising materials for removal of PFAS molecules to purify drinking water.

# CHAPTER II

# BACKGROUND AND LITERATURE REVIEW

## 2.1 Polymer Gels and Aerogels

### 2.1.1 Overview

Polymer gels and aerogels are a group of three-dimensionally crosslinked porous polymer networks which can be categorized into two groups namely a chemical gel or physical gel[6]. A chemical gel is formed by a network of covalent bonds whereas a physical gel is formed by a reversible gelation mechanism by externally induced topological change of chains. When there is a liquid entrapped within the porous network it is called a gel and when the liquid is replaced by air, it is called an aerogel. Aerogels were first reported by Kistler in 1931 in a paper titled " Coherent expanded aerogels and jellies"[1]. In this paper, Kistler showed that a liquid present within a porous polymer network can be replaced by air with little to no shrinkage by using a liquid which has a low critical temperature. The process used to make the aerogel was as follows: the polymer gel or jelly was prepared in a suitable solvent followed by replacing the solvent with a low critical temperature solvent such as alcohol or ether. Subsequently, the polymer gel was placed in an autoclave and the temperature was raised to above the critical temperature while maintaining the pressure at or above the vapor pressure of the solvent, to avoid evaporation of the solvent. The liquid solvent gets converted directly to a gas with minimum capillary pressure on the polymer

network, hence preserving the porous morphology. Extremely low density (0-1 g/cm$^3$) materials could be prepared using this method. Kistler developed several organic and inorganic aerogels such as metal oxide, silica, cellulose, egg albumin using this method. The process used by Kistler was however extremely tedious and time consuming. It was only thirty years later that Tiechner et al. improved the aerogel preparation process and considerably reduced its preparation time from days to several hours[7]. Tiechner et al. prepared a silica aerogel using a sol-gel transition method followed by supercritical drying to make it. Tetramethyl orthosilicate (TMOS) along with methanol was used as the precursor material to form the aerogel which was later replaced by a less toxic alternative named, tetraethyl orthosilicate (TEOS). Earlier it was methanol, that was subjected to supercritical conditions to convert it into a gas. But the critical temperature and pressure for methanol for example were 243 ℃ and 7.9 MPa respectively. This was subsequently succeeded by the use of liquid carbon dioxide which had a significantly low supercritical temperature of 50 ℃[8].

Applications of aerogels were limited until ~ 1970's, when they were found to be suitable for Cherenkov radiation detectors[9]. The refractive index of the silica aerogel was in the range of 1.01-1.10 and therefore its detection threshold for pion detection was calculated to be 0.3-1 GeV/c. Detecting particles with momentum lower than 2.4 GeV/c was problem back then and the use of the silica aerogel seemed to address this problem effectively. Parallelly, several researchers then began exploring these materials and widening their scope for various applications. Aerogels were a unique class of materials with outstanding properties, including high porosity (> 90%), extremely low density (as low as 0.002 g/cm$^3$), low thermal conductivity[10,11], low dielectric constant (as low as ~ 1.03)[12,13] and low refractive index[4,14] and high surface area (200- 1000 m$^2$/g)[15,16]. These unique properties enabled the use of aerogels for various applications such as catalysts[17], thermal insulators[18,19], radiation detectors, cosmic dust collection[20], capacitors, drug delivery vehicles[21,22], energy storage[23] and many more. In 1997 and 2004, NASA used aerogels in its space exploration

programs called the Mars Pathfinder and Stardust, respectively[24]. In the former, aerogel was used as a thermal insulator to protect the batteries of the rovers from extreme temperatures of Mars whereas in the case of the latter, silica aerogel was used to capture particles. The broad commercialization of aerogels was however limited largely due to their weak mechanical strength and high costs until the 2000's when exciting developments led to development of flexible mechanically strong aerogel systems. Aspen Aerogels was the first company to commercialize the aerogel technology. They developed a novel aerogel composite blanket by casting silica gel onto a fibrous mat and subsequently supercritically drying the blanket. Since then Aspen has developed several products under the Pyrogel and Cryogel category for high temperature and cryogenic temperature insulation applications[25]. Today several researchers are working with innovative ideas and designs to create robust functional aerogel materials to broaden the scope of these materials[3,26–28].

### 2.1.2 Syndiotactic polystyrene aerogels

Syndiotactic polystyrene (sPS) was first synthesized in 1985 by Ishihara et al.[29,30] It was prepared using activated titanium as a polymerization catalyst and methyl aluminoxane as co-catalyst. The melting point of sPS was about 270 ℃ which is about 40 ℃ higher than an isotactic polystyrene[31]. Compared to its isotactic variant, sPS has a higher crystallization rate which is comparable to that of polyethylene which gives it a great advantage. This enabled advantageous processing benefits by extrusion and injection molding and post commercialization of the transition metal catalyst, sPS was commercialized in 1999. High heat resistance, excellent chemical resistance to acids, bases, water, low polymer density (~ 1.05 g/cm$^3$), low moisture absorption are some of the advantages of sPS over other polymers. The crystallization of sPS is in a planar zigzag configuration with a periodicity of 5.06 Å. sPS has been used in various applications in

automotives, electrical appliances and electronic devices. One major drawback of sPS is its highly brittle nature which is overcome by addition of fillers or blending it with other materials[32].

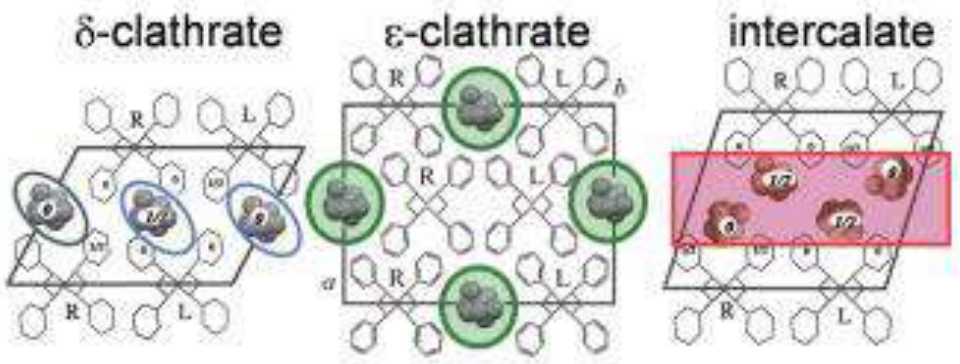


Figure 2.1. Representation of the three different sPS cocrystal structures[33] *Reproduced with permission from Reference 33 Copyright Royal Society of Chemistry 2010*

sPS exhibits a polymorphism behavior which suggests it can crystallize into various different crystalline forms such as α, β, γ, δ, ε; and several other non-equilibrium structures. The processing conditions play a great role in determining the crystallization form of the sPS. For example, the α-, β- form with a planar zig-zag configuration is adopted as a result of melt crystallization or thermal annealing[31]. The other three forms i.e. γ, δ, ε are adopted when sPS undergoes solvent processing. In presence of a suitable solvent sPS has the ability to host the solvent molecules within the polymer network which assumes a s(2/1)2 helical configuration[34,35] and form co-crystals taking one of the three mentioned configurations. The sPS co-crystals are called clathrate and generally have a guest/monomer unit ratio of 1:4. The images of guest molecules trapped within a sPS network structure are shown in Figure 2.1. It is the δ- and ε- form of the sPS which is of typical interest for the formation of sPS gels and aerogels. The guest molecules in the case of the δ- form are isolated. In addition, the plane of these guest molecules is perpendicular to the helical axis. Solvents such as toluene[36], dichloroethane, carbon disulfide[37], iodine[38], ortho-dichlorobenzene[39] form the δ-clathrate form. The ε-clathrate form is the one in which the guest molecules are imprisoned into the channel-shaped cavities. For planar guest

molecules, molecular planes tend to assume orientations parallel to the axis of the crystalline chain contrary to it being perpendicular in the case of the δ- clathrate form.

It is known that sPS forms physical gels with several organic solvents. The gels where the polymer-rich phase is characterized by the helical s(2/1)2 confirmation forms stable gels. It has been confirmed with the X-ray diffraction and Fourier transform infrared experiments that the polymer rich phase consists of the co-crystalline phase[40]. Several solvents such as toluene, benzene, chloroform, tetrahydrofuran, etc. have been used to form the sPS gels and aerogels[41,42]. Owing to its polymorphic nature, care should be taken to access the helical configuration and not locking the planar configuration. It has been found that the solvent type and quenching rate play an important role in deciding this. For solvents such as tetrahydrofuran[43], toluene[41], chloroform[44] which are considered good solvents for sPS, the helical configuration exists as a thermodynamically stable state and can be accessed easily by merely cooling the sPS-solvent solution at low solid concentrations. For the bad solvents, the planar configuration is favored over the helical configuration and the latter can be achieved only through rapid quenching. The sPS gels formed using good solvents are of interest to us due to their ease of formation by easily accessing the helical configuration.

Typically, to form the sPS gel using a good solvent, let's take for example, toluene. Figure 2.2 shows the temperature vs sPS concentration phase diagram for a sPS-toluene system. As per the phase diagram, a single liquid phase sPS-toluene mixture is formed at temperatures > 110 °C with sPS solid concentration of < 0.1 g/cm$^3$ of toluene. The system then is allowed to cool where it phase separates into a polymer-rich and solvent-rich phases by going through spinodal decomposition[34]. This leads to rapid vitrification of the system and locking of the fibrillar polymer network. This structure is termed as the gel. The gel subsequently goes through solvent exchange steps and finally through the supercritical drying process to form the sPS aerogel.

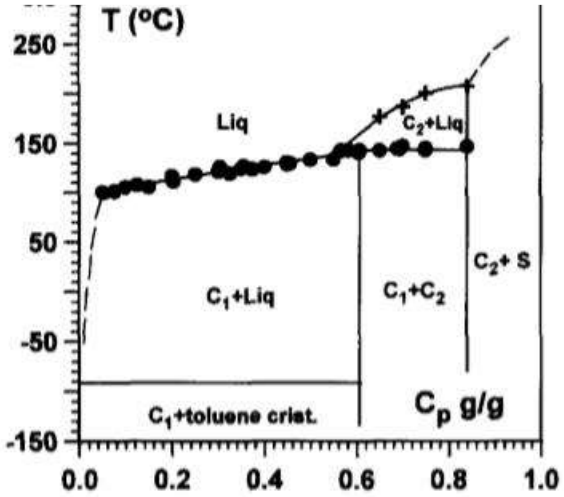


Figure 2.2 Phase diagram of sPS in a good solvent i.e. Toluene. $C_1$ corresponds to the helical conformation phase[41] *Reproduced with permission from Reference 41 Copyright Elsevier 1997*

Several research papers reported various modifications possible for sPS aerogels in terms of its surface energy, surface area, and pore sizes. Wang et al. reported the surface energy modification of sPS aerogels by creating hybrid aerogels with silica[45] or by using polyethylene oxide as a wettability modifier[46].The creation of the hybrid sPS-silica aerogel led to ~ 2 times higher surface area and higher mesoporosity due to the incorporation of the silica aerogel. The incorporation of the PEO along with the sPS led to improved hydrophilicity for the sPS aerogels which showcased a rose petal effect which is contrary to the lotus leaf effect shown by

superhydrophobic sPS aerogels. Wang et al.[47] and Venditto et al.[48] also reported a sulfonated syndiotactic polystyrene (ssPS) for improving the volatile organic compound absorption capacity and use of polystyrene for other applications such as air filters working on particle separation by electrostatic forces, supercapacitors. Kim et al. reported use of sPS aerogels for applications in air filtration for nanoparticle capture. The sPS aerogel monoliths were able to separate the nanoparticles from air with an almost 99.99 % separation efficiency and with an air permeability of the order of $10^{-10}$ $m^2$. Depth filtration was identified as the filtration mechanism[49]. Another work by Kim et al. reported an electrostatically active hybrid sPS polyvinylidene (PVDF) aerogel for separation of airborne nanoparticles. The hybrid material showed a higher separation efficiency (~99.999%) compared to a sPS aerogel. Recently Kulkarni et al. reported the use of syndiotactic polystyrene aerogel coated 3D constructs for removal of emulsified water droplets from diesel fuel, hence extending the application of sPS aerogels for liquid filtration[50]. Absorption of volatile organic compounds such as toluene, benzene, phenol from water was reported by Mancuso et al.[51] The ability of sPS aerogels to absorb VOC's has also been explored to make chemical sensors for VOC vapors[52].

### 2.1.3 Polyimide aerogels

Polyimide is a polymer with excellent chemical and thermal stability. They are thermally stable upto 350 °C[53], have low dielectric constant[54] and excellent durability. Polyimide aerogels were first reported in a patent by Aspen Aerogels in 2003[55]. A combination of diamine and dianhydrides were discussed in this patent for preparation of polyimide aerogels. Kawagishi et al. reported the fabrication of polyimide aerogels with high porosity values using supercritical drying process since polyimide aerogels prepared prior to his work had low porosity values since they were not able to preserve the pore architecture[56]. Kawagishi was able to form different morphologies of the polyimide aerogel such as crisp fragments, minute network and highly

connected beads with sizes in the range of 50-800 nm. The competition between liquid-liquid phase separation and crystallization induced due to the chemical reaction between the dianhydride and diamine resulted into these different structures. Polyimides are synthesized using the two step process pioneered by DuPont. The first step is the formation of polyamic acid where there is a reaction between the anhydride and the amine groups. Once, the polyamic acid with dianhydride end group is formed, a multifunctional amine is added to the solution, to form a crosslinked network structure. In the second step, the amic acid groups are dehydrated using a suitable dehydrating agent to form the imide group[57].

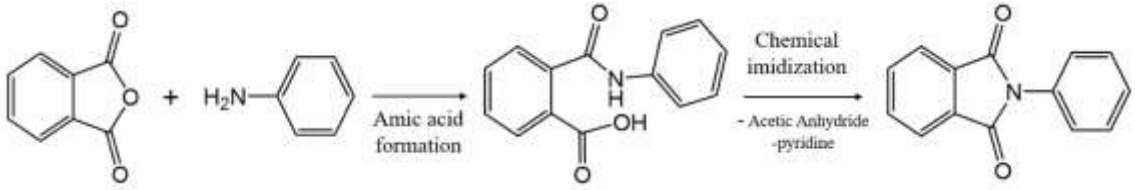


Scheme 2.1 Formation of the amic group by reaction of pthalic anhydride and aniline as model compounds followed by formation of the imide group by dehydrating the amic group using acetic anhydride and pyridine.

The first step of the reaction is reversible; however, the forward reaction has a much higher reaction rate compared to the backward step. This large forward reaction rate leads to the formation of a high molecular weight polyamic acid. The rate of reaction is largely dependent on the choice of monomers. This step is a nucleophilic acyl substitution reaction, where the amine group ( nucleophilic) attacks the carbonyl group (electrophilic). Therefore, more the electrophilicity of the carbonyl group, the faster is the reaction rate. The electrophilicity of the carbonyl group is estimated by looking at its electron affinity values. For example, pyromellitic dianhydride (PMDA) with an electron affinity value of 1.98 eV has a faster rate of polyamic acid formation compared to a biphenyl-tetracarboxylic acid dianhydride (BPDA) with electron affinity value of 1.38. Similarly, the nucleophilicity of the amine group also affects the rate of the first reaction which forms the polyamic acid[57]. Solvents are also said to affect the rate of polyamic acid formation. Dipolar aprotic

solvents such as tetrahydrofuran, dimethyl formamide, dimethylacetamide significantly speed up the first reaction and hence are used for preparation of the polyimide aerogels[2]. Furthermore, the presence of acidic solvents also tend to have a higher reaction rate compared to basic solvents. The presence of water is extremely detrimental to the synthesis of the polyamic acid since water competes with amine to react with the dianhydride and forms dicarboxylic acids, which results in a lower molecular weight of the polyamic acid chain. The next step in the reaction as mentioned above is the conversion of the amic groups into imide groups. This can be achieved by two ways: i) chemical imidization or ii) thermal imidization. The initial polyimides that were prepared were said to be thermally imidized by raising the temperature of the polyamic acid system to 200 °C. This causes closing of the amic acid ring and liberation of water molecules. In chemical imidization, a dehydrating agent such as acetic anhydride or n-butyric anhydride in the presence of catalysts such as pyridine, triethylamine, n-methylmorpholine (added to speed up the imidization reaction) are added to get rid of the water group from the amic acid groups to form the imide group[57–59]. This is called the cyclo-hydration reaction.

The initial polyimide aerogels to be prepared were mechanically weak and to address this aspect, Kawagishi utilized a trifunctional crosslinker to increase the crosslink density of the system and hence, improve its mechanical strength. A polyimide aerogel with > 90% porosity was formed as a result of this effort[56]. Since then, there have been several researchers working towards improving the mechanical properties of the polyimide aerogels by tuning the morphology, pore size, surface area, and their gelation times. At NASA Glenn Research Center, Meador et al. carried out pioneering work in this domain of polyimide aerogels. One of their work, reported formation of polyimide aerogels with different mechanical and physical properties by using several dianhydrides and diamines[3]. The structure-property relationship knowledge was utilized in this work to create polyimide aerogels which have less shrinkage, high flexibility which could even be

folded back onto themselves without damage to the pore architecture. The high flexibility polyimide aerogels were formed by using 4,4′-oxydianiline or 2,2′dimethylbenzidine as the monomers. It should be noted that this formulation could be used to create thin polyimide aerogel films using a roll-to-roll casting process. Furthermore, it was found that the polyimide aerogel prepared using p-phenylene diamine as the backbone diamine led to an aerogel with high onset of decomposition (above 600 °C). In another work by Guo et al., the flexibility of the polyimide aerogel system was increased by adding an aliphatic diamine i.e. 1,1,2-dodecyldiamine (DADD)[60]. Along with variation in monomers used for polyimide aerogel synthesis, a study reported the effect of different crosslinkers on polyimide aerogel properties . Several crosslinkers such as 1,3,4-tris(4-aminophenyl)benzene (TAB)[56], 2,4,6-tris(4-aminophenyl)pyridine (TAPP)[61], amine functionalized polyoligomeric silsesquioxane (POSS)[58] and 1,3,5-benzenetricarbonyl trichloride[62] have been studied. Along with variations in the mechanical and physical properties of the polyimide aerogels, there has been a considerable amount of work done to vary the shape and pore sizes of the polyimide aerogels. Polyimide aerogels have been fabricated in monolith, spherical microparticle[63], pill shaped microparticle[64], gyroid shaped complex architectures[26] and lego shaped blocks[28]. Recently, Agrawal et al. created a polyimide aerogel based air filter by coating them on fabrics[65]. Farrell et al. and Teo et al. also showed that the polyimide aerogel foams with pore sizes ranging from mesopores (2-50 nm) to macrovoids (micrometer sized) can be created by using an emulsion templating process[66,67]. Meador et al. also reduced the dielectric constant of the polyimide aerogel from 1.30 to 1.08 by using a fluorinated dianhydride monomer[68]. This opened up applications of the polyimide aerogel for antenna substrates. Polyimide aerogels due to their superior properties have been utilized for several applications ranging from thermal insulation, outer space exploration, filtration, etc.

2.1.4. Silica aerogels

Silica aerogels were the first type of aerogels to be produced by Kistler in 1931[1]. Silica aerogels are prepared in a two-step process - (i) hydrolysis of the precursor chemical which is generally a tetraethyl orthosilicate (TEOS) or a tetramethyl orthosilicate (TMOS) and (ii) condensation of the -hydroxyl (-OH) groups to form the crosslinked gel network (Scheme 2.2). Teichner was first to use tetra alkoxysilanes as precursors as a replacement of sodium silicate, used by Kistler. This led to reduction in the time required to prepare these materials from several days to a couple of hours[7]. Once the gel network is formed due to the condensation reaction, suitable solvent exchange steps are done followed by supercritical drying step to get the silica aerogel. Hydrolysis and condensation reactions are generally carried out in solvents such as ethanol or methanol since the alkoxysilanes

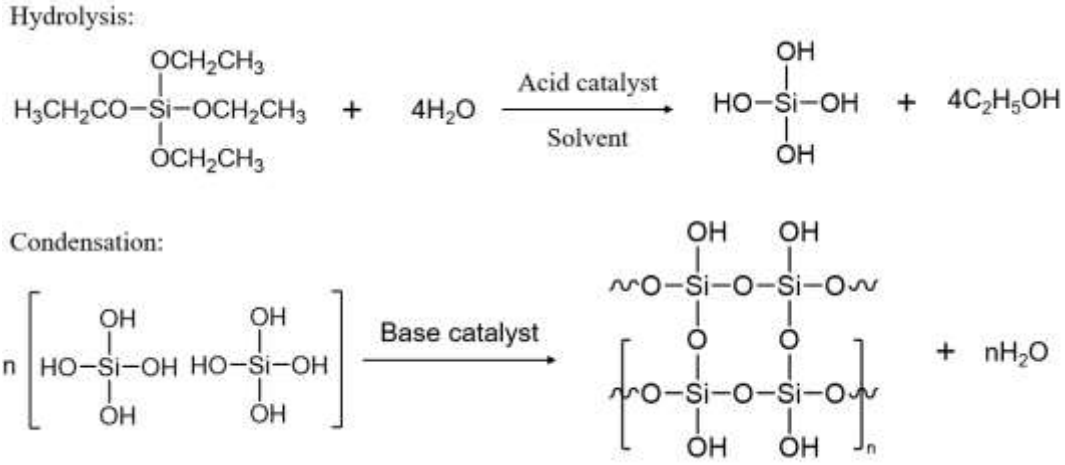


Scheme 2.2 Chemical reaction scheme for formation of silica gel using TEOS as the precursor.[69]

are easily soluble in it. In addition, alcohols can be easily solvent exchanged with liquid carbon dioxide for the supercritical drying process, hence reducing the solvent exchange steps and the time for aerogel preparation. The choice of alcohol has a great effect on the pore structure of silica aerogel. A comprehensive review regarding the different solvents, precursors, gelation conditions used by different researchers is given by Soleimani et al.[70] The hydrolysis reaction needs to be

catalyzed. It could either be acid catalyzed, base catalyzed, or a two- step acid/base catalyzed reaction. Chemicals such as hydrochloric acid, sulphuric acid, nitric acid could be used for the acid catalysis whereas ammonia is used for carrying out a base catalyzed hydrolysis reaction. An acid-catalyzed reaction leads to formation of long linear chains with almost no crosslinking whereas the base catalyzed structure leads to formation of colloidal particles. But the reaction rates of a single catalyst system are very slow. Brinker et al. studied the effect of pH on the hydrolysis and condensation reaction rates (shown in Figure 2.3) and eventually proposed a two-step catalysis process wherein, the hydrolysis step was carried out in an acid catalyst and the condensation step was carried out in a base catalyst to increase the rate of gel formation[71].

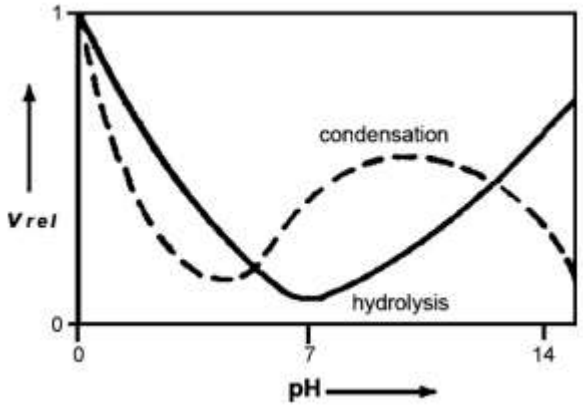


Figure 2.3 Dependence of the hydrolysis and condensation reaction rate for silica gel formation on pH of the solution[70] *Reproduced with permission from Reference 70 Copyright Elsevier 2008*

The solution to gel transition occurs when both the hydrolysis and condensation reactions are complete. The crosslink density of the gel depends on the concentration of the precursor used. The silica gel is a network of primary silica spherical particles (< 1 nm) aggregating together to form a secondary silica particle of ~10 nm size, which are connected to each other in a pearl-necklace type arrangement as shown in Figure 2.4. Such a weak interconnected particle morphology is the reason for its extremely brittle nature. The weak mechanical properties of the silica aerogel hindered its widespread commercialization for quite some time. To address this

problem several researchers came forward and began to create silica aerogels with enhanced mechanical properties using reinforcement methods, post processing techniques, and modifications in the synthesis steps.

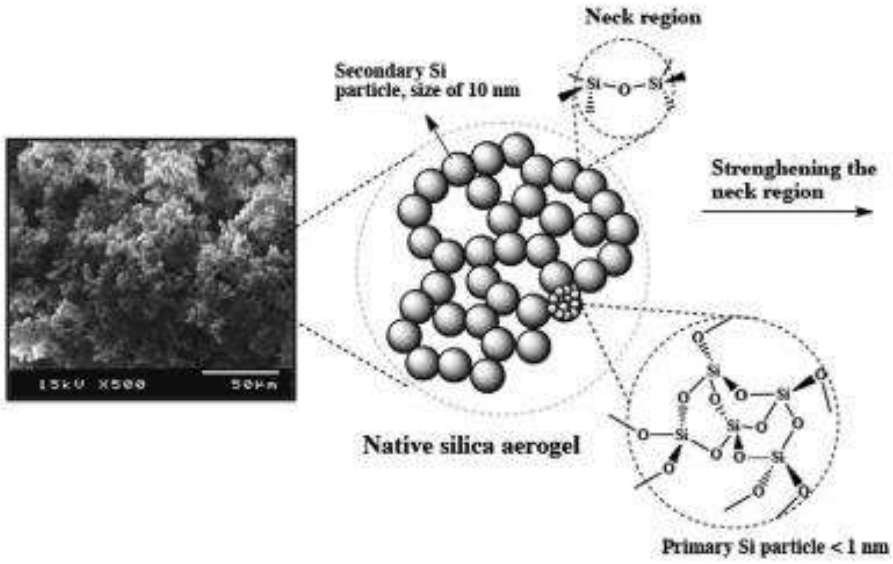


Figure 2.4 Schematic of primary and secondary silica particles along with an SEM image of the silica aerogel[69]. *Reproduced with permission from Reference 69 Elsevier 2014*

Yang et al. created a fiber reinforced silica aerogel which could bear a higher load compared to a non-reinforced silica aerogel without sacrificing its thermal insulating properties[72]. In another work by Duan et al., silane precursors such as TEOS were mixed with silane-end-capped polyurethanes for improving the mechanical strength of the silica aerogel[73]. Leventis et al. reinforced the silica aerogels by reacting the hydroxyl end groups present on the secondary silica particles with isocyanates to widen the neck region. This conformal coating on the silica particles led to strengthening the neck region and resulted in silica aerogels with a 300 times higher force to break[74]. Meador et al. added amine functionality to a TMOS derived silica aerogels[75]. The amine group was then reacted with di-tri-tetra-functional epoxies. This led to an increase in the density of the aerogel by 2-3 times but also led to a 2 order of magnitude in the mechanical strength of the

aerogel. Wang et al. grew silica aerogels within a syndiotactic polystyrene aerogel to create a hybrid high mechanical strength organic-inorganic aerogel system[45]. In addition, several researchers incorporated fillers such as ceramic fibers[76], polymer nanofibers[77–80], and fiber glass[81] to form silica aerogel composite systems. Silica aerogels are widely used for various applications due to their exclusive properties and tunable and versatile chemistry. The extremely high surface area (900-1000 $m^2/g$), low thermal conductivity (0.004-0.003 W/mK), low dielectric constant (1.1-1.2), low refractive index, high porosity (>90%) has led to its niche applications in thermal insulation, high energy physics molecular separation, air filtration[9,16,45,82].

### 2.1.5 Polyurea aerogels

The first report of polyurea aerogels was in the later 1990s by Vos and Biesmans[83]. A series of organic aerogels namely polyurea, polyurethane, polyallophanate were mentioned in it. Subsequently, Lee et al. made a comparison between polyurea, silica, and polyurethane aerogels in a paper published in 2009[5]. The polyurea was synthesized by reacting 4,4'-diphenylmethane diisocyanate (MDI) with a long chain aliphatic amine in the presence of a triethylamine catalyst with acetone as the solvent. The polyurea gels were similar to silica aerogel with nanoparticle morphology. The resultant aerogel had low density (0.12 $g/cm^3$), high porosity (~90%), and high surface area (190 $m^2/g$). Later, Leventis et al. reported a synthesis approach in which water was used as a reactant instead of the trifunctional amine to obtain the polyurea aerogel[84].

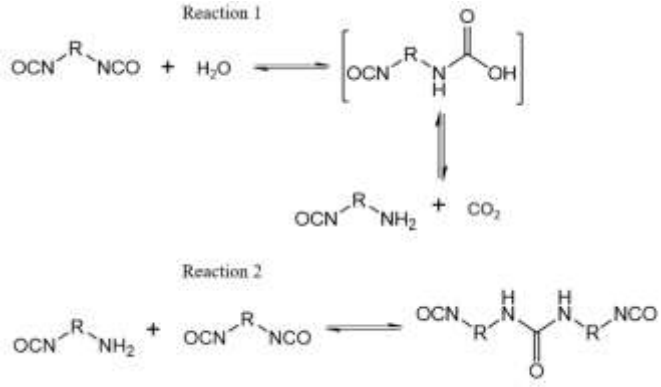


Scheme 2.3 Reaction scheme of reacting a diisocyanate with water to form polyurea[84]

Scheme 2.3 depicts the reaction scheme for formation of polyurea from a starting diisocyanate by the method developed by Leventis et al.[84] Reaction 1 is a reaction between the diisocyanate and water in the presence of a catalyst to form the carbamic acid. The carbamic acid yields an amine because of decomposition of the unstable carbamic acid. This causes the release of carbon dioxide. Reaction 2 is a reaction between the amine byproduct of reaction 1 and the unreacted isocyanate monomers to form the urea linkage. They worked with Desmodur N3300A, Desmodur RE and Desmodur N3200, three different types of multifunctional isocyanates to produce polyurea aerogels. The aerogels were found to have variable morphologies from fibrous to particulate and it varied with varying the concentration of the isocyanate. It was found that the primary particles aggregated into secondary aggregates to form fibers. Polyurea aerogels with different densities (0.016-0.055 g/cm$^3$) were prepared and characterized. However, it was seen that there were several macrovoids present in the polyurea aerogels. This was possibly due to the generation of carbon dioxide from the reaction between isocyanate and water. To circumvent this, Shinko et al. prepared polyurea aerogels with amine-isocyanate reaction[85]. They used MDI, 2,2'-dimethylbenzylamine or 4,4'-oxydianiline along with 1,3,5-Tris(4-aminophenoxy)benzene (TAB) as the crosslinker. They also varied the number of repeating units forming a single polyurea oligomer to study its effect on crosslink density and aerogel properties. Predominantly mesoporous aerogels were obtained by this synthesis route, with mean pore diameter in the range of 9-16 nm, surface areas of 100-300 m$^2$/g, and porosity ~ 80-90 %. Shinko et al. went a step ahead and produced crosslinked polyurea-co-polyurethane aerogels with hierarchical pore architecture and low stiffness[86].

## 2.2 Separation of oil-water mixtures and emulsions

### 2.2.1 Overview

This section discusses the emulsion separation problem, its relevance, and the various technological solutions that have been developed to address this problem. In addition, a brief discussion is presented regarding definition of emulsions, their classification, formation, and stabilization of emulsions by adsorption of emulsifiers or surfactants at the oil-water interface, the selection of a suitable emulsifier, and characterization of emulsions.

The separation of oil-water mixtures or emulsified oil-in-water or water-in-oil solutions is a problem which has been around for quite some time. The discharge of oily wastewater from industries such as textiles, food, pharmaceuticals, petrochemical along with frequent oil spills into the ocean has been a huge problem to tackle[87–89]. These oil spills lead to disturbance in the aquatic ecosystem. The other big problem has been with water-in-oil emulsions encountered in the automotive engine fuel, crude oil recovery processes, petroleum industry, etc[90]. Specifically, the presence of emulsified water droplets in fuel leads to detrimental effects on fuel ignition performance and other effects such as corrosion and microbial growth[91–93]. Water can enter the fuel at various stages during transportation, storage, or actual use in engine[93]. The water droplets in fuel also reduce the life of the fuel engine system parts and raises several environmental concerns due to the release of toxic gases into the atmosphere. The fuel pump causes the breakdown of large water droplets into small droplets by shear induced forces and it is extremely difficult to separate such droplets from diesel. The situation is further exacerbated by the presence of surface-active agents or additives which stabilize the oil-water interface. Therefore, removal of such micrometer sized, surfactant-stabilized water droplets from fuel has been an active area of research.

### 2.2.2 Emulsions

#### 2.2.2.1 Emulsion: Introduction, formation, stability, and industrial applications

Emulsions are a class of liquids in which two or more immiscible liquids are present. Liquid droplets of one phase called the ‘ dispersed phase’ are dispersed in the other liquid phase called the ‘ continuous phase’. They could be divided into several categories such as water-in-oil emulsions, oil-in-water emulsion, oil-in-oil emulsions, water-in-oil-in-water, or oil-in-water-in oil emulsions, etc. The formation of a stable emulsion, however, requires a third component called the emulsifier or a surfactant. The type and nature of the emulsifier plays a crucial role in determining the stability of the emulsion. There are several types of emulsifiers which could be used to form the emulsions such as an ionic surfactant, non-ionic surfactant, polyelectrolytes, mixed surfactants, and solid particles. Examples of ionic surfactants are sodium dodecyl sulphate, cetyl trimethylammonium bromide, that of non-ionic surfactants are polyethylene oxide-polypropylene oxide tri-block or di-block copolymers, alcohol ethoxylates, etc. Emulsions stabilized using solid particles are called Pickering emulsions. The stabilization mechanism for each of these surfactants is different, for example an ionic surfactant stabilizes the emulsified droplets by electrostatic repulsive forces whereas a non-ionic or a polymeric surfactant uses steric hindrance or repulsion force to not allow droplets to come close to each other.

An unstable emulsion would show one or more of the following scenarios: creaming, sedimentation, flocculation, phase inversion, coalescence, or Ostwald ripening (Figure 2.5). Creaming or sedimentation are cases where due to density difference between the two immiscible liquids phases, the dispersed phase droplets move to the top or bottom respectively when the gravitational forces exceed the thermal motion of the droplets. Flocculation is a case where dispersed droplets come together due to attractive van der Waal’s forces acting between them to form aggregates. Ostwald ripening is observed in liquids which have some degree of solubility in

each other. The smaller sized droplets in the emulsion solubilize in the continuous liquid phase with time and deposit themselves on the surface of the large droplets due to higher solubility compared to large droplets. Therefore, the large droplets keep getting larger in size and the droplet size distribution shifts toward large sized droplets. Coalescence of droplets is referred to as a process

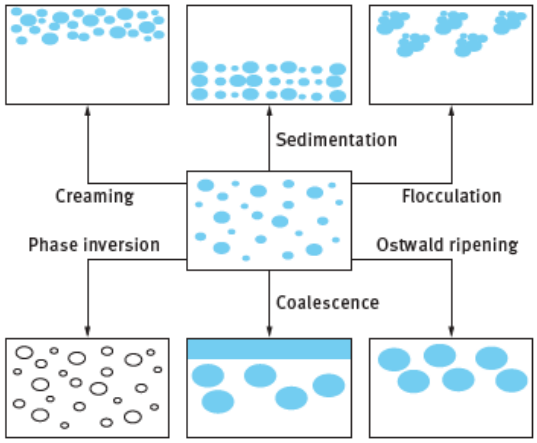


Figure 2.5. Schematic explaining the various emulsion destabilization processes[94]

of thinning or disruption of the interfacial liquid film between two dispersed phase droplets. This thin interfacial liquid film is present in the case of sedimentation or creaming. Once the liquid film between the droplets is disrupted, the droplets come together and make a larger droplet. The limiting case for coalescence is separation of the two liquids into two separate phases. Figure 2.8 depicts all these processes pictorially.

Now, let us take a look at the thermodynamics of emulsion formation. Consider two scenarios, scenario 1 has a single large droplet of area '$A_1$' and scenario 2 has several smaller droplets formed by breaking the large droplet in scenario1 with area '$A_2$'. The interfacial tension between the two liquids ($\Upsilon$) is the same for both cases. Therefore, the change in the Gibbs free energy of the system going from case 1 to case 2 is made up of two contributions, (i) the surface energy term, $\Upsilon^*\Delta A$, where $\Delta A= A_2-A_1$, this term is positive since there is an increase in the interfacial area of the system as a droplet is broken down into several small droplets. (ii) The

entropy (TΔS) term, which is also positive since the total entropy of the system increases in the presence of several small droplets. Therefore, the change in free energy of the system by breakup of a droplet into smaller droplets is always positive. Hence, emulsion formation is a thermodynamically unstable process and in the absence of external energy used in preparation of emulsions and the emulsifiers that stabilize the emulsion, the emulsion would break down by the several processes mentioned earlier[95]. The surfactant provides an energy barrier for emulsion droplets to come together, and it merely acts in kinetically stabilizing the emulsion. The stability of an emulsion is governed by the magnitude of three forces namely the van der Waal's attractive forces and the two repulsive forces namely electrostatic and steric repulsion forces. The higher magnitude of the attractive force in comparison to the repulsive force leads to breaking down of the emulsion whereas the vice versa leads to its stabilization. The electrostatic repulsive forces are created by charged surfactants species which creates an electrical double layer whose structure was given by Gouy Chapman, Stern and Grahame[96]. The steric repulsive forces are caused by non-ionic or polymeric surfactants which encapsulate the dispersed phase droplets and repel the droplets from each other. When two droplets covered with the polymeric surfactant come close to each other, one of the two scenarios would take place (i) the polymer chains at the interface overlap with each other or (ii) the polymer chains compress each other without no interpenetration. However, in both cases, the local density of the polymer chains increases in the interfacial region. If the continuous liquid phase is a good solvent for the dangling polymer chains, there is an increase in the repulsion forces between the two droplets. An effective steric stabilizer is a molecule which can completely cover the dispersed phase droplets, has good solubility in the continuous phase, and should be strongly anchored on the droplet. Hence emulsifiers such as a polyethylene oxide (PEO)-polypropylene oxide (PPO)-polyethylene oxide (PEO) (A-B-A) type are good stabilizers for oil-in-water emulsions because of the good solubility of PEO chains in water and PPO chain's strong anchoring ability to the oil droplet surface.[94] In the case of water-in-oil emulsions encountered in the

petroleum or crude oil industry, interface-active species such as asphaltenes, naphthalenic acids play the role of the emulsifier[97].

Emulsions are ubiquitous and are found in several industrial applications ranging from the food industry in products such as mayonnaise, creams, beverages to cosmetics and hygiene care products such as hand lotions, moisturizers, sunscreens, pharmaceuticals, drug delivery systems to the paints and coatings industry[98–100].

2.2.2.2 Adsorption of surfactants at the liquid-liquid interface

The interfacial tension of an interface is given by the energy per unit area. The units for it are Newton/metre or Joule/metre$^2$. Two approaches are generally used to study adsorption of surfactants at liquid-liquid interfaces, (i) the Gibbs approach and (ii) equation of state approach. We will only delve into the physical significance of these approaches and limit ourselves from the mathematical formulae and derivations related to it. Gibbs derived a relation between the interfacial tension (ϒ) and adsorption per unit area, surface excess, Γ defined in equation 2.1, where C is the concentration of surfactant in bulk solution in mol dm$^3$, R is universal gas constant, and T is temperature.

$$\Gamma = \frac{-1}{RT} \times \left(\frac{dY}{d\ lnC}\right) \tag{2.1}$$

The above equation allows us to obtain the adsorption per unit area of the surfactant from the relationship of surface tension  with surfactant concentration. The surface excess of the surfactant is the slope of the plot of surface or interfacial tension and the natural log of concentration of the surfactant. The surface excess value for the surfactant is important to understand the orientation of the surfactant molecules at the interface and to know the effects of several parameters such as ionic strength of solution or addition of other additives on the presence of surfactant at the interface. In addition, the interfacial tension vs. surfactant concentration plot also gives us the

critical micelle concentration (CMC) of the surfactant. Above CMC, the surfactant molecules form self-aggregated micelles in the bulk liquid phase. It should be noted that this approach is an idealized model and no lateral interactions between the surfactant molecules are considered. This can be applied only at low surface coverage of the surfactant where the surfactant molecules are farther apart from each other and hence have no lateral interactions. Several modified equations have been reported such as the Langmuir, Frumkin, or Szyskowski to consider the case of higher surfactant coverage at the surface[94]. All these equations have an important term called the surface excess concentration at surface saturation ($\Gamma_m$). This term signifies the effectiveness of the surfactant to adsorb at the liquid-liquid interface[101].

There are various methods used to measure the surface or interfacial tension of the liquid-air or liquid-liquid interface respectively. Category 1 methods such as the pendant drop method, and Wilhelmy plate method measure the properties of the meniscus to extract information regarding the surface or interfacial tension. These methods measure the surface or interfacial tension under equilibrium conditions. The other set of methods are the du Nüoy ring and droplet volume method which work under non-equilibrium conditions. These methods are faster but cause premature rupture or depletion of adsorbed molecules from the interface. In the Wilhelmy plate method, a plate made of glass is detached from the interface. The total force for detachment of the plate from the interface is a summation of the weight of the plate and the interfacial tension times the contact length of the plate. For the pendant drop method, a drop of oil/water is suspended from a capillary of known radius. The drop assumes a stable size at equilibrium and is a unique function of the capillary radius, interfacial or surface tension, the liquid density and gravitation forces acting on it[102].

### 2.2.3 Different methods or materials for separation of oil-water mixtures or stable emulsions

#### 2.2.3.1 Aerogels for separation of oil-water emulsions

Polysaccharide and graphene based aerogels are the ones which have been widely reported for separation of oil/water mixtures or emulsions. Polysaccharides are a group of three polymers namely alginate cellulose and chitosan. In 2021, Yu et al. reported a highly compressible and durable superhydrophobic cellulose polyvinyl alcohol hybrid aerogel for separation of water-in-oil emulsions[103]. The hybrid aerogel was created by dissolving cotton fibers into a sodium hydroxide urea aqueous solution followed by addition of *N,N'*-methylenebisacrylamide as the crosslinker. Subsequently polyvinyl alcohol was added to the mixture and allowed to react to form the cellulose-PVA hybrid aerogel. The surface of the hybrid aerogel was made superhydrophobic by depositing methyl trichlorosilane using the chemical vapor deposition method. This aerogel was also said to have a high flux and extremely high compressive stress of 490 kPa at 90 % strain. The high mechanical performance of the aerogel is able to sustain the stresses it would undergo in a liquid-liquid separation application. Because of the superhydrophobicity of the aerogel, it only allowed oil to selectively pass through its porous structure and upheld the emulsified water droplets on the upstream side. A separation efficiency of 95% was reported for removal of water droplets from cyclohexane. Zhou et al. reported a similar superhydrophobic cellulose aerogel system showing >99% separation efficiency for water-in-oil emulsions. The prepared aerogels had a water contact angle of ~ 168° which created an antifouling surface for easy water removal from the surface[104]. Liu et al. reported a superior graphene-polyvinyl alcohol Janus aerogel with dual wettability for separation of both oil-in-water and water-in-oil emulsions[105]. The aerogels were reported to have ultrahigh permeability and high rejection efficiency. In another innovative approach, Jiang et al. reported an aerogel prepared from polyacrylonitrile and polydimethylsiloxane coaxially spun nanofibers[106]. The nanofibers were first obtained by coaxially spinning the polymer solution

followed by homogenizing the nanofibers followed by crosslinking and freeze drying to obtain the corresponding aerogel. The aerogels showed an excellent water-in-oil emulsion separation performance, elasticity, and recycling. Shen et al. reported a similar nanofibrous aerogel made up of polyimide and silicone nanofilaments to produce a superhydrophobic aerogel structure[107]. It should be noted that the overarching theme behind producing materials for oil-water separation is generation of a superhydrophobic or superoleophobic surface for the emulsion separation, which facilitates permeation of only one liquid phase through the aerogel and creation of such a surface more often than not requires a treatment with another material or a surface coating approach.

2.2.3.2 Membrane separation

Several polymeric membranes have been developed for separation of oil-water emulsions. The ease of fabrication of the membranes, their high separation efficiencies, and ability to separate emulsions which have droplets of sizes < 10 micrometer makes them a good candidate for certain liquid-liquid separation applications. Ultrafiltration (UF), microfiltration (MF) and nanofiltration have evolved as the three membrane processes for separation of oil-water emulsions. Polymers such as polyacrylonitrile, polyethersulfone, polyamide, polyimides, cellulosic and polyvinylidene fluoride have been at the forefront of materials for polymer membrane preparation due to their low cost and effective performance. The porous membranes are obtained by techniques such as phase inversion techniques such as thermally induced phase separation[108], evaporation or vapor induced phase separation[109,110] or non-solvent induced[111]. Sometimes even a combination of these methods is used to prepare the membrane. The non-solvent induced phase separation (NIPS) is the most widely used technique for membrane preparation today[112]. Figure 2.6 shows the schematic for a polymer membrane formation by non-solvent induced phase separation method. Generally, a porous mechanical support is coated by a polymer solution which consists of a polymer dissolved in a good solvent. The polymer coated film is subsequently dipped in a coagulation bath which

includes a poor or non-solvent and may contain additives. The polymer film then slowly solidifies due to exchange of the solvent and non-solvent. Therefore, the solvent and non-solvent need to be miscible with each other[113]. Different applications require membranes with different physical and chemical properties and Guillen et al. have summarized this aspect in detail[111]. Adjusting several parameters such as the polymer concentration, solvent and non-solvent type or adding different additives allows to vary the pore structures of the membrane to meet the desired requirements.

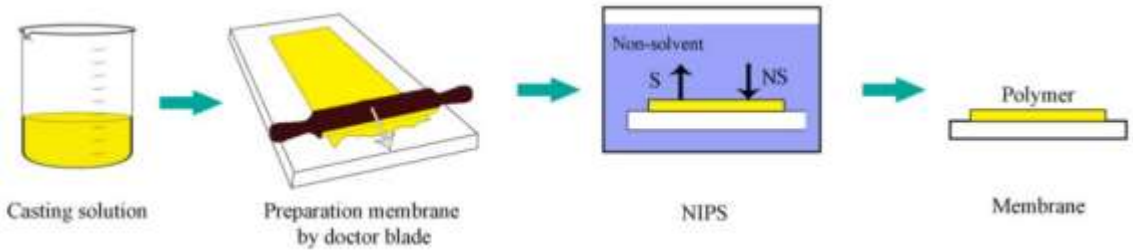


Figure 2.6 Polymer membrane formation schematic by non-solvent induced phase separation[112]

Different membrane pore structures can be obtained, for example, by having two solvent-non-solvent pairs, one which is highly miscible with each other and another which has low miscibility. The one with high miscibility leads to faster solvent-nonsolvent exchange resulting in a finger-like morphology whereas the one with low miscibility leads to a sponge like porous architecture as shown in Figure 2.7.

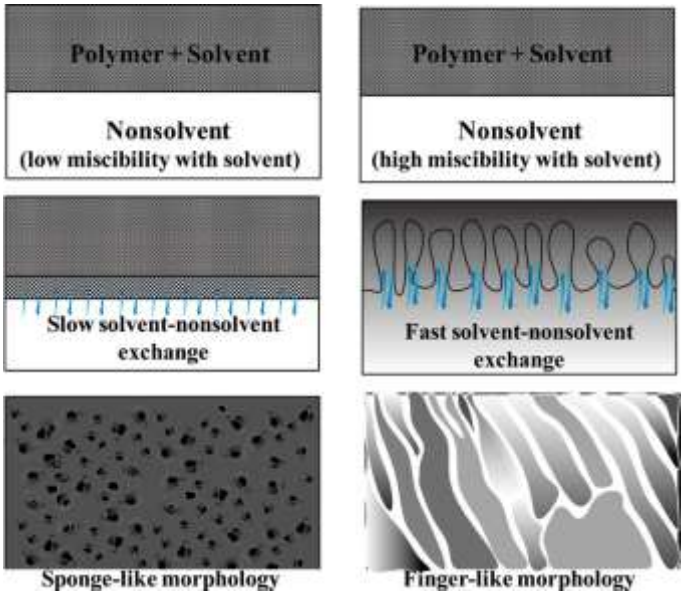


Figure 2.7 Schematic of polymer membrane formed by non-solvent induced phase separation using two different solvent-nonsolvent pairs with different miscibility[111] *Reproduced with permission from Reference 111 Copyright © 2011, American Chemical Society*

Commercial membranes are generally semi-hydrophobic in nature, with water contact angles in the range of 80-100° which leads to extensive fouling of these membranes by oils[114,115]. Several chemical and physical hydrophilization techniques have been employed to counter this problem. Chemical hydrophilization refers to the creation of a new polymer surface on the membrane or addition of hydrophilic functional groups or grafting hydrophilic polymers on the membrane surfaces. This technique allows for precise control and localization of surface hydrophilicity in addition to the long term stability of the membrane wettability. The physical hydrophilization on the other hand refers to addition of hydrophilic additives such as acetates[116], polyethylene glycol[117], inorganic substances[118], polyvinylpyrrolidone[119]. Several of these membranes have been used for oil-water mixture and emulsion separation.

2.2.3.3 Coalescence filtration using fiber based media

The membrane separation technique mentioned in the section earlier has several drawbacks such as very small pore sizes, i.e. 0.1-10 μm for microfiltration and 0.001-0.1 μm for ultrafiltration membranes, which cause high pressure drop across the membrane leading to high operational and capital costs along with severe fouling. Therefore, most of the time a pre-treatment stage is installed in several applications where the majority of the large droplets are filtered out using another technique and the membrane filtration techniques are further downstream in the separation process. Coalescence filtration is a widely used technique for effective separation of oil-water emulsion generally of dispersed phase sizes <100 μm. The droplets in the size range of 10- 100 μm do not settle down or separate at the top by buoyancy or gravitational effects due to their low settling velocities. The settling of these droplets from the continuous liquid phase is facilitated by coalescence filters which help in making the droplets bigger in size and therefore, increasing their weight and settling velocity. The coalescence filters are usually made up of fibrous media which could be inorganic or organic, have pore sizes usually bigger than those found in membranes, hence result in a lower pressure drop across the media.

There are three major steps involved in separation of emulsion by a coalescence filter and this was explained well by Hazlett et al.[120] The three steps are the following - approach of the dispersed droplet to a fiber surface, attachment of the water droplet, and finally release of the enlarged droplet downstream of the filter. The principal mechanism of droplets being captured by a fiber surface is direct interception where a droplets following a streamline of a laminar flow are captured by the fiber because both the droplet and fiber have a finite size. There are several other processes such as

diffusion, inertial impaction, electrostatic attraction, gravitational forces superimposed on the process of direct interception (Figure 2.8). Vinson et al. showed that electrostatic and gravitation

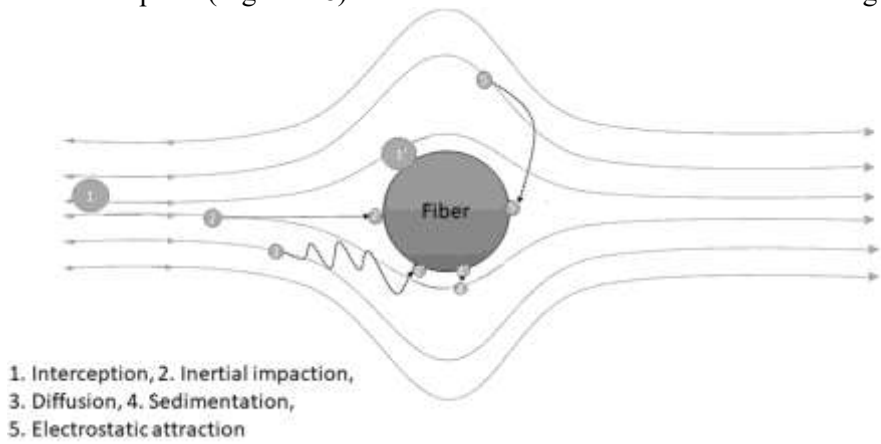


Figure 2.8 Representation of several droplet capture mechanisms by fiber[121] *Reproduced with permission from Reference 121 Copyright © 2022, © SAGE Publications*

forces have minimal effect for approach mechanism in fibrous media for coalescence filtration[122]. The equation developed by Langmuir for interception of droplets by fibers shows the effect of fiber size, flow velocity and droplet diameter on droplet capture efficiency (Figure 2.9). It was even experimentally shown that an increase in the flow velocity and smaller fiber diameters increases the efficiency of droplet capture. It can be clearly seen in Figure 2.9 that the efficiency of interception and droplet capture of a 2 micrometer fiber is much higher compared to a 5 and 10 micrometer fiber for intercepting a 5 micrometer diameter water droplet.

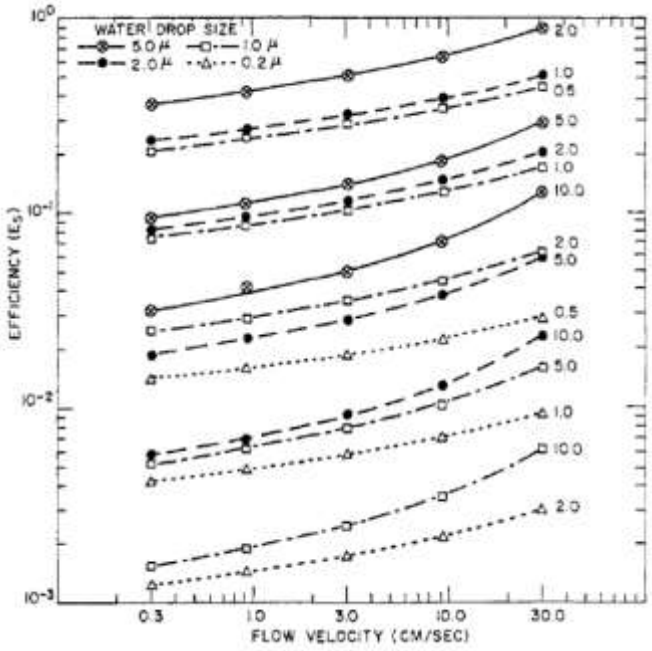


Figure 2.9 Dependence of flow velocity, fiber and droplet diameter on water droplet interception efficiency[120] *Reproduced with permission from reference 120 Copyright © 1969, American Chemical Society*

The second step in the coalescence process is the attachment of the droplet to the fiber surface. Since coalescence filtration is majorly used for separation of water-in-oil emulsions, we will discuss the attachment of water droplets to a filter surface. Once the water droplet approaches the fiber surface, the desired action is spreading of the droplet on the fiber surface. However, this process is resisted by the oil layer coating the fiber surface. Therefore, the water droplet needs to displace the oil film and preferentially wet the fiber surface. This process is facilitated by using fibers of high surface energy or hydrophilicity such as glass fibers or hydrophilic polymer fibers. Subsequently, other droplets flowing the liquid stream are intercepted by these attached water droplets and they both coalesce into a larger droplet. Once a critical size of the water droplet is reached, the enlarged water droplet is released from the fiber surface. There are two type of coalescence filtration : (a) depth coalescence and (b) surface coalescence filtration (Figure 2.10).

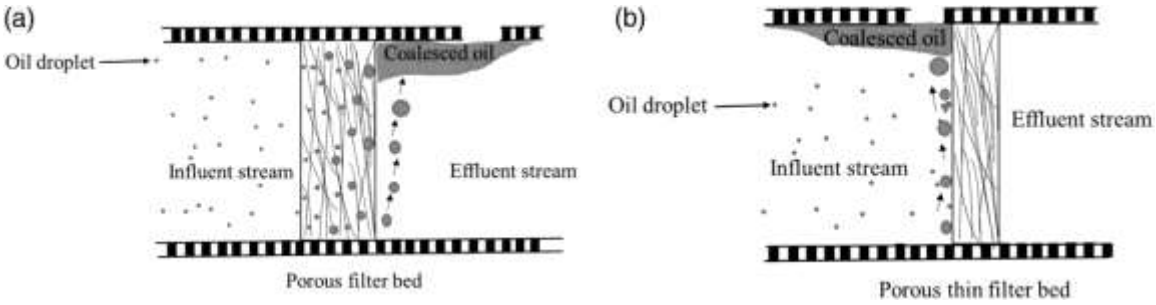


Figure 2.10 Two different types of coalescence filtration (a) depth (b) surface coalescence filtration. *Reproduced with permission from Reference 121 Copyright © 2022, © SAGE Publications*

In depth coalescence filtration, the droplets move through the entire filter media and the enlarged water droplets are released downstream of the filter surface whereas in a surface coalescence filter media, the droplets are rejected at the surface due to smaller filter pore size than droplet size. The droplets in turn stick to the surface, grow in size, and eventually settle down, upstream of the filter media surface.

The fiber diameter[123–125], fiber wettability[126,127], flow rate of the liquid stream, interfacial tension of the oil-water phase, pore size of the media all play a deciding role in determining the performance of the coalescing filter media. The specific surface area provided by the filter media scales inversely with the fiber diameter. Therefore, for two different filter media with the same porosity but with different fiber diameter, the one with a smaller fiber diameter provides higher surface area per unit volume and also greater number of fibers.[121] Therefore, the probability of droplet capture by smaller diameter fibers is higher. This leads to an effective coalescence filtration performance with smaller fiber diameter filter media

Surface wettability is the most important parameter for droplet coalescence. It controls the droplet attachment and detachment process from the fiber surface. A fiber surface can either be hydrophobic or hydrophilic for a water droplet coming near it. If the fiber surface is hydrophilic, it will readily wet the fiber and stick to it, allowing instantaneous draining of the oil film surrounding

the fiber. The surface chemistry and roughness of the fiber play a role in deciding its wettability characteristics. The fiber needs to have an optimum wettability to allow easy wetting and at the same time easy release of the water droplet, which would lead to a lower pressure drop across the filter bed. To this end several researchers used a mixture of hydrophobic-hydrophilic fibers, coated the fiber surface, have created innovative designs to allow effective droplet capture and drainage of enlarged droplets to facilitate effective coalescence media performance[126–129]. Several polymeric and inorganic fibers have been used to make coalescence fiber media such as polypropylene[127], polyethylene terephthalate[126], polyvinylidene fluoride[130], polyester, nylon, polystyrene[131], polyacrylonitrile[132], etc. Some researchers utilized cotton fibers[133], kapok fibers[134], kenaf fibers[123] for filtration applications as well.

2.2.3.4 Demulsification

Many techniques have been developed for demulsification of stable emulsions and separate the oil and water phases. One of the primary method uses chemical demulsifiers due to their effectiveness and efficiency. Emulsions are a kinetically stable suspension of a dispersed phase in a continuous phase stabilized by an effective emulsifier. Hence, demulsification of emulsions proceeds by breaking the interfacial emulsifier layer that surrounds the dispersed phase droplets. It should be noted that water-in-oil and oil-in-water emulsions require different types of demulsifiers as the emulsion stabilization mechanisms are different. The demulsifiers used to demulsify water-in-oil emulsions are called ‘emulsion breakers’ and those used to demulsify oil-in-water emulsions are called ‘reverse emulsion breakers’[97].

Prior to delving into the demulsification mechanism and the type of demulsifiers used, the stabilization mechanism of the two types of emulsions is discussed here. The water-in-oil emulsions, frequently encountered in the crude oil industry and in enhanced oil recovery processes, are stabilized by interface-active species such as asphaltenes, naphthenic acid, or fine solids[135–137].

These interface-active species forms a rigid interfacial film which influence several parameters such as the droplet size, interfacial layer stability and bulk properties of the emulsion. Asphaltenes are said to be the primary cause for emulsion stabilization in crude oil industries. Asphaltenes are petroleum fractions soluble in aromatic solvents such as toluene, but insoluble in paraffinic solvents such as heptane, hexane, pentane, etc[138,139]. They are composed of polycyclic aromatic rings with several functional groups such as amines, hydroxyls, carboxyls present on them, which vary the polarity of these molecules. The different polarities and carbon chain length of asphaltenes greatly influence the interfacial activity of these molecules[140].

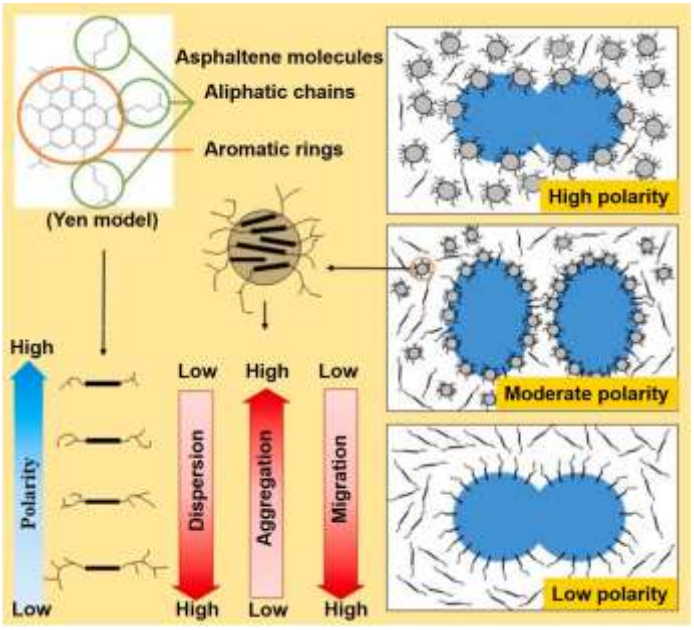


Figure 2.11 Asphaltene structure and the effect of its polarity on emulsion stability[140]. *Reproduced with permission from reference 140 Copyright Elsevier Ltd 2020*

The asphaltenes with low polarity migrate easily at the oil-water interfaces. However, they are not able to create a stable emulsion due to their inability to persist at the interface under external forces. On the contrary, asphaltenes with high polarity tend to aggregate amongst themselves and hence are not able to form a stable emulsion. It is only the asphaltenes with medium polarity that

are able to effectively stabilize the oil-water interface. This is shown schematically in Figure 2.11. The primary mechanism of stabilization in water-in-oil emulsion stabilization is said to be the steric stabilization provided by the bulky asphaltene or polymer chain groups. In the case of oil-in-water emulsions, generally along with steric stabilization, electrical double layer repulsion also plays a significant role in stabilizing the oil droplets in water[97]. Ionic surfactants such as sodium dodecyl sulfate and cetyl trimethyl ammonium bromide lead to an electrostatic stabilization of oil droplets due to the presence of charge on them. Therefore, the mechanism for demulsification of the oil-in-water and water-in-oil emulsions is different and hence requires different type of demulsifiers.

For demulsification of water-in-oil emulsions, several emulsion breakers (EB's) such as propylene oxide (PO)-ethylene oxide (EO) block copolymers[141,142], polyalkylene glycols, cardinal based polymers[143] and alkyl phenol alkoxylates, ethyl cellulose, nano-titania particles[144], amphiphilic ionic liquids[145] have been developed over the years. These demulsifiers are able to access the oil-water interfaces and change the properties of the interfacial surfactant layer to promote droplet coalescence. The commercially used EB are the EO-PO di- or tri-block copolymers. Three steps are said to take place that lead to demulsification of water-in-oil emulsions by the block copolymers - (i) adsorption of the demulsifier to the oil-water interface, (ii) breaking the interfacial film, and (iii) enhancement of film drainage by decreasing interfacial tension gradient[97,146]. The structural features of the block copolymer whether it is linear, branched, or star like, the hydrophilic-lipophilic balance (HLB- scales from 0-20), the % EO and % PO content of the polymer all greatly influence the performance of the demulsifiers and the amount of demulsifier required. Previous studies reported that the branched structural isomers perform better than the star-type which in turn perform better than the linear copolymers[147,148]. The EO-PO block copolymers with intermediate HLB values perform the best as demulsifying agents[149]. Polydimethylsiloxane modified EO and PO block copolymers have also been used commercially for demulsification[150].

These amphiphilic copolymers work by entering the interfacial oil-water film, replacing the interfacial active species such as asphaltenes, resins, acids and then modifying the interface film making it thinner and softer and hence, facilitating easy coalescence of the droplets. Ethyl cellulose (EC) is another type of demulsifier, obtained from natural sources and is biodegradable. It consists of a six membered glucose ring. The hydrophilicity of the molecule can be tuned by controlling the degree of substitution of the hydroxyl groups.. Figure 2.12 shows how quickly the values of storage (G′) and loss modulus (G″) of the oil-water interfacial changes when ethyl cellulose is added to it. At 2000 s, the addition of 23 ppm ethyl cellulose caused a drastic drop in both the G′ and G″ which suggests two things, (i) ethyl cellulose easily migrates to the oil-water interface and occupies it and (ii) the migration of the ethyl cellulose to the interface results in a less rigid interfacial film which results in promotion of droplet coalescence and hence demulsification.

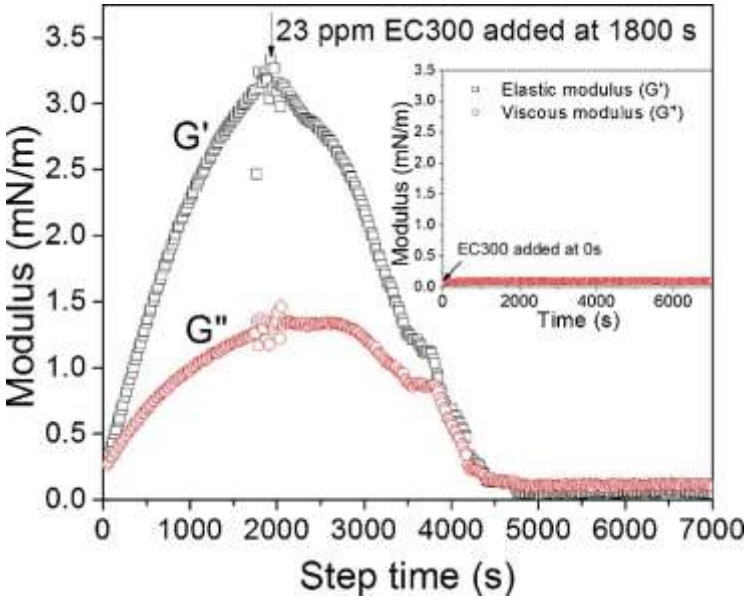


Figure 2.12 In situ change in storage and loss moduli after the addition of ethyl cellulose to the emulsion as a function of time[151]. *Reproduced with permission from reference 151 Copyright Elsevier Ltd 2018*

Contrary to the steric stabilization in the case of water-in-oil emulsions, electrical double layer stabilization is the dominant mechanism for stabilizing oil-in-water emulsions. Thus,

countering the electrostatic repulsion between oil droplets is a task carried out by the reverse emulsion breakers (REB's) used to demulsify oil-in-emulsions. The primary objective of REB's is

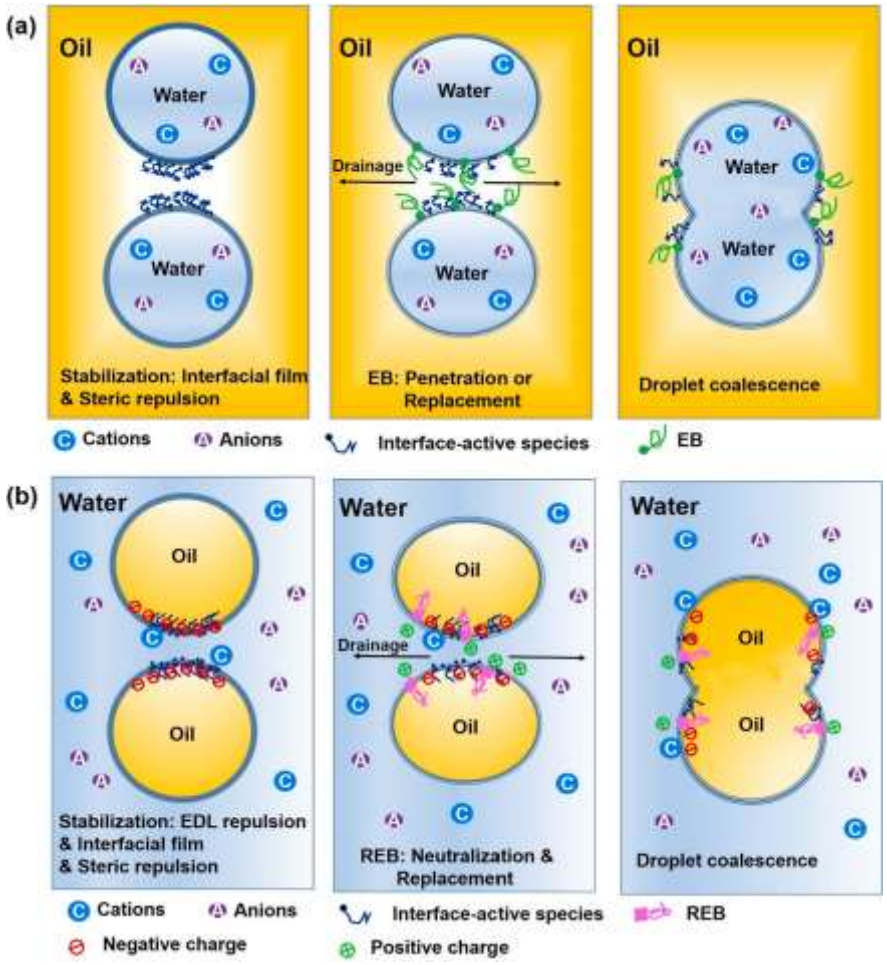


Figure 2.13 Schematic of demulsfication of (a) water-in-oil and (b) oil-in-water emulsions. *Reproduced with permission Copyright Elsevier Ltd 2020*

to stabilize the negative charge carried by the oil droplets. This is done using cationic demulsifiers or ionic liquids with positive charge. Some examples of cationic demulsifiers include polyquaternary ammonium salts[152], polyether-polyquaternium copolymers[153], polyamidoamine[154] and alkyl trimethylammonium halides[155]. The cationic demulsifiers move to the oil-water interfaces driven by electrostatic interactions. The magnitude of the surface charge on the oil droplets reduces and this helps to thin the interfacial film ultimately causing coalescence of the oil droplets. In

addition to the above mentioned demulsifiers, dendrimers and ionic liquids have also been used to demulsify oil-in-water emulsions[156,157]. Furthermore, Katepalli et al. showed the demulsification ability of colloidal silica particles for surfactant stabilized oil-in-water emulsions[158].

## 2.3 Adsorption of non-ionic surfactants at solid-liquid interfaces

Surfactant adsorption at solid liquid interfaces is a topic of great interest for solving many technological problems such as oil-water emulsion separation, enhanced oil-recovery processes, surface modification, surfactant aided membrane processes like micellar enhanced ultrafiltration, drug delivery, etc. Surfactants are amphiphilic molecules which have a natural tendency to occupy interfaces because of the hydrophilic and hydrophobic segments they consist of. The three different classes of surfactants namely ionic, non-ionic, and zwitterionic surfactants adsorb on solid surfaces via different mechanisms depending on several factors such as the surfactant charge, surfactant size, solid properties, pH of the liquid, etc. This discussion, however, has been limited to non-ionic surfactants and their adsorption on solid surfaces.

Gu et al. in 1991 published a paper discussing the adsorption of surfactants at liquid-liquid interfaces[159]. In this paper, Gu et al. discussed the theory and mechanism of surfactant adsorption and put forward the idea of a two-step adsorption model. The first step involves the adsorption of the surfactant molecules on the solid surface by electrostatic interactions, e.g., in case of ionic surfactants and charged solid surface or van der Waals forces. The second step involves the adsorption of additional surfactant molecules by interactions between the surfactant molecules. The adsorption isotherms present an understanding of the adsorption mechanism and structural configuration of the adsorbed species at the solid-liquid interfaces,. Three type of adsorption isotherm shapes have been reported, (i) the Langmuir (L)- type (ii) Sigmoidal (S)- type, and (iii) the LS type (Figure 2.14). The L-type curve is represented by the Langmuir equation. The Langmuir

equation is derived with the assumption that the solid surface is homogeneous, the adsorbed species form a monolayer on the surface and no lateral interactions between the adsorbed species[159]. However, the Langmuir case of monolayer adsorption is rarely seen in practice, especially with surfactant molecules and hence there have been several other models which have been developed to explain their adsorption which include multilayer adsorption, micelle formation, hemi-micelle formation which need to take into consideration the interactions between surfactant molecules themselves.

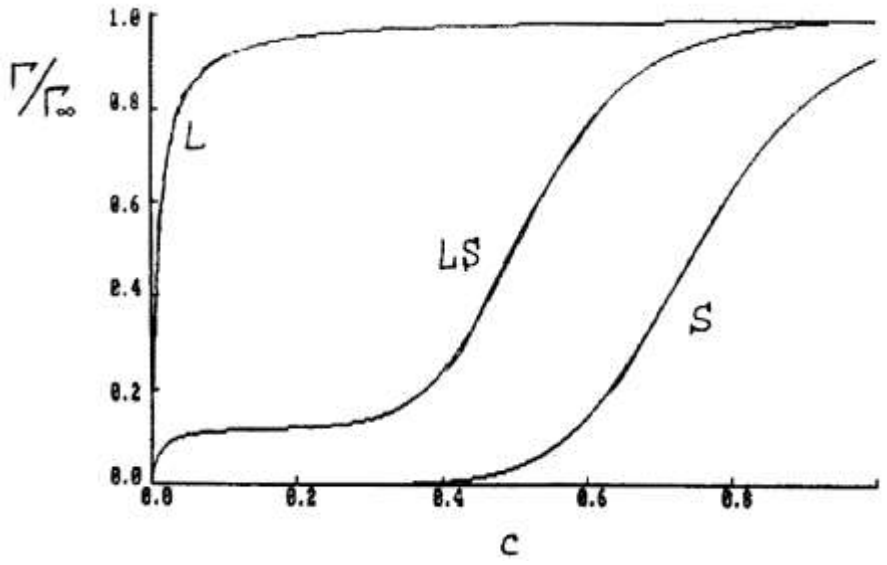


Figure 2.14 Three different types of adsorption isotherms with the amount adsorbed plotted on Y axis and the bulk concentration of the adsorbate in the liquid present on the X axis[160].

The LS- and S- type adsorption isotherms depict a multilayer adsorption which results in formation of higher order structural configurations by the surfactant molecules at the solid-liquid interface. Several researchers have reported the adsorption of different non-ionic surfactants on solid surfaces and their structural configuration, mechanism of adsorption, maximum capacity of solid surfaces to adsorb surfactants. Shar et al. reported the absorption of PPO-PEO block

copolymer based surfactants on polystyrene latex particles[161]. The PEO-PPO-PEO block copolymers adsorb readily onto hydrophobic surfaces using the PPO block as the anchor and the PEO block remaining extended into the water phase. The adsorption isotherm and adsorption layer thickness were found to be dependent on the block size of the PPO and PEO segment. The adsorption isotherm adopted the S-shaped curve for most PEO-PPO block copolymer surfactants, suggesting a sudden rapid increase in adsorbed surfactant amount as a function of the bulk surfactant concentration which suggests aggregation of surfactants at the solid surface. Partyka et al. studied the adsorption of several non-ionic surfactants of the oxyethylenic alkylphenol, oxyethylenic alkyl ether and poly(oxyethylene) glycol type on a precipitated silica gel[162]. The adsorption isotherms in this case followed an S-shaped curve. It was found that the cross-sectional area occupied by the molecules at saturation was directly dependent on the oxyethylenic chain length which suggested that it was the oxyethylenic group ($-OCH_2CH_2$) which adsorbs onto the silica surface. The surfactant molecules were believed to form a bidimensional micelle structure. In the first stage, the surfactant molecules were attracted to the surface and lie flat on the surface, the next stage is dominated by cooperative interactions between the surfactant molecules. The hydrophilic group on the surfactant interacted strongly with the polar surface of the silica gel. This cooperative adsorption was mentioned to be the reason for sudden rise in the amount of surfactant adsorbed. As the critical micelle concentration of the surfactant is achieved, the surfactants have already formed a higher order structure and hence, the adsorption curve reaches a plateau and there is no adsorption at or above the CMC. Muter et al. studied the adsorption of n-alkyl poly (oxyethylene) abbreviated at $C_nE_m$ on porous silica glass with different pore sizes (7.5 to 50 nm) where strong aggregative adsorption was observed at concentration well below the CMC[163]. Tiberg et al. also studied the adsorption of the $C_nE_m$ type surfactants and found that the amount of surfactant adsorbed, and its structural configuration varied significantly on a hydrophobic and a hydrophilic surface (Figure 2.15)[164]. At low surfactant bulk concentration in water, the amount of

surfactant adsorbed by a hydrophobic surface was higher compared to a hydrophilic surface. At a certain critical concentration below the CMC, called as critical surfactant aggregation concentration (c.s.a.c.), it can be seen that the surfactant molecules have aggregated into higher order structures on the silica surface. As the bulk surfactant concentration is increased on a hydrophilic surface, the surfactants formed a bilayer structure whereas on a hydrophobic surface the surfactants formed a monolayer

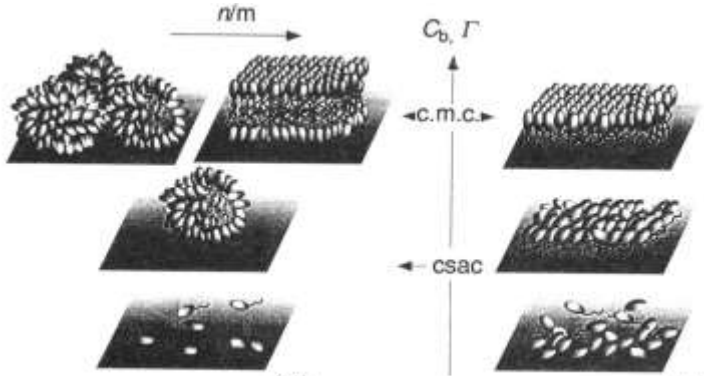


Figure 2.15 Schematic of $C_nE_m$ type surfactant adsorption on (a) hydrophilic silica and (b) hydrophobic silica surface[164] *Reproduced with permission from reference 163 Copyright Royal Society of Chemistry 1997*

structure. This suggests the importance of surface wettability and physical properties of the solid surface on influencing adsorption of small molecules. There have been limited studies on adsorption of non-ionic surfactants on meso- or macroporous solids. Shin et al. reported adsorption of alkyl ethoxylate type surfactants ($C_{10}E_5$ and $C_{12}E_5$) on mesoporous cylindrical silica porous gels with pore diameters of 8 nm[165].Small angle neutron scattering (SANS) was utilized to elucidate the structural configuration of the surfactants within the ordered cylindrical mesopores. The surfactants showed a strong aggregative adsorption behavior suggested by the sigmoidal adsorption isotherm. The SANS results suggested that the surfactants formed discrete aggregates on the solid surface which increased in number as the bulk surfactant concentration was increased and finally merging into interconnected patches at the surfactant CMC. The reason for the high surfactant affinity to the

surface and the strong aggregative adsorption behavior was mentioned to be the confined pore architecture which has pore sizes close to the size of the surfactant micelle aggregates.

## 2.4 Separation of per- and poly-fluoroalkyl substances (PFAS) from water

Per- and poly-fluoroalkyl substances (PFAS) have been recognized as a contaminant of great concern by the US EPA. The US EPA has identified a total of 430 PFAS molecules from several water sources. Among these, EPA listed 74 chemicals in their priority testing list[166,167]. These are a group of manmade chemicals which are extremely hazardous to human health because of their toxicity, bioaccumulation, and ability to persist in the environment for a long period, due to the extremely stable carbon-fluorine bonds. These chemicals are, therefore, also termed as forever chemicals[168,169].Approximately 110 million Americans in the United States alone are affected by PFAS contaminated drinking water which is roughly 66% of the US population[170]. There has been a considerable peer review work published describing the negative effects of PFAS molecules on the human body, such as its association with cancer, damage to the reproductive system, reduced fertility, increased cholesterol, obesity, and many more health concerns[171]. In addition, its negative effects on the aquatic ecosystem cannot be disregarded. These materials have been around since 1930's and has been used in several applications ranging from non-sticky coatings, packaging, clothing, hydrophobic and oleophobic coatings, stain resistant fabric, firefighting foams, etc[172,173]. Due to their ubiquitous use, they have led to a widespread soil, water, and land contamination problem for us, which needs to be tackled as soon as possible to avoid its negative effects on humans as well as animals. There have been several techniques which have been developed over the years for removal of these molecules and they can be categorized as ex- or in-situ techniques. In-situ techniques include chemical oxidation[174], foam fractionation[175], activated carbon injection[176] and some examples of the popular ex-situ techniques include coagulation[177,178], adsorption[179–181], and filtration[182,183]. In this section, a brief overview of some of

the important and commercially used techniques for PFAS separation and remediation has been made.

### 2.4.1 Foam fractionation

Foam fractionation is a widely used technique in water treatment for removal of several surface active species such as proteins[184], heavy metal ions[185], organic matter[186], dyes[187] from water and has also been extensively studied for removal of PFAS molecules in recent years[188,189]. In this techniques, bubbles or foam is used to separate the surface active substances from the liquid phase due to the affinity of the molecules towards the air-liquid interfaces[190]. The first report of PFAS separation by foam fractionation was in 2017 by Lee et al.[191] They studied the separation of perfluorooctane sulphonate (PFOS) and perfluorooctanoate (PFOA) using foam flotation in the presence of metal aids/activators such as aluminium, iron, lanthanum, cadmium, and potassium. The presence of iron (III) proved to be the most effective for separation of both PFOA and PFOS with a separation efficiency of > 99% in 5 min. The pH of the water affected the separation performance. At a pH higher than 7, the hydroxide ions competed with the PFOA and PFOS ions for the iron sites and hence this led to a reduced separation performance. The best separation performance was observed at a pH of ~ 2. A schematic of how foam fractionation occurs is shown in Figure 2.16. The image on the left shows the presence of the PFOA and PFOS molecules in water. After air is bubbled through the liquid, the PFAS molecules are seen adsorbed at the bubble-liquid interface and are concentrated at the top of the liquid. The affinity of the PFAS molecules

for the air-liquid interface is due to the presence of hydrophobic fluorine moieties on these molecules.

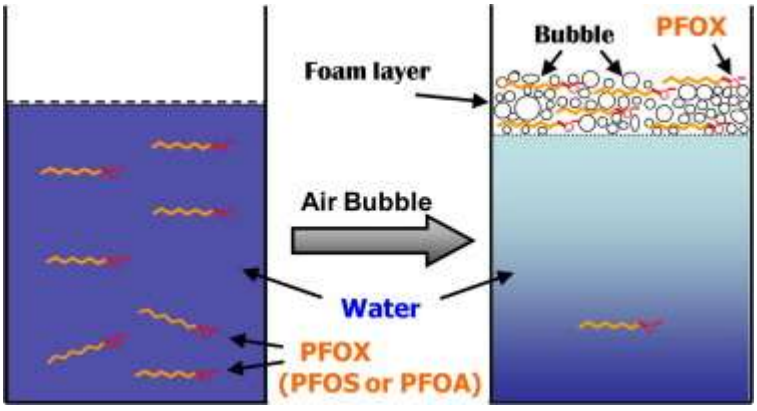


Figure 2.16 Schematic of PFOA and PFOS separation from water using foam fractionation[191]

*Reproduced with permission from reference 190 copyright Elsevier B.V. 2016*

Foam fractionation is mostly carried out in elongated cylindrical columns which are larger in length compared to its width. This geometry is optimized to allow enough residence time for the bubbles to adsorb the PFAS molecules and rise in the column. There are several factors which affect the PFAS separation performance by foam fractionation, such as addition of external surfactants, addition of metal activators, effect of ionic strength, effect of PFAS composition in feed, effect of gas flow rate, bubble size, gas type, foam height and temperature. A higher gas flow rate increases the foam generation and therefore, a higher amount of PFAS is separated from the liquid[192]. Wang et al. showed that the separation of PFAS molecules increased from 75 to 85 % by increasing the gas flow rate from 15 to 20 L/min[193]. However, an optimum gas flow rate needs to be found since studies by Boonyasuwat et al. showed that a very high gas flow rate leads to breaking of the air bubbles and hence reduction in PFAS removal efficiency[194]. Bubble size has an inversely proportional relation with PFAS separation performance and addition of external surfactants to the liquid leads to increased foaming and, therefore, higher removal of PFAS[195]. Morrison et al. studied the effect of temperature on PFAS removal and found that temperature had negligible effect on

removal of long chain PFAS such as PFOA but it affected the separation performance of short chain PFAS such as perfluorobutane sulphonate (PFBS), where the separation efficiency of PFBS reduced from 40 to 0% as the temperature was increased from 4 to 37 ℃[196].

### 2.4.2 Adsorption

Adsorption of PFAS by organic or inorganic adsorbents is the most widely used technique for PFAS removal because of its low cost and the ease of application. Several adsorbent media are used such as powdered or granular activated carbon, ion- exchange resins, aminated adsorbents such as chitosan, polyaniline, β-cyclodextrin, nanoparticles, molecularly imprinted polymers, etc. There are several mechanisms by which adsorption of PFAS proceeds which include electrostatic attraction, hydrogen bonding and hydrophobic interactions[168]. Since PFAS molecules like PFOA, PFOS, or PFBA are present in anionic form due to their low dissociation constant, the major mechanism of adsorption is electrostatic attraction. In addition, functional groups such as -COOH, -OH on adsorbents can lead to hydrogen bonding with the oxygen groups of the PFAS molecules[197]. Hydrophobic interactions between the hydrophobic carbon-fluorine chain is also a mode of adsorption and is greatly influenced by the chain length of the PFAS. A long chain PFAS has the

ability to strongly interact by hydrophobic interactions compared to a short chain PFAS. The hydrophobic interactions may also lead to formation of micelles or hemi-micelles in narrow spaces.

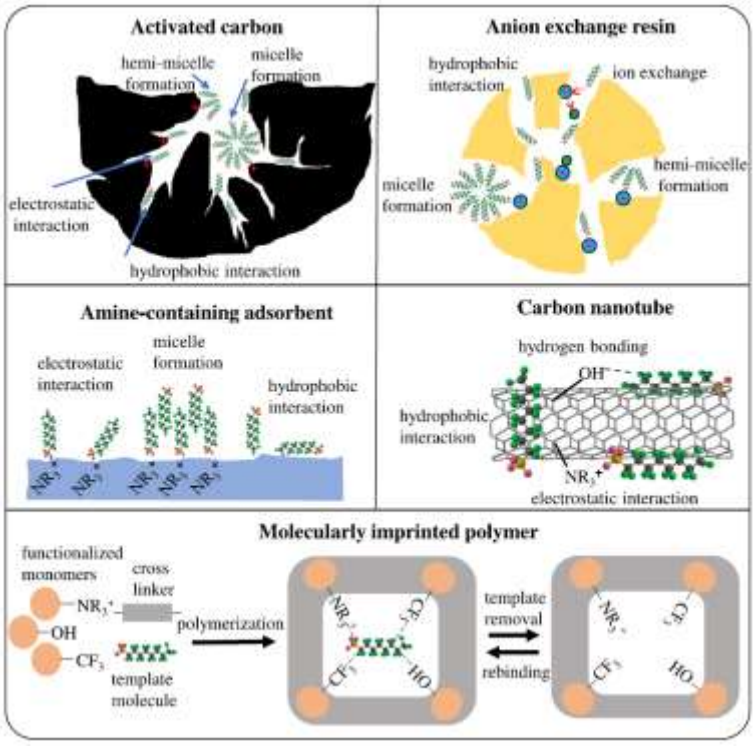


Figure 2.17 Adsorption mechanisms of PFAS by different adsorbents[168] *Reproduced with permission from reference 167 copyright American Chemical Society 2022*

Activated carbon has been a very common adsorbent media for several contaminants in water or removal of taste, odor and is available commercially at a cheap price. Raw materials such as coconut shell, bituminous coal, brown coal, wood are used for preparing activated carbon adsorbents. The adsorption performance is strongly influenced by the raw materials used for activated carbon preparation. Pabon et al. was the first one to report the use of powdered activated carbon (PAC) for removal of perfluoroalkyl carboxybetain[198]. These researchers used two different activated carbon materials one with pore size in the range 10-20 Å (Acticarbon 25K) and the other with pore size range 30-100 Å (Acticarbon ENO ). The perfluoroalkyl carboxybetain has a chain length of 18 Å and hence Acticarbon ENO was more effective for its removal because of the larger

pore sizes. Xiao et al. showed that the adsorbent size and the surface area influences the PFAS removal performance[199]. They studied the adsorption performance of granulated activated carbon (GAC) and biochar for removal of 30 different PFAS molecules. It was found that GAC with smallest particle size and higher surface area was most effective for PFOA and PFOA removal. Park et al. showed that the charge present on the activated carbon also improves the adsorption performance for PFAS removal due to additional electrostatic interactions[200]. They used 4 different bituminous coal based activated carbons and found that the one with a net positive charge has a higher PFAS adsorption. It was also shown that it is more difficult to adsorb the short chain PFAS compared to the long chain PFAS because of the lower hydrophobicity of the short chain[201]. It has also been shown in several studies that adsorption of PFOS is easier compared to PFOA on activated carbon based adsorbents because of the one extra carbon in the chain, allowing stronger hydrophobic interaction. Even though activated carbon adsorbent media is effective for long chain PFAS removal, its adsorption kinetics is slow and it has lower effectiveness for short chain PFAS removal. In addition, regeneration, and disposal of used adsorbent media is a big challenge with activated carbon.

Ion exchange resins are another adsorbent media which have been extensively reported for PFAS removal. Polymer based ion exchange resins are functionalized polystyrene or polyacrylic acid beads containing a charged functional group balanced by a counter ion. Woodard et al. compared the performance of ion exchange resins and GAC for PFAS removal along with their in-situ regeneration performance[202]. It was found that the ion exchange resin had a small empty bed contact time compared to a GAC column and the resin also treated 8 times more volume water compared to GAC. Specifically, the resin removed four times more PFAS per gram compared to GAC before breakthrough was observed. It was easier to regenerate the ion exchange resin bed using a solution of organic solvent like methanol, ethanol, and brine. In another work, Conte et al.

showed that ion exchange resins which have higher hydrophobicity perform more efficient for PFAS removal[203]. Although ion exchange resins have been proven to be effective for PFAS removal, they too suffer from slow adsorption kinetics, contamination by other background contaminants in water, high cost, and frequent regeneration of adsorbent beds.

Other adsorbent media include aminated adsorbents such as β-cyclodextrin, chitosan, polyaniline which have been reported for PFAS removal. The performance of amine containing adsorbents is superior compared to activated carbon and ion exchange resins but not many of them are available on a commercial scale today except β-cyclodextrin which is produced by CycloPure, Inc[204]. The electrostatic interactions between the positively charged amine groups and the negatively charged PFAS ions is the dominant mechanism of interaction. Amine containing adsorbents have a higher adsorption ability for PFOS compared to PFOA due to the higher hydrophobicity of the former[205]. The aminated adsorbents are very quick in removal of PFAS from water. For example, Aetia et al. showed fast adsorption kinetics (~ 2 h) and high removal efficiency of PFAS by poly (ethylenimine- functionalized) cellulose crystals from environmentally relevant concentration regimes. The effectiveness of short chain PFAS removal is a problem even with amine containing adsorbents and the long chain PFAS have the ability to replace the adsorbed short chain PFAS on the adsorbent surfaces, hence leading to overshoot problems[168,206]. Cyclodextrins, a group of cyclic oligosaccharides have been a promising candidate for PFAS removal in recent years. They have unique properties such as a cavity which is approximately the size of PFAS molecules, hence working like a lock-key mechanism for PFAS removal. Kawano et al. reported cyclodextrin surface tethering on polystyrene particles and used them for removal of PFOS, PFOA and perfluorohexanoic acid (PFHxA)[207]. It was observed that the polystyrene particles with 36% β-cyclodextrin were able to remove all types of PFAS tested completely. Acetone, methanol, and aqueous sodium hydroxide were used to study the regeneration performance of the adsorbents.

Another adsorbent was prepared by crosslinking the β- cyclodextrin using a crosslinking to form its corresponding polymer. This produces a mesoporous adsorbent which has far superior performance compared to GAC and ion exchange resins[208]. In another work, Ching et al. studied the performance of five different adsorbents namely Dexsorb, Dexsorb+ (commercial name for β-cyclodextrin produced by CycloPure), aminated cyclodextrin, Purofine PFA694E (anion exchange resin) and Purofine PFC 100 (cation exchange resin) for removal of 11 different types of PFAS[209]. The Dexsorb was the best performing for zwitterion PFAS molecules, whereas the non-ionic PFAS was not effectively removed by the ion exchange and the cyclodextrin based polymers. Dexsorb+ showed a very high affinity for the anionic PFAS molecules.

2.4.3. Membrane filtration

Membrane filtration especially reverse osmosis (RO), nanofiltration (NF) have been extensively investigated for PFAS removal. The PFAS molecular size, membrane pore size, membrane surface charge are the important parameters governing the PFAS separation performance since size exclusion and electrostatic interactions are the mechanisms of removal by this method. There are two types of membranes (i) low pressure membranes and (ii) high pressure membranes. This distinction is based on the pore size of the membranes, the low pressure membranes have pore sizes in the range of 10-100 nm and theoretically they are not suitable for PFAS removal because of their large size. This was also proven experimentally when a low pressure membrane was used to treat PFAS contaminated water[210]. The RO and NF membranes are the ones which are suitable for removal of dissolved PFAS molecules from water as their pore sizes lie between 1-10 nm[211]. Wang et al. prepared a poly(piperazine-amide) NF composite membrane with a pore size of 0.912 nm which also had a negative charge. The membrane showed 92.5 % separation efficiency for PFOS and 50.4% for PFBS at a bulk concentration of 150 μg/L[212]. The PFAS characteristics, water quality, and operating conditions affect the performance of NF membranes

more strongly compared to RO membranes[168]. Membrane fouling however is a big concern with using high pressure membranes, because it leads to reduction in water flux across the membrane and increased cost of operation due to higher pressure drop across the membrane. The effect of fouling on PFAS rejection has been debatable. Some works report the fouling increases the PFAS rejection ability whereas some works have reported otherwise[168,213,214]. Tang et al. reported the flux and rejection performance of different RO and NF membranes under cross-flow conditions. The separation efficiency with RO membrane was > 99% whereas that with NF membrane was 90-99%. Therefore, membrane separation is a promising technique to achieve desirable separation performance for PFAS for short periods, but the high cost, high energy requirement has limited its widespread commercial use.

# CHAPTER III

# MESO- AND MACRO-POROUS POLYMER GELS FOR EFFICIENT ADSORPTION OF BLOCK COPOLYMER SURFACTANTS

## 3.1 Abstract

An understanding of surfactant adsorption at solid-liquid interfaces is important for solving many technological problems. This work evaluates surfactant adsorption abilities of high surface area (200-600 $m^2/g$), high porosity (> 90%), hierarchically structured open pore polymer gels. Specifically, the interactions of a non-ionic block copolymer surfactant, polyethylene oxide-polypropylene oxide-polyethylene oxide (PEO-PPO-PEO), with three polymer gels, namely syndiotactic polystyrene (sPS), polyimide (PI), and polyurea (PUA) offering different surface energy values are evaluated at surfactant concentrations below and well above the critical micelle concentration (CMC). Two distinct surfactant adsorption behavior are identified from surface tension and nuclear magnetic resonance data. At concentrations below CMC, the surfactant molecules adsorb as monolayer on polymer strands, inferred from the Langmuir type adsorption isotherm, with the adsorbed amount increasing with specific surface area of the polymer gel. The study reports for the first time that the gels show strong surfactant adsorption above CMC with the effective surfactant concentration in the gel reaching several folds of the CMC values. The effective surfactant concentration in the gel is analyzed using surfactant micelle size, polymer surface energy, and pore size of the gel. The findings of this study may have strong implications in liquid-liquid

separation problems and in removal of small dye molecules, heavy metal ions, and living organisms from aqueous streams.

## 3.2 Introduction

An understanding of surfactant adsorption at solid-liquid interfaces is essential to solve many technological problems. Oil-water emulsion separation[215,216], modification of surfaces[217] or wettability of solid surfaces[218], surfactant aided membrane processes such as micellar liquid chromatography[219], and micellar enhanced ultrafiltration[220] are a few examples that benefit from surfactant adsorption studies. Published literature often focuses on adsorption of surfactants on conventional solid substrates such as flat surfaces[164,221] or spherical particles[222,223]. In this context, very limited literature exists on surfactant adsorption on solid substrates with inherent porous structures presenting confined geometries. Prior work established that molecular transport and adsorption-desorption processes at nanoscale are different from those observed for bulk, micrometer size solid substrates[224]. Mesoporous silica gels with pores in 2-50 nm range exhibit an array of interactions with various ionic and non-ionic surfactant systems[165,225–227]. For example, at concentration below the critical micelle concentration (CMC), the surfactant molecules show aggregative adsorption at the solid-water interfaces [165]. This aggregation follows a two-step process. In the first step, the surfactant molecules anchor onto the polymer surfaces by hydrophobic-hydrophobic or hydrogen bonding interactions. In the second step, surfactant molecules organize into aggregates via lateral interactions [228] in the form of hemimicellar, micellar[222] or bilayer[164] structures. However, to the best of our knowledge, a similar study does not exist on surfactant adsorption in polymer gel systems. This study advances understanding of the underlying physics of surfactant adsorption in confined pores of polymeric materials with pore diameter in 10-200 nm range and polymer substrates offering different levels of surface energy and specific surface area.

We note that polymer gels differ from silica gel systems in surface chemistry, polarity, pore sizes, and the architecture of solid surfaces, e.g., typical polymer gels have strands of a few tens of nanometer diameter compared to spherical silica particles of 1-5 nm diameter with a plenty of surface silanol groups. A majority of polymer gels reported to date are hierarchically porous with interconnected networks of mesopores (2-50 nm diameter) and macropores (diameter > 50 nm).[3,82,85,229] In conjunction, the polymer gels offer high specific surface area (200-800 $m^2/g$)[230–232] which can be leveraged for high amounts of surfactant adsorption. It is imperative, therefore, that studies on surfactant adsorption behavior in porous polymer gel systems may yield interesting observations that can advance understanding of several liquid-liquid separation problems, e.g., using porous polymer gel as adsorbents.

Several porous gel-forming polymer systems have been reported in literature, such as syndiotactic polystyrene (sPS)[230,233], polyimide (PI)[58,231], polyurea (PUA)[85], polyurethane[234], cellulose[229] to name a few. The corresponding aerogels obtained by supercritical drying of the gels provide high surface area (250-800 $m^2/g$) and high porosity (>90%). Extensive work shows that pore size[231,232,235] and wettability[45] can be tuned and the gels can be fabricated into various shapes and sizes[26,63,64] to suit desired applications of aerogels, such as thermal insulation[236], air filtration[49,82], and dye removal from waste water streams[64].

The three polymer gels used in this work are sPS, PI, and PUA. All three gels offer high porosity with hierarchical porous structures composed of meso- and macropores. However, PI offers the highest mesopore fraction while sPS gels contain primarily macropores. The three polymer systems also differ in surface energy values thus presenting different levels of interactions with surfactants. sPS gels are formed by a thermoreversible gelation mechanism of sPS in a good solvent[237,238]. The inherent tacticity of sPS allows rapid gelation by spinodal decomposition route when the sPS solution is quenched. Daniel et al. reported sPS aerogel first in 2005[237]. Both PI and

PUA gels are formed by chemical crosslinking of respective monomer systems. A two-step reaction process is used for polyimide gels[55]. In the first step, selected diamine and dianhydride molecules react to form a linear polyamic acid. In the second step, a trifunctional crosslinker is used along with acetic anhydride and pyridine to convert polyamic acid into polyimide gel with 3-dimensional polymer networks[3,239]. PUA aerogels were first reported in a United States patent by Biesmans et al.[240] The PUA based gels are synthesized by reacting an isocyanate with water in presence of a catalyst[232,241,242].

In this work, the interactions of polyethylene oxide-polypropylene oxide-polyethylene oxide (PEO-PPO-PEO) block copolymer surfactants with three polymer gels in the form of sPS, PI, and PUA were studied. It was hypothesized that surface energy of the polymer constituting the gel would play significant role in deciding surfactant adsorption at the polymer-water interface. As will be seen later, sPS, PI, and PUA gels offered similar porosity values, pore morphology, and interconnected porous structures but different surface energy values.

The PEO-PPO-PEO block copolymer surfactant was chosen for its significance in emulsion science, drug delivery, and surface modification[243]. Significant prior work exists in literature on adsorption of ionic surfactants, but studies on non-ionic surfactants are limited. The surfactant adsorption by the gels at below CMC and well above CMC was studied. As will be seen, PEO-PPO-PEO block copolymer surfactant produced different size micelles that were useful for investigation of surfactant adsorption behavior at concentration regimes above CMC. The influence of surfactant micelle sizes and polymer gel pore sizes on surfactant adsorbed amounts by gels were investigated. The results of this study present an important first step towards understanding demulsification of oil-water emulsion systems using high surface area polymer gels.

## 3.3 Experimental Section

### 3.3.1 Materials

sPS (Mw ≈ 300,000 g/mol, 98%) was obtained from Scientific Polymer Producers Inc. (Ontario, NY, USA). 2,2′dimethylbenzidine (DMBZ) was purchased from Shanghai Worldyang Chemical Co. Ltd (Shanghai, China). Pyromellitic dianhydride (PMDA, ≥ 96.5%), tris(2-aminoethyl) amine (TREN, ≥ 95.5%) crosslinker, acetic anhydride( ≥ 99%) , and toluene (≥ 99.9%) were purchased from Sigma-Aldrich (Milwaukee, WI, USA). Pyridine (≥ 99%) and acetone (≥ 99.5%) were purchased from Fisher Scientific (Ontario, NY, USA). N,N-dimethylformamide (DMF, ≥ 99.5%) was purchased from VWR International (Radnor, PA, USA). Ethanol was purchased from Decon Laboratories Inc. (King of Prussia, PA, USA). Desmodur N3300A (tri-isocyanate) and triethyl amine (TEA) were procured from Covestro (Pittsburg, PA) and Sigma Aldrich (Milwaukee, WI, USA) respectively. Three different PEO-PPO-PEO surfactants were used in this work namely, Pluronic® L35, Pluronic® P123 and Pluronic® F-127 with molecular weight of 1900, 5800, 12600 g/mol respectively and PEO content 50, 30, 70 wt.% respectively. All these surfactants were procured from Sigma Aldrich (Milwaukee, WI, USA). Deuterium oxide ($D_2O$, deuteration degree min ≥ 99.95%) was purchased from Sigma Aldrich (Milwaukee, WI, USA). All the chemicals were used without further purification.

### 3.3.2 Fabrication of sPS gels and aerogels

sPS gels were obtained by thermo-reversible gelation of solutions of sPS in toluene. The solutions were prepared by dissolving sPS in toluene in sealed vials at 100 °C at a solid concentration of 0.06 g/mL and allowed to cool under ambient conditions for 1 min and then poured into a covered cylindrical glass mold of diameter 15 mm for gelation. The gels were allowed to stand in the mold for 5 h to ensure complete gelation, demolded, and solvent exchanged first with ethanol and finally with deionized (DI) water to obtain water-filled sPS gels for the next steps.

The ethanol-filled sPS gels were solvent-exchanged with liquid carbon dioxide and dried under supercritical condition of carbon dioxide at 50 °C and 11 MPa pressure to recover solid sPS aerogels. The aerogels were used for evaluation of surface energy and examination of pore size.

### 3.3.3 Fabrication of PI gels and aerogels

PMDA and DMBZ were dissolved separately in DMF, and the solutions were mixed together at room temperature under magnetic stirring for 2 min at 1200 r.p.m. to form linear polyamic acid solution in DMF. Subsequently, TREN, acetic anhydride, and pyridine were added to polyamic acid solution and magnetically stirred for 3 min. The final solution was poured into a cylindrical mold of diameter 16 mm and gelation occurred within 10 mins. The gels were aged in the mold for 24 h and solvent exchanged with mixtures of DMF and acetone in ratio 75:25, 50:50, 25:75 v/v followed by 3 additional solvent exchange steps with 100% acetone. The acetone in the gels were then exchanged with liquid carbon dioxide and dried under supercritical condition of carbon dioxide at 50 °C and 11 MPa pressure to obtain aerogels. The water-filled PI gels were obtained by solvent-exchange of gels filled with acetone using acetone- DI water mixtures of increasing water concentration and finally with 100% DI water. PI gels of 7.5 wt.% polymer concentration were obtained from 0.686 g of PMDA, 0.636 g of DMBZ, 92 μL of TREN, 1.847 mL of acetic anhydride, and 1.909 mL of pyridine in 15 mL DMF.

### 3.3.4 Fabrication of PUA gels and aerogels

The tri-isocyanate was first dissolved in DMF at room temperature with magnetic stirring followed by mixing with DI water for 3 min and additional mixing for 2 min after TEA was added. The mixture was transferred to a cylindrical mold of diameter 15 mm and allowed to stand and gel at room temperature for 50-60 minutes, followed by 24 h of aging in the mold. The PUA gels were synthesized using tri-isocyanate, water, and TEA in molar ratio 1:3:1 with 0.15 M concentration of tri-isocyanate. The PUA gels filled with acetone and suitable for supercritical drying were obtained

by solvent exchanging in steps with mixed solvents DMF-acetone in the ratio 75: 25, 50: 50, 25: 75 v/v followed by 3 solvent exchanges in 100% acetone. The acetone-filled gels were solvent exchanged in liquid $CO_2$ and subsequently dried under supercritical condition of $CO_2$ at 50 °C and 11 MPa pressure to obtain aerogels. Deionized water-filled gels were obtained by exchanging acetone in acetone-filled gels with acetone-water mixtures with increasing concentration of DI water and finally with DI water.

### 3.3.5 Characterization

3.3.5.1 Surfactant adsorption: The amount of surfactant adsorbed by water-filled gels from a solution of surfactant of concentration 0-15 wt.% in DI water was determined after allowing the polymer gel of known mass dipped in the solution to equilibrate over a period of 24 h at room temperature. The value of surface tension (σ) of water was determined before and after dipping the gel and the concentration of surfactant in water after adsorption by the gel was determined from the calibration curve of σ vs. surfactant concentration. It is noted that at above the CMC, σ assumes a constant value ($\sigma_{CMC}$). Such solutions were diluted to below CMC by adding known aliquots of DI water until the value of σ was found greater than $\sigma_{CMC}$. All adsorption experiments were repeated thrice for each data point. In this work, σ was obtained from pendant drop method using the drop shape analyzer (DSA25S, Krüss GmbH, Germany).

3.3.5.2 $^1$H NMR: Solution $^1$H NMR data were obtained for precise characterization of surfactant concentration within the polymer gel especially at surfactant concentrations above CMC. The polymer gels were dipped in an aqueous surfactant solution of known initial concentration for a period of 24 h. Subsequently, 0.6 g of polymer gel was inserted into the NMR tube and filled with 0.5 mL deuterium oxide ($D_2O$) used as the solvent. The $H_2O$:$D_2O$ ratio was approximately 1:1. Solution-state $^1$H NMR spectra were recorded on an Agilent NMR 500 MHz (Santa Clara, CA) at 298 K. A 90 degrees pulse of 14.12 µs was used to excite $^1$H NMR signals. Accumulation number

and recycle delay were set to 64 and to 5 s, respectively. $^{1}H$ spin lattice relaxation time in the laboratory frame ($T_1$) was measured by inversion recovery method for 0.1 wt.% and 15 wt.% Pluronic ® L35 aqueous surfactant solutions. $T_1$ relaxation time for the water peak was found to be 0.9 s and those for the surfactant peaks at 3.63, 3.5 and 1.1 ppm were found to be 0.8, 0.55 and 0.70 s respectively, and hence the recycle delay was set to 5 s to ensure complete relaxation of all the proton signals. Under such condition, the NMR spectroscopy data produced quantitative measure of surfactant concentration within the polymer gel.

3.3.5.3 Bulk density, skeletal density, and porosity measurements: The bulk density ($\rho_b$) of aerogel specimens was measured from mass and volume while the skeletal density ($\rho_s$) was obtained from Helium pycnometer (AccuPyc II 1340, Micromeritics Instrument Corp., Norcross, GA). The porosity ($\rho_T$) of the aerogel specimens was calculated using equation (1).

$$\rho_T = (1-\rho_b/\rho_s)\times 100 \quad (1)$$

3.3.5.4 Brunauer−Emmett−Teller (BET) Adsorption-Desorption: The specific surface area and mesopore volume ($V_{meso}$) of aerogel specimens were obtained from BET analysis of $N_2$ adsorption-desorption isotherms obtained at 77 K using a Micromeritics Tristar II 3020 analyzer (Micromeritics Instrument Corp., Norcross, GA). The BET isotherm was obtained at 77 K to improve the detection accuracy of the instrument for nitrogen adsorption. It is noted that the specific surface area reported in the manuscript corresponded to that of the aerogels, although surfactant adsorption experiments were conducted using corresponding gels with slightly higher pore volumes. The volume shrinkage of the gel during supercritical drying in all cases was small, around 10% and the specific surface area reported for aerogels come close to that in the gel state. The macropore (diameter > 50 nm) volume ($V_{macro}$) was obtained from the difference of total pore volume ($V_{total}$, equation 2) and sum of $V_{meso}$ and micropore volume ($V_{micro}$). Since the micropore volume fraction for the gels utilized in this work is extremely low (≤ 0.01), we considered it

negligible for our purpose [231].The nonlocal density functional theory (NLDFT) model was used to obtain the mesopore volume fraction from $N_2$ isotherms at 77 K. The total pore volume and fraction of meso ($\phi_{meso}$) and macropores ($\phi_{macro}$) were calculated using equations (2-4). The pore size distribution was obtained using the Barrett-Joyner-Halenda (BJH) analysis of nitrogen isotherms.

$$V_{total} = \frac{1}{\rho_b} - \frac{1}{\rho_s} \tag{2}$$

$$\phi_{meso} = \frac{V_{meso}}{V_{total}} \tag{3}$$

$$\phi_{macro} = \frac{V_{macro}}{V_{total}} = 1 - \phi_{meso} \tag{4}$$

3.3.5.5 Contact angle and surface energy of polymer specimens: The water contact angle on compressed aerogel discs was measured using sessile drop method and analyzed using Kruss drop shape analyzer. For this purpose, aerogel specimens were compressed as discs between two clean, flat metal platens at 13.8 MPa pressure to remove the pores so that only the chemistry of the polymer affects the contact angle values. In each measurement, a water droplet of 10 µL volume was placed on the surface of the compressed disc. The contact angle between water and the polymer surface was read from the optical image using ImageJ software.

The surface energy of polymer specimens and its polar and dispersive components were calculated using Wu's theory[244] as per equation (5). For this purpose, the contact angle values of water and diiodomethane were measured on compressed polymer disks.

$$\gamma_{LS} = \gamma_L + \gamma_S - \frac{4\gamma_L^d \gamma_S^d}{\gamma_L^d + \gamma_S^d} - \frac{4\gamma_L^p \gamma_S^p}{\gamma_L^p + \gamma_S^p} \tag{5}$$

In equation (5), $\gamma_{LS}$ is the interfacial tension between liquid and solid, $\gamma_L$ is the surface tension of the liquid, $\gamma_S$ is the surface energy of the solid, and $\gamma^d_S$ and $\gamma^p_S$ are the dispersion (nonpolar) and polar components of liquid surface tension, respectively. The standard values of $\gamma_L^d$ = 21.8 dyn/cm

and $\gamma_L^p$ = 50.7 dyn/cm for water and $\gamma_L^d$ = 44.1 dyn/cm and $\gamma_L^p$= 6.7 dyn/cm for diiodomethane were used in the calculations[244]. The surface energy of polymer is obtained from the sum of dispersive ($\gamma^d_S$) and polar ($\gamma^p_S$) components as in equation (6).

$$\text{Polymer surface energy } (\gamma_S) = \gamma_s^d + \gamma_s^p \quad (6)$$

The polymer-liquid interfacial energy ($\gamma_{LS}$) was calculated using Young-Laplace equation as in equation (7) where $\gamma_L$ is surface tension of the liquid and Θ is the contact angle on polymer surface.

$$\gamma_S = \gamma_{LS} + \gamma_L cos\theta \quad (7)$$

3.3.5.6 Morphology: The morphology of aerogel specimens was examined using scanning electron microscope (SEM JSM5310, JEOL,MA).

3.3.5.7. Dynamic light scattering (DLS) : The size of micelles of surfactants in DI water was determined using DLS at 25 ℃. For this purpose, 5 wt.% surfactant solution was prepared in deionized water and analyzed using Zetasizer Nano ZS90 (ZEN3690, Malvern Instruments Limited, Worcestershire, UK).

3.3.5.8. Surfactant desorption: Syndiotactic polystyrene gel was used in adsorption of Pluronic® L35 surfactant at two bulk concentrations of 0.1 wt.% and 5 wt.% respectively below and above the CMC (1 wt.%). A 10 mL aqueous solution at desired surfactant concentration was prepared and a sPS gel specimen was dipped to adsorb the surfactant over a period of 24 h. The sPS gel along with adsorbed surfactant was subsequently placed in 10 mL DI water and kept for 24 h to allow possible desorption of the surfactant from the gel at room temperature. The surface tension of this water was then measured to obtain the amount of surfactant released by the gel using s vs. surfactant concentration calibration curve.

3.4 Results and discussions

*3.4.1 Surfactant adsorption onto polymer gels*

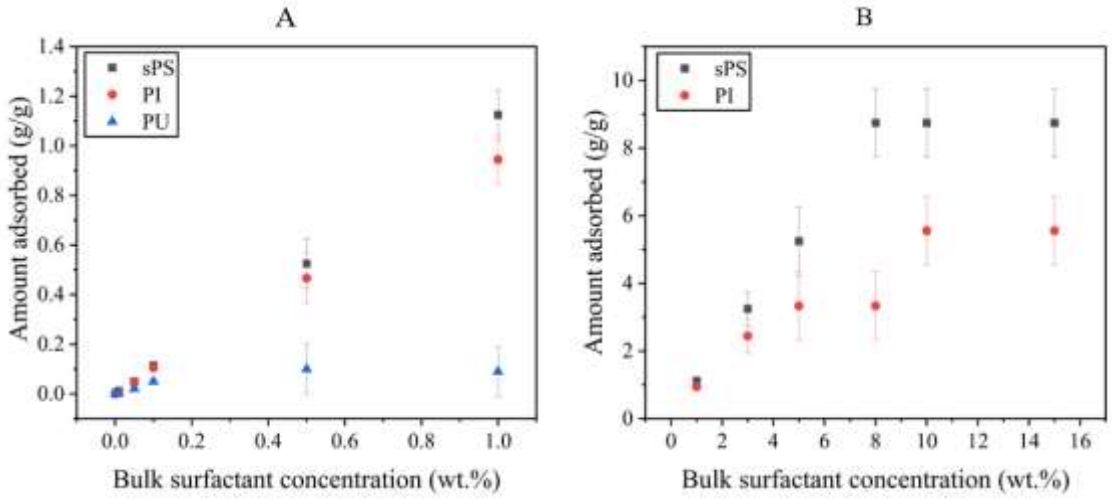


Figure 3.1 Pluronic® L35 surfactant adsorption by sPS, PI, and PUA gels at 25 °C. A) bulk surfactant concentration below CMC and B) bulk surfactant concentration above CMC.

The surfactant adsorption experiments were conducted by dipping water-filled gels of sPS, PI, and PUA of known solid mass in aqueous solutions of Pluronic® L35 surfactant for a prescribed time followed by analysis of the surface tension values of the aqueous phase. The concentration of the surfactant in aqueous phase was inferred from a calibration curve of σ vs. surfactant concentration, as presented in Figure 3.2. The calibration curve was obtained in the absence of any gel; therefore, Figure 3.2 applies to all gels considered in this work. The amount of surfactant adsorbed by the gel was obtained from the difference of original and residual quantities of the surfactant in the aqueous phase.

It is noted that the surfactant molecules can assume two structurally different regimes in aqueous solutions based on concentration. In regime I at low bulk concentrations ($C_{bulk}$), the surfactant molecules are present as unimers or isolated molecules and in regime II they are predominantly present as aggregated structures known as micelles as the surfactant concentration

goes beyond the critical micelle concentration (CMC). Above the CMC, the micellar structure is thermodynamically favored in aqueous solutions[245]. The CMC for Pluronic® L35 surfactant was found to be 1 wt.%, as reflected from Figure 3.2. This value of CMC is corroborated by data reported elsewhere[246]. In view of this, the surfactant solutions below and above the CMC were prepared and the surfactant-polymer gel interactions were studied.

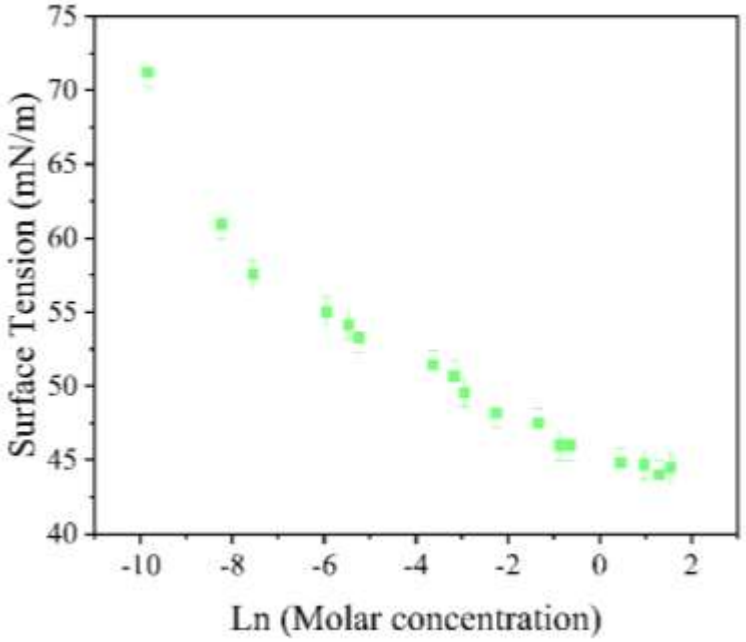


Figure 3.2 Pluronic® L35 surface tension vs Ln (molar concentration) calibration curve (The x-axis was changed from wt.% to Ln (molar surfactant concentration)

At $C_{bulk}$ below CMC, the amount of Pluronic® L35 surfactant adsorbed was low, at less than 1.2 g/g as seen in Figure 3.1A. Among the three gels, sPS gels adsorbed slightly higher amounts of surfactant than PI while PUA gels adsorbed very small quantities of the surfactant, at less than 0.1 g/g. At CMC, e.g., at 1 wt.% surfactant, sPS, PI, and PUA gels adsorbed respectively 1.1 g/g, 0.95 g/g, and 0.09 g/g of surfactant. The possible factors for low surfactant adsorption amount by PUA gels will be discussed later. At or above CMC, the surfactant adsorption amount for sPS and PI were much greater than observed below CMC, e.g., in the range of 1-9 g/g for sPS gel and 1-6 g/g for PI gels for surfactant concentrations in the range of 1-15 wt.%. Such data are

presented in Figure 3.1B. It is noted that PUA gels did not show additional adsorption at concentrations above the CMC.

We realized that the use of σ vs. concentration calibration curves presented in Figure 3.2 might not have enough sensitivity to determine and analyze the extent of surfactant adsorption at above the CMC values. As an alternative, we resorted to estimation of surfactant adsorption by the gel using solution NMR data (Figure 3A1). Figure 3.3 presents surfactant adsorption amounts on polymer gel specimens from solution NMR data. The $^{1}$H NMR spectra for the three gels at different Pluronic® L35 surfactant concentrations can be found in Figure 3A2. A large difference in surfactant adsorption amounts by the gels inferred from surface tension vs. concentration data and from $^{1}$H NMR data is clearly evident.

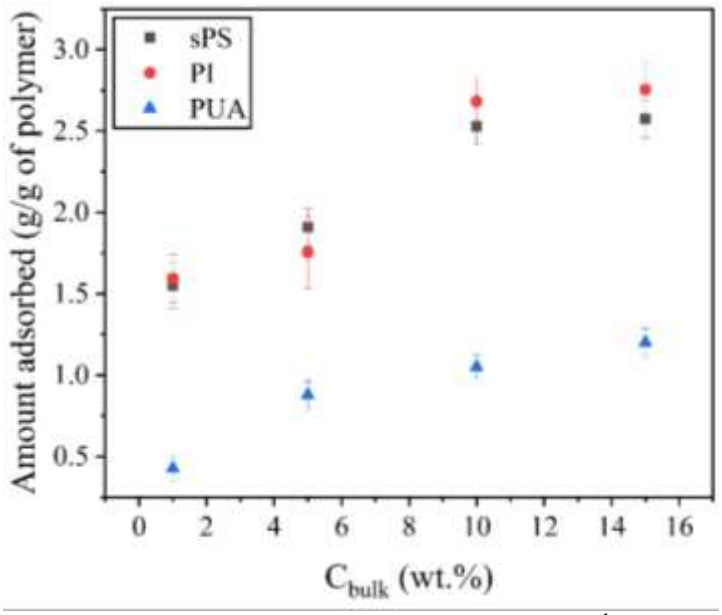


Figure 3.3 Surfactant adsorbed by the polymer gels calculated using $^{1}$H NMR spectra at different values of $C_{bulk}$.

The surfactant adsorption amounts inferred from s vs. $C_{bulk}$ calibration curve and that from NMR come close at or below CMC of 1 wt.% surfactant concentration. However, above CMC, the difference between the two data sets widened. For example, surfactant adsorption amount by PUA

gels above CMC was not sensitive to $C_{bulk}$ with a maximum adsorbed amount of 0.09 g/g at or beyond $C_{bulk}$ of 1 wt.% (Figure 3.1B). However, as seen in Figure 3.3, the amount of surfactant adsorbed inferred from NMR data continued to increase with $C_{bulk}$ from ~0.5 g/g at $C_{bulk}$ of 1 wt.% to ~1.2 g/g at $C_{bulk}$ of 15 wt.%. The adsorption capacity from NMR data at $C_{bulk}$ of 15 wt.% was 2.6 g/g for sPS and 2.7 g/g for PI compared to 9 g/g for sPS and 6 g/g for PI obtained as inferred from σ vs. $C_{bulk}$ calibration curve. In the rest of this work, therefore, we resorted to the use of σ vs. $C_{bulk}$ calibration curve at surfactant concentration below CMC for its convenience and for $C_{bulk}$ above CMC, we used NMR data for its higher sensitivity.

We now examine a few questions on surfactant adsorption by water-filled gels as reflected from the data presented in Figure 3.1 and Figure 3.3. First, what is the driving force for surfactant adsorption onto polymer gels? Second, why different polymer systems offer different adsorption capacity for the same surfactant?

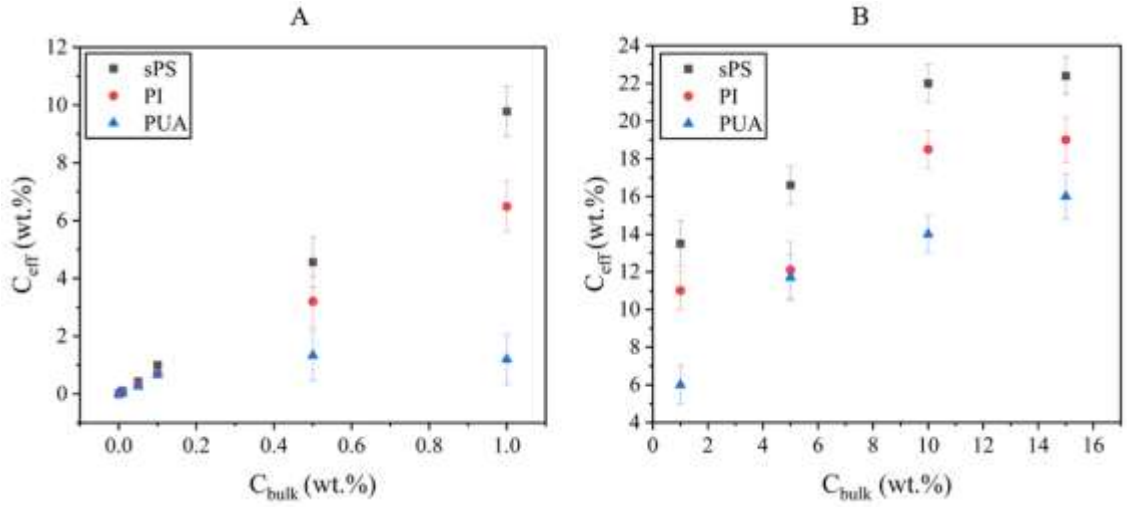


Figure 3.4 $C_{eff}$ as a function of $C_{bulk}$. (A) below and (B) above CMC for sPS, PI and PUA.

Third, why does the surfactant adsorption dynamics depend on surfactant concentration? One can easily conceive of two driving forces that govern surfactant adsorption onto polymer gels. First is the concentration gradient of the surfactant between the bulk aqueous phase and the internal

pores in the gel that drives surfactant molecule diffusion into the gel until an equilibrium is reached. The second driving force is the favorable free energy change associated with transfer of the surfactant molecules from the aqueous solutions to the polymer-water interfaces[247]. The favorable surfactant-polymer interactions are responsible for reduction of the net free energy of the system and may originate from electrostatic interactions, covalent bonding, hydrogen bonding, or hydrophobic-hydrophobic interactions between the surfactant and the polymer[248]. Therefore, to understand the driving force for surfactant adsorption, the effective concentration ($C_{eff}$) of the surfactant within the polymer gel was compared with the values of $C_{bulk}$.

The value of $C_{eff}$ within the gel was calculated from the amount of surfactant adsorbed by the gel and the amount of water present within the gel. The amount of water within the gel was calculated from the total pore volume of the gel assuming that the pores were completely filled with water. The total pore volume was obtained from the product of volume of the aerogel and the porosity given in equation (1).

The total pore volumes of three types of aerogels are listed in Table 3.1. As an example, the effective concentration of surfactant within the sPS gel dipped in a 0.5 wt.% surfactant solution, i.e., below the CMC, is calculated as follows. In this case, the total pore volume of sPS aerogel was 11.5 $cm^3/g$, porosity of 93% (Table 3.1) and the amount of surfactant adsorbed by the sPS gel was $0.53 \pm 0.1$ g/g (Figure 3.1A). In view of the above, the value of $C_{eff}$ was found to be 4.6 wt.%, which is 4.6 times the CMC. When the bulk surfactant concentration was above CMC, the surfactant concentration within the gel was determined from integration of the area under the peaks in the proton NMR spectrum for the surfactant and water. The analysis is elaborated in Figure 3A2.

Table 3.1 Bulk density, skeletal density, % porosity, and total pore volume of sPS, PI, and PUA aerogels.

| Polymer aerogel | Bulk density ($g/cm^3$) | Skeletal density ($g/cm^3$) | Porosity (%) | Total pore volume ($cm^3/g$) |
|---|---|---|---|---|
| sPS | 0.08 | 1.05 | 93 | 11.5 |
| PI | 0.07 | 1.36 | 95 | 14.6 |
| PUA | 0.12 | 1.25 | 90 | 7.5 |

The data presented in Figure 3.4A and 3.4B show that the value of $C_{eff}$ in the gel strongly depended on the type of polymer gel used in addition to the value of $C_{bulk}$. For $C_{bulk}$<CMC, e.g., 0.5 wt.%, the value of $C_{eff}$ was 9, 6, and 2 times the $C_{bulk}$ for gels of sPS, PI, and PUA respectively with PUA gels adsorbing the least amount among three gels. At above CMC, the ratio of $C_{eff}$ and $C_{bulk}$ was much smaller, e.g., for a 10 wt.% bulk surfactant solution, the value of $C_{eff}$ in the gel was approximately 2 times the $C_{bulk}$ for sPS and PI and 1.4 times the $C_{bulk}$ for polyurea.

In all cases, higher values of $C_{eff}$ than $C_{bulk}$ indicate a reduction of free energy of the system originating from favorable interactions between the surfactant molecules and the polymer gel surface. The relatively lower values of $C_{eff}/C_{bulk}$ ratio at or above CMC than below CMC indicates a reduction of driving force, suggesting a distinct change of the dynamics of surfactant adsorption at $C_{bulk}$ below and above the CMC.

To understand the above trend, we need to examine the trend of surfactant adsorption by the three polymer gels. Surfactants have a natural tendency to concentrate at the interfaces due to their unique structures, e.g., well-defined hydrophilic and hydrophobic segments[245]. The preferential location of a surfactant at the polymer-water interface minimizes interfacial energy of the system. In this context, a polymer with higher interfacial energy with water may show higher

extent of surfactant adsorption. Vijayendran et al. [249] studied adsorption of an ionic surfactant - sodium dodecyl sulphate - on polymers of varying polarity values and observed that polymer-water interfacial energy had strong influence on the amount of surfactant adsorbed. To corroborate the observations of other researchers, the surfactant-polymer gel interfacial energy was calculated from the values of polymer surface energy and water contact angle values on polymer surfaces. These results are summarized in Table 3.2. The images of water droplets showing contact angle are found in Figure 3.5. The data in Table 3.2 show that sPS had the highest interfacial energy (48.3 mN/m) with water followed by PI (28.7 mN/m) and PUA (13.7 mN/m). This trend of interfacial energy values supports the highest amount of surfactant adsorbed by sPS gels among the three gels used in this work.

Table 3.2. The surface energy of sPS, PI, and PUA polymer gels along with their interfacial energy with water.

| Polymer | Water contact angle (°) | Diiodomethane contact angle (°) | Polar component (mN/m) | Dispersive component (mN/m) | Polymer surface energy (mN/m) | Interfacial energy (mN/m) |
|---|---|---|---|---|---|---|
| sPS | 96 ± 1 | 41 ± 2 | 2.3 | 38.5 | 40.8 | 48.3 |
| PI | 77 ± 2 | 32 ± 3 | 10.6 | 34.4 | 45.1 | 28.7 |
| PUA | 64 ± 2 | 48 ± 1 | 19.9 | 25.5 | 45.5 | 13.7 |

We now analyze the amounts of surfactant adsorbed by the gels in reference to what was reported in literature from earlier work. Prior work reported adsorption of surfactants on various porous and non-porous solid materials in the form of cylindrical nanoporous silica gels, colloidal silica alumina, polystyrene latex[161,165,224,250–252]. Martin et al. reported extremely low maximum amount of adsorption (0.08-0.092 g/g) for different PEO-PPO-PEO block copolymer surfactants on colloidal silica particles[252] whereas other surfactant-polymer surface systems studied reported

adsorption amounts < 0.3-0.5 g/g [165,222,250,252]. These are one or two orders of magnitude lower than what are being reported in this work.

The higher extent of surfactant adsorption in the present study is attributed to higher specific surface area of the gels and the presence of confined geometry. The BET surface area and the fractions of macro- and mesopores of the three gels are listed in Table 3.3. The BET surface area for sPS, PI, and PUA aerogels were respectively 260, 614, and 263 $m^2/g$ and the corresponding BET adsorption isotherms of the three aerogels are available in Figure 3.6. In terms of the specific surface area alone, PI gels should account for twice as much adsorption as sPS gels. However, the much higher adsorption observed for sPS gels are attributed to much higher interfacial surface energy than PI.

Figure 3.5 Water contact angle for A) sPS B) PI and C) PUA compressed aerogel disk

PI and PUA gels used in this work had similar meso-macropore volume fractions while the mesopore fraction of sPS gel was the lowest (0.05) as listed in Table 3.3. The micelle size of the Pluronic® L35 surfactant used with the three gels was reported to be ~2.75 nm (see Table 3.4). These micelles are much smaller compared to the most probable mesopore size (typically 30 nm).

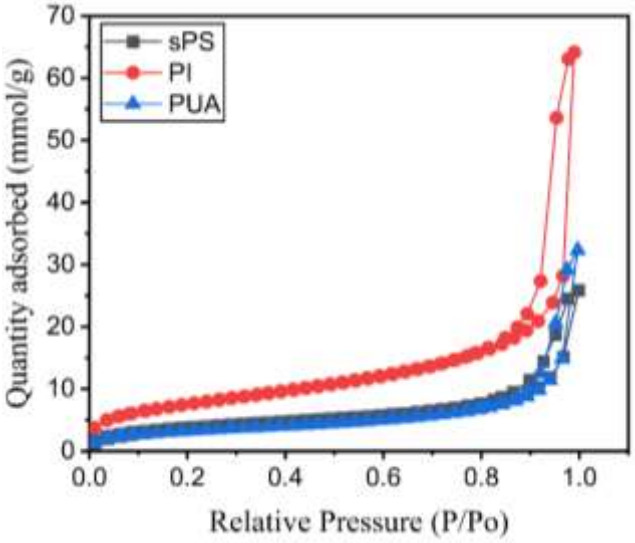


Figure 3.6 BET adsorption isotherm for the three polymer aerogels

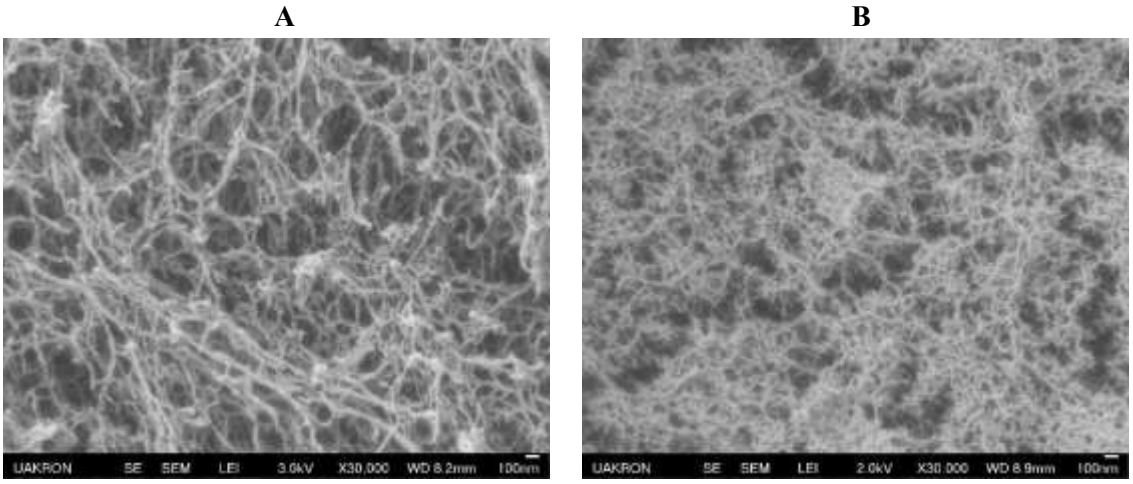


Figure 3.7 Representative SEM images of A) sPS and B) PI aerogels at 30,000 magnification (Figure 3.7A) and 10-100 nm for PI aerogel (Figure 3.7B).

These pores would not present much size exclusion possibility for the much smaller micelles and all macropores contained in the gels. A set of representative SEM images in Figure 3.7 show appreciable open pores of size in the range of 100-300 nm for supercritically dried sPS aerogel

Accordingly, the relative fractions of pores in meso- and macropore categories in the gels would not have much distinctive effects on surfactant adsorption amounts. However, the mesopore fractions of the gel may certainly influence the structural assembly of the surfactants once within the pores due to confinement effects and molecular packing[165]. A thorough analysis of the confinement effects offered by meso- and macropores is beyond the scope of this work and will be pursued in a future study.

Table 3.3 BET surface area and meso-and macropore volume fraction of the aerogels.

| Polymer | BET surface area ($m^2/g$) | Total pore volume ($cm^3/g$) | Mesopore fraction (2-50 nm) | Macropore fraction ( >50 nm) |
|---|---|---|---|---|
| sPS | 260 ± 20 | 11.5 | 0.05 | 0.95 |
| PI | 614 ± 15 | 14.6 | 0.11 | 0.89 |
| PUA | 263 ± 15 | 7.5 | 0.10 | 0.90 |

Another question that needs to be answered is the structural configuration of the PEO-PPO-PEO block copolymer surfactant molecules at the polymer gel-water interface at $C_{bulk}$ below the CMC. The nature of the adsorption isotherm is generally used to identify the adsorption mechanism and to describe the structural features of the adsorbed surfactant molecules[245]. Below the CMC, the adsorption isotherm for Pluronic® L35 surfactant uptake by the gels showed a linear plot as shown in Figure 3.1A similar to a Langmuir adsorption isotherm. This suggests that a monolayer adsorption process was followed by the surfactant with no lateral interactions between the surfactant molecules at concentrations below the CMC. The surfactant is possibly interacting with

a polymer gel by the weaker hydrophobic-hydrophobic interactions between the PPO segment of the surfactant and the polymer surface. Shar et al.[161] reported such interactions between the PEO-PPO-PEO block copolymer surfactants with polystyrene latexes. Other researchers reported the formation of surfactant aggregate structures like hemimicelles or bilayers at the polymer-water interfaces characterized by a steep rise in the adsorption isotherm at a surfactant concentration below the CMC of the surfactant [165,253]. The absence of such a steep rise in adsorption isotherms below the CMC shown in Figure 3.1A for sPS, PI and PUA gels therefore does not suggest such aggregative behavior.

The data from NMR spectroscopy provide useful evidence about adsorbed surfactant layers and the dynamics of this layer[254]. The established model for an adsorbed layer shall consist of directly bound rigid 'trains' that interact with a solid surface and of tails that do not directly interact with the surface but experience reduced mobility due to covalent bonding to the trains[254]. The characteristic NMR peak width increases leading to a broadened NMR spectrum for molecules that have reduced mobility in the liquid phase due to strong adsorption on a solid surface. The extent of peak broadening is dependent on the strength of interactions between the adsorbed layer and the adsorbent surface. Thus, we can estimate the strength of interactions between the gel surfaces and the surfactant molecules using solution NMR data. The $^{1}$H NMR spectra for the three polymer gels

at a bulk surfactant concentration of 0.1 wt.% are shown in Figure 3.8 along with the spectrum for Pluronic® L-35 surfactant solution at the same concentration.

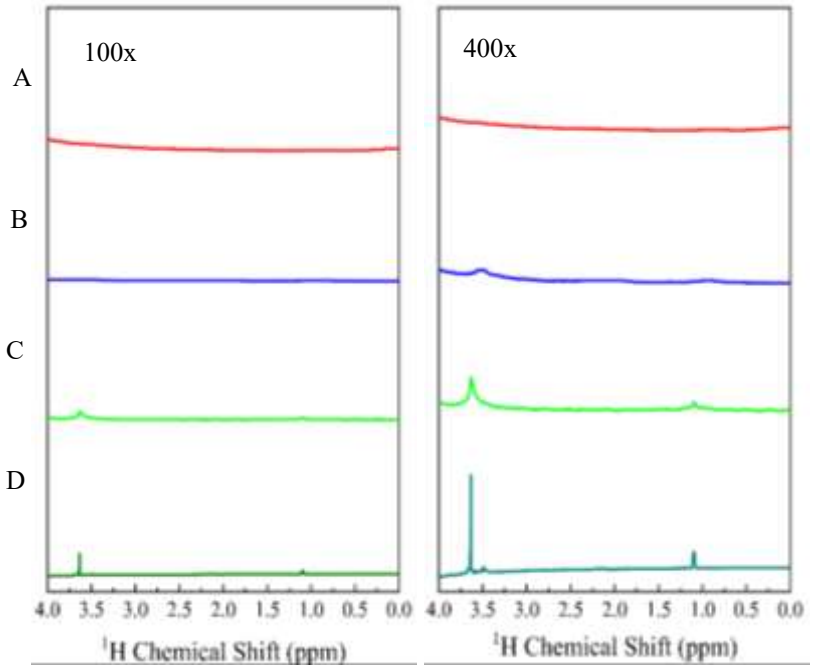


Figure 3.8 $^{1}$H NMR spectrum at 100x and 400x magnification for the Pluronic® L35 surfactant adsorbed on A) sPS, B) PI, C) PUA, and D) Pluronic ®L35 surfactant at 0.1 wt.% bulk concentration in DI water.

PEO-PPO-PEO block copolymer surfactants have three proton NMR peaks around 3.6, 3.50 and 1.1 ppm for the EO ($-CH_2$), PO ($-CH_2$) and PO ($CH_3$) respectively[255]. Sharp proton NMR peaks at these positions for the Pluronic ® L35 surfactant can be seen in Figure 3.8D. The NMR spectrum of adsorbed surfactant on the sPS gel (Figure 3.8A) do not show surfactant peaks at the above-mentioned positions. This suggests significant broadening of the surfactant proton signals due to strong interactions of the surfactants with polymer gels with almost a solid-like layer with reduced mobility in the aqueous phase. In case of PI gels (Figure 3.8B), slightly broadened peaks are visible in the spectrum indicating relatively higher degree of mobility of surfactant molecules and hence relatively weaker interactions with PI gel in comparison to what was observed for sPS

gels. In the case of PUA gels (Figure 3.8C), the peaks are relatively sharper and hence suggest an even weaker interaction of surfactant molecules with the gel surface. This tells us that the interfacial energy at the polymer gel-water interface does play a significant role in determining the intensity of interaction of the surfactant molecule with the polymer gel.

Another interesting observation was the surfactant uptake by the gels at concentrations above the CMC. To the best of our knowledge, all the works reported on surfactant adsorption showed that the adsorption ability of the material reached a saturation value above the CMC, which means that more surfactant molecules cannot be adsorbed by the solid surface when they are predominantly present as aggregate micellar structures in a solution[165,253,256]. An opposite trend was observed in this study as discussed in conjunction with Figure 3.4. Such a trend is now further elaborated.

*3.4.2 Surfactant adsorption by polymer gels at concentrations above the CMC*

Somasundaran et al.[248] reported the thermodynamics of transfer of hydrocarbon (-$CH_2$) groups from a micellar environment to a solid-liquid interface. The free energy plot showed that it was not thermodynamically possible for a -$CH_2$ group to transfer from a highly stable micellar state to a solid-liquid interface as the free energy of transfer would be a positive value and hence not a thermodynamically favorable process. This meant that adsorption of surfactant molecules onto the polymer surface by breaking the micellar structure would not be ideally possible. This poses a question on the possibility of high ratio of $C_{eff}$ and $C_{bulk}$ as observed in Figure 3.4B and gives birth to another hypothesis to explain the surfactant adsorption above the CMC. In this hypothesis, two steps are involved. In step 1, the adsorption of the available surfactant unimers as a monolayer on the polymer surface is governed by the interfacial energy of the polymer gel-water interface, similar to adsorption below CMC. Step 2 involves the transfer of the surfactant micelle structures within the pores of the polymer gels. The presence of the amphiphilic surfactant molecules as adsorbed

molecules and micelles at the interface can possibly serve the purpose of lowering the interfacial energy of the system.

$^{1}$H NMR spectra for the sPS gels along with different Pluronic® L-35 surfactant concentrations above the CMC were obtained to estimate the level of interactions between the polymer gel and the surfactant molecules above the CMC. The NMR spectra for different values of $C_{bulk}$ for sPS gels are shown in Figure 3.9A-E. At $C_{bulk}$ of 0.1 wt.% (below CMC) the absence of surfactant peaks indicate adsorption of surfactant on polymer gel and stronger interactions between surfactant molecules. As the concentration increases to CMC and above CMC, the surfactant peaks become sharper with much reduced peak broadening indicating surfactant molecules were present dominantly in the liquid phase as a micelle. These data provide proof for our hypothesis that surfactant micelle adsorption above the CMC occurs by the two-step process discussed above where the micelles as a whole are captured within the pores of the polymer gels.

To strengthen the hypothesis that micelle diffusion within the gel was the underlying mechanism by which surfactant adsorption occurs at concentrations above the CMC, another experiment was performed wherein three different surfactants with the same PEO-PPO-PEO block copolymer chemistry, but different micelle sizes were chosen namely Pluronic® L35, Pluronic® F127, and Pluronic® P123.

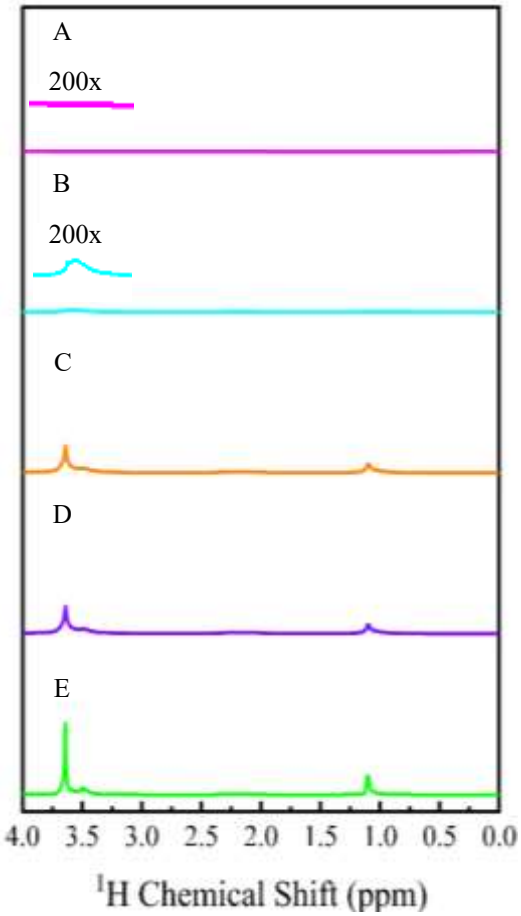


Figure 3.9 $^{1}$H NMR spectrums for sPS gel and Pluronic® L35 surfactant at several values of $C_{bulk}$, curve A at 0.1 wt.%, B at 1 wt.%, C at 5 wt.%, D at 10 wt.%, and E at 15 wt.%.

The micelle sizes for these surfactants were measured using dynamic light scattering (DLS) and the results are reported in Table 3.4. The size distribution curves obtained using DLS for the three surfactants are provided in Figure 3.10. It is evident from Figure 3.10 that the micelle size distribution was bimodal for surfactants Pluronic® P123 with 91% of micelles in the range of 7-25 nm and a most probable diameter of 14 nm. The rest 9% of micelles had broad size distribution in 80-150 nm range. The size distribution of micelles was trimodal for Pluronic® F127 with approximately 10% of micelles having most probable diameter 3.6 nm, 47% of micelles having most probable diameter 16 nm, and the rest 43% with most probable diameter 135 nm (Table 3.4).

The mean hydrodynamic diameter calculated from the size distribution data for Pluronic® L35 surfactant micelles was the lowest (2.5 nm) followed by Pluronic® P123 (14.5 nm) and Pluronic®

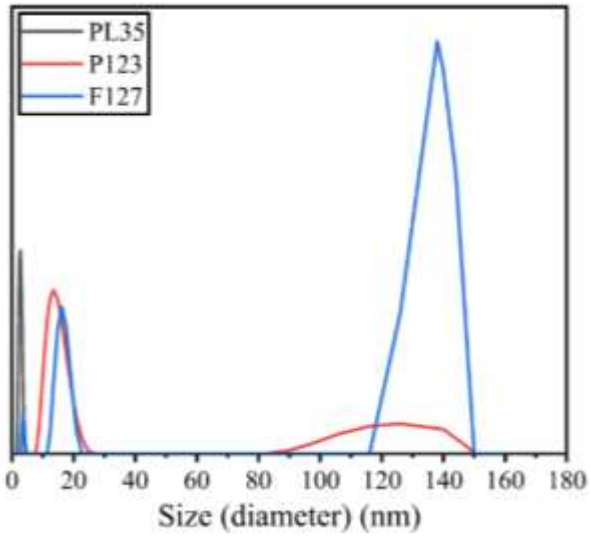


Figure 3.10 Dynamic light scattering micelle size data for Pluronic® L35, Pluronic ® P123 and Pluronic® F127 surfactants

F127 (36.8 nm). The measured hydrodynamic diameter for the Pluronic® L35, Pluronic® F127, and Pluronic® P123 are in agreement with the values reported in literature[257,258]. The CMC for Pluronic® P123 and Pluronic® F127 were found to be around 0.1 wt.% and 1 wt.% respectively[259]. sPS gels were chosen for this part of the study due to their high surface energy being conducive for surfactant adsorption.

Table 3.4 Measured micelle size of the three surfactants at a concentration of 5 wt.% using DLS.

| Surfactant | Most probable size (nm); Frequency (%) | Most probable size (nm); Frequency (%) | Most probable size (nm); Frequency (%) | Hydrodynamic diameter (nm) |
|---|---|---|---|---|
| Pluronic ® L35 | 2.75 ± 0.5; 100 | - | - | 2.75 |

| | | | | |
|---|---|---|---|---|
| Pluronic ® P123 | 14 ± 3.1; 91 | 119 ± 13.5; 9 | - | 14.52 |
| Pluronic ® F127 | 16 ± 2; 46.7 | 135 ± 4.9; 43 | 3.6 ± 0.35; 10 | 36.82 |

It is hypothesized that the size of micelles should play a dominant role in deciding surfactant adsorption if surfactant ingress into gels occurs via micelle diffusion through the porous networks as seen in Figure 3.7A. In this context, surfactants with larger size micelles should experience higher resistance to diffusion through the meso- and macroporous polymer networks and hence should adsorb in lesser quantities by the gel. Figure 3.11A and 3.11B show the adsorbed amounts by sPS gels and the effective concentration within the sPS gels for the three surfactants. The $^{1}$H spectrum for the sPS gel with adsorbed Pluronic ® F-127 and Pluronic P123 are found in Figure 3A3 and 3A4.

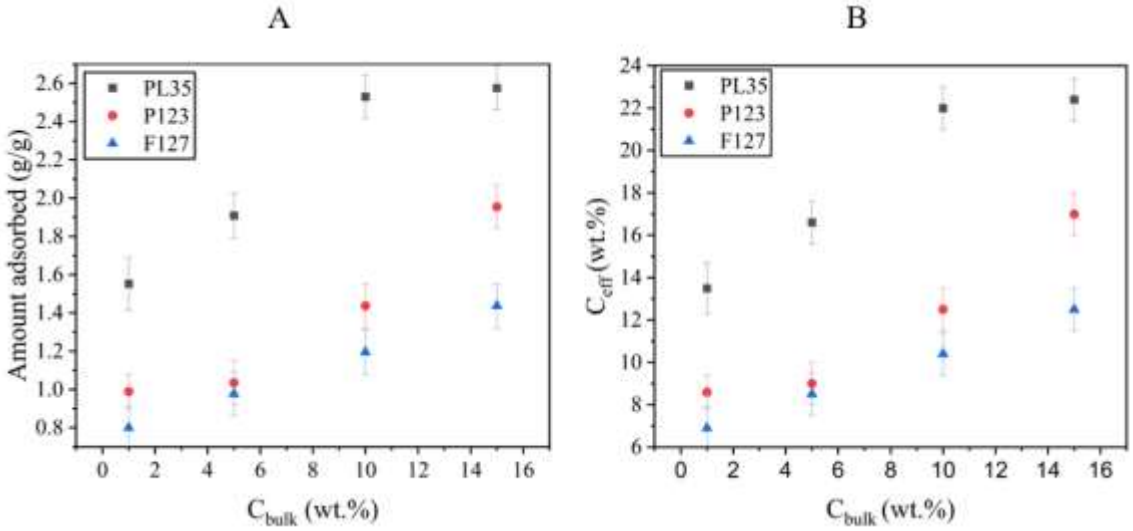


Figure 3.11 Pluronic® L35, Pluronic® P123 and Pluronic® F127 surfactant A) adsorption by the sPS gel B) $C_{eff}$ within the *s*PS gel.

It is seen that surfactant adsorption amounts by sPS gel follow the reverse order of the size of micelles, e.g., Pluronic®L35>Pluronic®P123>Pluronic®F127 surfactant. The surfactant Pluronic®L35 with smallest size micelles (2.75 nm) showed strongest adsorption onto sPS gel,

e.g., 2.5 g/g and $C_{eff}$ of 22 wt% at $C_{bulk}$ of 10 wt%. In comparison, at the same $C_{bulk}$ value, Pluronic®P123 and Pluronic®F127 surfactants produced respectively adsorbed quantities of 1.4 g/g and 1.2 g/g and $C_{eff}$ of 12.5 wt% and 10.4 wt%. It is noted that $C_{bulk}$ was well above the respective CMC values. These data support our hypothesis that micelle diffusion and confinement of micelles into aggregate structures within the gel network are two mechanisms of surfactant adsorption by the gels when $C_{bulk}$ is above the CMC values.

*3.4.3 Desorption of surfactant once adsorbed by the polymer gel*

It is important to understand if surfactant molecule adsorption by the gel is irreversible at $C_{bulk}$ below CMC. In addition, it is important to understand if confinement of micelles within the gel network at $C_{bulk}$ above CMC is irreversible. We examined the above possibilities using sPS gel-Pluronic® L35 system by placing sPS gel with previously adsorbed surfactant into DI water as described in Section 2.5.8. Table 3.5 lists the amounts of surfactant released by the gel upon dipping in water.

Table 3.5 Amounts of Pluronic® L35 surfactant desorbed by sPS gel.

| | $C_{bulk}$ (wt.%) | Amount of surfactant released by the gel (wt.%) |
|---|---|---|
| Below CMC | 0.1 | ~ 0 |
| Above CMC | 5 | ~ 0.001 |

It is observed from the data in Table 3.5 that the amount of surfactant desorbed from sPS gel is negligible. Accordingly, one can infer that the surfactant irreversibly adsorbed onto the gel at concentration below CMC. At above CMC, approximately 0.001 wt.% of surfactant was released

into DI water which is negligibly small compared to the adsorbed amounts as previously discussed. Accordingly, it is inferred that at above CMC, the surfactant molecules were predominantly confined within the pores of the gel as micelle aggregates and such aggregation was irreversible.

## 3.5 Conclusion

The data presented in this paper indicate that high surface area polymer gels with meso- and macropores can strongly adsorb nanometer size surfactant molecules driven by high specific surface area and high surface energy values. The gels derived from sPS, PI, and PUA present an array of interfacial energies with water and accordingly show distinct surfactant adsorption behavior. The data from $^{1}$H NMR spectra and surface tension measurements established two distinct regimes of surfactant adsorption - as a monolayer on the gel surface below CMC and as trapped micelles within the pores of polymer gel above CMC, both regimes were found to be irreversible. At above CMC, the amount of adsorbed surfactant reduced with an increase of the size of micelles, indicating a strong role of micelle diffusion through the pores in the gel. Future research is needed to understand the structural dynamics of surfactants within confined geometries of the pores.

## 3.6 Acknowledgement

This work was partially supported by ACS Petroleum Research Fund under grant number PRF# 59000-ND7, U.S. National Science Foundation under grant number CMMI 1826030, and industrial members of Coalescence Filtration Nanofibers Consortium at The University of Akron.

3.7 Appendix

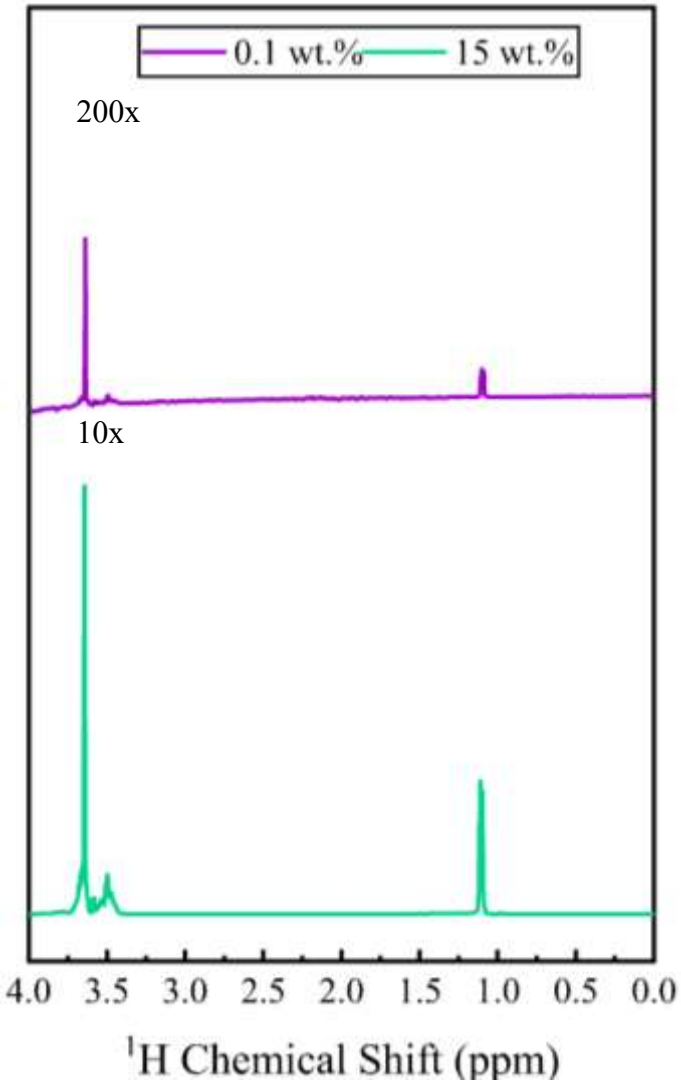


Figure 3A1. Proton NMR spectrum for Pluronic®L35 surfactant at concentrations of 0.1 wt. % and 15 wt.%

The scale for both the spectra in Figure S2 is intentionally different so that the peaks can be clearly seen for the low concentration surfactant sample.

An example surfactant concentration calculation is shown below for a known Pluronic® L35 surfactant aqueous solution.

Theoretical surfactant concentration calculation:

We took 1.5 g of surfactant in 10 ml water ($H_2O$). The surfactant has a density of 1.06 g/ml. Hence, the volume of surfactant in 10 ml water is 1.415 ml. Therefore, the total volume of the solution is 11.415 ml.

From this solution, 0.5 ml is taken along with 0.5 ml of $D_2O$ for the NMR experiment. The amount of $H_2O$ present in the NMR tube is 0.437 ml and amount of surfactant present is 0.066 g. Therefore, surfactant concentration (wt.%) w.r.t. $H_2O$ is 13.1 wt.%.

Experimental surfactant concentration obtained from proton NMR spectrum:

$$X = (\text{Area under PO } (-CH_3)\text{peak}/3 + \text{Area under PO } (-CH_2)\text{ peak}/2) * \text{Mol. wt. of PO } + (\text{Area under EO } (-CH_2)\text{ peak}/4) * \text{Mol. wt. of EO}$$

$$\text{Surfactant concentration (wt.\%)} = \left(\frac{X}{X + \text{Area under water peak} * \text{Mol. wt. of water}/2}\right) * 100$$

$$\text{surfactant concentration (\% wt.)} = \frac{\left(\left(\frac{1}{3}+\frac{0.67}{2}\right)*58+\left(\frac{1.94}{4}\right)*44\right)*100)}{\left(\left(\frac{1}{3}+\frac{0.67}{2}\right)*58+\left(\frac{1.94}{4}\right)*44\right))+18*\frac{36}{2}}$$

$$= 15.6 \text{ wt.\%}$$

The theoretical and experimental surfactant concentrations were approximately close with a difference of 2.5 wt.%.

Similar, calculations were performed for characterizing the surfactant concentration within the polymer gels.

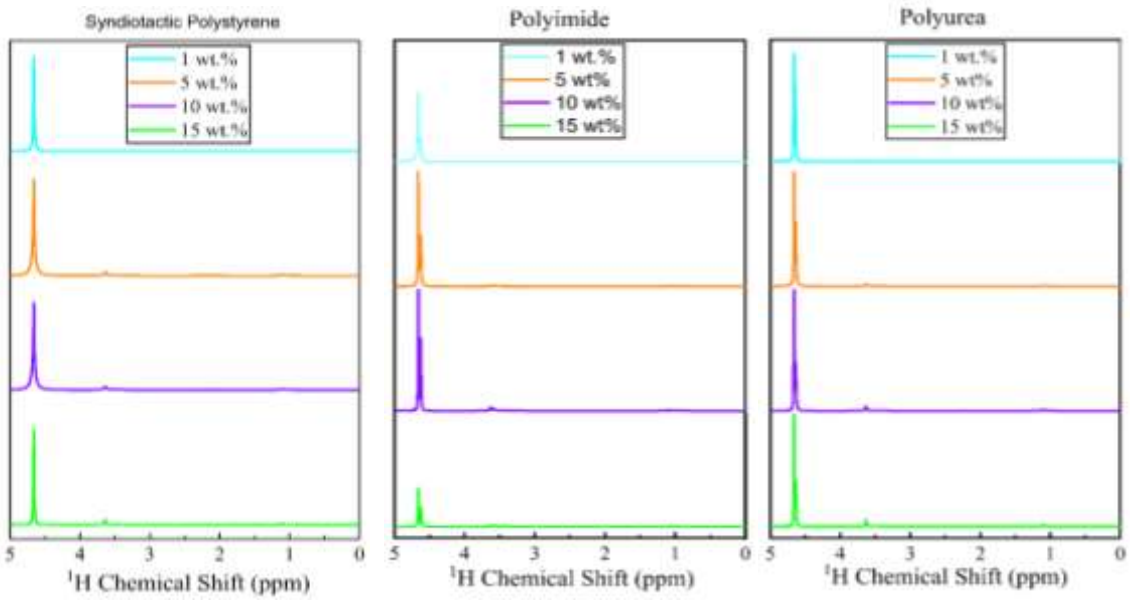


Figure 3A2. $^1$H NMR spectra for Pluronic L-35 surfactant taken up by sPS, PI and PUA gels

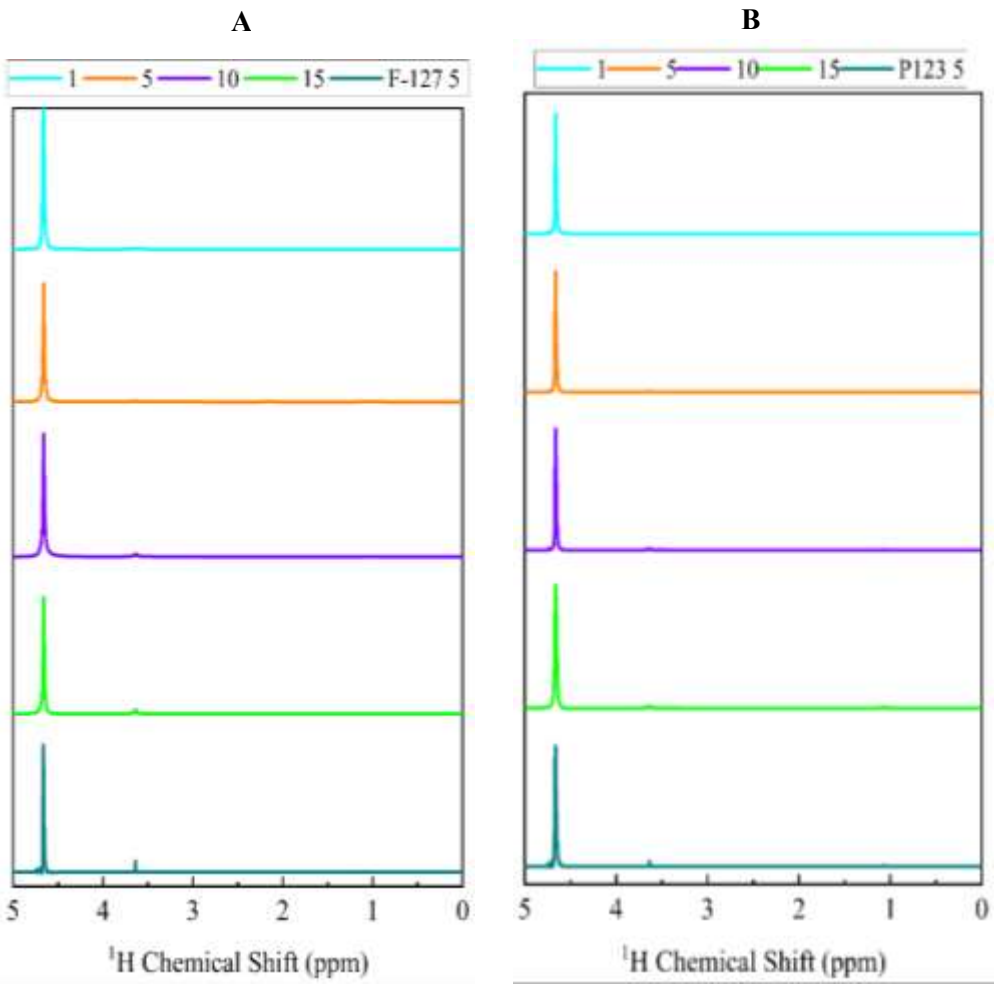


Figure 3A3 $^{1}$H NMR spectra for A) sPS+F127 surfactant and B) sPS+P123 surfactant at bulk surfactant concentrations of 1,5,10 and 15 wt.% along with pure surfactant NMR at 5 wt.% concentration

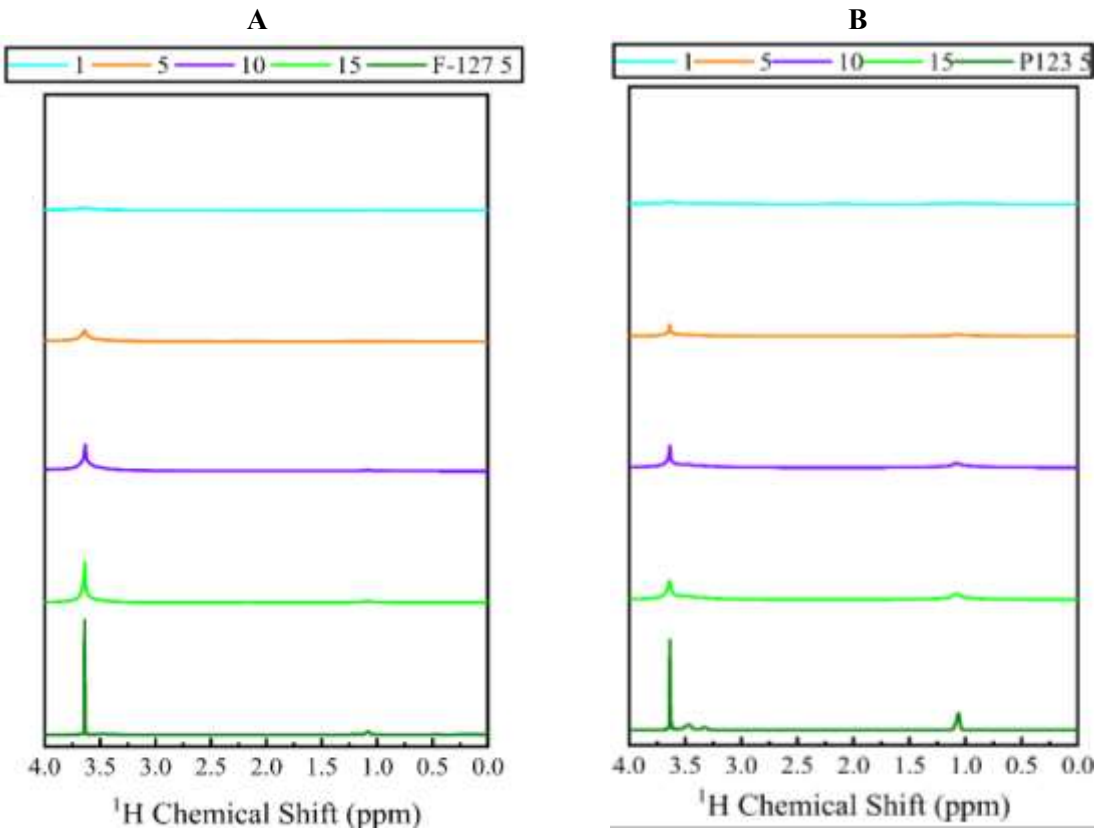


Fig 3A4 Magnified $^{1}H$ NMR spectra for A) sPS+F127 surfactant and B) sPS+P123 surfactant at bulk surfactant concentrations of 1,5,10 and 15 wt.% along with pure surfactant NMR spectrum at 5 wt.% concentration

CHAPTER IV

# UNDERSTANDING SEPARATION OF OIL-WATER EMULSIONS BY HIGH SURFACE AREA POLYMER GELS USING EXPERIMENTAL AND SIMULATION TECHNIQUES

## 4.1 Abstract

In this work, an attempt was made to evaluate whether the high surfactant adsorption abilities of high surface area polymer gels also translate into strong oil-water emulsion separation performance. In the process, an understanding of the factors and steps that influence the emulsion separation process was developed. Specifically, four different polymer gels namely syndiotactic polystyrene (sPS), polyimide (PI), polyurea (PUA) and silica gels with different surface energies were evaluated for their oil-water emulsion separation performance. It was found that the emulsion separation performance of the polymer gels scaled directly with their surfactant adsorption abilities. sPS and PI gels were able to deplete the surfactant present in the emulsion, hence destabilize and separate the emulsions. It is reported that once the oil droplets are stripped off the surfactant layer surrounding it, the oil droplets are absorbed by the sPS and PI gels. This was attributed to the

preferential wettability of the sPS and PI gels for the oil phase over the water phase. In addition, simulation experiments were performed to understand the adsorption characteristics of two different polyethylene oxide(PEO)-polypropylene oxide (PPO)-PEO block copolymer surfactants and an attempt was made to correlate the obtained simulation results with the emulsion separation performance shown by the polymer gel.

## 4.2 Introduction

Oil-in-water or water-in-oil emulsions are frequently encountered in crude oil producing industries, enhanced oil recovery processes, oily industrial effluents, or recurrent oil spills[260,261]. The presence of the highly viscoelastic surfactant film at the oil-water interface results in the formation of a stable emulsion which causes severe problems like fouling, corrosion in addition to increasing production and operation costs[262]. Several techniques have been developed over the years to break emulsions which include addition of chemical additives[263], thermal[264] or microwave irradiation[265,266], membrane separation[267], and use of electric[268] or acoustic fields[269]. However, these techniques present shortcomings, such as secondary pollution, low separation efficiencies, and high cost in terms of capital and energy consumption. To overcome these challenges, we have investigated the prospect of using high surface area polymer gels for separating oil-water emulsions which capitalizes on their ability to deplete high amounts of surfactant from the liquid[270,271].

Surfactant molecules readily absorb at the oil-water interface due to their amphiphilic nature. Oil and water are immiscible phases, but the presence of the surfactant molecules helps in lowering the interfacial tension and facilitates dispersion of one liquid into another in the form of discrete micrometer sized droplets. The surfactant molecules provide steric or electrostatic barriers at the oil-water interfaces inhibiting neighboring droplets from overcoming the attractive van der Waals forces[137,262]. Demulsification is a process by which the dispersed phase droplets are allowed to flocculate, coalesce, and eventually segregate into a separate bulk liquid phase[158]. An effective

emulsion destabilizer should deplete the surfactant molecules from the continuous phase as well as from the oil-water interface. Chemical demulsification is the most commonly used technique to break emulsions. Chemical demulsifiers work by penetrating or rupturing the existing surfactant film due to their higher interfacial activity[262,272,273].The new film formed by the demulsifier is weaker in strength and facilitates the coalescence of oil droplets. Cationic quaternary ammonium salt based[153,274] or acrylic latex-based polymers, dendrimers[156], ionic liquids[275,276], graphene oxide nanosheets[273] are example of chemical demulsifiers which work on this principle. However, the use of chemical demulsifiers does not permanently solve the problem, since mixing or agitation can again lead to emulsion formation again due to the presence of surfactants in the system. In addition, the use of additional chemicals in the liquid stream is considered to be a source of secondary pollution. To counter this, Katepalli et al. reported the use of fumed silica colloidal particles as demulsifiers for a non-ionic triton X100 stabilized oil-in-water emulsion[158]. The partially hydrophobic silica particles were able to adsorb the surfactant onto their surface by H-bonding and hydrophobic interactions leading to flocculation and coalescence of oil droplets. However, fumed silica is considered a pollutant and removal of these extremely small particles from liquid streams would be a cumbersome and economically unviable step. In this context, we have investigated a new demulsification pathway which utilizes high surface area polymeric gels that have the ability to adsorb high amounts of surfactant molecules from liquids, hence depleting surfactant molecules from the oil-water interface and the continuous liquid phase, thereby inducing separation of the oil and water phases. The polymer gels can be easily removed from the system once the desired separation has been achieved.

Polymer gels are formed either by a chemical or physical crosslinking mechanism[3,85,277]. These polymer gels provide extremely high specific surface areas (200-900 $m^2/g$) and have an interconnected pore network consisting of meso-(2-50 nm) and macro-pores (>50 nm).

Syndiotactic polystyrene (sPS)[50,278], polyimide[58] (PI), polyurea (PUA)[85,242], silica[16], cellulose[279], polyurethane[83] are examples of some gel forming polymer systems reported in literature. Gotad et al. investigated the adsorption abilities of different surface energy polymer gels for non-ionic surfactants based on polyethylene oxide (PEO)- polypropylene oxide (PPO)-polyethylene oxide (PEO) block copolymer chemistry[270]. The findings reported that for efficient adsorption of surfactant molecules, a high interfacial energy solid-liquid interface coupled with high specific surface area was essential. One of the interesting and novel observations reported in this work was the high amount of surfactant adsorption at concentrations above the critical micelle concentration (CMC). Stable oil-water emulsions form only at concentrations above the CMC, hence the hypothesis for this work was that the effective removal of surfactants even from the above CMC concentration regime should facilitate the demulsification or breaking of the oil-in-water emulsions. If we take a look at some of the surfactant adsorbing systems[164,165,280], a plateau in surfactant adsorption ability is reached as the CMC of the surfactant is approached and hence, they would not be suitable for such demulsification applications which was not the case with the high surface area meso-macro-porous polymer gels studied in this work.

Here, we firstly investigated the effect of different surface energy polymer gels on non-ionic PEO-PPO-PEO block copolymer stabilized oil-in-water emulsions. It should be noted that the polymer gels have the ability to absorb the oil as well and hence it was imperative to deconvolute the two steps in emulsion separation, (i) surfactant adsorption from the liquid phase and (ii) oil absorption by the polymer gels, to understand which of the two steps governs the demulsification process. This was done by using two different non-ionic PEO-PPO-PEO block copolymer surfactants, (i) short chain surfactant (Pluronic L35), with high adsorption ability by the polymer gels and (ii) long chain surfactant (Pluronic F127), with poor adsorption ability by the polymer gels. The difference in emulsion separation performance between these two systems was

analyzed to draw conclusions regarding which step governs the separation. Further, atomistic simulation techniques were employed to understand the difference between the adsorption of a short and long chain PEO-PPO-PEO surfactants. Questions of why the short chain surfactant adsorbs more effectively onto the polymer gel surface compared to the long chain surfactant, were answered in terms of their structural configuration on the polymer surface, their binding energy, and the surface area occupied by the molecules. An implication of these results on the oil-water emulsion separation is presented in this chapter.

## 4.3 Experimental section

### 4.3.1 Materials

sPS (Mw ≈ 300,000 g/mol, 98%) was obtained from Scientific Polymer Producers Inc. (Ontario, NY, USA). 2,2′dimethylbenzidine (DMBZ) was purchased from Shanghai Worldyang Chemical Co. Ltd (Shanghai, China). Pyromellitic dianhydride (PMDA, , ≥ 96.5%), tris(2-aminoethyl) amine (TREN, ≥ 95.5%) crosslinker, acetic anhydride (≥ 99%), and toluene (≥ 99.9%) were purchased from Sigma-Aldrich (Milwaukee, WI, USA). Pyridine (≥ 99%) and acetone (≥ 99.5%) were purchased from Fisher Scientific (Ontario, NY, USA). N,N-dimethylformamide (DMF, ≥ 99.5%) was purchased from VWR International (Radnor, PA, USA). Ethanol was purchased from Decon Laboratories Inc. (King of Prussia, PA, USA). Desmodur N3300A (tri-isocyanate) and triethylamine (TEA) were procured from Covestro (Pittsburg, PA, USA) and Sigma Aldrich (Milwaukee, WI, USA) respectively. Pluronic L35 (PL35) and Pluronic F127 (PF127) each with a molecular weight of 1,900 and 12,600 g/mol respectively along with sodium dodecyl sulphate (SDS) and cetyltrimethylammonium bromide (CTAB) were obtained from Sigma-Aldrich (Milwaukee, WI, USA). Tetraethyl orthosilicate (TEOS, reagent grade, 98%), nitric acid (purity, 64−66%), and ammonium hydroxide solution (28−30%) were purchased from Sigma Aldrich (Milwaukee, WI, USA). Ultralow sulphur diesel (ULSD) fuel was procured from a local gas station

and was treated with Fuller's Earth Filter (Jaxon Filtration, GA) to remove the impurities and surfactants, if any. All the chemicals were used as obtained without further purification.

### 4.3.2 Fabrication of sPS gels and aerogels

sPS gels were prepared using a thermo-reversible gelation mechanism of sPS solutions in toluene. A solid concentration of 0.06 g/ml was dissolved in toluene in sealed vials at 100 °C. The solution was allowed to cool under ambient conditions for 1 min and were subsequently poured in cylindrical glass molds of diameter 15mm for gelation. The gels were allowed to age in the mold for 5 hours to ensure complete gelation and were then demolded and solvent exchanged first with ethanol and finally with deionized water to obtain the water filled sPS gels. To form the diesel filled sPS gels, the ethanol filled sPS gels were exchanged with acetone followed by solvent exchanges with diesel.

The sPS aerogels were obtained by solvent exchanging ethanol filled gels with liquid carbon dioxide followed by supercritical drying at 50 °C and 11 MPa. The sPS aerogels were used for surface energy, pore sizes and morphology analysis.

### 4.3.3 Fabrication of polyimide gels and aerogel

PMDA and DMBZ were mixed together for 2 mins at room temperature at 1200 r.p.m. followed by addition of TREN and acetic anhydride and pyridine. The resulting solution was poured into a cylindrical mold of diameter of 16 mm. The gelation of this system occurred within 10 mins. The gels were then allowed to age for 24 hours prior to demolding them. The gels were subsequently solvent exchanged with DMF/acetone mixtures of 75:25, 50:50, 25:75 v/v followed by 3 additional solvent exchange steps with 100% acetone. The water filled polyimide gels were obtained by solvent exchanging with acetone- DI water mixtures of increasing water concentration and finally with 100% DI water. Similarly, the diesel filled polyimide gels were obtained by solvent exchanging acetone filled gels with 100 % diesel six times. Polyimide gels with 7.5 wt.% polymer

concentration were prepared using 0.686 g of PMDA, 0.636 g of DMBZ, 92 μL of TREN, 1.847 mL of acetic anhydride, and 1.909 mL of pyridine in 15 mL DMF.

The acetone filled polyimide gels were exchanged with liquid carbon dioxide and dried under supercritical carbon dioxide at 50 °C and 11 MPa pressure to obtain polyimide aerogels for morphology, wettability, and pore size characterization.

### 4.3.4 Fabrication of polyurea gels and aerogels

The PUA gels were prepared using tri-isocyanate, water, and TEA in molar ratio 1:3:1 with 0.15 M concentration of tri-isocyanate. The triisocyanate was dissolved in anhydrous DMF at room temperature for 30-45 mins followed by addition of deionized water for 3 mins. TEA was added to the mixture and the resulting solution was allowed to be mixed for additional 2 mins. The PUA gels filled with acetone and suitable for supercritical drying were obtained by solvent exchanging in steps with mixed solvents DMF-acetone in the ratio 75: 25, 50: 50, 25: 75 v/v followed by 3 solvent exchanges in 100% acetone. The acetone-filled gels were solvent exchanged in liquid $CO_2$ and subsequently dried under supercritical condition of $CO_2$ at 50 °C and 11 MPa pressure to obtain aerogels. Water-filled polyurea gels were prepared by solvent exchange with acetone:water mixtures with increasing the concentration of water and finally with 100% DI water three times. Diesel filled polyurea gels were obtained by solvent exchanging acetone filled gels with 100% diesel six times. Polyurea aerogels for characterization purposes were obtained by solvent exchanging acetone filled gels in liquid $CO_2$ and subsequent drying under supercritical condition of $CO_2$ at 50 °C and 11 MPa pressure.

### 4.3.5 Fabrication of silica gels and aerogels

The silica gels were prepared using tetraethyl orthosilicate (TEOS) (10.4 g) as the precursor monomer. The TEOS was solubilized in ethanol (10 mL) and water (2.6 mL). Nitric acid was added to it to partially hydrolyze TEOS at a pH of ~2.0 and mixed for 10 mins. Subsequently, a solution

of ammonium hydroxide ($NH_4OH$) (0.25 mL), water (3.6 mL) and ethanol (20 mL) was added to it. The resulting solution was allowed to mix for 10 mins and then was poured in cylindrical molds of diameter 1.5 cm. The sol was allowed to gel in these molds overnight. The gels were demolded, and solvent exchanges were carried out with ethanol: water mixtures of 75:25, 50:50, 25:75 v/v followed by 4 additional solvent exchange steps with 100% water to form the water filled silica gels.

To make the silica aerogels, the silica demolded gels were solvent exchanged with 100 % ethanol 6 times followed by solvent exchanges with liquid carbon dioxide. Finally, the silica gels were dried in supercritical $CO_2$ at 50 °C and 11 MPa pressure to obtain silica aerogels.

### 4.3.6 Preparation of surfactant stabilized oil-water emulsions

The oil-in-water emulsions were obtained using water as the continuous phase and ultra-low sulphur diesel (ULSD) fuel as the dispersed phase. Emulsions with 1 vol.% of ULSD in water were prepared using a planetary centrifugal THINKY® mixer at 1000 r.p.m for 10 mins. The surfactants, PL35 and PF127 at a concentration of 2 wt.% (above the c.m.c.) were added to stabilize the emulsion. The emulsions were stable for the duration of the experiments which was inferred from the stable droplet size distributions over a period of 24 h.

### 4.3.7 Simulation details

The initial structures of Pluronic L35 and F127 were constructed using the Materials Studio package (*Material Studio™, by Dassault Systèmes BIOVIA, UK (Accelrys®), (License purchased by The University of Akron).* Subsequently, single chains of L35 and F127 were immersed in 15,000 and 20,000 water molecules, respectively, utilizing the Polymatic package[281]. Molecular dynamics simulations were conducted using the LAMMPS package[282], applying periodic boundary conditions in all dimensions. The SPC/E[283] water model and the force field developed by Ercan et al.[284] for Pluronic molecules were utilized to characterize both bonded and non-bonded interactions,

with a cutoff distance of 12Å for van der Waals and short-range electrostatic interactions. Long-range electrostatic interactions were calculated using the PPPM algorithm with an accuracy of $10^{-4}$. The initial simulation box underwent equilibration for 15 ns under the NPT ensemble, with temperature and pressure set to 298 K and 1 bar, respectively, using Nose-Hoover thermostat and barostat. Once the box density reached equilibrium, simulations continued under the NVT ensemble at the same temperature. In all the simulations, step time and dumping frequency was 1fs and 5ps, respectively. The bulk simulation for PF127, featuring a greater number of monomers and slower dynamics, lasted over 480 nanoseconds, while PL35 required a shorter simulation time of 250 nanoseconds.

To integrate the polystyrene film into the water/polymer simulation box, periodicity in the z-direction of the equilibrated water-polymer box was eliminated. Subsequently, the new water-polymer box was positioned 3Å above the polystyrene film. The syndiotactic polystyrene film consists of 160 chains, each comprising 40 monomers. Its equilibrated dimensions are approximately 108Å × 102Å × 106Å in the x, y, and z directions, containing a total of 103,200 atoms. Details regarding the preparation of the polystyrene film can be found elsewhere[285]. Furthermore, the OPLS-AA force field[286] was employed to describe both bonded and non-bonded interactions of the polystyrene chains.

### 4.3.8 Characterization

*4.3.8.1 Bulk density, skeletal density, and porosity measurements:* Helium pycnometer (AccuPyc II 1340, Micromeritics Instrument Corp., Norcross, GA) was used to measure the skeletal density ($\rho_s$) of the aerogel specimens and the bulk density ($\rho_b$) was obtained by measuring their mass and volume. The porosity of the aerogels was calculated using equation (1).

$$\rho_T = (1-\rho_b/\rho_s)\times 100 \quad (1)$$

*4.3.8.2 Brunauer−Emmett−Teller (BET) Adsorption-Desorption:* $N_2$ adsorption-desorption isotherms obtained at 77 K using a Micromeritics Tristar II 3020 analyzer (Micromeritics Instrument Corp., Norcross, GA) were used to obtain the BET surface area and mesopore volume fraction of the aerogel samples. The mesopore volume was obtained using the nonlocal density functional theory model from $N_2$ isotherms at 77 K. The total pore volume ($V_T$),the mesopore volume fraction and the macropore volume fraction were obtained using equation (2-4).

$$V_{total} = \frac{1}{\rho_b} - \frac{1}{\rho_s} \quad (2)$$

$$\phi_{meso} = \frac{V_{meso}}{V_{total}} \quad (3)$$

$$\phi_{macro} = \frac{V_{macro}}{V_{total}} = 1 - \phi_{meso} \quad (4)$$

*4.3.8.3 Morphology:* Scanning electron microscope (SEM JSM 5310, JEOL,MA) was used to obtain the morphology of the aerogel specimens.

*4.3.8.4 Polymer surface energy and contact angle measurements:* The polymer surface energy was obtained using Wu's theory using equation 5. The contact angle values of water and diiodomethane were measured on compressed polymer disks.

$$\gamma_{LS} = \gamma_L + \gamma_S - \frac{4\gamma_L^d\gamma_S^d}{\gamma_L^d + \gamma_S^d} - \frac{4\gamma_L^p\gamma_S^p}{\gamma_L^p + \gamma_S^p} \quad (5)$$

In equation (5), $\gamma_{LS}$ is the interfacial tension between liquid and solid, $\gamma_L$ is the surface tension of the liquid, $\gamma_S$ is the surface energy of the solid, and $\gamma^d_S$ and $\gamma^p_S$ are the dispersion (nonpolar) and polar components of liquid surface tension, respectively. The standard values of $\gamma_L^d$ = 21.8 dyn/cm and $\gamma_L^p$ = 50.7 dyn/cm for water and $\gamma_L^d$ = 44.1 dyn/cm and $\gamma_L^p$= 6.7 dyn/cm for diiodomethane were used in the calculations[244]. The surface energy of polymer is obtained from the sum of dispersive ($\gamma^d_S$) and polar ($\gamma^p_S$) components as in equation (6).

$$\text{Polymer surface energy } (\gamma_S) = \gamma_s^d + \gamma_s^p \quad (6)$$

The polymer -liquid interfacial energy ($\gamma_{LS}$) was calculated using Young-Laplace equation as in equation (7) where $\gamma_L$ is surface tension of the liquid and Θ is the contact angle on polymer surface.

$$\gamma_S = \gamma_{LS} + \gamma_L cos\theta \quad (7)$$

The polymer-water and polymer-diesel contact angles were obtained by placing a 10 μL droplet of the respective liquid on a compressed polymer disk. For this purpose, aerogel specimens were compressed as discs between two clean, flat metal platens at 1.8 MPa pressure to remove the pores so that only the chemistry of the polymer affects the contact angle values. Water has a surface tension of 72.5 mN/m and diesel has a surface tension of 26 mN/m.

## 4.4 Results and Discussion

### 4.4.1 Effect of polymer gel surface energy on emulsion separation

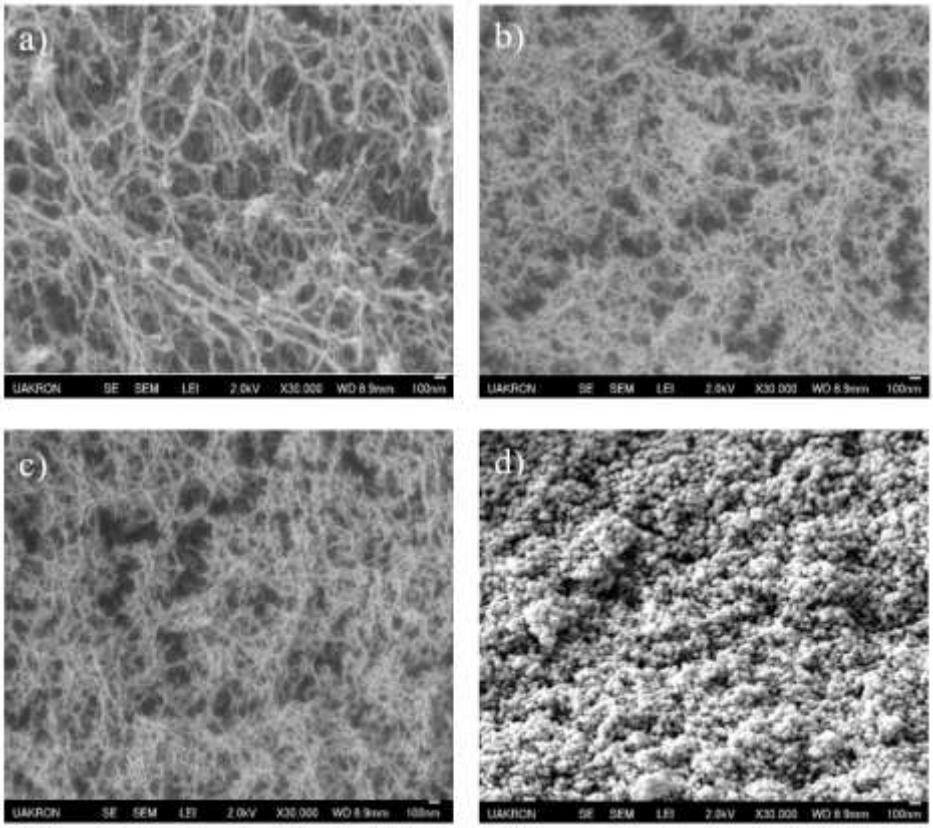


Figure 4.1 High magnification SEM images of a) sPS b) PI c) PUA and d) silica aerogels

Here, we investigated the performance of four different surface energy porous polymer gels namely syndiotactic polystyrene (sPS), polyimide (PI), polyurea (PUA) and silica, for separation of surfactant stabilized ultralow sulphur diesel (ULSD, oil)-in-water emulsions. Firstly, the hypothesis was that since these polymer gels show surfactant adsorption ability at concentrations above the CMC, they should be able to break emulsions by depleting surfactant molecules from the liquid phase and the oil-water interfaces. Secondly, the surfactant adsorption ability of the different polymer gels was said to be governed by their respective surface energies. Gotad et al. showed that the surfactant adsorption by the polymer gels followed the order sPS > PI> PUA[270].This result was attributed to the high energy interface created by the hydrophobic sPS nanofibers which led to a

large amount of surfactant adsorption by the sPS gel and this phenomenon was also reported by Vijayendran et al.[249] PI and PUA with lower interfacial energy compared to sPS showed lower surfactant adsorption performance. A similar discussion is raised in this work; however, in the context of emulsion separation.

Table 4.1 Bulk density, % porosity, BET surface area, volume fraction of mesopores and macropores of the four different polymer aerogel systems

| Polymer | Bulk density ($\rho_b$) ($g/cm^3$) | % Porosity | BET surface area ($m^2/g$) | $\phi_{meso}$ | $\phi_{macro}$ |
|---|---|---|---|---|---|
| sPS | 0.08 ± 0.01 | 93 | 290 ± 20 | 0.05 | 0.95 |
| PI | 0.07 ± 0.01 | 95 | 614 ±15 | 0.11 | 0.89 |
| PUA | 0.12 ± 0.04 | 90 | 263 ±15 | 0.10 | 0.90 |
| Silica | 0.13 ± 0.02 | 93 | 787 ± 30 | 0.33 | 0.67 |

However, before the oil-water separation performance of the polymer gels is discussed, a brief description of the material properties of the polymer gels is presented here. The high magnification SEM images along with the specific surface area, bulk density, and pore sizes can be found in Figure 4.1 and Table 4.1. The morphology, surface area and pore size characteristics of the polymer gels were obtained after converting the gels into aerogels (see experimental section for detailed information on sample preparation). The nanofibrous polymer network formed by the sPS, PI and PUA gels with fiber sizes ~ 10-30 nm can be observed in the SEM images (Figure 4.1). The silica gel forms a different morphology, more like a pearl-necklace structure where spherical beads are connected to each other to form the three-dimensional gel network. The specific surface area provided by the four polymer gel systems is given in Table 4.1. sPS, PI, PUA and silica have a BET surface area of 290 ± 20, 614 ± 15, 263 ± 15 and 787 ± 30 respectively. The BET adsorption-

desorption isotherms are shown in Figure 4.2. The meso-and macro-pore volume fraction is different for the different polymer gels, with silica (0.33) having the highest amount of mesoporosity followed by polyimide (0.11), polyurea (0.10) and sPS (0.05). All the polymer gels have an open pore network which is essential for unrestricted diffusion or movement of molecules through the gel network and assessing the entire surface area provided by the gels. Table 4.2 depicts the surface energy characteristics of the four different polymer gels. The water and diiodomethane contact angles on the polymer surfaces were used to calculate the polymer surface energy and its corresponding interfacial energy with water. sPS being highly hydrophobic has a water interfacial energy of 48.3 mN/m followed by PI, PUA and silica with water interfacial energies of 28.7, 13.7 and 3.3 mN/m respectively.

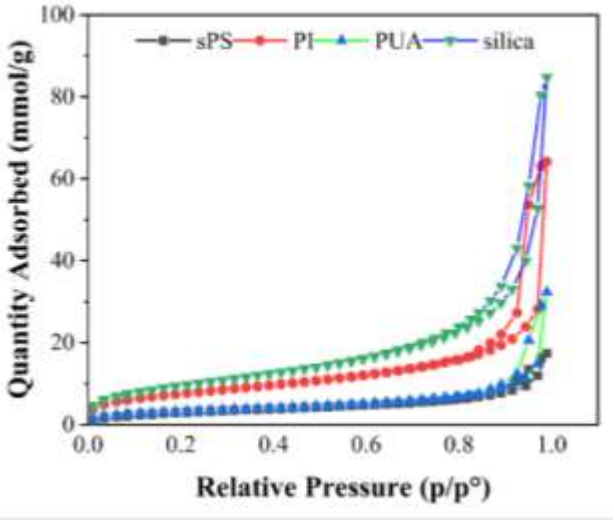


Figure 4.2 BET adsorption isotherm for the four polymer aerogels

Table 4.2 The surface energy of sPS, PI, PUA and silica gels along with their interfacial energy with water.

| Material | Water contact angle (°) | Diiodomethane contact angle (°) | Polar (mN/m) | Dispersive (mN/m) | Polymer surface energy (mN/m) | Interfacial Energy (mN/m) |
|---|---|---|---|---|---|---|
| sPS | 96 ± 1 | 41 ± 2 | 2.3 | 38.5 | 40.8 | 48.3 |
| PI | 77 ± 2 | 32 ± 3 | 10.6 | 34.4 | 45.1 | 28.7 |
| PUA | 64 ± 2 | 48 ± 1 | 19.9 | 25.5 | 45.5 | 13.7 |
| Silica | 25 ± 3 | 27 ± 1 | 38 | 31 | 69 | 3.3 |

Surfactant molecules because of their amphiphilic nature have a natural tendency to remain at the interfaces. Therefore, in the case of an oil-water emulsion, the surfactant molecules occupy the unstable oil-water interface and stabilize it. However, when a high surface area solid polymer gel is bought in contact with an emulsion, the surfactant now has two interfaces to choose from- (i) the oil-water interface and (ii) the solid-water interface presented by the polymer gel. According to thermodynamic principles, the oil-water-polymer gel system will always strive to achieve a state of minimum Gibbs free energy[248]. The minimum Gibbs free energy state can be achieved by various means such as reducing the number of unstable interfaces in the system[249], increasing the favorable interactions within the system, i.e., between the polymer-surfactant molecules which may have the ability to interact by electrostatic forces, hydrogen bonding, hydrophobic interactions, etc. or formation of energetically stable structural organizations[159,164,165] by the surfactant molecules on the polymer surface. Adsorption is therefore a complex process dependent on various factors. In this regard, we believe the first thing to consider would be the oil-water and the polymer-water interfacial energies that would play a significant role in deciding the fate of the surfactant molecules

present in the system. If the oil-water interface had a higher interfacial energy compared to the polymer-water interface, the surfactant would prefer to stay at the oil-water interface and there would be no demulsification or separation of the emulsion observed. On the contrary, if the polymer-water interfacial energy is higher than the oil-water interfacial energy, the surfactants would spontaneously desorb from the oil-water interface and adsorb on the polymer-water interface, to lower the total energy of the system. This would lead to demulsification of the oil droplets and their subsequent coalescence and separation from water.

The interfacial energy of the oil (ultralow sulphur diesel)-water interface was measured using the pendant drop method and it was found to be 21 ± 1 mN/m. From Table 4.2, it can be seen that two of the polymer gel systems namely sPS (48.3 mN/m) and PI (28.7 mN/m), have interfacial energy higher than the oil-water interface whereas the other two gels i.e., polyurea (13.7 mN/m) and silica (3.3 mN/m) have a lower interfacial energy. Therefore, hypothetically, the demulsification performance of the polymer gels should be in the following order: sPS (highest demulsification)> PI > PUA=Silica (no demulsification).

The oil-water emulsion separation experiment was performed by bringing the different polymer gels in contact with a Pluronic L35 surfactant stabilized oil-in-water emulsion for a period of 12 h. The emulsion preparation method is described in detail in the experimental section. Optical microscope images were obtained for the emulsion before it was brought in contact with the polymer gels (control emulsion) and after it was in contact with the different polymer gels for 12 h. The images are shown in Figure 4.3 (a-e). Five hundred droplets were analyzed for each emulsion to obtain the droplet size distribution presented in Figure 4.3f. The control emulsion (Figure 4.3a

and Figure 4.3f (Light green)) was stable for a week and had a broad oil droplet size distribution ranging from ~ 5- 50 μm with a most probable oil droplet size ~ 20 μm.

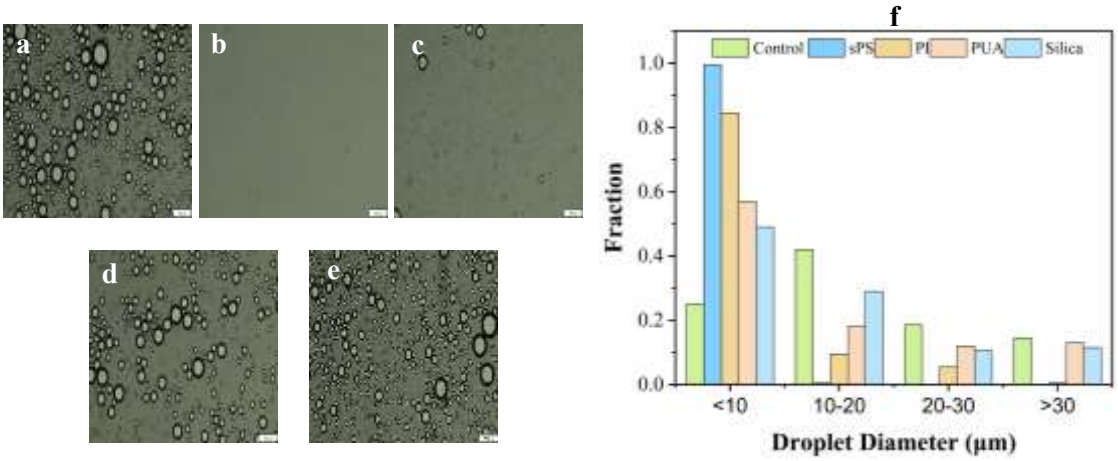


Figure 4.3 Optical microscopy images of oil-in-water emulsions a) Control emulsion and emulsions after they were bought in contact with b) sPS c) PI d) PUA e) silica gels and f) oil droplet size distribution for all emulsions analyzed using ImageJ software

sPS gels (Figure 4.3b) showed an extremely high oil droplet separation performance followed by the polyimide gels (Figure 4.3c). This is clearly evident from the reduction in the number of oil droplets from the emulsion for these two polymer gels. The oil droplet size distribution for both these cases shifted significantly towards the left indicating effective separation of oil droplets of size > 10 μm. The sPS gel performed superiorly compared to the polyimide gel and this can be attributed to its high interfacial energy and therefore, larger driving force for surfactant adsorption compared to a PI gel. In the case of the polyurea and silica gels there was very little to no change in the optical microscopy images and the corresponding oil droplet size distribution suggested little to no demulsification/destabilization of the emulsion. Therefore, the theory of competitive surfactant adsorption between the two available interfaces and it being governed by their corresponding interfacial energies seems valid and this data is the first evidence to prove that the emulsion separation is governed by surfactant adsorption abilities of the polymer gels.

The next question that arises from this discussion is where do the oil droplets go in the case of sPS and PI gels ? If it was a case of only surfactant adsorption, the oil droplets would have coalesced into larger droplets with depletion of surfactants from the system as shown by several researchers when chemical demulsifiers are used[158,262,273,276], but it is not the case. Large, coalesced oil droplets were not observed in the emulsion. This brings up the point of volumetric oil absorption by the polymer gels. Therefore, understanding whether it is the oil absorption by the polymer gel or the surfactant adsorption by the gel leading to emulsion separation becomes imperative.

All the polymer gels have a porosity > 90% and these open pores are filled completely with water. For the gel to absorb oil, the water within the pores needs to be displaced by the oil. A simple experiment was performed to illustrate whether the four gels show water displacement ability when brought in contact with an oil to confirm their oil absorption abilities. Figure 4.4a and 4.4b shows snapshots of a water filled sPS and PI gel when brought in contact with ULSD (oil) respectively. When a sPS gel was brought in contact with the ULSD, there was instantaneous displacement of water by the oil phase observed. The water within the gel trickled down as tiny droplets from the gel surface and oil was absorbed by the gel. This process continued until all the water present in the gel was replaced by the oil. A similar phenomenon happened in the case of the polyimide gel, however, the rate of water displacement by the oil was extremely slow. In addition, as can be observed in Figure 4.4a and 4.4b, the size of water droplets released from the sPS gel were small compared to those released from the PI gel. The water droplets tend to adhere to the PI gel surface for a longer time. This is because of the higher polar nature and high affinity for the water phase by the PI surface compared to the sPS surface as shown in Table 4.2. When the same experiment was performed with a PUA and silica gel, no absorption of oil phase by these gels took place which suggests, they prefer to remain wetted by the water phase. This experiment showed the volumetric oil absorption ability of the sPS and PI gels by displacement of the water present within the pores.

This observations brings up the question of whether emulsion separation is governed by surfactant adsorption or merely by oil absorption from the system.

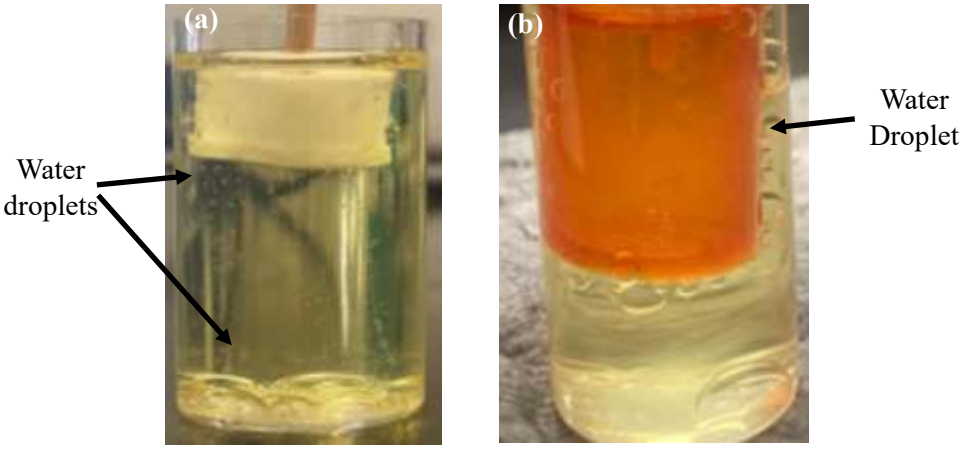


Figure 4.4 Displacement of water within the pores of the (a) sPS gel and (b) PI gel when brought in contact with ULSD (oil).

To understand this, another emulsion separation experiment was performed by bringing a sPS gel in contact with a Pluronic F127 surfactant stabilized oil-in-water emulsion. Gotad et al.

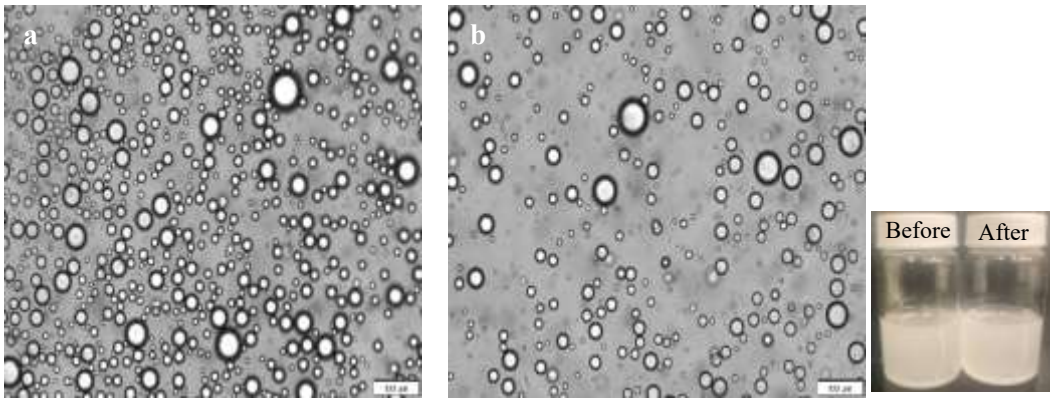


Figure 4.5. Optical microscopy images for Pluronic F127 stabilized oil-in-water emulsion a) Control emulsion b) in contact with sPS gel for 12 h along with before and after visual images of the emulsion

showed that the sPS gel did not absorb the Pluronic F127 surfactant as effectively as the Pluronic L35 surfactant. Therefore, the hypothesis for this experiment was that if the emulsion separation

by the sPS gel was governed by the surfactant adsorption ability of the gel, a poor emulsion separation would be seen. However, if it was the oil absorption ability of the gel governing the separation, a high oil removal performance similar to the Pluronic L35 surfactant case would be observed. The results for this experiment are shown in Figure 4.5. Figure 4.5 showed that there is considerable reduction in the number of oil droplets (Figure 4.5b) compared to the control emulsion (Figure 4.5a) suggesting a certain degree of emulsion separation. However, the sPS gel is not as efficient in removal of oil droplets from the F127 surfactant stabilized emulsion as it was with a Pluronic L35 stabilized emulsion. This difference in the emulsion separation performance can be attributed to the difference in the adsorption ability for the two surfactants by the sPS gel. The sPS gel showed a higher adsorption ability for the Pluronic L35 surfactant compared to the Pluronic F127 surfactant. Therefore, the ineffective emulsion separation in the case of the Pluronic F127 stabilized emulsion suggests the governing role of surfactant adsorption over direct oil absorption.

The role of surfactant size on adsorption performance by the sPS gel was mentioned in our previous work. The large size of the Pluronic F127 surfactant molecules was said to be a reason for its poor adsorption behavior by the meso-macro-porous sPS gel. In the discussion that follows, we delve deeper and understand other factors such as structural configuration of the adsorbed surfactant molecules, their interaction energy and occupied surface area, which might determine the adsorption behavior of the surfactant molecules onto the sPS surface. In the next section we describe atomistic simulation of the surfactant-sPS surface system, that were performed to answer these questions.

### 4.4.2 Short chain PEO-PPO-PEO surfactant vs long chain PEO-PPO-PEO surfactant adsorption on a syndiotactic polystyrene surface

Adsorption is a complex process which is determined by several factors such as the solvent type, adsorbent surface characteristics, type of interactions between the adsorbent-adsorbate or

adsorbate-adsorbate, the strength of those interactions, adsorbate size, etc.[248]. The simultaneous working of several factors for facilitating adsorption of a molecule on a solid surface makes it difficult to narrow down the primary reasons responsible for governing the adsorption process. The adsorption isotherms provide us with valuable information regarding the adsorbed species such as the adsorption energy, probable structural configuration of the adsorbed molecules, this information is however, theoretical. The approach of performing an atomistic simulation of the adsorbate-adsorbent system with relevant force fields shall be a more reliable approach to obtaining some of this information. Therefore, herein, we created atomistic simulation of the short chain and long chain PEO-PPO-PEO surfactants and studied their adsorption behavior on a sPS surface. The purpose was to understand the difference in adsorption of the two surfactants on the sPS surface, the structural configuration of the molecules at the surface, their interaction energy, the area occupied by the molecules on the solid surface and the possibility of aggregation of the surfactant molecules to form higher order structures on the sPS surface.

But prior to showing the adsorption characteristics of the molecules, the behavior of the molecules in bulk water is shown. Figure 4.6 shows the radius of gyration ($R_g$) distribution for the short chain (PL35) and long chain (PF127) surfactant in water where the corresponding $R_g$ of each PEO and PPO parts of the chain as well as whole single chain are depicted. The time evolution of the $R_g$ of L35 and F127 chain in water can be found in Figure 4.7. The total $R_g$ for L35 was found to oscillate between 1 to 2 nm with an average of 1.47 nm and that for F127 was found to oscillate between 2.5 to 6 nm and the average was 4.01 nm. In the case of L35, the mean $R_g$ values for the PEO and PPO blocks are 0.59 nm and 0.92 nm, respectively. Notably, PEO block displays a shorter range of oscillations compared to both the PPO block and the entire chain. When examining the longer PF127 chain, the mean $R_g$ values for the PEO and PPO blocks are 2.56 nm and 2.28 nm, respectively. This is accompanied by a strong oscillation of PEO blocks in contrast to PPO. The

Gaussian characteristics of the PEO and PPO blocks in the chain are evident in both L35 and F127. However, the less smooth curve observed in F127 indicates a greater need for sampling, requiring significantly longer simulations (> 500 ns). Conducting such atomistic simulations would be challenging due to their computational time requirements. Moreover, the findings depicted in Figure 4.7, which shows time evolution of $R_g$, demonstrate the spatial exploration of the chains as they undergo cycles of extension and contraction throughout the simulation.

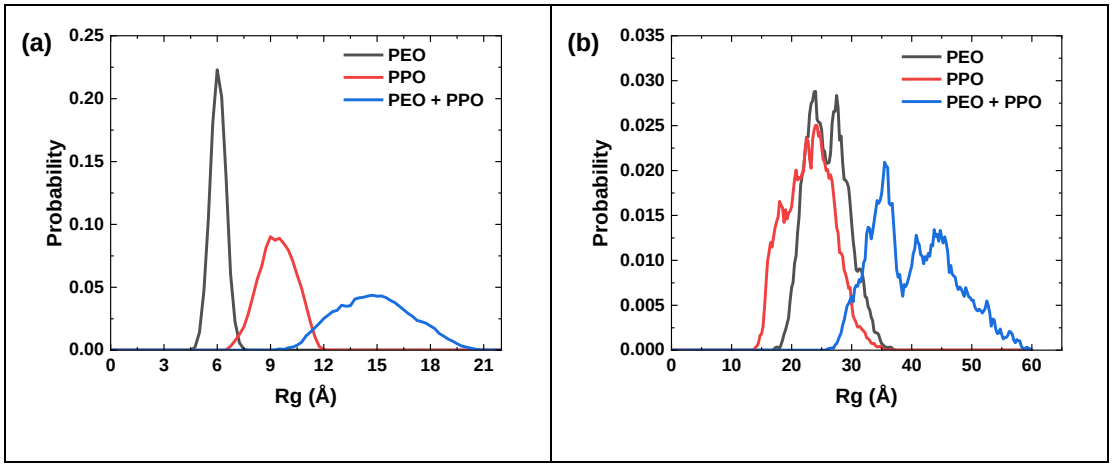


Figure 4.6 Radius of gyration distribution for (a) short chain PL35 surfactant and (b) long chain PF127 surfactant in water

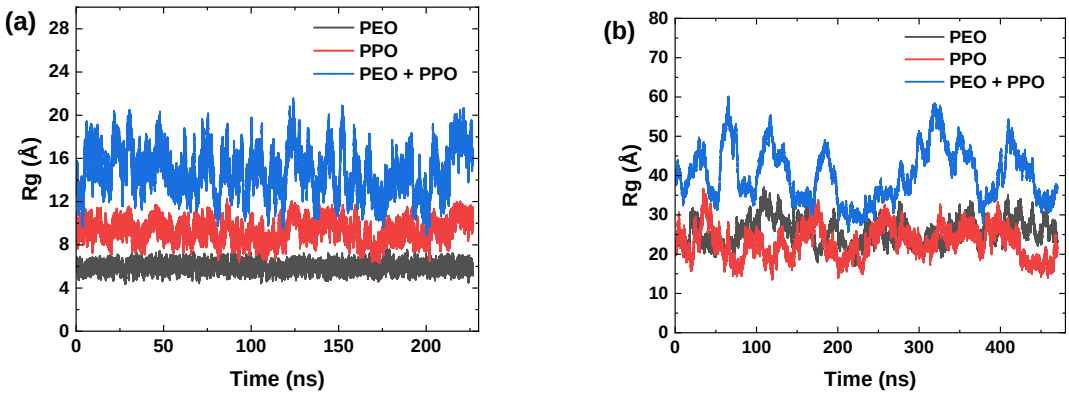


Figure 4.7 Radius of gyration versus time for (a) short chain PL35 surfactant and (b) long chain PF127 surfactant in water.

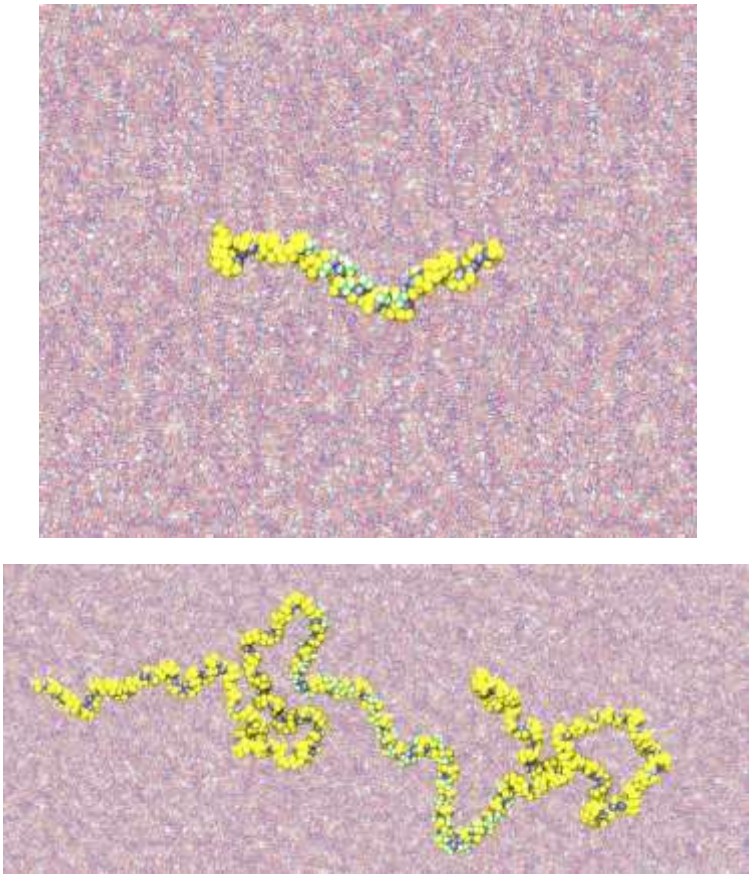

Figure 4.8 Snapshots of the (a) short chain PEO-PPO-PEO surfactant (Pluronic L35) and (b) long chain PEO-PPO-PEO surfactant (Pluronic F127) adsorption on a sPS surface (yellow circles: -$CH_2$ group, -green circle: -$CH_3$ group)

There are several studies which have reported the adsorption of a PEO-PPO-PEO block copolymer surfactant on solid surfaces. Most of the works reported a structural configuration where the PPO- segment adsorbs onto the solid surface and the PEO- chains remain extended in the solvent phase. The high hydrophobicity of the PPO- chain because of the pendant methyl group was said to be the reason for the differing solubility of the two blocks of the surfactant and the PPO- segment acting as a necessary anchor for the surfactant molecules to adsorb onto solid surfaces. The length of the PPO- and PEO segments, since it affects the solubility of the molecules in the solvent, along with the nature of the adsorbent, are reported to affect the structural organization of the adsorbed molecules[256]. Reports of a phase separated PPO-layer, or formation of loops, train conformations of the PPO segment[287] or a tightly coiled PPO- segment[256] on the solid surfaces have been found. Polystyrene and silica have been the frequently studied solid surfaces for adsorption of these molecules. In the case of polystyrene surface, hydrophobic interactions between the surfactant and surface led to their adsorption whereas in the case of the silica surface, hydrogen bonding was said to be the dominant binding mechanism[164,165,256].

Contrary to the reports that have been found in literature, the simulation we ran for the Pluronic L35 and Pluronic F127 surfactant showed adsorption of both the PEO- and PPO segments on the sPS surface (Figure 4.8). The PEO- segment in most studies was reported to extend into the solvent phase forming tail conformation with the PPO- segment acting as an anchor, which was not observed here. Figure 4.9a and 4.9b illustrate the atomistic distances of chain monomers in relation to the adjacent sPS surface atoms for L35 and F127, respectively. Because of the sPS surface roughness, calculating the instantaneous surface was essential, and measuring the atomistic distance required considering the local position of the surface atoms[288].

In the case of Pluronic L35, the PPO block of the molecule lies completely flat on the sPS surface, exhibiting strong adsorption of PPO to the surface. Meanwhile, the PEO blocks either

adsorb onto the surface or adopt a loop conformation, with tail conformation being less common. The conformation is different in the case of the Pluronic F127, where the PPO- block still lies strongly adsorbed onto the sPS surface while the PEO- block adsorbs on the surface partially and the non-adsorbed monomer unit forms coil and loops on the surface. In other words, the PEO- block is absorbed on the sPS surface only at a certain number of contact points. Additionally, the average number of monomers corresponding to loop conformation in L35 (< 10) are fewer than F127 (> 12). This could lead to more extended loop and coil conformation for F127 as they are farther away from the sPS surface where their interactions with the surface reduced.

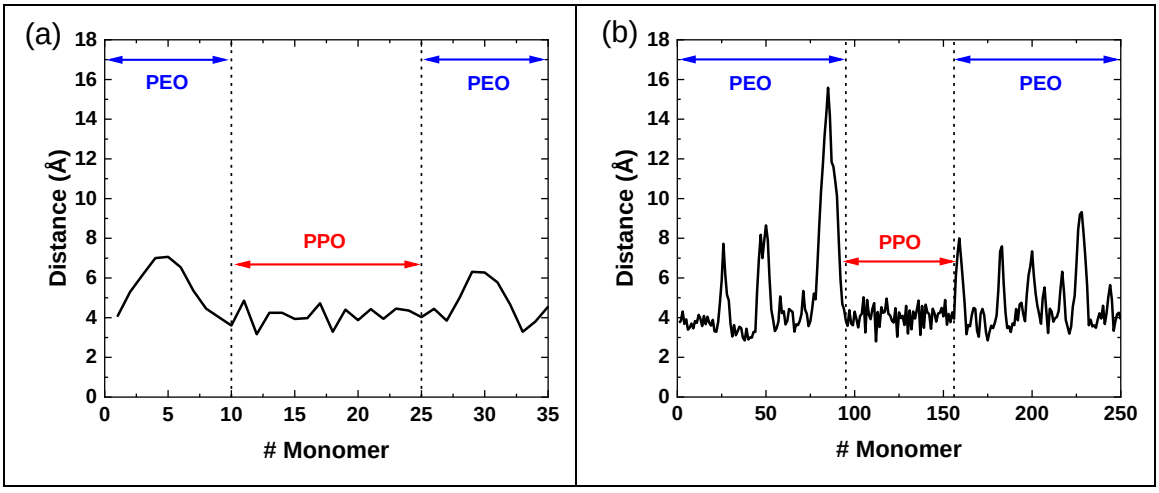


Figure 4.9. The distance of oxygen in each monomer from the polystyrene surface for (a) short chain of PL35 (b) long chain of PF127. The dot lines illustrate the monomer number where PPO block starts and ends

Another interesting observation from Figure 4.8a and 4.8b was that the oxygen groups of the PEO and PPO segments always oriented themselves towards the water phase thereby maximizing their interactions with the water molecules instead of the sPS surface. This allowed the $-CH_2$ group of the PEO-block to interact with the sPS surface and led to its adsorption on the surface. A radius of gyration analysis similar to Figure 4.6 was made for the case of the surfactants at the sPS-water interface and is shown in Figure 4.10. For short Pluronic chain of L35, single chain was

simulated as corresponding radius of gyration distribution is shown in Figure 4.10a. Due to slower relaxation time of F127 long chain, two different conformations were prepared to avoid excessive simulation needed to observe chain adsorption and equilibration. In the first case for F127, PEO blocks are placed initially in proximity to sPS surface while PPO blocks are further away from the surface. The second case was for the conformation where PPO is close to sPS surface and PEO tails are placed at further distance relative to the surface. In Figure 4.10b and 4.10c, the distribution of radius of gyration as well as their corresponding $R_g$ block are shown for case one and case two, respectively. The adsorption of the surfactant molecule at the sPS-water interface led to restricted movement of the molecule which is clearly observed by the multi peaks of the $R_g$ distribution of the molecule. For the short chain PL35 surfactant depicted in Figure 4.10a, the molecule seems to lie more in the stretched state with a $R_g$ of 1.51 nm whereas in the case of the long chain PF127 surfactant, the total $R_g$ could be conformation dependent as multiple adsorption conformation can exist in real. For case one where PEO is initially close to the sPS, $R_g$ value is about 5.61 nm which is higher than corresponding value in the bulk as shown in Figure 4.10b. The figure also exhibits that PPO block is more stretched than PEO counterparts. However, for the other case where PPO block is initially placed close to the surface, the average $R_g$ is almost comparable to that of in the bulk, which is about 3.82 nm, shown in Figure 4.10c. Unlike case 1, PPO block has less degree of extension where PEO block has higher average $R_g$ value. The time evolution radius of gyration for the two surfactants at the sPS-water interface is shown in Figure 4.11.

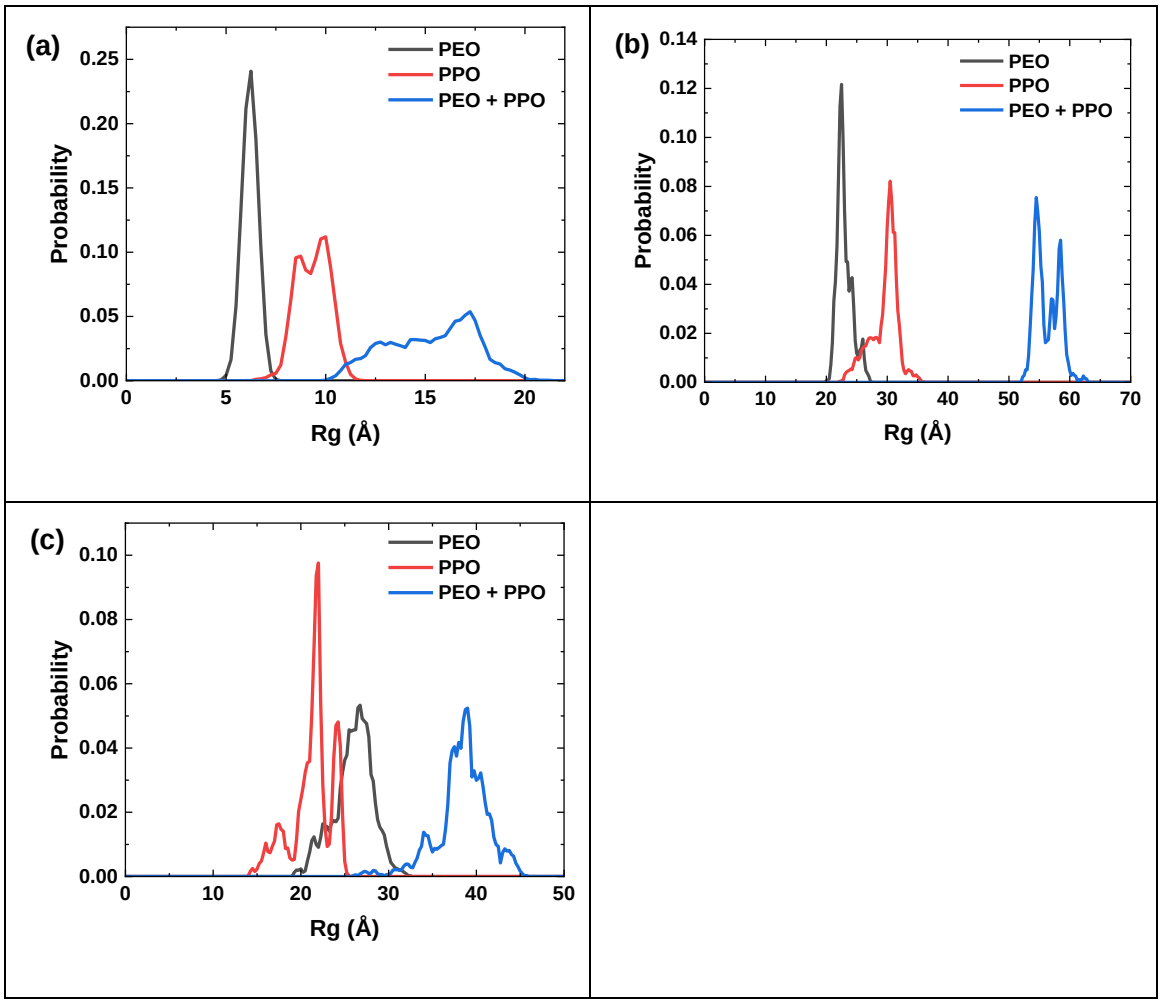


Figure 4.10 Radius of gyration distribution of (a) short single chain PL35 surfactant (b) long chain PF127 surfactant (PEO blocks placed close to sPS surface)(c) long chain PF127 surfactant at the sPS-water interface (PPO blocks placed close to sPS surface)

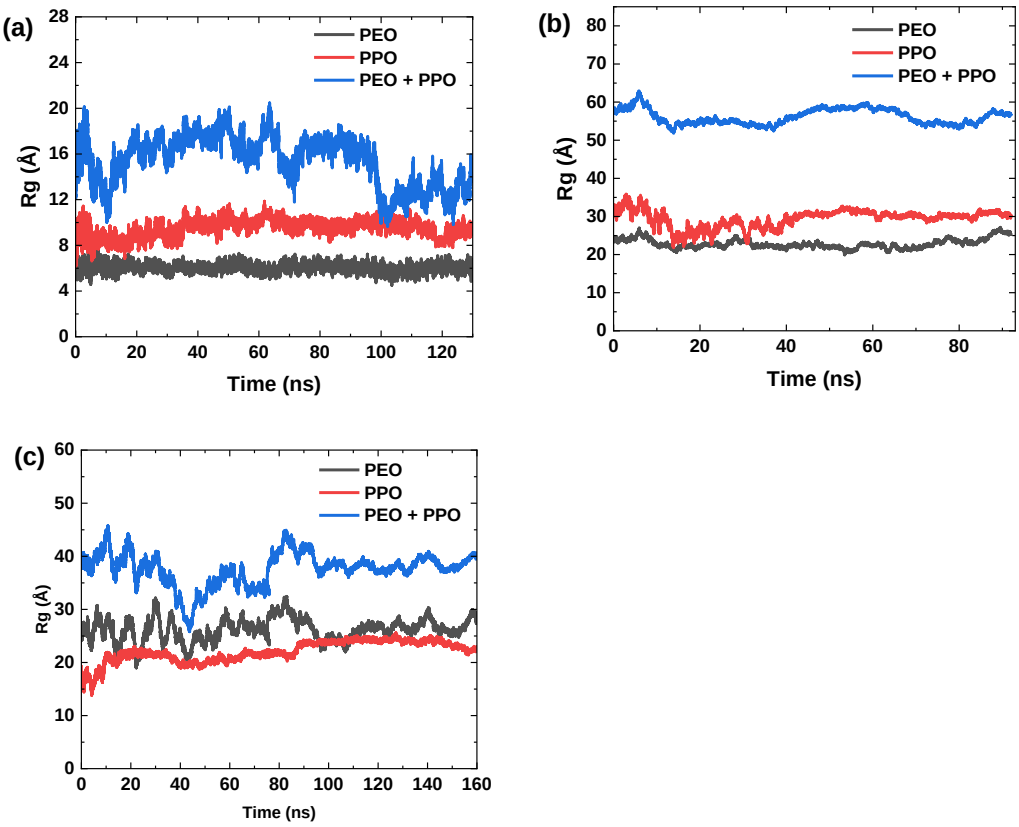


Figure 4.11 Time evolution of radius of gyration of (a) short single chain PL35 surfactant at the sPS-water interface (b) long chain PF127 surfactant at the sPS-water interface where PEO block initially placed close to the surface (c) long chain PF127 surfactant at the sPS-water interface where PPO block initially placed close to the surface

It is known that the oxygen groups on the PEO-PPO-PEO surfactants have the ability to form hydrogen bonds with water molecules. The geometrical criteria was employed for hydrogen bond analysis where further details can be found here[289]. These hydrogen bonding interactions have been quantified in Table 4.3 below for both the short and long chain surfactants in bulk water and after their adsorption at the sPS-water interface. For the case of the short chain PL35 surfactant, the hydrogen bonds per monomer for the PEO- did not change (~1.29) for the bulk water and sPS-water interface cases however, those for the PPO- group changed from 1.06 to 0.88 hydrogen bonds per monomer which suggests loss of certain degree of hydrogen bonds by the PPO-segment of the

surfactant after its adsorption on the sPS surface. For the case of the long chain PF127 surfactant, the hydrogen bond per monomer for the PEO- and PPO- groups both reduced from 1.31 (in water) to 1.21 (at sPS-water interface) and 1.06 (in water) to 0.80 (at sPS-water interface), respectively. It should be noted that both scenarios (either PEO/PPO initially placed in proximity of sPS) for long chain F127 leads to the same average values of hydrogen bonds which shows hydrogen bonds are local and almost independent of overall chain conformation.

Table 4.3 Hydrogen bond per monomer for the short and long chain PEO-PPO-PEO surfactants in bulk water and after adsorption at the sPS-water interface

| System | | Hydrogen Bond per monomer |
|---|---|---|
| PL 35 short chain in water | PEO- | 1.29 ± 0.12 |
| | PPO- | 1.06 ± 0.08 |
| PL 35 short chain at sPS-water interface | PEO- | 1.29 ± 0.14 |
| | PPO- | 0.88 ± 0.14 |
| PF 127 long chain in water | PEO- | 1.31 ± 0.04 |
| | PPO- | 1.06 ± 0.04 |
| PF 127 long chain at sPS-water interface | PEO- | 1.21 ± 0.04 |
| | PPO- | 0.80 ± 0.05 |

The interaction energy of the PEO- and PPO- segments of the two surfactants with the sPS surface and the water molecules surrounding the sPS surface were calculated and are given in Table 4.4. It can be observed that the PEO- and the PPO- segments of both the surfactants have a favorable interaction energy with the sPS surface suggested by their large negative values. The interaction energy per PEO- monomer was higher for the short chain surfactant (-2.69 ± 0.77 kcal/mol) compared to the long chain surfactant (-1.94 ± 0.11 kcal/mol) and this could be because of the formation of loops and coil structures by the PEO-block of the long chain surfactant. The number

for case two of PF127 shown in the parentheses follows the same trend while stronger interaction energy exists between PEO and sPS. The interaction energy of the PEO- segment per monomer with the water molecules for the short chain (-16.23 ± 1.65 kcal/mol) was found to be comparable than the long chain surfactant (-16.39 ± 0.39 kcal/mol). However, the energy fluctuations for the short chain are more than those of the long chain F127. This could result from the lower count of PEO monomers in PL35, making it more reliant on local chain conformations like loops and tails. The exact reason for formation of such coil, loop and tail structures by the PEO-chain is not exactly known but it could be to reduce its interaction area with the sPS surface. The PPO-segment of the large chain surfactant (-2.83 ± 0.15 kcal/mol) interacts with the sPS surface similar to the short chain surfactant (-2.82 ± 0.39 kcal/mol). For the case two of long chain, interaction energy is higher, but still looks comparable to the short chain value once error bars considered within the calculation. These results raise the question of, if both the short chain and long chain surfactant show a relatively similar adsorption on the sPS surface with negative interaction energies, why is there a disagreement in the simulation results and the experimental adsorption values or their emulsion separation performance?

Table 4.4 Interaction Energy of the PEO- and PPO- segments of the two surfactants with the sPS surface and water. The number in parentheses belongs to case two where in the initial conformation of the chain, PPO block placed in proximity to the surface.

| | Pluronic L35 (short chain) | Pluronic F127 (long chain) |
|---|---|---|
| Interaction energy per PEO-monomer with sPS surface (kcal/mol) | -2.69 ± 0.77 | -1.94 ± 0.11 (-2.00 ± 0.10) |

| | | |
|---|---|---|
| Interaction energy per PPO-monomer with sPS surface (kcal/mol) | -2.82 ± 0.39 | -2.83 ± 0.15 (-3.14 ± 0.14) |
| Interaction energy per PEO-monomer with water (kcal/mol) | -16.23 ± 1.65 | -16.39 ± 0.39 (-16.65 ± 0.40) |
| Interaction energy per PPO-monomer with water (kcal/mol) | -11.47 ± 2.03 | -10.70 ± 0.47 (-10.42 ± 0.40) |

There could be several reasons hypothesized for such observations. Let us look at each of these possible reasons in little detail. When we imagine an oil- in- water emulsion stabilized by a PEO-PPO-PEO surfactant, the PEO chains will be suspended in the water phase and the PPO- chain will be interacting with the oil phase. Therefore, when an oil droplet stabilized by a surfactant comes in contact with the sPS surface, it is the PEO- segment which is going to interact first with the sPS surface. Therefore, the adsorption effectiveness of the PEO- segment would determine the initial threshold to desorbing the surfactant from the oil-water interface. In the case of the short chain surfactant, the PEO- segment is short in length with only 10 repeating units and as shown in Figure 4.8a it adsorbs very well on the sPS surface. However, in the case of the Pluronic F127 surfactant, the PEO- chain is longer in length with 95 repeating units and does not adsorb as effectively onto the sPS surface. This is evident from the loop and coil structure formation which suggests they prefer to stay surrounded by water molecules. Therefore, ineffective adsorption of the PEO segment could be one reason for the difference in emulsion separation performance. Secondly, for the Pluronic L35 surfactant, the area occupied by the molecule on the sPS surface is 2123 $Å^2$ and similarly for the Pluronic F127 surfactant the area occupied on the sPS surface is 14,444 $Å^2$. Therefore, the higher adsorption surface area required by the Pluronic F127 results in limited adsorption of the surfactant from the emulsion and hence, a comparatively poor emulsion separation performance results from it. There is another theory explored in this work which was

the structural aggregation of the PEO-PPO-PEO molecules on the sPS surface. Aggregation of surfactants at solid-liquid interfaces has been reported by several researchers[164,165,290,291]. The formation of higher order structures such as bilayers, hemi-micelles, or micelles at the solid-liquid interfaces have been shown to drive the surfactant adsorption process. A total of 4 surfactant molecules of the Pluronic L35 surfactant were taken and added to the simulation run along with the sPS surface in the presence of water as the solvent. A snapshot of how these 4 surfactant chains assembled on the sPS surface is shown in Figure 4.12. Given the $R_g$ of the multi chain shown in Figure 4.13, the average values are comparable to the single chain. It was observed that the 4 Pluronic L35 chains did not adsorb onto the sPS surface at isolated points, rather they chose to adsorb close to each other, with the PEO-end chains of the surfactant being connected to each other end-to end. To the best of our knowledge, such an end-to-end connected structure formation by a PEO-PPO-PEO block copolymer chain has not been reported in literature. This type of aggregation suggests a monolayer formation of the block copolymer on the sPS surface. Formation of such a structure on the sPS surface might facilitate the adsorption of a Pluronic L35 surfactant from the liquid phase of the emulsion. A similar experiment could not be performed for the Pluronic F127 case, due to it being computationally very time consuming and expensive. But the formation of the coil and looping structures by the PEO-chains, its attempt to minimize its interaction area with the

sPS surface and limited contact points on the sPS surface suggest there might not be formation of such end-to-end structures in this case.

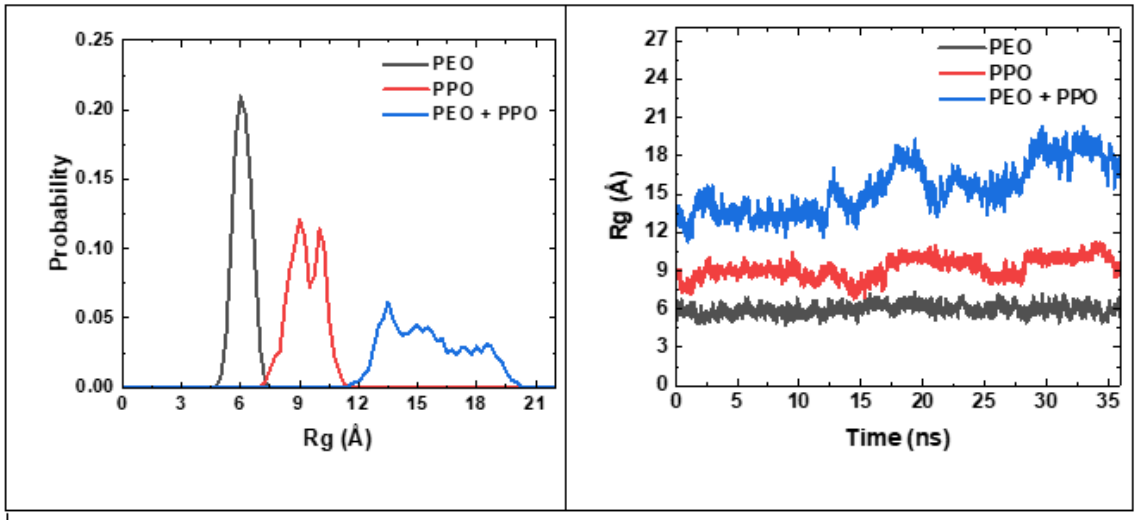


Figure 4.12 Time evolution of radius of gyration of short multi chains PL35 surfactant and at the sPS-water interface

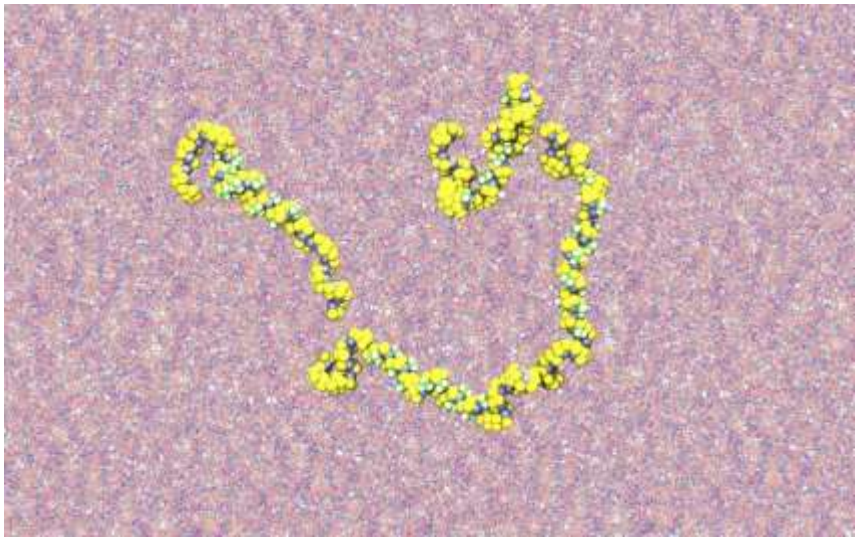

Figure 4.13. Snapshot of 4 Pluronic L35 surfactant chains adsorbed onto a sPS surface forming an end-to-end connected structure.

## 4.5 Conclusion

The data in this work suggests that the high surface area meso-macroporous polymer gels can be used for effective oil-water emulsion separation. The polymer gels destabilize the emulsion by

depleting the surfactant molecules from the liquid system. The emulsion separation ability of the polymer gel scales directly with their surfactant adsorption abilities and the surfactant adsorption ability of the polymer gel have a direct relation with the surface energy of the polymer gel. The syndiotactic polystyrene gel showed better emulsion separation performance compared to polyimide gels which was followed by polyurea and silica gel. The removal of the surfactant from the liquid phase was followed by absorption of the oil by the porous polymer gel due to its preferential wettability for the oil phase. The simulation results showed that both the short and long chain PEO-PPO-PEO surfactants adsorbed on the sPS surface, however, they did so in distinct ways. The short chain lay completely flat on the sPS surface with both the PEO- and PPO- chains effectively interacting with the sPS surface whereas for the long chain surfactant, formation of loop or coil-like structures by the PEO- chains was observed. The area occupied by the short chain on the sPS surface was significantly lower compared to the long chain surfactant. In addition, the adsorption of four different short chain molecules on the sPS surface showcased the ability of the surfactant to form higher order end-to-end connected structures which might be the reason for its effective adsorption by the sPS gel.

## 4.6 Acknowledgement

This work was partially supported by ACS Petroleum Research Fund under grant number PRF# 59000-ND7, U.S. National Science Foundation under grant number CMMI 1826030, NSF (DMR-2215940), and industrial members of Coalescence Filtration Nanofibers Consortium at The University of Akron

# CHAPTER V

# AEROGEL-GLASS FIBER COMPOSITE FILTER MEDIA FOR EFFECTIVE SEPARATION OF EMULSIFIED WATER DROPLETS FROM DIESEL FUEL

## 5.1 Abstract

This work evaluated several mechanisms of separation of surfactant-stabilized emulsified water droplets from diesel fuel using high surface area (50-370 $m^2/g$) and high porosity (>90%) filter media fabricated by combining aerogels and glass fiber mats. Specifically, high surface area, porous gels of syndiotactic polystyrene (sPS) and silica were developed inside glass fiber mats via dip coating in corresponding sol followed by sol-gel transition. The resultant materials were supercritically dried to obtain aerogel-coated separation media. The abundant meso- and macropores of the aerogel network and the different surface energy of sPS and silica produce cooperative functioning of the mechanisms of size exclusion, coalescence filtration, surfactant adsorption, and volumetric water absorption for removal of emulsified water droplets from ultralow sulfur diesel fuel under continuous flow conditions. The role of each separation mechanism was

elucidated. The results revealed high water separation efficiency of ~ 92% compared to ~30% for the glass fiber mats.

## 5.2 Introduction

The presence of small volume, micrometer size water droplets dispersed in diesel fuel is detrimental to fuel ignition performance. The water droplets also cause corrosion of fuel system parts and promote microbial growth thereby reducing the lifetime of fuel injection systems in addition to causing severe environmental concerns[90] due to release of noxious chemicals[91].Therefore, separation of water from diesel fuels is an important problem to tackle[292]. The low tolerance for sulfur in advanced emission control systems demands utilization of ultra-low sulfur diesel fuel (ULSD)[91,293]. The essential lubricants added to ULSD are known to stabilize oil-water interfaces and deter water droplet coalescence[93,294]. The inherently present asphaltenes and resins also provide interfacial stability in oil-water systems[295,296].

The coalescing filtration technique is widely used in separation of emulsified water from oil[129,297]. A thick fibrous media made of polymeric melt spun, gas-jet assisted spun or electrospun fibers such as polypropylene[127], polyesters[126], polyvinylidene fluoride[130], polyamide[297], polyvinyl acetate[129], polyacrylonitrile[297], and glass fibers[127,298] have been traditionally used for this purpose. It is noted that the fiber size, fiber surface area, and wettability of fibers play a significant role in governing the separation performance and the pressure drop across the filter media. Three fundamental steps govern coalescence filtration[299] - (1) interception of the water droplets by the fiber, (2) de-wetting of the oil film on the fiber surface and its subsequent wetting by water, and (3) the growth of water droplets on the fiber surface until it reaches a critical droplet size and the gravitational forces exceed the adhesion forces and the droplets detach from the filter surface. The fiber size and fiber surface area govern step 1, whereas the wettability of the media governs the second and third steps[128,297,299]. To this end, earlier researchers varied the fiber diameter and its

surface energy. They used small diameter fibers produced via electrospinning[297,300], gas jet assisted spinning[129,301], and centrifugal spinning[302], coated the fiber surfaces with different chemical agents[128], and used a combination of hydrophobic/hydrophilic fibers[126,127,129,303]. The hydrophobic/hydrophilic fibers and chemically coated fibers produced distinct levels of wettability by water.

It is well documented that smaller fibers produce higher droplet interception efficiency and higher separation performance[297,299]. In this context, fiber surfaces of intermediate wettability are preferred since they allow quick wetting by water and quick release of accumulated water droplets at a later stage. This avoids blocking of the pores by water and reduces the pressure drop in the media[128]. It is gleaned from prior work that a couple of centimeter thick filter media are often needed to achieve separation efficiency of 80-90 %, thereby increasing the overall pressure drop across the filter media. A performance parameter called the quality factor (Q.F.) or filtration index (FI) is used to report the combined effects of separation performance and pressure drop as in equation (1)[297,304]. Most coalescing filter media reported to date have a low quality factor in the range of 0.1-1.5[126,128,131] indicating high energy consumption to achieve a desired filtration performance. In view of the above, alternative material solutions must be identified to achieve higher values of quality factors.

$$\text{Q. F.} = \frac{-\,\text{Ln}\,(1-\text{E})}{\Delta\,\text{P}} \qquad (1)$$

Several materials systems such as membranes[305], fabrics[306], modified metal meshes[307], and 3D porous materials[308,309] were used in oil-water separation processes. However, all these studies were conducted with oil-water systems that were either non-emulsified[306,308,310,311] or unstable mixtures[308,312,313]. In some cases, batch experiments were conducted to remove oil from water or vice versa by dipping porous media in oil-water mixtures[306,310,311,314]. In latter studies, the effects of

hydrodynamic forces and continuous flow process on filtration performance were not captured. A detailed investigation of the fundamental science involving mechanisms namely size exclusion, surfactant adsorption, water absorption, and coalescing filtration is needed to qualify new separation media, such as aerogels.

The above questions and problems were assessed in this work considering the performance of aerogel media in water-diesel separation under *continuous flow conditions*. The developments of aerogels spanning over ninety years led to creation of several high-value materials in the fields of thermal insulation[16,315], energy storage[23] , air filtration[49,316,317], and small molecule adsorption[270]. The aerogel filter materials present several interesting attributes for oil-water separation. These include porous networks consisting of predominantly meso (2-50 nm) and macropores (> 50 nm), the extremely small polymer fibril diameter (20-30 nm) in most aerogels, high pore volume (> 90%), high specific surface area (200-1000 $m^2/g$), and low bulk density (typically < 0.1 $g/cm^3$). In conjunction, an assortment of polymers can be used to tune the surface energy and wettability characteristics[1,3,45,83,85,233,316,317].

In a recent work, Kulkarni et al.[50] fabricated an aerogel filter media for separation of water droplets from ULSD. These authors hosted aerogels of syndiotactic polystyrene (sPS) and polyimide (PI) in 3D-printed scaffolds of respectively high impact polystyrene (HIPS) and nylon and studied continuous separation of water droplets from ULSD with an efficiency of up to 97%. The roles of size exclusion of water droplets and nonionic surfactant adsorption were discussed. However, the unique contributions of water droplet coalescence, the balance of hydrophilic/hydrophobic surfaces, and water droplet absorption in the capillaries of the aerogel media were not reported.

In present work, a filter media developed by coating commonly used glass fiber mats with aerogels was considered for separation of micrometer size emulsified water droplets from ULSD

in a continuous flow system with special emphasis on water droplet coalescence, hydrophobic/hydrophilic balance of the media, and capillary absorption of water droplets in conjunction with further elaboration of the roles of surfactant adsorption and water droplet size exclusion as reported by Kulkarni et al.[50]. Specifically, the filter media was produced from hydrophobic sPS aerogel grown on a thin (~0.1 cm) glass fiber mat. The pores of sPS aerogel were optionally filled with hydrophilic silica aerogel to obtain an appropriate hydrophilic/hydrophobic balance. The presence of silica and sPS aerogel systems produced conditions of intermediate wettability. The central hypothesis of this work was built on the surface energy and high surface area of aerogel to deliver high separation performance due to cooperative functioning of several filtration mechanisms such as water droplet coalescence, size exclusion by the pores of the media, surfactant adsorption onto polymer surface and into pores[270], and capillary absorption of water into small pores of the media. The role of size exclusion and surfactant adsorption reported in Kulkarni et al.[50] was further elaborated in this work. These mechanisms were investigated in detail in this work in reference to a continuous flow system. In reference to the work of Kulkarni et al.[50], this is the first study on the cooperative functioning of several filtration mechanisms in single filter materials. The performance of aerogel-glass fiber media is analyzed in reference to existing studies on water separation from ULSD.

## 5.3 Experimental

### 5.3.1 Materials

Syndiotactic polystyrene (Mw ≈ 300,000 g/mol, 98%) was procured from Scientific Polymer Producers Inc. (Ontario, NY, USA). Toluene, tetraethyl orthosilicate (TEOS, reagent grade, 98%), nitric acid (purity, 64−66%), and ammonium hydroxide solution (28−30%) were purchased from Sigma Aldrich (Milwaukee, WI, USA). Ethanol was purchased from Decon Laboratories Inc. (King of Prussia, PA, U.S.A.). Microfiber glass fiber B (fiber diameter 5-6 μm)

mats were obtained from Hollingsworth & Vose (Groton, MA) and were used as received for filter media fabrication. Ultralow sulfur diesel (ULSD) fuel was procured from a local gas station and was treated with Fuller's Earth Filter (Jaxon Filtration, Franklin, GA, USA) to remove the existing impurities and surfactants, if any. Glycerol monooleate was used as the surfactant and was procured from Fischer Scientific (Waltham, MA, U.S.A.). All chemicals were used as received.

### 5.3.2 Fabrication of the sPS coated glass fiber media

A simple dip coating strategy was utilized to prepare sPS-coated glass fiber mats. Three solid polymer concentrations of sPS in toluene - 0.02, 0.04 and 0.06 g/mL - were prepared. sPS was taken in a hermetically sealed glass vial along with toluene and allowed to dissolve at a temperature of 100-110 °C with continuous stirring using a magnetic stir bar. After ensuring complete dissolution, the glass vial was allowed to cool for 1 minute and transferred to another glass container. The glass fiber mat was dipped in sPS solution for 10 s and subsequently annealed in toluene vapor for 1 minute. The sPS-coated fiber media was then dipped in ethanol for aging and exchange of the solvent. Six additional solvent exchange steps were completed with 100% ethanol before supercritical drying. The fiber mats filled with ethanol were placed in an autoclave and solvent-exchanged five times with liquid carbon dioxide. Subsequently, the temperature and pressure of the autoclave were raised to 50 °C and 11 MPa respectively to achieve supercritical conditions of $CO_2$, the gas was allowed to escape the autoclave, and the dried aerogel media was recovered.

### 5.3.3 Fabrication of hybrid silica-sPS aerogel coated glass fiber mat

The silica-sPS hybrid aerogel was prepared as per the process outlined in Wang and Jana[45]. The ethanol-filled sPS coated fiber media of approximate dry weight 0.7 g, prepared in Section 2.2 was dipped in a solution of TEOS (20.8 g), ethanol (40 mL), and water (5.4 g) overnight. This ensured diffusion of TEOS molecules into pores of sPS gel. Nitric acid was then added to partially

hydrolyze TEOS at a pH of ~2.0. The media was subsequently dipped in a solution of ammonium hydroxide (0.5 mL), water (7.2 g), and ethanol (30 mL) for 24 h. This step led to condensation of silane into a silica gel. The media was solvent exchanged with ethanol six times to remove residual water and loosely bound silica gel and finally, transferred to an autoclave for solvent exchange with liquid carbon dioxide followed by supercritical drying as presented in Section 2.2.

5.3.4 Characterization of filter media

*5.3.4.1 Porosity, skeletal density, and bulk density*: Helium pycnometer (AccuPyc II 1340, Micromeritics Instrument Corp., Norcross, GA) was used to obtain skeletal density ($\rho_s$). The bulk density ($\rho_b$) was obtained from the weight and volume of representative rectangular shaped media specimens. The bulk and skeletal density values were used to obtain total porosity ($\rho_T$) of the filter media as per equation (2).

$$\rho_T = (1 - \rho_b/\rho_s) \quad (2)$$

*5.3.4.2 Pore size and surface area characterization*: The final aerogel media contained three types of pores –the inherent mesopores (2-50 nm) and macropores (> 50 nm, typically 100 nm) of aerogels, and the micrometer size pores (called macrovoids) of the glass fiber mats. The macrovoids were characterized using a capillary porometer (Porous Materials Inc, Ithaca, NY, USA) with a wetting liquid of low surface tension (15.9 mN/m) and low vapor pressure, Galwick® (Porous Materials Inc., Ithaca, NY). The technique is based on the displacement of the wetting fluid from the pores of a sample by using air pressure exerted on one side of the specimen. The Brunauer-Emmett-Teller (BET) adsorption-desorption analysis was used to obtain the specific surface area and the mesopore volume ($V_{meso}$). Micromeritics Tristar II 3020 analyzer (Micromeritics Instrument Corp., Norcross, GA) was used to obtain $N_2$ adsorption-desorption isotherms at 77 K. The macropore (diameter > 50 nm) volume ($V_{macro}$) was obtained from the difference of the total pore volume ($V_{total}$) and mesopore volume ($V_{meso}$). The total pore volume $V_{total}$ was obtained from the

product of specimen volume ($V_0$) and porosity $P_T$. The nonlocal density functional theory (NLDFT) model was used to obtain the mesopore volume fraction. The fraction of meso- ($\phi_{meso}$) and macropores ($\phi_{macro}$) were calculated using equations (3-4).

$$\phi_{meso} = \frac{V_{meso}}{V_{total}} \quad (3)$$

$$\phi_{macro} = \frac{V_{macro}}{V_{total}} = 1 - \phi_{meso} \quad (4)$$

*5.3.4.3 Morphology and fiber diameter*: Scanning electron microscopy (SEM JSM 5310, JEOL, MA) was used to obtain high magnification images of the filter media. The diameter of sPS fibrils in the aerogel and of glass fibers in the mat were noted.

*5.3.4.4 Wettability of filter media*: As this work relates to separation of water droplets from ULSD, the wettability of the media by water was examined by placing a test water droplet on the media immersed in ULSD. The test water droplet rested on the media surface under gravity. Subsequently, the ability of the water droplet to wet the filter media and displace the diesel film present on fiber surface was captured using a high-speed video camera at a speed of 240 frames/s. The video images were analyzed using ImageJ software to obtain water contact angle and to understand the wetting behavior as function of water droplet size. The prospect of coalescing filtration was examined by placing a representative filter media specimen at an angle of 90° inside ULSD and studying the motion of a 10 μL water droplet placed on the vertical media surface using a syringe and needle set up. The ability of the water droplet to instantaneously wet the filter surface was noted. In addition, data were taken on the approximate size to which the water droplet would grow on the filter surface before falling off due to gravitational pull.

The polymer surface energy was obtained using Wu's theory using equation (5)[244]. The contact angle values of water and diiodomethane were measured on compressed sPS and silica aerogel disks.

$$\gamma_{LS} = \gamma_L + \gamma_S - \frac{4\gamma_L^d \gamma_S^d}{\gamma_L^d + \gamma_S^d} - \frac{4\gamma_L^p \gamma_S^p}{\gamma_L^p + \gamma_S^p} \quad (5)$$

In equation (5), $\gamma_{LS}$ is the interfacial tension between liquid and solid, $\gamma_L$ is the surface tension of the liquid, $\gamma_S$ is the surface energy of the solid, and $\gamma^d_S$ and $\gamma^p_S$ are the dispersion (nonpolar) and polar components of liquid surface tension, respectively. The standard values of $\gamma_L^d$ = 0.00218 mN/m and $\gamma_L^p$ = 0.00507 mN/m for water and $\gamma_L^d$ = 0.0041 mN/m and $\gamma_L^p$= 0.00067 mN/m for diiodomethane were used in the calculations. The surface energy of polymer ($g_s$) is obtained from the sum of dispersive ($\gamma^d_S$) and polar ($\gamma^p_S$) components as in equation (6) and polarity was obtained using equation (7).

$$\gamma_S = \gamma_s^d + \gamma_s^p \quad (6)$$

$$Polarity = \frac{\gamma_s^p}{\gamma_s^p + \gamma_s^d} \quad (7)$$

The polymer-liquid interfacial energy ($\gamma_{LS}$) was calculated using Young-Laplace equation as in equation (8), where $\gamma_L$ is surface tension of the liquid and Θ is the contact angle on polymer surface.

$$\gamma_S = \gamma_{LS} + \gamma_L cos\theta \quad (8)$$

*5.3.4.5 Filtration experiment*: Deionized water (0.2 % v/v) was dispersed in ULSD using glycerol monooleate as the surfactant. Glycerol monooleate was added to reduce the interfacial tension between water and ULSD to 10-12 mN/m. ULSD and water were mixed for 10 mins using an

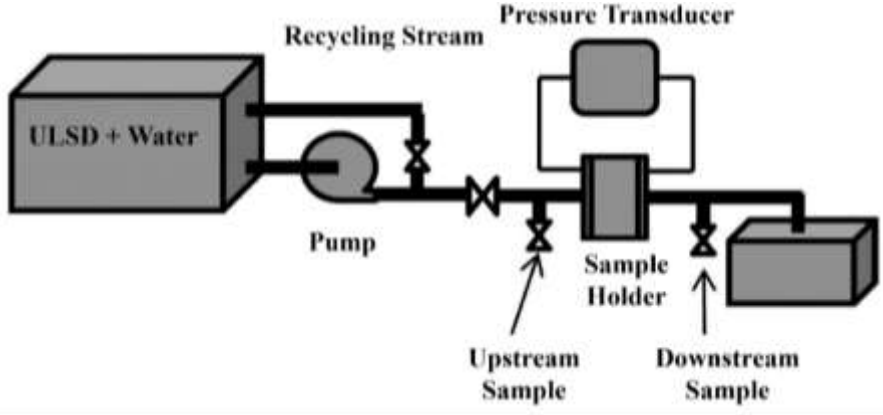


Figure 5.1 Schematic of the ULSD-water separation experiment.

impeller and then pumped into a recycle loop for 30 mins to generate a fine stable dispersion of water droplets of average diameter 20-30 μm. Figure 5.1 shows the schematic of the ULSD-water separation experiment used in this work.

The water droplet size distribution of the upstream and downstream emulsion samples were obtained using a particle counter, Accusizer 780, PALS-Particle Sizing Systems (Entegris, Bellerica, MA). The separation efficiency (% *E*) of the filter media was obtained using equation (9).

$$\% \, \mathrm{E} = \frac{C_{\mathrm{in}} - C_{\mathrm{out}}}{C_{\mathrm{in}}} \times 100 \tag{9}$$

In equation (9), $C_{\mathrm{in}}$ is the mass concentration of water upstream and $C_{\mathrm{out}}$ is the mass concentration of water downstream of the filter media. The mass concentration was calculated from droplet size distributions using equation (10).

$$\mathrm{C_k} = \frac{\sum \mathrm{N_i} \pi \mathrm{d_i^3} \rho}{6} \tag{10}$$

In equation (10), $C_k$ (k= in, out) is the mass of water per unit volume of ULSD, $N_i$ is the number of water droplets of diameter $d_i$ per unit volume and ρ is the density of water. The pressure drop across the filter media was obtained from electronic pressure gauges with pressure taps positioned upstream and downstream of the filter holder. The filter face velocity was set at 4 cm/min. All experiments were performed three times to ensure reproducibility. The quality factor of the filter media was calculated using equation (1).

*5.3.4.6 Water content measurement*: The water contest measurement test kit was procured from Sandy Brae Laboratories (Delaware, USA) and used to analyze the water content present in ULSD. This method uses reagent A (calcium hydride), reagent B, and the sample to be mixed in fixed proportions (as described in the operating manual) to obtain the total water content in diesel fuel. Briefly, 16 mL reagent B, 4 mL of the liquid ULSD test sample, and 3 micro-heaps of reagent A were added together in the reaction vessel and allowed to react for 15 mins with agitation after

every 1 min. Water and calcium hydride react to produce hydrogen gas which generates pressure in the reaction vessel. The value of pressure generated was used in a calibration curve to obtain % water content in diesel.

*5.3.4.7 Interfacial tension measurement*: The interfacial tension between water and ULSD was determined using the pendant drop method. A droplet of water was suspended in ULSD, and its shape was analyzed using a drop shape analyzer (DSA25S, Krüss GmbH, Germany). These experiments were repeated thrice for each data point.

## 5.4 Results and Discussion

### *5.4.1 Morphology, fiber diameter, porosity, pore size and surface area of sPS and silica aerogels*

As alluded to in Introduction, this study evaluated several mechanisms of separation of emulsified water droplets from ULSD. The glass fiber/aerogel media used in this work provided high specific surface area and coexisting meso- and macroporous architecture of the aerogel in conjunction with macrovoids of glass fiber mat and appropriate balance of surface energy derived from hydrophobic sPS and hydrophilic silica. The data for sPS and silica aerogels are first analyzed.

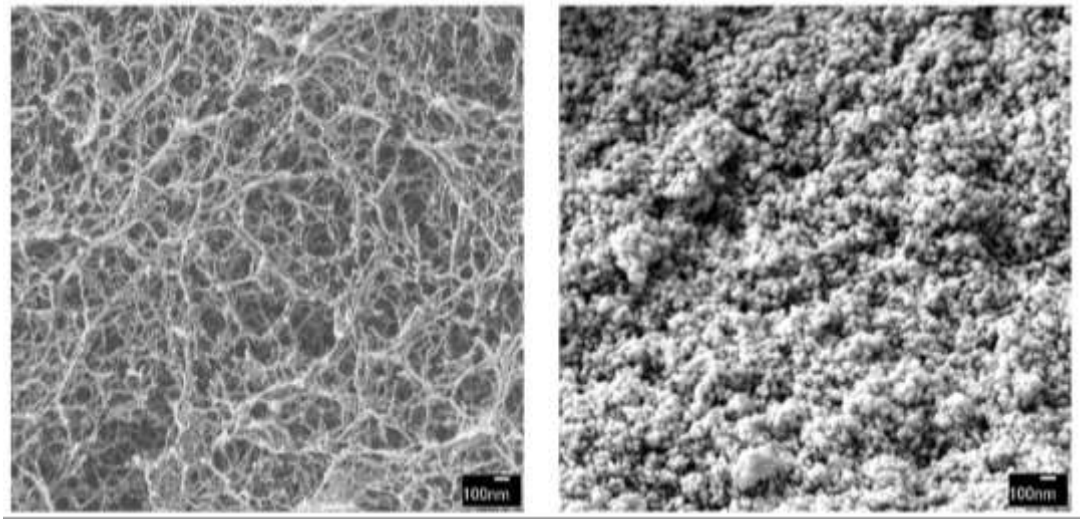


Figure 5.2 High magnification SEM image of (a) sPS aerogel (0.06 g/mL solid concentration) (b) silica aerogel

The regular tacticity of sPS allows crystallization of sPS chains into a helical δ-form intercalate[318] from liquid-liquid de-mixing via spinodal decomposition when cooled from solution in toluene under ambient conditions[278]. The scanning electron microscope image of sPS aerogel in Figure 5.1(a) shows polymer fibrils of 30-50 nm thickness forming open pores of 2-200 nm diameter. Prior work showed that the porosity decreases with an increase of polymer concentration[49,235]. The morphology of silica aerogel shown in Figure 5.1(b) is composed of a pearl-necklace structure formed by spherical silica particles. The sPS aerogel showed 92% porosity and bulk density of 0.08 g/cm$^3$ while silica aerogel had a porosity of 93% and bulk density of 0.13 g/cm$^3$. Such data are listed in Table 5.1. It is noted that sPS ($\rho_s$~1.05 g/cm$^3$) is much lighter than silica ($\rho_s$~1.8 g/cm$^3$).

Table 5.1. Bulk density, skeletal density, and porosity of the sPS and silica aerogel.

| **Aerogel** | **Bulk Density ($\rho_b$; g/cm$^3$)** | **Skeletal Density ($\rho_s$; g/cm$^3$)** | **Total Porosity ($\Pi_T$) (%)** |
|---|---|---|---|
| **sPS** | 0.08 ± 0.01 | 1.05 ± 0.04 | 92 |
| **Silica** | 0.13 ± 0.02 | 1.80 ± 0.01 | 93 |

The specific surface area and meso- and macropore volume fractions of sPS and silica aerogels are listed in **Table 5.2**. The mesopore fraction was much higher in silica aerogel ($f_{meso}$~33%) than in sPS aerogel ($f_{meso}$~5%). The sPS and silica aerogels had respectively 95% and 67% pore volume in macropore category. The pearl-necklace structure of silica aerogel with secondary particles of ~ 5 nm diameter produced much higher BET surface area, ~787 m$^2$/g compared to ~260 m$^2$/g for sPS aerogel. In the latter case, the polymer fibrils had 30-50 nm thickness, as seen in **Figure 5.1(a)**. These are in good agreement with values reported in literature[45,230,235,270].

**Table 5.2.** BET surface area, meso- and macropore volume fraction of the sPS and silica aerogel.

| Aerogel | BET Surface Area ($m^2/g$) | Mesopore volume fraction ($\phi_{meso}$) | Macropore volume fraction ($\phi_{macro}$) |
|---|---|---|---|
| **sPS (0.06 g/mL)** | 260 ± 20 | 0.05 | 0.95 |
| **Silica** | 787 ± 30 | 0.33 | 0.67 |

*5.4.2 Morphology, porosity, pore size distribution and surface area of filter media*

The filter media used in this work was prepared by coating the glass fiber mat with sPS solution of concentration 0.02, 0.04, and 0.06 g/mL. The solid concentration allowed tuning of porosity of sPS aerogel coatings and the coverage of the macrovoids in the glass fiber mat. Figures 5.2a and 5.2b show low magnification SEM images of the uncoated and sPS aerogel-coated glass fiber media, respectively. It is apparent from Figure 5.3a that the glass fiber media had ~ 5 mm diameter glass fibers forming macrovoids of 10-100 mm diameter. The low magnification image in Figure 5.3b indicates that a large fraction of macrovoids of the glass fiber mat was covered by sPS gel. As will be seen later, such coverage affected the overall porosity of the media and the mean size of surviving macrovoids, both perceived important for water droplet separation.

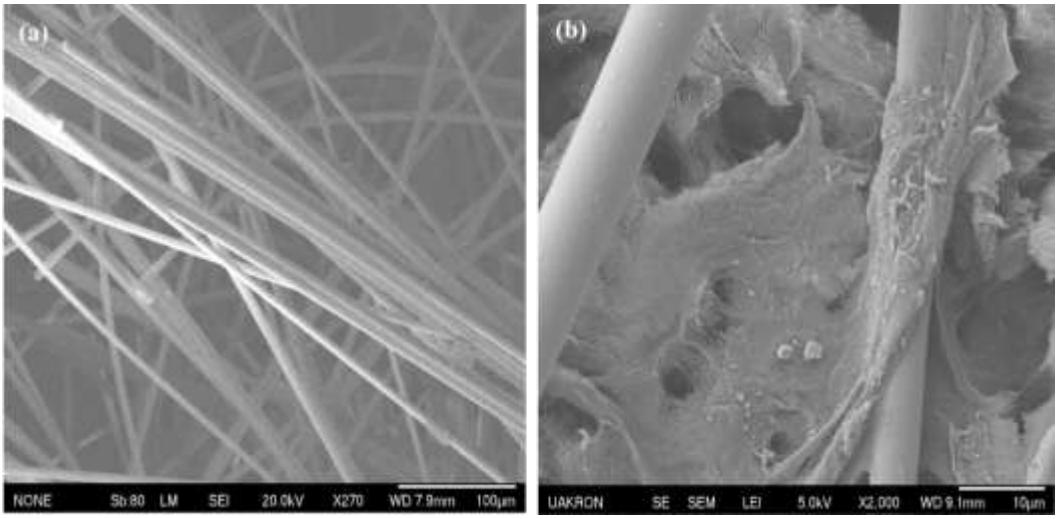

Figure 5.3 SEM image of (a) uncoated glass fiber and (b) glass fiber coated with sPS aerogel produced with 0.02 g/mL sPS solution.

The optical and SEM images of aerogel-coated media obtained with sPS solutions of 0.02, 0.04, and 0.06 g/mL concentration are presented in Figure 5.4. The amounts of aerogel coating on glass fiber mat were calculated from the difference of weights of the supercritically dried aerogel and the corresponding uncoated glass fiber media. Such data are presented in Table 5.3. Intuitively, the density of aerogel coatings seen in Figure 5.3 and the amount of aerogel coating per gram of glass fiber mat increased with an increase of sPS concentration in the precursor solution. The amount of coated sPS was 0.88 g/g, 0.63 g/g, and 0.22 g/g respectively at concentrations of 0.06, 0.04, and 0.02 g/mL of sPS. Accordingly, the specific surface area of sPS aerogel-coated media also increased, from 49 $m^2/g$ at sPS concentration of 0.02 g/mL to 162 $m^2/g$ at sPS concentration of 0.06 g/mL. The data in Table 5.3 show that glass fiber mat used in this work had a bulk density of 0.095 $g/cm^3$ and porosity of 96%. However, despite significant coverage of the macrovoids originally present in glass fiber mats by the aerogel coatings, the porosity reduced only by a small fraction, e.g., to 89% for media coated with 0.06 g/mL sPS solution and to 92% for media coated

with 0.06 g/mL sPS solution compared to 96% for glass fiber mat. This is attributed to the high inherent porosity of 92% for sPS aerogel

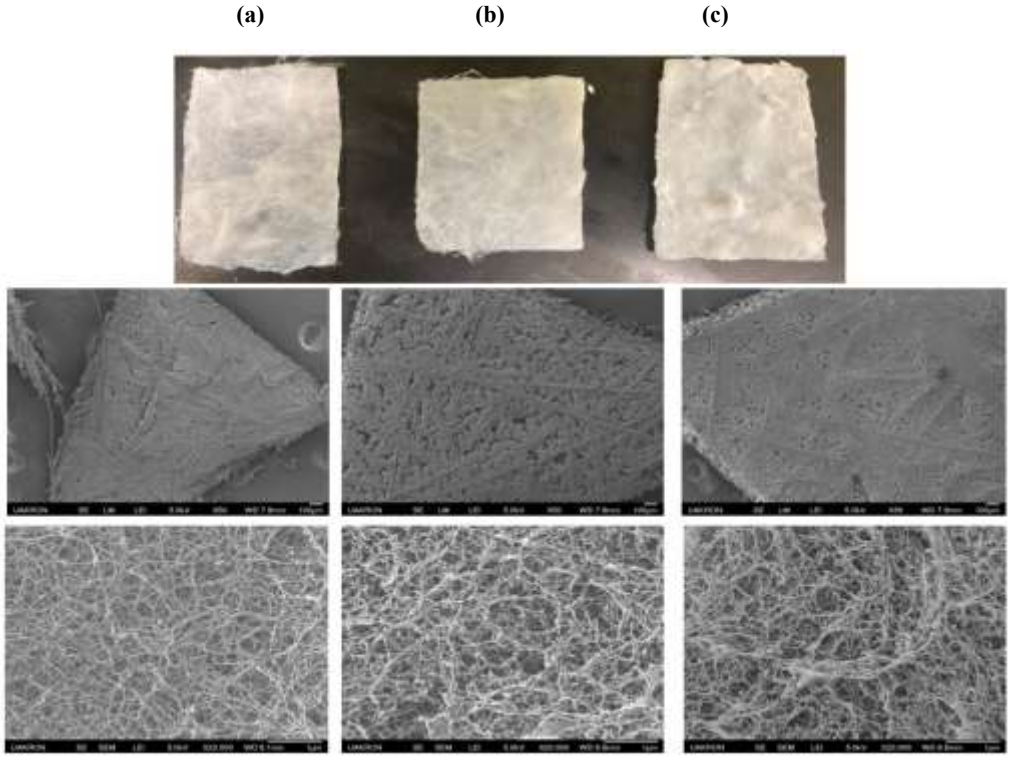


Figure 5.4 Glass fiber media coated with sPS aerogel obtained from sPS solution at concentration (a) 0.02 g/mL, (b) 0.04 g/mL, and (c) 0.06 g/mL. Top row: Optical image of coated filter media. Middle row: Low magnification SEM image. Bottom row: High magnification SEM image

Table 5.3 Properties of the uncoated and sPS aerogel-coated glass fiber media

| Material | Weight ratio of sPS Aerogel: GF | Bulk Density ($\rho_b$; g/cm$^3$) | Skeletal Density ($\rho_s$; g/cm$^3$) | Porosity ($P_T$; %) | BET surface area (m$^2$/g) |
|---|---|---|---|---|---|
| Glass Fiber (GF) | 0 | 0.095 | 2.48 | 96 | Negligible |

| | | | | | |
|---|---|---|---|---|---|
| sPS-GF (0.02) | 0.22 | 0.127 | 1.69 | 92 | 49 ± 5 |
| sPS-GF (0.04) | 0.63 | 0.170 | 1.69 | 90 | 107 ± 10 |
| sPS-GF (0.06) | 0.88 | 0.192 | 1.69 | 89 | 162 ± 20 |

The images in the middle row of Figure 5.3 highlight several regions of the glass fiber media that were not coated by the aerogel. These uncoated regions define the surviving and incompletely filled macrovoids initially present in the glass fiber mats. These macrovoids in aerogel-coated media were anticipated to handle the primary liquid flow through the media. The size distribution of macrovoids was inferred from capillary porometer data and is summarized in Table 5.4. It is seen that the glass fiber mat had a mean pore size of 312 ± 2 mm, largest pore size of 380 ± 52 mm, and smallest pore size of 42 ± 2 mm. The glass fiber mat coated with sPS aerogel from 0.02 g/mL precursor sPS solution showed significant coverage of its macrovoids. In this case, the mean, largest, and smallest pore sizes all reduced respectively to 8 ± 0.4 mm, 31 ± 2 mm, and 4 ± 0.4 mm. The mean pore size reduced further to 1 ± 0.3 mm and 0.3 mm respectively when sPS solution concentration was raised to 0.04 and 0.06 g/mL.

Table 5.4. Macro-void pore sizes for the uncoated and coated glass fiber media

| Material | Largest detected pore diameter (μm) | Smallest detected pore diameter (μm) | Mean pore diameter (μm) |
|---|---|---|---|
| GF | 380 ± 52 | 42 ± 2 | 312 ± 2 |
| sPS-GF (0.02) | 31 ± 2 | 4 ± 0.4 | 8 ± 0.4 |
| sPS-GF (0.04) | 9 ± 2 | 0.3 ± 0.2 | 1 ± 0.3 |
| sPS-GF (0.06) | 3.3 | 0.2 | 0.3 |

The reduction of mean macrovoid size seen in Table 5.4 in aerogel-coated specimens indicates the growing importance of size exclusion of water droplets. As will be seen later, the

emulsified water droplets with size 10-100 μm were much bigger than the macrovoids found in aerogel-coated media. The reduction of macrovoid size with aerogel coating, however, is anticipated to increase the pressure drop through the media, thus affecting the quality factor. In this context, the incorporation of silica aerogel was expected to produce additional reduction of macrovoid size. In view of this, silica aerogel was grown in sPS aerogel coated media produced from only 0.02 g/mL sPS concentration. A select set of properties of the silica aerogel containing media are listed in Table 5.5.

Table 5.5. Physical properties and pore sizes of silica containing sPS aerogel-coated glass fiber media.

| | |
|---|---|
| Bulk density ($\rho_b$; g/cm$^3$) | 0.175 ± 0.02 |
| Skeletal density ($\rho_s$; g/cm$^3$) | 1.67 ± 0.1 |
| Porosity ($P_T$; %) | 89 |
| BET surface area (m$^2$/g) | 370 ± 30 |
| Largest detected pore diameter (μm) | 9.4 ± 0.7 |
| Smallest detected pore diameter (μm) | 0.15 ± 0.5 |
| Mean pore diameter (μm) | 0.30 ± 0.1 |

The mean size of macrovoids in silica incorporated filter media reduced to 0.30 ± 0.1 mm compared to 8 ± 0.4 mm for sPS aerogel-coated media. The largest macrovoid size also reduced from 31 ± 2 mm to 9.4 ± 0.7 μm. The type IV BET adsorption-desorption isotherms for sPS and silica-sPS coated glass fiber media presented in Figure 5.4 indicate significant mesopores in the filter media. The corresponding BET surface area of the filter media increased from 49 ± 5 m$^2$/g for sPS aerogel coated media to 370 m$^2$/g for the media with silica aerogel. This more than 7-fold increase in surface

area is expected to be beneficial in water droplet interception, expedited water wetting, and stronger surfactant adsorption.

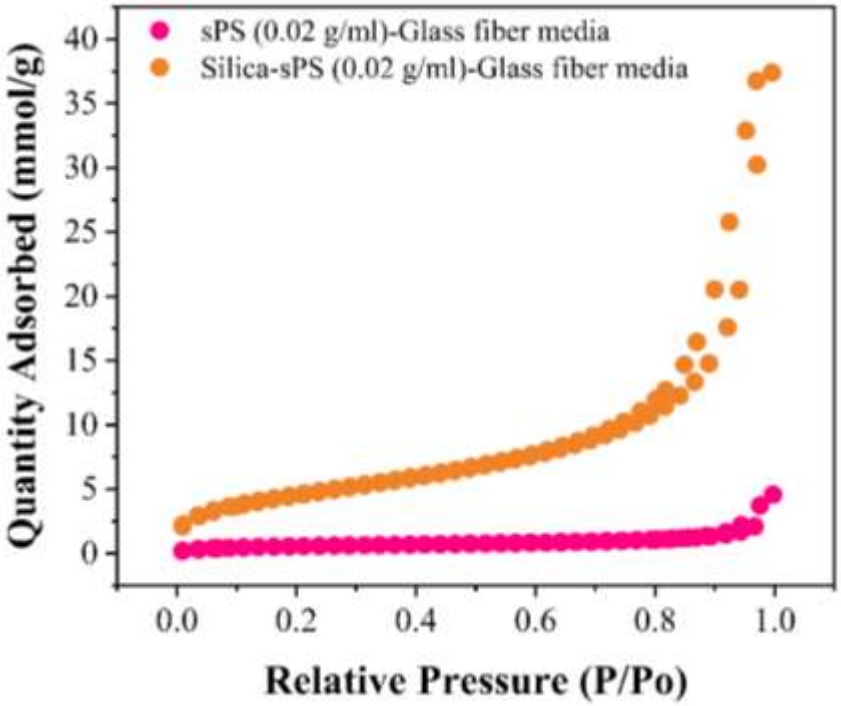


Figure 5.5 BET adsorption-desorption isotherms of sPS aerogel coated media and the media containing silica produced with sPS concentration of 0.02 g/mL

5.4.3 Wettability of filter media

The wettability of filter media is an important parameter to determine the mechanism and efficiency of water separation from ULSD. As alluded to earlier, the water droplets approaching the filter media surface under flow should be able to effectively displace the diesel film and wet the media surface in a process called the diesel film drainage[299]. A water droplet that can wet and attach to the media surface is able to promote coalescence with other colliding droplets. To study this feature, a demonstration experiment on diesel film drainage was conducted using a non-porous glass slide with similar wettability as the glass fibers in the mat considered in this work. A high-speed camera at 240 f.p.s. shooting rate was used to capture the movement of water droplets. Figure 5.5 shows the snapshots of the water droplet as it approached the glass slide immersed in ULSD

(Figure 5.5a) and stationed on the surface due to gravity (Figure 5.5b). The progress of drainage of the diesel film is shown in Figure 5.5 c-d eventually leading to wetting by water.

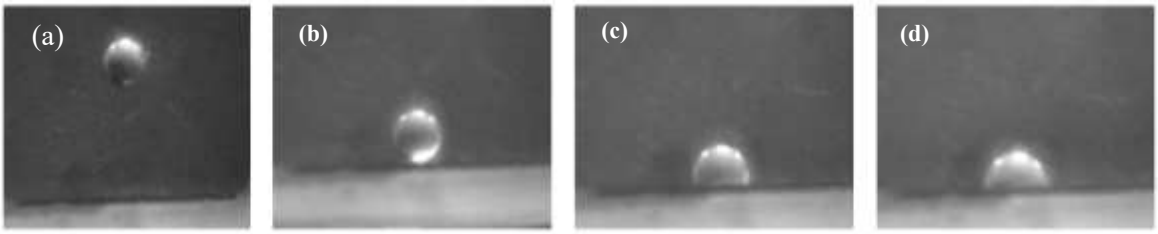


Figure 5.6 Snapshots of a water droplet as it approaches a glass slide immersed in ULSD in film drainage process, (a) approaching, (b) touching, (c-d) spreading.

Similar experiments were performed on three filter media developed in this work – the glass fiber mat, sPS-coated glass fiber mat, and silica aerogel containing sPS-coated glass fiber mat. A water droplet of diameter ~1500 μm was dropped onto each media immersed in ULSD and the wetting behavior was evaluated. Figure 5.6 shows the snapshots of the water droplet in each case. It is seen that the water droplet held its spherical shape in Figure 5.6a and 5.6b, while it led to ULSD film drainage in Figure 5.6c. The contact angle of water droplets was measured to be (137 ± 3)°, (144 ± 5)°, and (45 ± 6)° for the glass fiber mat, sPS-coated GF, and the silica containing sPS-coated GF fiber media, respectively.

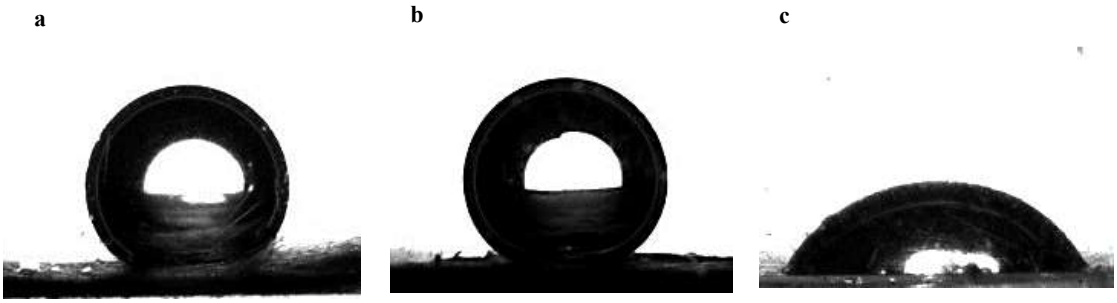


Figure 5.7 Water droplet wetting of (a) glass fiber mat, (b) sPS-coated glass fiber mat, and (c) silica containing sPS-coated glass fiber mat immersed in ULSD. The images were taken 10 s after the droplet touched the media.

The almost instant wetting of silica containing sPS-coated glass fiber media (Figure 5.6c) can be interpreted using surface energy values of sPS and silica, listed in Table 5.6. The highly polar silica showed a polarity of 0.55 due to abundant silanol (-SiOH) groups, while highly nonpolar sPS had a low polarity of 0.05. The total surface energy of silica, 69 mN/m, is close to the surface tension of water, 72 mN/m, indicating spontaneous wetting of silica by water. The sPS surface with low polarity (~0.05) is easily wetted by ULSD.

Table 5.6 Surface energy of sPS and silica surface.

| Polymer | Water contact angle (°) | Diiodomethane contact angle (°) | Polar component (mN/m) | Dispersive component (mN/m) | Polymer surface energy (mN/m) | Polarity |
|---|---|---|---|---|---|---|
| sPS | 96 ± 1 | 41 ± 2 | 2.3 | 38.5 | 40.8 | 0.05 |
| Silica | 25 ± 2 | 27 ± 2 | 38 | 31 | 69 | 0.55 |

Recall from Figure 5.6 that water contact angle on glass fiber mat immersed in ULSD was large, 137 ± 3°, even though glass fiber mat is considered an efficient coalescing media for water separation from ULSD[319]. Also recall from experimental section that large water droplets of approximately 1500 μm diameter were used to obtain the images in Figure 5.6. Such large size water droplets were used to ascertain interactions with glass fiber surface in view of 96% porosity and a large gap between adjoining fibers in the glass fiber mat.

However, Lawson et al. reported strong dependence of diesel film drainage on droplet size[299,320]. For example, more efficient drainage of diesel film was observed for smaller water droplets. To evaluate this relationship, experiments were conducted on wettability of the filter media considered in this work as a function of water droplet diameter, varied in the range, 500-1500 μm. The ratio of spreading distance (SD) of water droplet on the filter media and the initial

droplet diameter (D) were used to characterize wetting and film drainage behavior. The spreading distance is the horizontal distance that the droplet spreads on the surface. A higher value of SD/D indicates better fiber surface wetting and greater film drainage. The dependence of SD/D ratio on D is shown in Figure 5.7. Several trends can be inferred from Figure 5.7. First, sPS aerogel-coated fiber mat had poor water wettability due to low polarity of sPS and, therefore, poor ULSD film drainage apparent from SD/D ratio of ~ 0.4 with weak dependence on water droplet diameter in the range, 500-1500 mm. Second, the glass fiber mat showed higher SD/D ratio 0.6-0.8 for 500 mm≤D≤1100 mm and 0.4 for 1400 mm and 1500 mm diameter droplets. This behavior can be approximated as a linear dependence of SD/D vs. D with a negative slope indicating a higher probability of interactions between small size water droplets and glass fiber surface. The water contact angle of the glass fiber media reduced from ~137° for a 1500 μm size droplet to ~110° for a 500 μm droplet. Therefore, it is possible that water droplets smaller less than 100 μm may show better wetting performance than larger water droplets, e.g., 1500 mm in diameter. For silica containing sPS aerogel-coated glass fiber media, excellent wettability was observed with SD/D ratio varying between 1.1 and 1.6. This can be attributed to high surface area, hydrophilic silica particles that promote droplet wetting and attachment to a filter surface.

A surface coalescing filter is customarily used in a vertical filtration setup, e.g., the filter media is placed vertical, normal to the flow direction. This allows the large, coalesced water droplets hanging from the filter surface to detach and trickle down under gravity. This arrangement

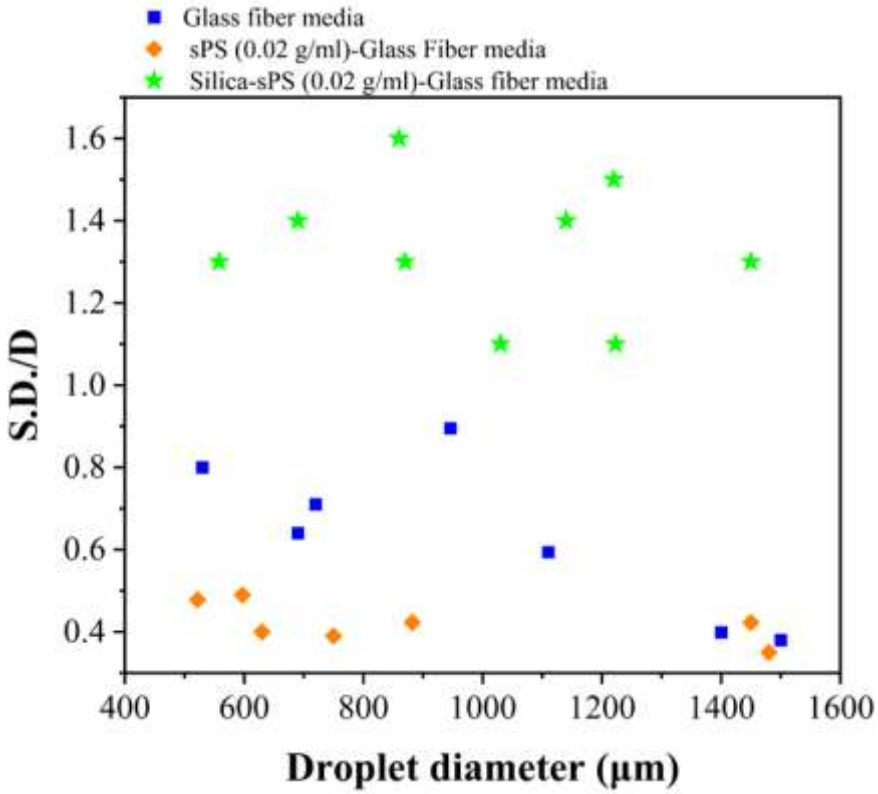


Figure 5.8 Spreading distance (SD) and droplet diameter (D) ratio as function of D. Silica containing sPS-coated glass fiber media was produced with 0.02 g/mL concentration of sPS

avoids formation of a continuous water film on the filter surface that in turn increases the pressure drop across the filter media. The weight of a water droplet adhering to the filter media is supported by the adhesion force. In view of this, the magnitude of adhesion force of water droplet to the media was evaluated by placing increasingly bigger size water droplets on the filter media surfaces until the gravitational force exceeds the adhesion force and the droplet detaches from the filter surface.

It was found that a 10 µL water droplet placed on vertical filter media of glass fiber mat or sPS coated glass fiber mats did not adhere and trickled down instantaneously. However, the water

droplet instantaneously adhered onto silica containing sPS-coated GF fiber media. This is a result of the combined action of high polarity of silica causing extremely short diesel drainage time and capillary absorption of a part of the water droplet by the mesopores of silica aerogel. In this case, additional water droplets were added to the attached one for the combined size to grow until the droplet reached a critical size, detached from the media surface, and dropped to the bottom under gravity. Figure 5.8 shows five images showing how initially smaller (10 µL) water droplets grow and finally detach from the silica-sPS GF media kept immersed in ULSD. The initial water droplet placed on the media surface (Figure 5.8a) grew with the placement of additional water droplets (Figure 5.8 b-d). Eventually gravity wins over adhesion force and the drop falls off (Figure 5.8e). The total volume of water placed on the surface until it fell off was ~ 75 µL, corresponding to ~5.2 mm diameter spherical droplet. Therefore, it is presumed that the emulsified water droplets in ULSD would grow to roughly 5 mm diameter droplets on silica containing sPS-coated media before

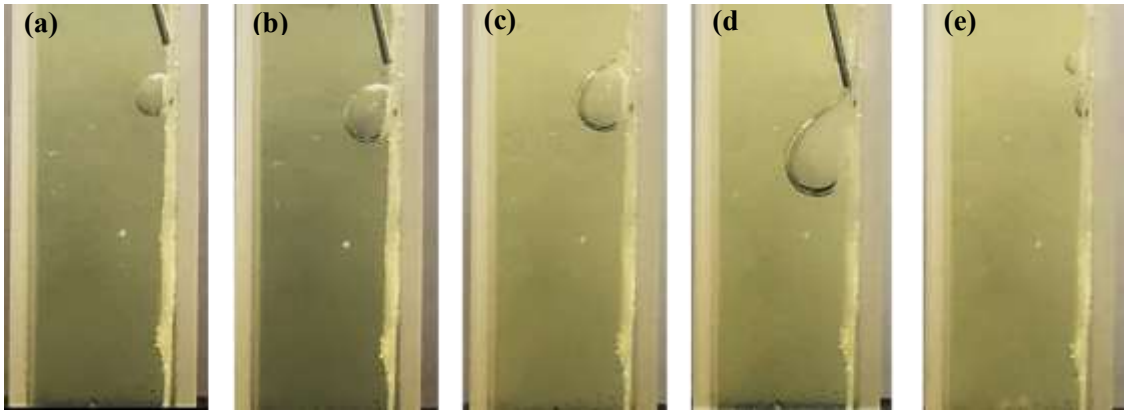

Figure 5.9. A water droplet placed on a silica-sPS (0.02 g/mL)-glass fiber media at 90° immersed under ULSD, (a) 10 µL water droplet placed on media, (b-d) additional water droplets added to the attached droplet until the large droplet (~75 µL) detached from the media surface (e).

falling off. As pointed out earlier, one cannot foresee coalescence of water droplets to such a large diameter on low surface area (such as glass fiber mat) and low polarity filters (such as sPS-coated

glass fibers). In this context, the high surface area, mesoporous silica aerogel particles introduced in sPS-coated glass fibers promoted coalescence filtration.

*5.4.4 Surfactant adsorption and water absorption by the media*

A significant surfactant adsorption capability of meso-and macroporous sPS and polyimide gels was reported in an earlier work[270]. It was anticipated that sPS gel used in this work would show similarly strong surfactant adsorption behavior and facilitate coalescing filtration. The interfacial energy between sPS and ULSD and between silica and ULSD systems were calculated from respective contact angle values of ULSD on compressed sPS and silica aerogel surfaces following Young Laplace equation. These values are listed in Table 5.7. The silica surface had high interfacial energy (~ 45.6 mN/m) with ULSD indicating significant surfactant adsorption on silica aerogel from diesel fuel. sPS aerogel on the other hand would not adsorb much surfactant from ULSD.

Table 5.7 sPS/silica-ULSD contact angle and interfacial energy.

| Polymer | Contact angle (°) | Interfacial energy (mN/m) |
|---|---|---|
| sPS | 12 ± 1 | 15.3 |
| Silica | 26 ± 3 | 45.6 |

The surfactant adsorption experiments were conducted by immersing ULSD filled silica and sPS polymer gels in ULSD with 0.1 wt.% glycerol monooleate dissolved in it. At this concentration, glycerol monooleate surfactant reduced the value of interfacial tension (I.F.T.) between ULSD and water system from 21±1 mN/m to 10.5±0.2 mN/m. The ULSD filled silica and sPS gels with solid weight of approximately 100 mg were dipped in 10 mL ULSD solution for 24 h and the interfacial tension between water and ULSD was measured. After exposure to silica gel, the interfacial tension increased from 10.5 mN/m to 20.5±1 mN/m, taking it close to the value for

ULSD-water system without the surfactant. Thus, silica gel was able to remove almost all the surfactant present in ULSD. In the case of sPS gel, the interfacial tension increased only slightly from 10.5 mN/m to 11.8±0.3 mN/m. Thus, sPS gel was not able to adsorb much of glycerol monooleate in line with the low surface energy values discussed above.

A separate set of experiments was conducted to understand the kinetics of glycerol monooleate adsorption by silica gel by dipping a specimen in 0.1 wt.% glycerol monooleate solution in ULSD over time ranging from 5 min to 24 h and measuring interfacial tension between water and ULSD.

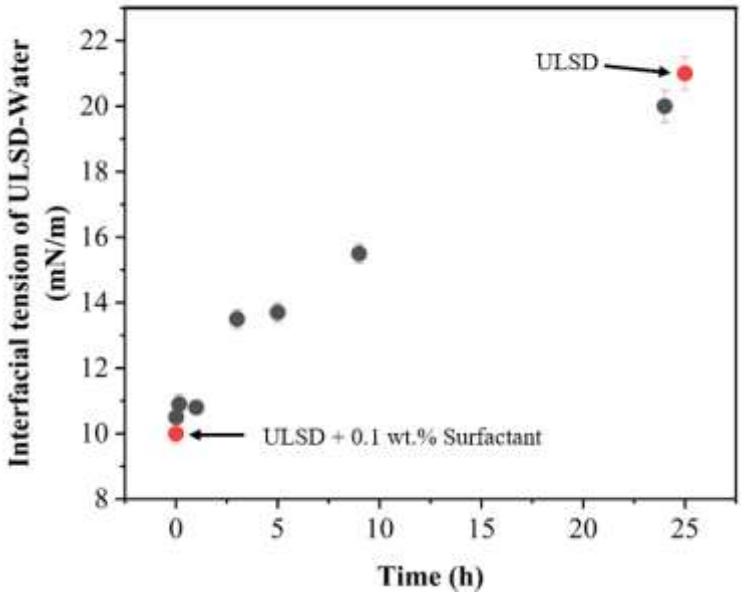


Figure 5.10 Glycerol monooleate adsorption from ULSD by ULSD filled silica gel as a function of time.

These results are presented in Figure 5.9. The data suggests that surfactant adsorption by silica gel is a transient process. It is possible that some surfactant molecules adsorbed instantaneously onto gel surface, but this aspect could not be ascertained using interfacial tension measurement technique. A more accurate characterization technique such as quartz crystal microbalance (QCM) is required.

In the next set of experiments, water-in-ULSD emulsion stabilized by glycerol monooleate surfactant was brought in contact with silica and sPS gels for a period of 3 h alongside a control emulsion that had no gel. The water droplet count in the liquid emulsion before and after exposure to the gel were obtained using an Accusizer droplet counter. The solid mass of the gel was 100 mg, and the emulsion volume was 10 mL. The water droplet count in the case of silica gel markedly reduced with about 93% separation efficiency, as per equations (SI: 9) and (SI: 10). The percentage separation efficiency was merely 15% in the case of sPS gel. The corresponding water droplet size distributions are shown in Figure 5.10a. In the case of silica gel, the droplet size distribution shifted significantly to smaller most probable size (~5 mm) compared to ~12 mm for sPS coated glass fiber media. The time-dependence of separation efficiency in the

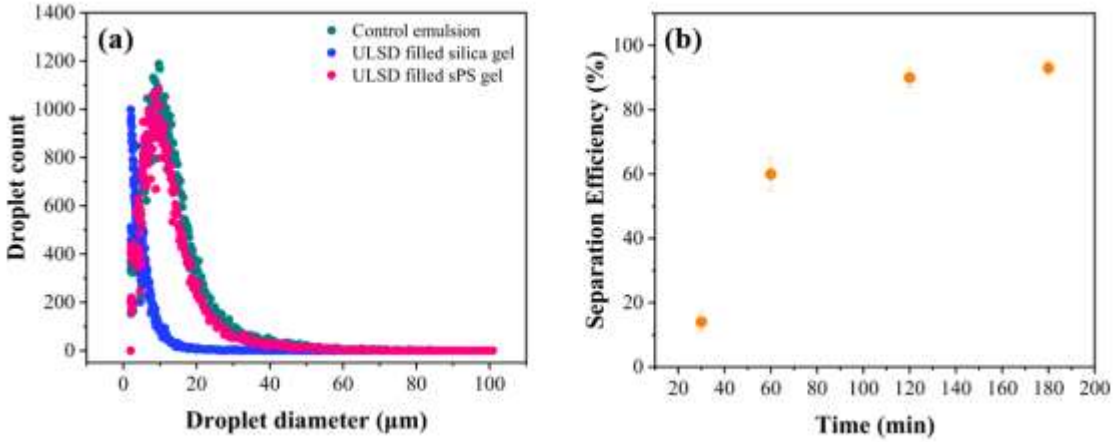


Figure 5.11 (a) Water droplet diameter distribution in ULSD and (b) separation efficiency in the presence of ULSD filled silica gel as a function of time.

case of silica gel specimen was obtained by dipping silica gel specimen in water/ULSD emulsions for 30, 60, 120, and 180 min. It was found that the % separation efficiency followed a trend like that of surfactant adsorption (Figure 5.10b). The separation efficiency increased from approximately 14% at 30 min to 60, 90, and 93 % at 60,120, and 180 min of contact time, respectively.

The discussion above presents clear evidence that silica gel functions in improving the separation efficiency via surfactant adsorption. However, the data in Figure 5.9 and Figure 5.10b indicate that both the extent of surfactant adsorption and the separation efficiency are time dependent. In this context, it is not clear if such results would translate well to a continuous flow separation system. Another question is the fate of water droplets that come in contact with the media. A part of such water droplets undergoes coalescence and settles down at the bottom of the container. Another part of water droplets may be removed from the emulsion via volumetric absorption within the pores of the gel. This aspect was examined by keeping the uncoated glass fiber media, sPS coated glass fiber media, and silica-sPS coated glass fiber media in the emulsion for a period of 5 h and the water content of the emulsion was measured at regular intervals using the method described in the experimental section.

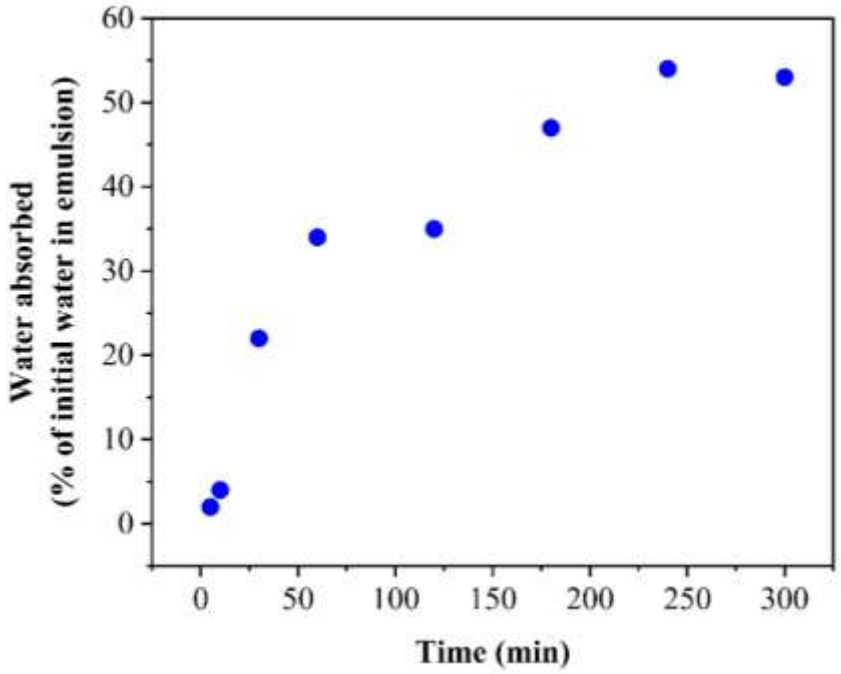


Figure 5.12 Water droplet absorption from a water-in-ULSD emulsion using silica-sPS (0.02 g/mL)-glass fiber media as a function of time.

The sPS coated glass fiber media did not absorb any water from the emulsion due to hydrophobic nature of sPS. The silica-sPS- glass fiber media, however, did absorb a significant amount of water from the emulsion as function of time (see Figure 5.11). It is seen that the silica-sPS GF media removed 50-60 % of initial water droplets from the emulsion in 5 h.

*5.4.5 Evaluation of filtration performance in a continuous flow system*

The filtration performance of the three-filter media was evaluated using a continuous filtration setup. All filtration experiments were performed with a liquid face velocity of 40 mm/min and 5 layers of filter media. The filtration experiments were run for an hour. The separation efficiency, pressure drop, and quality factor values were calculated and listed in Table 5.8.

Table 5.8 % Separation efficiency, Pressure Drop and Quality factor of the filter media

| Media | Separation efficiency (%) | Pressure drop (kPa) | Quality factor (1/kPa) |
|---|---|---|---|
| Glass fiber (GF) | 30 ± 9 | 0.2 | 1.78 |
| sPS-GF (0.02) | 68 ± 8 | 0.6 | 1.8 |
| Silica-sPS (0.02)- GF | 92 ± 3 | 1.1 | 2.4 |

As expected, the silica-sPS-glass fiber media provided the highest water droplet separation efficiency of 92% followed by 68% for sPS-glass fiber media and 30% for the glass fiber media. The reduced pore size of the filter media due to incorporation of silica and sPS coatings resulted in an increase in the pressure drop across the filter. However, its quality factor (2.4) is higher than the glass-fiber media (1.78). It is noted that the quality factor is an essential parameter signifying filter media quality. The water droplet size distributions for the upstream and downstream emulsion

passing through the filter media are shown in Figure 5.12a along with the images of the emulsion before and after passing through the silica-sPS-glass fiber filter (Figure 5.12c).

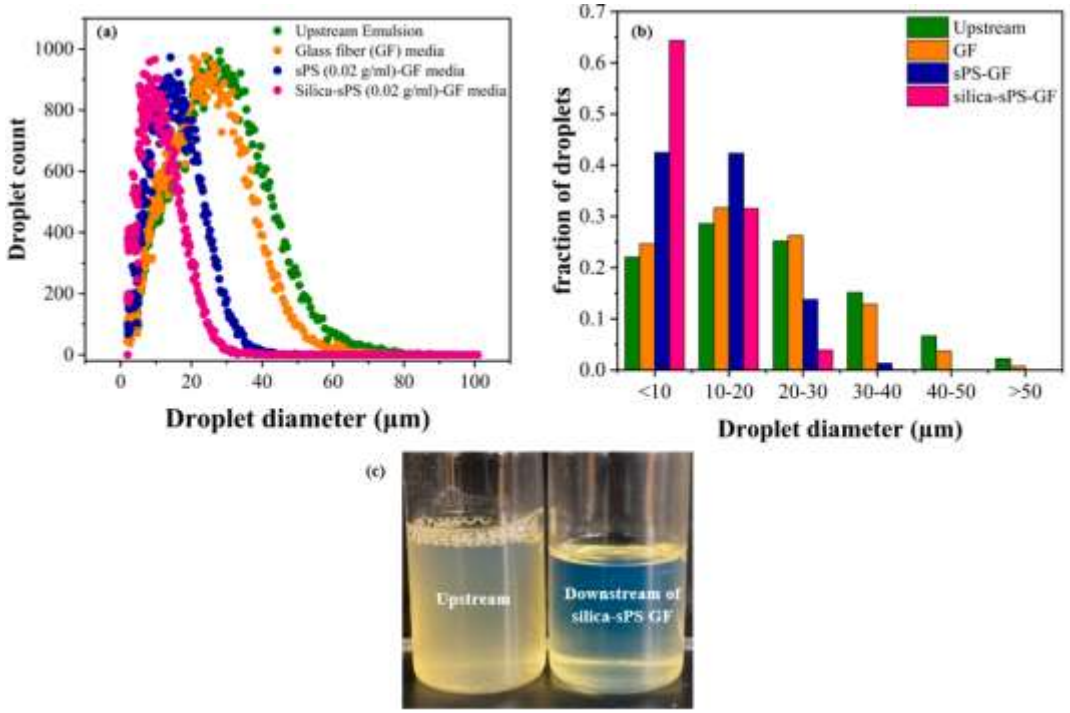


Figure 5.13 (a) Water droplet size distribution obtained using Accusizer for the upstream emulsion and after the emulsion was passed through the three filter medias, (b) fraction of droplets upstream and downstream (after the emulsion was passed through the three filter medias) (c) Upstream emulsion and downstream emulsion after passing through the silica-sPS GF media.

It is observed in Figure 5.12a that the water droplet size for the upstream emulsion (shown in green) had a most probable size of ~ 30 µm. The water droplet distribution did not significantly change when the emulsion was passed through the control, glass fiber media (shown in orange). In the case of sPS aerogel coated filter media, the downstream water droplet distribution shifted significantly towards the smaller size with the most probable droplets of ~18 µm diameter. This indicates that most droplets were rejected by size exclusion at the filter surface. The downstream droplet size distribution shifted to an even smaller size (most probable diameter ~10 µm) when silica containing sPS coated glass fiber media was used. The water droplet volume calculated from

water droplet diameter and number frequency of water droplets using equation (10) also reduced. In addition, Figure 5.12b shows the fraction of water droplets passing through the three filters as a function of droplet diameter. The upstream emulsion contains approximately ~ 20 % droplets of size < 10 μm, ~ 20 % > 30 μm and ~ 60 % in between 10-30 μm. When the emulsion is passed through an uncoated glass fiber media, there is no significant change in the water droplet distribution, showing the ineffectiveness of the glass fiber media to intercept and subsequently reject the water droplets. This is because the pore sizes offered by a fiber mat are significantly larger than the water droplet sizes. However, when the emulsion is passed through the sPS coated glass fiber media, the fraction of droplets > 30 μm significantly drastically reduces (~ 2%), which underscores the size exclusion mechanism discussed earlier where, droplets larger than the pore size of the filter are rejected by the filter. This size exclusion effect is more pronounced when the silica-sPS coated glass fiber media is used, as no water droplets of size > 30 μm are allowed to pass through the filter. Furthermore, there is a significant reduction in fraction of droplets of sizes between 10-30 μm to ~ 35 % from 60 % in upstream emulsion. This higher water droplet rejection ability of the silica-sPS glass fiber media is a combined result of a smaller filter pore size and improved water wettability ensuring effective water droplet interception and capture.

Summarizing the data discussed up to this point, a schematic as in Figure 5.13 can be used to illustrate the mechanism of filtration taking place at the silica-sPS- glass fiber filter surface, leading to separation of emulsified water droplets from diesel fuel. The water droplets covered by a layer of surfactant molecules flow towards the filter surface (Figure 5.13a). A majority of water droplets are rejected at the filter surface due to smaller size pores. It is noted that emulsified water droplets are much bigger (10-100 μm) than the pores of the filter media. It is conceivable that some small water droplets of diameter ~1-10 μm might still pass through the macrovoids of the filter media (Figure 5.13b). The rejected water droplets stick to the filter surface (Figure 5.13b) due to the

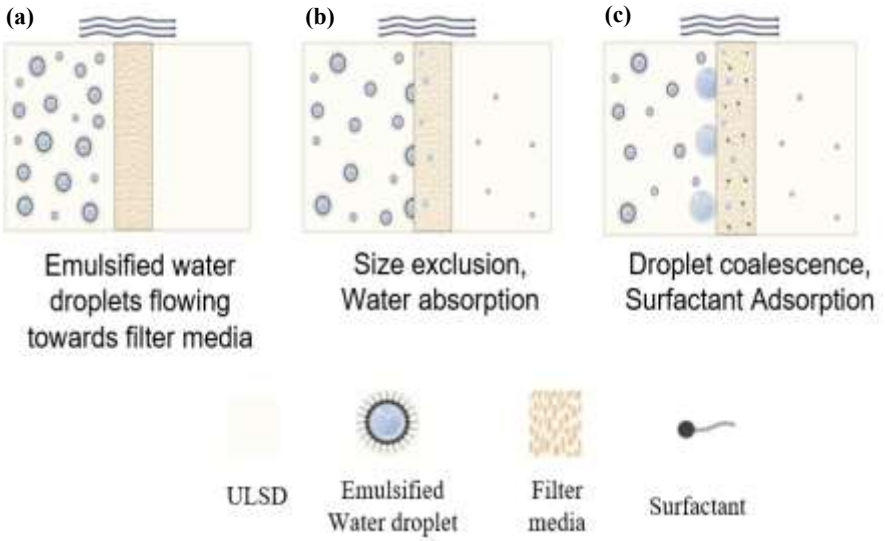


Figure 5.14 (a) Water droplets approaching filter media under flow conditions, (b) size exclusion of water droplets, droplet attachment and water absorption within the pores of the filter, (c) water droplet growth, detachment from surface, and surfactant adsorption by the media.

preferential wettability of the filter for water droplets similar to the experiment shown in Figure 5.8. These water droplets participate in coalescence as other water droplets collide with them forming larger droplets. At a critical size, gravitational force drives droplet detachment (Figure 5.13c) (~ 5 mm droplet diameter as discussed earlier). Simultaneously, there is desorption of

surfactant molecules from the attached droplet surface which makes the process of two droplets coalescing easier and effective (Figure 5.13c).

The amount of surfactant adsorbed onto the filter surface is time dependent as determined in Figure 5.9 and 5.10b. In addition, some amounts of water droplets were absorbed by the mesopores and macropores of the silica aerogel by the action of capillarity as shown in Figure 5.11. Therefore, in summary, four different separation mechanisms work in tandem for separation of emulsified water droplets in the case of a silica containing sPS coated glass fiber filter media and yielded a high separation efficiency, ~92%.

To the best of our knowledge, apart from Kulkarni et al.[50], there is no existing literature on water separation from ULSD using polymer aerogels or aerogel coated media. In this context, we now present a comparison of water separation performance achieved in this work with a set of representative studies that used coated and uncoated glass fibers, polymer fibrous media like polyethylene terephthalate (PET), polyvinylpyrrolidone (PVP), polypropylene (PP), polystyrene (PS), fluorinated polymer fibers such as polyvinylidene fluoride (PVDF), and polytetrafluoroethylene (PTFE). The data on separation efficiency and quality factor are listed in Table 5.9. It is noted that filtration efficiency, pressure drop across the media, and the quality factor are dependent on filter media thickness, face velocity, type and concentration of surfactant used to stabilize the emulsion, initial water content, and the flowrate in filtration. Unfortunately, the data reproduced in Table 5.9 were not obtained under similar conditions and thus a direct comparison with the present study cannot be made. Nevertheless, the data listed in Table 5.9 indicate that a separation efficiency greater than 90% was achieved only when the filter media consisted of multiple layers of glass fibers with typical thickness of 1-2 cm and functional polymer nanofibers, e.g., by Kulkarni et al.[126], with a compromise on quality factor. Rajgarhia et al.[129] reported excellent values of filtration efficiency and quality factor using a composite media of glass fibers and

interpenetrating-type nanofibers of PVP and polyvinyl acetate. Du et al.[321] coated filter papers with PTFE and PS nanoparticles, Zhang et al.[322] used PVDF membranes, and Zhang et al.[323] used metal meshes coated with PTFE and PVDF to obtain high separation efficiencies (95-99%). However, there is increasing concern on the use of fluorinated polymers in technical applications and alternative technologies must be identified to alleviate such concerns. In this context, the polymer aerogel coated glass fiber media with separation efficiency > 90% developed in this work lay the foundation for a new set of high-quality filter materials.

Table 5.9 Summary of filter media performance for water-in-ULSD emulsion separation inferred from prior work.

| Reference | Filter Media | Separation Efficiency (%) | Quality Factor (Q.F.) (1/kPa) |
|---|---|---|---|
| Clayfield et al.[324] | Untreated glass fibers | 51.2 | NA |
| | Glass fibers coated with (3-heptafluoroisopropoxy)propyltrichlorosilane | 55.9 | NA |
| | Glass fibers coated with AEAPTMS (N-(2-aminoethyl)-3-aminopropyltrimethoxysilane) | 97.8 | NA |
| Shin et al.[131] | Glass fiber | 64 | 0.07 |
| | Glass Fiber and recycled expanded polystyrene nanofiber (0.1 g nanofiber/g of glass fiber) | 89 | 0.11 |
| Rajgarhia et al.[129] | Glass Fiber | 48.5 | 0.74 |
| | Polyvinyl acetate (PVAc) nanofibers on glass fiber | 81.8 | 1.86 |
| | PVAc:Polyvinylpyrrolidone (PVP) 1:1 nanofibers onto glass fibers | 96.6 | 3.05 |
| | PVAc:PVP 1:2 nanofibers onto glass fibers | 95.3 | 1.25 |
| Kulkarni et al.[126] | Glass Fiber | 84 | 0.11 |
| | 8 layers of glass fiber + 2 layers of polypropylene nanofibers | 91 | 0.21 |
| | 8 layers of glass fiber + 2 layers of polyethylene terephthalate nanofibers | 93 | 0.12 |
| Moorthy[128] | Glass fiber | 86 | 0.16 |
| | Glass fiber coated with 3-aminopropyltriethoxy silane | 96 | 0.22 |
| Zhang et al.[322] | PVDF membranes | >99.95 | NA |

| | | | |
|---|---|---|---|
| Du et al.[321] | Filter paper treated with polytetrafluoroethylene and polystyrene nanoparticles | ~99% | NA |
| Zhang et al.[323] | PVDF and PTFE coated metal meshes for separation of different surfactant stabilized water-in-ULSD emulsions | ~40-95% | NA |
| Kulkarni et al.[50] | Polyimide aerogel coated 3D printed Nylon construct (20% infill, single pass efficiency) | ~ 85 | NA |
| | Syndiotactic polystyrene aerogel coated 3D printed HIPS construct (20% infill, single pass efficiency) | ~ 71 | NA |

## 5.5 Conclusion

This work established the cooperative functioning of a hybrid filter media of high specific surface area and high porosity aerogels and conventional glass fiber mats in achieving significant enhancement of efficiency of separation of emulsified water droplets from ULSD. These media exhibited size exclusion, surfactant adsorption, coalescence, and capillary absorption mechanisms working in tandem for achieving high efficiency (~92%) and high values of quality factor. The abundant meso- and macropores of aerogel networks provided size exclusion of water droplets. The high surface area, low surface energy sPS aerogel produced excellent wetting by ULSD while the high surface energy silica promoted wetting by water and removed surfactants. The hydrophilicity of silica and hydrophobicity of sPS in tandem produced conditions for water droplet separation via coalescence. These filter media present an alternative to using fluorinated polymer coatings to achieve high efficiency filtration.

## 5.6 Acknowledgement

This work was partially supported by ACS Petroleum Research Fund under grant number PRF# 59000-ND7, U.S. National Science Foundation under grant number CMMI 1826030, and industrial members of Coalescence Filtration Nanofibers Consortium at The University of Akron. Mr. William Imes is thanked for help with the filter media fabrication.

# CHAPTER VI

# SEPARATION OF PERFLUOROOCTANOIC ACID FROM WATER USING MESO- AND MACRO-POROUS SYNDIOTACTIC POLYSTYRENE GEL

## 6.1 Abstract

Per- and poly-fluoroalkyl substances are an emerging class of contaminants that are environmentally persistent, bioaccumulative, and noxious to human health. Among these, the perfluorooctanoic acid (PFOA) molecules are widely found in ground and surface water sources. A novel high surface area, meso- and macro-porous syndiotactic polystyrene (sPS) gel was used in this work as adsorbent of PFOA molecules from water at environmentally relevant PFOA concentrations (≤ 1 μg/L) and cleanse water to below the U.S. EPA's 2023 health advisory limit of 4 parts per trillion (ppt). The sigmoidal shape of PFOA adsorption isotherm indicates a two-step adsorption mechanism attributed to strong affinity of PFOA molecules for sPS surface and molecular aggregation at solid-liquid interfaces or within the pores of sPS gel. The adsorption kinetics and the effects of sPS gel porosity, pore size, and pore volume on removal efficiency were studied. The adsorption kinetics was seen strongly dependent on pore size and pore volume.

## 6.2 Introduction

Per-and polyfluoroalkyl substances (PFAS) are a group of manmade chemicals that are recognized as contaminants of emerging concern due to their toxicity, bioaccumulation, and ability to persist in the environment for a long period of time, largely due to their extremely stable carbon-fluorine bonds, thereby, receiving the notoriety as 'forever chemicals'[168,325]. A large scale contamination of ground and surface water sources by these chemicals has prompted United States Environmental Protection Agency (EPA) to list them among top priority contaminants[326]. An estimated 110 million people in the United States alone are exposed to PFAS-contaminated drinking water[170]. A number of prior studies linked PFAS accumulation in human bodies to certain types of cancers, liver damage, reduced immune response, negative impact on the reproductive system such as reduced fertility, birth defects, and many more health issues[326–328]. In addition, the negative ecological impact of these chemicals on the aquatic ecosystem is also a concern[329]. Therefore, addressing removal of PFAS from water streams is the growing need of the hour.

PFAS are used in large scale manufacturing of poly(tetrafluoroethylene) (Teflon®) and in numerous everyday consumer products such as food packaging, clothing, coatings, menstrual products, to name a few[168,330]. The US EPA identified around 430 PFAS molecules obtained from various water sources and included 74 chemicals in the top priority list targeted for obtaining additional toxicity data [166,167]. However, certain types of PFAS molecules, namely perfluorooctanoic acid (PFOA), perfluorooctanesulphonic acid (PFOS), perfluorobutanoic acid (PFBA), perfluorobutanesulphonic acid (PFBS), and GenX chemicals, came under stringent scrutiny due to their widespread use and proven adverse impacts on human health[169,331,332]. In 2022, the US EPA assigned a health advisory limit for PFOA of 0.004 ng/L and for PFOS of 0.02 ng/L compared to the previously set limit in 2016 of 70 ng/L for both these compounds [331,333]. In view of the above stringent advisory limits, this work addressed high efficiency separation of

perfluorooctanoic acid (PFOA), the most widespread PFAS contaminant present in the environment, using a novel mesoporous-macroporous adsorbent media.

Several techniques such as chemical oxidation[174], foam fractionation[334], coagulation[177], ion-exchange[202], and filtration[335] were studied for PFOA removal or degradation. However, the most viable and commercially scalable technology involves the use of natural or synthetic adsorbent media due to their greater effectiveness for separation of PFOA molecules compared to other available technologies. A few of the adsorbents considered as the frontrunners in terms of their performance are granular/powdered activated carbon[200,336,337], amine containing compounds[169,338], biochar[199], and ion exchange resins[181]. However, a few known drawbacks limit the performance of these adsorbents in PFOA separation[168]. For example, activated carbon is inexpensive but it suffers from poor adsorption of PFOA at environmentally relevant concentrations (≤ 1 μg/L), long adsorption times, low effectiveness for short-chain PFAS molecule separation, poor performance in the presence of other organic contaminants, and difficulty in regeneration of the adsorbent bed for sustainable use. In the same vein, a majority adsorption media, such as β-cyclodextrin (β-CD)[169], ion-exchange resins[181], offer extremely low specific surface area and hence, low adsorption capacities, thus requiring frequent regeneration of the adsorbent bed. In addition, ion exchange resins are highly selective towards either anionic or cationic PFAS. Their performance in separation of non-ionic molecules is poor and their effectiveness for PFAS separation in the presence of other salts in water is low[168].

Most importantly, the majority of adsorbent materials reported in literature were not associated with separation of PFOA at the desired low concentrations (≤1 μg/L), thus limiting their effectiveness for the separation task[338]. To the best of our knowledge, none of the currently available adsorbent materials can meet the June 2022 EPA guidelines for admissible levels of PFOA concentration (0.004 ng/L). In this context, novel adsorbent media are needed that offer high

affinity for PFOA at environmentally relevant concentrations, high adsorption capacity, rapid adsorption kinetics, and inexpensive regeneration to address the emerging stringent environmental limits and the ensuing health hazards that these molecules present. The above issues were addressed in this work by considering mesoporous and macroporous polymer gels, specifically syndiotactic polystyrene (sPS) wet gels as the adsorbent for separation of PFOA molecules from water initially available at industrially relevant concentration of ≤1 μg/L.

Polymer gels offer high surface area (200-1000 $m^2/g$)[2,229,270], high pore volume (> 90 %)[58,232,235,339], and an interconnected network of abundant mesopores (2-50 nm) and macropores (>50 nm). The pore-filling liquid in the polymer gels can be easily replaced by a gas in the supercritical drying step to obtain aerogels[1]. Aerogels can be rendered into various shapes and sizes such as monoliths[15], sheets[3,340], films[18], and spherical[63,229] or pill-shaped[64] microparticles. The pore size and surface energy of the materials can also be tuned for desired applications [2,45,317,341]. The development of this class of materials over 90 years led to several high value innovations in thermal insulation[342], air filtration[316,343,344], energy storage[23], molecular separation[64,270], and filtration[345].

An earlier study established high adsorption capacity of three polymer gels, namely sPS, polyimide, and polyurea, for removal of a non-ionic, triblock copolymer surfactant polyethylene oxide (PEO)-polypropylene oxide (PPO)-PEO from a solution in water[270]. An adsorption capacity of around 2-3 g/g was achieved in the case of sPS gels. Such adsorption capacities are unusually high in reference to the data available for other porous materials[161,165,224,250] and are attributed to high surface energy and high surface area of sPS gels. sPS aerogels were first reported in 2005 by Daniel et al[237]. This high specific surface area, large porosity, hydrophobic surface has made these materials suitable for applications as adsorbents[270], absorbents[51,346], in oil-water separation[50] and as a ultra- low dielectric constant material[347].

The present work investigated adsorption kinetics and separation efficiency of PFOA molecules by sPS wet gels starting at environmentally relevant concentrations ≤ 1 μg/L in water. The effects of polymer gel pore volume and surface area on adsorption performance were analyzed. Most known adsorbents have low specific surface area and these reach saturation adsorption limits quickly. Consequently, these materials can be reused only after regeneration by conducting desorption of PFOA molecules. As will be seen later, the sPS wet gels considered in this work had high surface area corresponding to a higher number of available adsorption sites and, thus, would have a higher adsorbent saturation capacity. To demonstrate this attribute, PFOA-loaded sPS wet gels obtained from one set of experiments were subjected to additional adsorption cycles in PFOA-water solution and the ability of the gel to remove additional PFOA molecules was investigated. The findings reported in this work demonstrate the strong promise of sPS gel for removal of PFAS molecules from solutions in water.

## 6.3 Experimental

### 6.3.1 Materials

Syndiotactic polystyrene ((Mw ≈ 300,000 g/mol, 98%) was procured from Scientific Polymer Producers Inc. (Ontario, NY, U.S.A.). Toluene was purchased from Sigma Aldrich (Milwaukee, WI, U.S.A). Ethanol was purchased from Decon Laboratories Inc. (King of Prussia, PA, U.S.A.). Perfluorooctanoic acid (PFOA, 96%) and perfluoroheptanoic acid (purity ≥ 98.0 %, used as an internal standard) were purchased from Sigma Aldrich (Milwaukee, WI, U.S.A). All chemicals were used as received without further purification.

### 6.3.2 Fabrication of sPS polymer wet gels and aerogels

sPS gels were obtained by thermo-reversible gelation of solutions of sPS in toluene. sPS solutions were prepared with solid concentrations of 0.02, 0.06, and 0.08 g/mL by dissolving sPS in toluene in sealed vials at 100 ℃ and allowing solutions to cool under ambient condition for 1

min followed by pouring into a covered cylindrical glass mold with 15 mm diameter for gelation. The gels were allowed to stand in the mold for 5 h to ensure complete gelation, demolded, and solvent exchanged first with ethanol and finally with deionized (DI) water to obtain water-filled sPS wet gels. To obtain sPS aerogels, the ethanol-filled sPS gels were solvent-exchanged with liquid carbon dioxide and dried under supercritical condition of carbon dioxide at 50 °C and 11 MPa pressure to recover sPS aerogels. The aerogels were used for BET surface area measurement and for examining morphology using scanning electron microscope (SEM).

### 6.3.3 Characterization

#### 6.3.3.1 Porosity, skeletal density, and bulk density

Helium pycnometer (AccuPyc II 1340, Micromeritics Instrument Corp., Norcross, GA) was used to obtain skeletal density($\rho_s$). The bulk density ($\rho_b$) was obtained from weight and volume of cylindrical aerogel monolith specimens. The bulk and skeletal density yielded total porosity ($P_T$) and total pore volume ($V_{Total}$) of the aerogels as expressed in equation 1 and 2 respectively.

$$\Pi_T = (1-\rho_b/\rho_s)\times 100 \quad (1)$$

$$V_{Total} = \frac{1}{\rho_b} - \frac{1}{\rho_s} \quad (2)$$

#### 6.3.3.2 Specific surface area and pore size analysis

The Brunauer−Emmett−Teller (BET) adsorption-desorption analysis was used to obtain specific surface area and mesopore volume ($V_{meso}$) of sPS aerogels. Micromeritics Tristar II 3020 analyzer (Micromeritics Instrument Corp., Norcross, GA) was used for this purpose to obtain $N_2$ adsorption-desorption isotherms at 77 K. The nonlocal density functional theory (NLDFT) model was used to obtain the mesopore volume fraction from $N_2$ isotherms at 77 K. The macropore (diameter > 50 nm) volume ($V_{macro}$) was obtained from the difference of total pore volume ($V_{Total}$,

equation 2) and the mesopore volume ($V_{meso}$). The fractions of meso- ($f_{meso}$) and macro-pores ($f_{macro}$) were calculated using equations (3-4).

$$\phi_{\text{meso}} = \frac{V_{\text{meso}}}{V_{\text{total}}} \quad (3)$$

$$\phi_{\text{macro}} = \frac{V_{\text{macro}}}{V_{\text{total}}} = 1 - \phi_{\text{meso}} \quad (4)$$

6.3.3.3 Morphology

The morphology of aerogel specimens was examined using scanning electron microscope (SEM JSM5310, JEOL,MA).

6.3.3.4 Mass spectrometry analysis of PFOA in water

Electrospray ionization mass spectrometry (ESI-MS) experiments were performed on a Bruker timsTOF Pro 2 (Bruker Daltonics, Billerica, MA). Solutions of PFOA in Millipore/DI $H_2O$ at various concentrations were diluted with MeOH containing the internal standard, perfluoroheptanoic acid (PFHA), at a concentration of 5.0 ng/mL. The final 1:1 $H_2O$/MeOH (v/v) working solutions were then filtered using a Supor Membrane 0.1 μm Filter (Pall Corporation, Port Washington, NY) and the concentration of each analyte was determined by using the internal standard technique. The solutions were introduced into the ESI source via direct injection and electrospraying at a flow rate of 5 μL/min. The end plate and capillary voltages were set to 400 V and 4.5 kV, respectively, while the nebulizing gas ($N_2$) pressure and drying gas flow rate and temperature were set at 1.5 bar, 4 L/min, and 300°C, respectively. The PFOA and PFHA ions were identified at m/z ~368.9 and 318.9, respectively. All data were acquired in triplicate via the MS scan mode with the instrument settings as follows: Deflection 1 Delta: -80 V, Funnel 1 RF: 350 Vpp, isCID Energy: 0 eV, Funnel 2 RF: 300 Vpp, Multipole RF: 300 Vpp, Transfer Time: 65 μs,

and PrePulse Storage: 5 µs. The DataAnalysis 6.1 program (BrukerDaltonics, Bremen, Germany) was used for post-acquisition data processing.

#### *6.3.3.5 PFOA adsorption experiments*

Calibration curve generation: Solutions of PFOA in Millipore/DI $H_2O$ at various concentrations (0.00001-10 µg/L) were diluted with methanol (MeOH) containing the internal standard, perfluoroheptanoic acid (PFHA), at a concentration of 5.0 ng/mL. The final working solutions were filtered using a Supor Membrane 0.1 µm Filter (Pall Corporation, Port Washington, NY) and the concentration of each analyte was determined by using the internal standard technique. The solutions were introduced into the Electrospray ionization mass spectrometer. The PFOA and PFHA ions were identified at m/z ~368.9 and 318.9, respectively. The ratio of the intensities of the PFOA and PFHA peaks were calculated and plotted on the y-axis as a function of PFOA concentration (x-axis). All data points were obtained after performing three replicates of each sample. The amount of PFOA present in water was determined using mass spectrometry technique mentioned in section 2.3.4 using a calibration curve (Figure 6.1,Table 6.1 and Figure 6.2, Table 6.2).

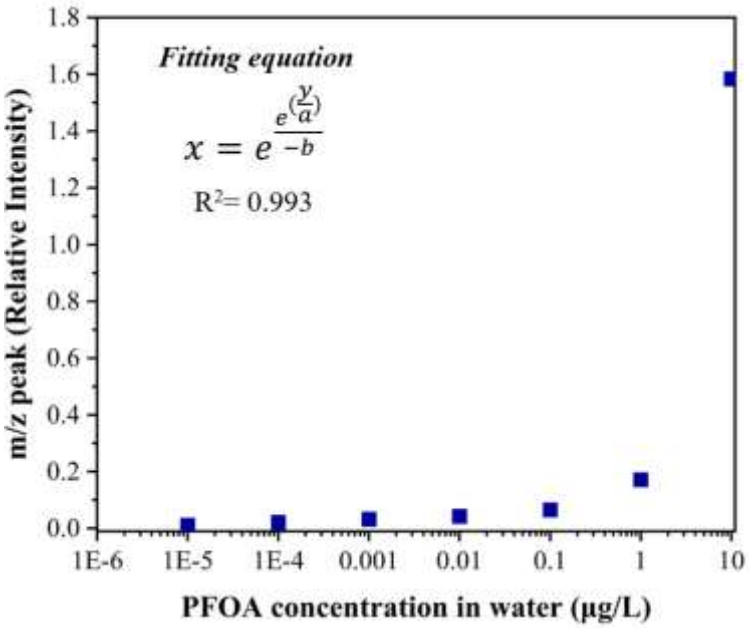


Figure 6.1.Relative m/z peak intensity vs PFOA concentration in water (Calibration curve), in the fitting equation a= -0.0326 and b= 0.0569, it is valid for concentration between (0- 1µg/L)

Table 6.1 PFOA calibration curve values (0.00001-1 µg/L)

| PFOA concentration in water (µg/L) | Relative intensity |
|---|---|
| 10 | 1.5842 ± 0.0032 |
| 1 | 0.1716 ± 0.0022 |
| 0.1 | 0.0656 ± 0.0002 |
| 0.01 | 0.0434 ± 0.0003 |
| 0.001 | 0.0328 ± 0.0009 |
| 0.0001 | 0.0219 ± 0.0005 |
| 0.00001 | 0.0115 ± 0.0001 |

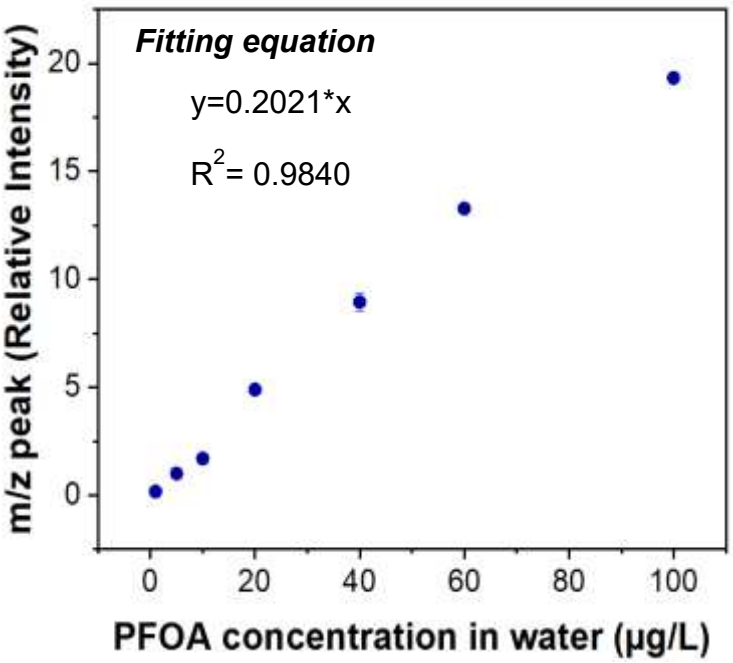


Figure 6.2.Relative m/z peak intensity vs PFOA concentration in water (Calibration curve) for PFOA concentration between 1-100 µg/L

Table 6.2 PFOA calibration curve values (1-100 µg/L)

| PFOA concentration in water (µg/L) | Relative intensity |
|---|---|
| 1 | 0.1716 ± 0.0022 |
| 5 | 1.0080 ± 0.0285 |
| 10 | 1.7009 ± 0.0300 |
| 20 | 4.8920 ± 0.0547 |
| 40 | 8.9519 ± 0.4184 |
| 60 | 13.2729 ± 0.1070 |
| 100 | 19.32201 ± 0.2119 |

For generating the adsorption isotherm, PFOA solutions of concentrations ranging from 0.0001-100 µg/L were used and a known solid mass of the sPS wet gel (diameter 1.5 ± 0.1 cm and height 0.85 ± 0.02 cm) was dipped in these solutions for 24 h. The PFOA water samples of different

concentrations were prepared by firstly making a stock solution of 10 mg/L and serially diluting it to reach the desired concentration of PFOA in water (0.0001-100 μg/L). The amount of PFOA adsorbed by the solid sPS gel was obtained by analyzing the before ($C_0$) and after amount ($C_1$) of PFOA present in water and this quantity was converted to mass of PFOA adsorbed (μg)/solid mass of sPS (g). The separation efficiency was obtained using equation (5).

$$\% \text{ Separation Efficiency} = \frac{C_0 - C_1}{C_0} \times 100 \quad (5)$$

For obtaining the adsorption kinetic curves, 10 mL solutions of 1 μg/L concentration of PFOA were taken and sPS wet gels, obtained with 0.06 g/mL sPS concentration, were dipped in them for different times (5-1440 min). The separation efficiency was obtained using equation (5). All experiments were performed three times.

## 6.4 Results and Discussion

### 6.4.1 PFOA adsorption isotherm and adsorption kinetics by sPS gel

The PFOA adsorption isotherms were generated by dipping a 0.06 g/mL sPS solid concentration water filled gel into 10 mL PFOA solutions of concentrations ranging from 0.0001-5 μg/L for 24 h. It should be noted that the environmentally relevant concentration of PFOA in water is 1 μg/L[338]. The adsorption isotherm was generated with PFOA concentrations well-below and above this concentration. Figure 6.3a (Blue) depicts the amount of PFOA adsorbed by the sPS gel in μg/g as a function of PFOA initial concentration in water. A sPS gel with a solid weight of 70 mg was used for these experiments.

The first striking observation is the shape of the adsorption isotherm curve. The curve is sigmoidal (S-shaped) (Figure 6.3b) with an inflection point around 2 μg/L indicating aggregation or multilayer adsorption of molecules on the adsorbent surface. The structural aggregation of the PFOA molecules can occur in one of the following manners - bilayers[164], hemi-micelles[348], micelles[222], or other forms. Such adsorption curves suggest a strong affinity between the adsorbate

and adsorbent and also between the adsorbed and non-adsorbed molecules[159,165]. At the highest PFOA initial concentration of 100 µg/L, the amount of PFOA adsorbed by the gel was ~ 12.17 µg/g and the equilibrium concentration of PFOA in liquid was 14.76 µg//L. However, this should not be mistaken to be the maximum adsorption capacity of the gel since a plateau or saturation in adsorbed amount cannot be ascertained at this concentration. PFOA concentrations higher than 100 mg/L in water were not considered in this work. A thorough study will be separately conducted to discover the adsorption regimes at concentrations higher than 100 mg/L.

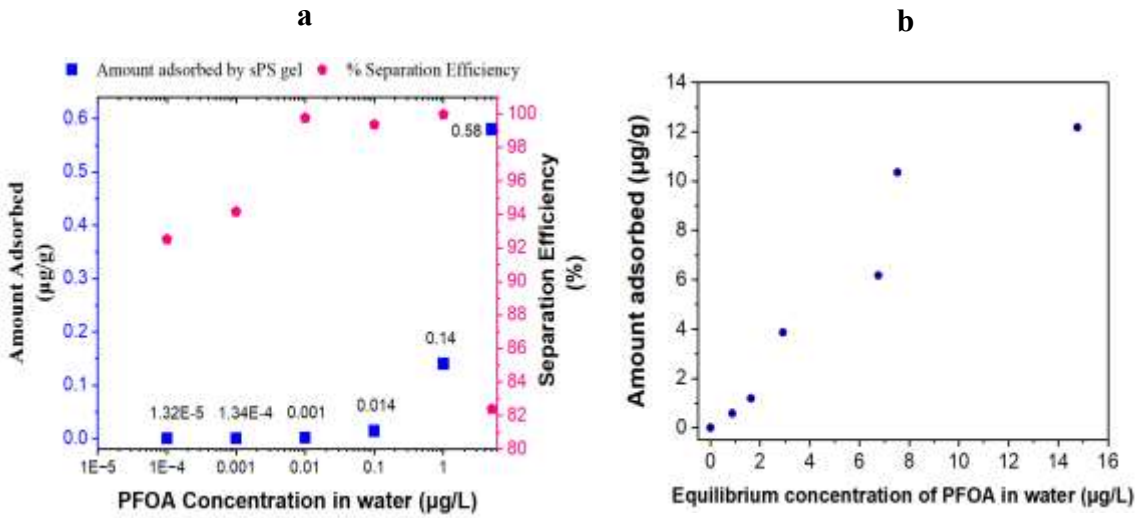


Figure 6.3 a) Blue: Amount of PFOA adsorbed (µg/g) as a function of PFOA concentration in water, Pink: % Separation Efficiency as a function of PFOA concentration in water, (b) Effective concentration of adsorbed PFOA within the sPS gel (0.06 g/mL solid concentration) as a function of PFOA concentration in water. sPS wet gel dimensions : diameter 1.5 ± 0.1 cm and height 0.85 ± 0.02 cm

Table 6.3 % separation efficiency of PFOA by sPS wet gels at different initial concentrations of PFOA in water

| PFOA initial concentration in water (μg/L) | % Separation efficiency |
|---|---|
| 0.0001 | 92.57 ± 1.59 |
| 0.001 | 94.13 ± 0.87 |
| 0.01 | 99.77 ± 0.02 |
| 0.1 | 99.37 ± 0.10 |
| 1 | 99.98 ± 0.01 |
| 5 | 82.39 ± 0.08 |

The second important observation is the trend of the separation efficiency curve as a function of bulk PFOA concentration (Figure 6.3a, pink data points). At the environmentally relevant concentration of 1 μg/L, the separation efficiency of the sPS gel was found to be 99.98 %, achieved in ~ 24 h. The PFOA concentration in water after adsorption by the sPS gel reduced to about 0.2 ng/L or 0.2 ppt in 24 h. In this context, a limited number of adsorbents such as β-cyclodextrin polymer (~ 99% separation efficiency in 24 h), polyethylenimine-functionalized cellulose microcrystals (~90-95% separation efficiency in 16 h), and aminated β-cyclodextrin (~ 99% separation efficiency in 9 h) produced such high separation performance for PFOA[169,205,209,349,350]. Two adsorbents commercially used for PFAS removal are activated carbon and ion-exchange resins. Therefore, to benchmark our materials, activated carbon supplied by Calgon corporation F-400 and ion exchange resin packaged in Zero Water filters was used for PFOA adsorption from 1 μg/L concentration in water. The specific surface area for the activated carbon and ion exchange resin were measured to be 730 and 80 $m^2/g$. The BET adsorption-desorption isotherms for the two materials are shown in Figure 6.4a and 6.4b. The solid weight of

each adsorbent was adjusted to reach a total surface area of 30 $m^2/g$ to keep the total available surface area for each adsorbent constant. The activated carbon and the ion exchange resin showed a separation efficiency of 81.10 ± 0.2 % and 43.10 ± 1.12 % respectively whereas the sPS wet gel shows a significantly higher separation efficiency of 99.98 ± 0.01%.

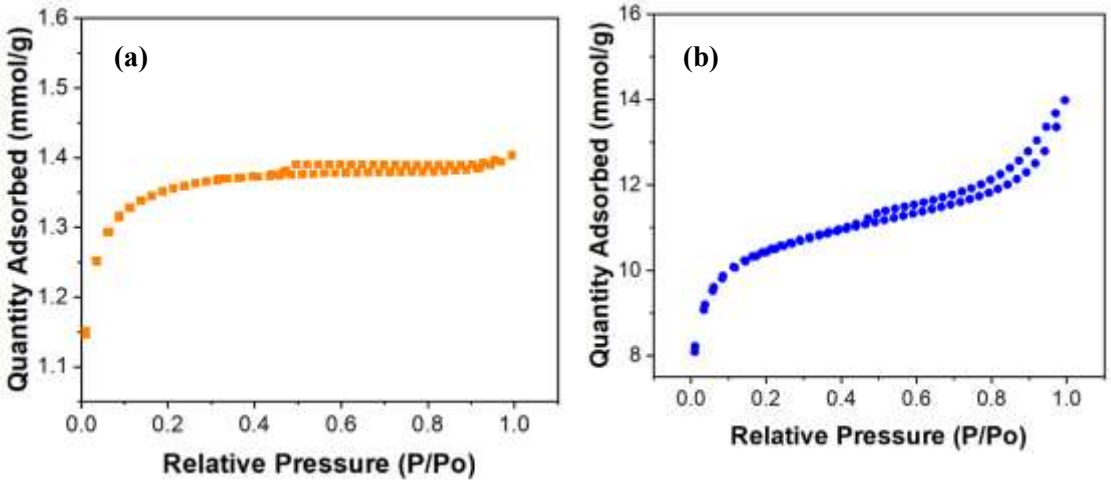


Figure 6.4 BET adsorption-desorption isotherm for (a) Calgon F-400 (activated carbon) and (b) Zero Water (ion exchange resin)

In addition, most adsorbents, such as activated carbon, take hours or even days to reach > 90% separation efficiency[168,351]. The slow adsorption kinetics in the case of activated carbons is attributed to the small pore size, which are predominantly microporous (< 2 nm), thereby, limiting the diffusion ability of the PFOA molecules with typical size ~ 2 nm. The third aspect to notice here is the adsorption performance of sPS gel at PFOA concentrations lower than 1 μg/L.

As is well-known, adsorption of molecules from liquids becomes increasingly challenging especially at low concentrations.[338] It was observed that the sPS gel considered in this work showed separation efficiency of > 90 % for all PFOA concentrations below 1 μg/L. Specifically, the value of separation efficiency were 92.5, 94.1, 99.7, and 99.3% for PFOA concentrations of respectively 0.0001, 0.001, 0.01, and 0.1 μg/L. We attribute this trend to the cooperative functioning of the diffusive flux of the surfactant from the bulk into the pores of sPS gel and the adsorption kinetics

of the surfactant on polymer strand surfaces inside the gel. The use of a finite size gel specimen of diameter 1.5 ± 0.1 cm and height 0.85 ± 0.02 cm did not allow all PFOA molecules present in the bulk to access high surface area polymer strands present inside the pores. The PFOA molecules must diffuse from the bulk to the macroscopic gel specimen surface, diffuse through the pores to access high surface area polymer strands, and finally adsorb onto polymer surfaces. The favorable interactions between sPS polymer strand surfaces in the wet gel and the PFOA molecules that diffused into the pores potentially led to thermodynamically stable structural configuration and aggregation of PFOA molecules on the adsorbent surface as was noted by Shin et al.[226] for a set of surfactant-silica systems. This in turn promotes further molecular diffusion from the bulk to the pores and from the water phase inside the pores onto sPS solid strands. A thorough characterization of PFOA aggregation on sPS strand surfaces, however, is needed to support an analogy with the work of Shin et al.[226]

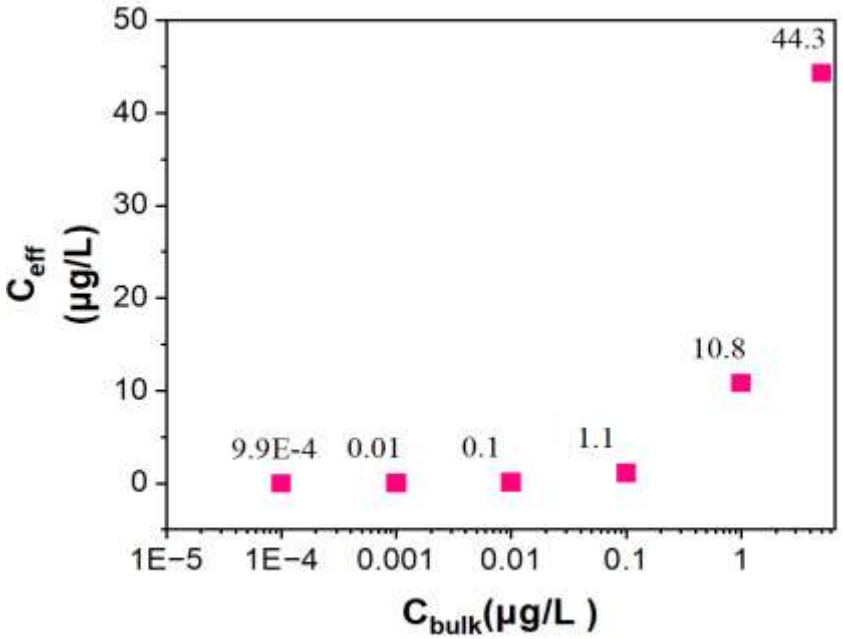


Figure 6.5 Effective concentration of adsorbed PFOA within the sPS gel (0.06 g/mL solid concentration) as a function of PFOA concentration in water.

At lower PFOA concentrations of 0.0001 and 0.001 μg/L, the concentration gradients across the bulk liquid and within the sPS gel were much smaller, respectively two and one order of magnitude compared to a PFOA concentration of 0.01 μg/L. Accordingly, the slower diffusion flux controlled the adsorption performance at lower concentration. The diffusive flux increased at higher PFOA concentration in the bulk liquid leading to quicker diffusion and adsorption of molecules. In this work, the adsorption experiments were performed for 24 h. It is conceivable that only a part of the available sPS gel surface was covered, yielding lower separation efficiency. This data presented in Figure 6.3(a) supports the idea that sPS wet gels are very effective in removing PFOA even when present in extremely low concentrations.

One can also quantify the adsorption performance in terms of an effective concentration ($C_{eff}$) of the adsorbed PFOA molecules within the sPS gel as function of bulk concentration ($C_{bulk}$). Such data are shown in Figure 6.5. The value of $C_{eff}$ within the gel was calculated from the mass of PFOA adsorbed by the gel and the volume of water needed to fill all the pores of the gel. As an example, the effective concentration of PFOA within the sPS gel dipped in a 0.01 μg/L PFOA solution, i.e., was calculated as follows. In this case, the sPS wet gel weight was 1 g and its porosity was 93% (Table 6.3). Therefore, 93% of the sPS gel weight is water and 7 % of its weight is sPS solid weight i.e. 0.93 mL or 0.00093 L of water and 0.07 g sPS solid weight. The amount of PFOA adsorbed by the sPS gel was 0.014 μg /g (Figure 6.3a). In view of the above, the value of $C_{eff}$ was found to be 0.014*0.07/0.00093, which is 1.1 μg/L . Therefore, $C_{eff}$ was approximately 11 times higher than $C_{bulk}$ for a bulk concentration of 0.1 μg/L . It is observed that $C_{eff}$ at the end of the adsorption process was approximately 10 times higher than $C_{bulk}$. This indicates that molecular diffusion worked only in the early periods. At later periods, $C_{eff}$ became greater than $C_{bulk}$, indicating favorable interactions between sPS gel and PFOA molecules leading possibly to structural assemblies of PFOA molecules within sPS gel. An earlier study by Gotad et al.[270] underlined the

role of high interfacial energy sPS-water interfaces in driving adsorption of block copolymer surfactants within the water-filled sPS gel. The amount of surfactant adsorbed scaled directly with the interfacial energy. A similar argument can be invoked in this work to explain the driving force for PFOA adsorption on sPS gels in view of similar molecular structure of the PFOA molecules to that of the surfactant considered by Gotad et al.[270], with a hydrophilic -COOH group at one end and the 8-carbon long chain with fluorine groups at the other.

Another important parameter determining the effectiveness of an adsorbent is the kinetics of adsorption of PFOA molecules from a solution in water. Figure 6.5 shows a representative plot showing separation efficiency as function of time for removal of PFOA using sPS gel produced from 0.06 g/mL sPS solution in toluene. In this case, cylindrical monolithic sPS wet gel (diameter 1.5 ± 0.1 cm and height 0.85 ± 0.02 cm) specimens of approximately 70 mg solid weight were dipped in 1 μg/L PFOA solution in water over a period of 24 h.

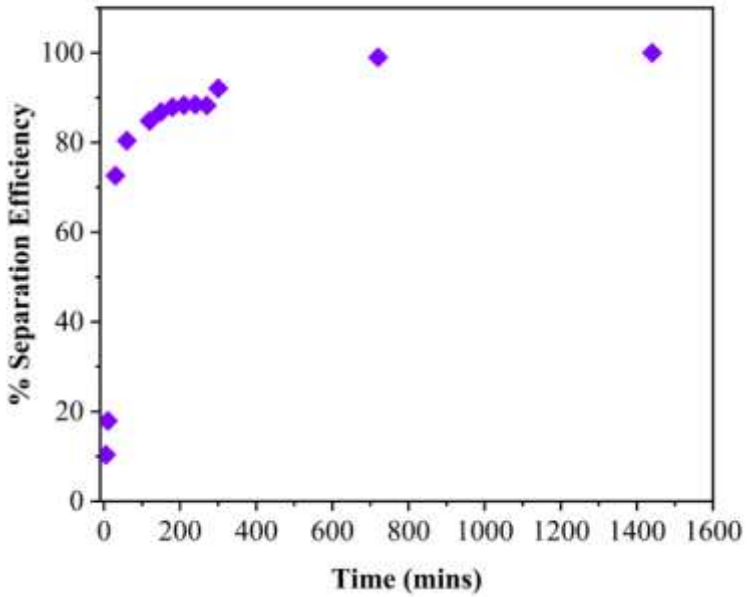


Figure 6.5 Time-dependent PFOA adsorption by sPS gels obtained from sPS solution of 0.06 g/mL solid concentration from 1 μg/L PFOA solutions in water. sPS wet gel dimensions : diameter 1.5 ± 0.1 cm and height 0.85 ± 0.02 cm

Table 6.4 % Separation efficiency of PFOA (initial concentration: 1μg/L) by a 0.06 g/mL sPS wet gel as a function of time

| Time (mins) | % Separation efficiency |
|---|---|
| 10 | 17.90 ± 0.74 |
| 30 | 72.60 ± 2.80 |
| 60 | 80.22 ± 3.30 |
| 120 | 82.87 ± 4.21 |
| 150 | 86.11 ± 5.05 |
| 180 | 87.02 ± 5.41 |
| 210 | 87.51 ± 4.14 |
| 240 | 88.10 ± 3.24 |
| 270 | 88.18 ± 0.73 |
| 300 | 92.01 ± 0.56 |
| 1440 | 99.98 ± 0.01 |

It is noted from prior work that the kinetics of adsorption are largely governed by the adsorbent pore size, adsorbent amount, and the shape of the adsorbent[199,352,353]. It is seen from Figure 6.5 that PFOA adsorption was fast at the beginning and reached an asymptote at a later period. For example, it took ~5 h (300 min) to reach 92 % separation efficiency and ~12 h and 24 h to attain separation efficiencies of 98.99 and 99.98% respectively. A steep rise in adsorption was observed in the 5-30 min interval, e.g., the separation efficiency increased from ~ 10 % at 5 min to ~ 72 % at 30 min. Such a steep rise in adsorption behavior indicates fast diffusion of PFOA molecules within the sPS gels and their subsequent fast adsorption onto the sPS surface. As will be illustrated later, faster adsorption kinetics can be achieved via manipulation of the pore sizes and pore volumes offered by the gel, achieving > 90% separation in an hour.

*6.4.2 Effect of sPS gel pore volume, specific surface area on PFOA adsorption*

In this section, the effects of sPS concentration in the gel on adsorption performance of PFOA molecules are discussed. sPS gels were prepared from 0.02, 0.06, and 0.08 g/mL sPS in toluene producing specimens with different values of total porosity ($P_T$), pore size, and specific surface area. Such data and the values of bulk and skeletal density are presented in Table 6.5.

A higher solid polymer concentration in the gel results in an increase of sPS strand diameter and a reduction of the pore size and pore volume of the gel (Table 6.5). The sPS aerogels showed porosity of ~ 97, 92, and 90 % and total pore volume of ~ 31, 11.5, and 8.6 $cm^3/g$ at sPS concentration of 0.02, 0.06 and 0.08 g/mL. It is apparent that the pore volume reduced from 31 $cm^3/g$ to 8.6 $cm^3/g$ with a four-fold increase of sPS concentration from 0.02 to 0.08 g/mL. The more open pore structure offered by the gel with 0.02 g/mL sPS is evident from the high magnification SEM images shown in Figure 6.6.

Table 6.5 Bulk density, skeletal density, porosity, pore volume, surface area, and meso-macropore volume fraction of sPS polymer aerogels.

| sPS solid concentration (g/mL) | Bulk density ($\rho_b$; $g/cm^3$) | Total porosity ($\rho_T$) (%) | BET surface area ($m^2/g$) | $\mathbf{V_{Total}}$ ($cm^3/g$) | $\phi_{meso}$; $\phi_{macro}$ |
|---|---|---|---|---|---|
| 0.02 | 0.031 ± 0.001 | 97.1 | 313 ± 7 | 31.3 | 0.02; 0.98 |
| 0.06 | 0.080 ± 0.003 | 92.3 | 296 ± 15 | 11.5 | 0.06; 0.94 |
| 0.08 | 0.105 ± 0.004 | 90 | 280 ± 10 | 8.6 | 0.07; 0.93 |

sPS skeletal density ($\rho_s$): 1.05 $g/cm^3$

The sPS strand diameter is thinnest at 0.02 g/mL of sPS concentration (Figure 6.6) with the highest specific surface area ~ 313 $m^2/g$ compared to 296 $m^2/g$ and 280 $m^2/g$ respectively for sPS gel with 0.06 and 0.08 g/mL concentration (Table 1). The BET adsorption- desorption isotherms for the three sPS aerogels are shown in Figure 6.7. The meso- and macropore volume fraction of the three sPS aerogels is also quite different. The sPS aerogel produced from 0.08 g/mL concentration had a mesopore volume fraction of ~ 7% which was highest among the three aerogels. It is followed by sPS aerogels produced with 0.06 g/mL (5%) and 0.02 g/mL (2%) concentration. Therefore, it is imperative to evaluate the effect of parameters such as the total pore volume, pore size, and specific surface area of sPS gel on PFOA adsorption performance. The PFOA adsorption experiments were performed by keeping the solid weight of the sPS gel for all the three systems

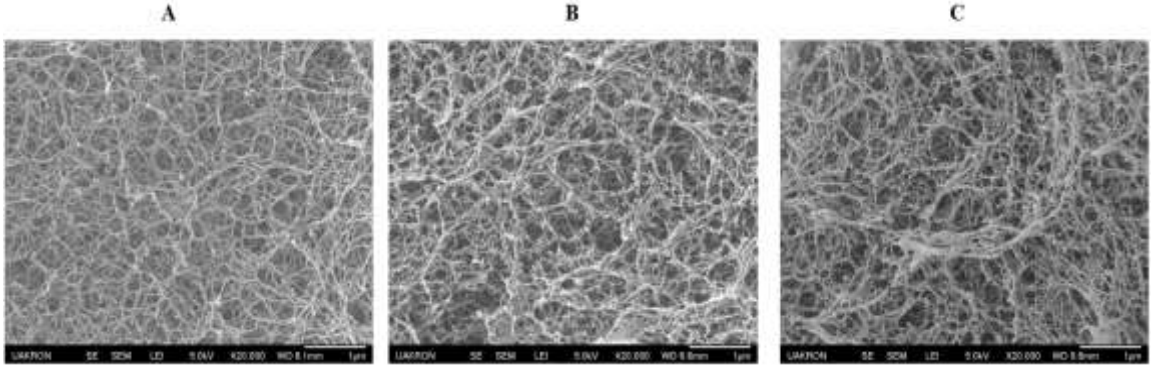


Figure 6.6 High magnification SEM images of sPS aerogel produced with (A) 0.02 g/mL, (B) 0.06 g/mL and (C) 0.08 g/mL concentration of sPS in solution.

constant at 100 mg allowing the total pore volume and total BET surface area to play a key role in governing the adsorption behavior.

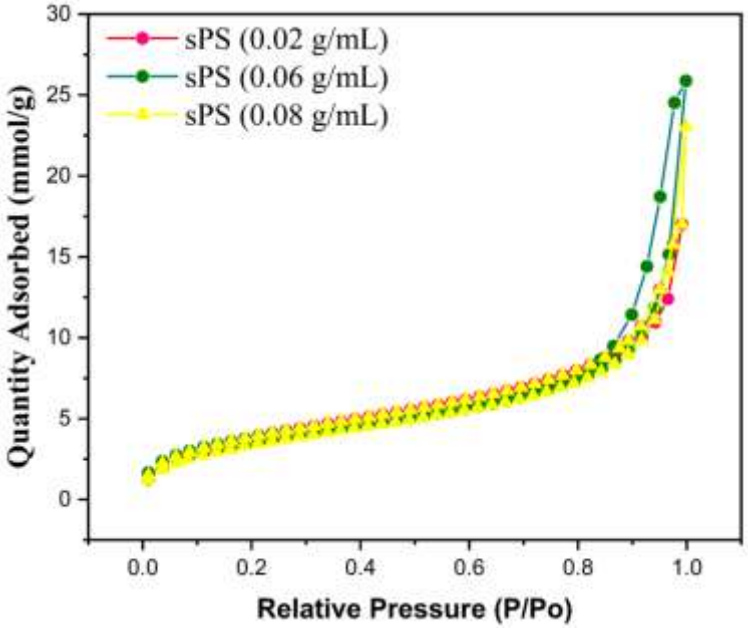


Figure 6.7. BET $N_2$ adsorption-desorption isotherm curves for the three different solid concentrations sPS aerogels, 0.02 g/mL (pink), 0.06 g/mL (green) and 0.08 g/mL (yellow)

Figure 6.8 shows the PFOA adsorption performance of the three sPS wet gels at three different times i.e., 30, 120, and 300 mins. The data clearly indicates that the sPS gel solid concentration played a significant role in determining the rate of adsorption. The sPS gel obtained from 0.02 g/mL sPS concentration in solution was able to reach ~ 84 % separation efficiency within 30 mins, while the other two gels with solid concentration of 0.06 and 0.08 g/mL reached separation efficiency values of ~ 72 and 32% within the same time. The difference in adsorption performance between the 0.02 g/mL and 0.08 g/mL sPS gel was quite large indicating that parameters pore volume, pore size, or specific surface area significantly affected the adsorption process. After 120 mins, the 0.02 g/mL sPS gel was able to remove ~ 99.2% of PFOA molecules. The sPS gel produced from 0.06 g/mL sPS concentration needed ~ 12 h to reach a 99% separation efficiency.

The above trend can be explained as follows. First, the PFOA adsorption kinetics would be controlled by how fast the diffusion of PFOA molecules occurs through the porous sPS wet gel. The 0.02 g/mL sPS gel has a higher pore volume and it can also be seen from the SEM images in Figure 6.6 that the diffusion of the molecules through a 0.02 g/mL sPS wet gel would be easier compared to a 0.06 g/mL and 0.08 g/mL sPS wet gel due to lesser restriction for PFOA diffusion through the tortuous porous network facilitated by smaller fiber diameters and larger pores of the 0.02 g/mL sPS gel. Thus, the sPS 0.02 g/mL gel, allowed higher surface area to be accessed by the PFOA molecules for adsorption resulting in fast adsorption kinetics.

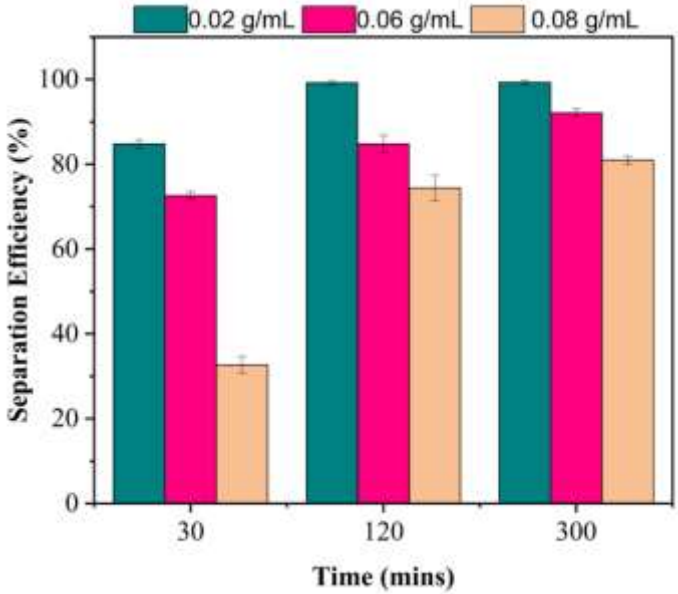


Figure 6.8 PFOA adsorption by the three different sPS gels of different solid concentrations, 0.02 g/mL (Green), 0.06 g/mL (Pink) and 0.08 g/mL (Brown) after 30, 120 and 300 mins. sPS wet gel dimensions : diameter 1.5 ± 0.1 cm and height 0.85 ± 0.02 cm

Second, as alluded to earlier, the PFOA adsorption by the sPS gel is a surface-area driven process. Thus, the gel specimen produced from sPS 0.02 g/mL with a surface area of 313 $m^2/g$ resulted in higher number of available adsorption sites for PFOA molecules compared to the gels produced from 0.06 g/mL and 0.08 g/mL sPS concentration and with specific surface area of 296 and 280 $m^2/g$ respectively. However, more thorough study is needed to understand the underlying

physics of how the PFOA molecules interact with sPS surface or with each other at the sPS-water interface. This will be considered in a future investigation.

6.4.3 Extent of reusability of sPS gel for PFOA adsorption

An experiment was performed to test the extent of reusability of the sPS wet gels for removing the PFOA molecules from water until a separation efficiency of less than 90% was observed. This test answered if a gel that adsorbed say 99.98% of PFOA from an industrially relevant concentration in water has more capacity to adsorb PFOA molecules when dipped in a fresh PFOA solution in water. For this purpose, a water filled sPS gel of 70 mg solid weight produced with 0.06 g/mL solid concentration was dipped in a 10 mL solution of 1 μg/L PFOA. The gel was allowed to adsorb PFOA molecules for 24 h and subsequently transferred to another 10 mL solution of 1 μg/L PFOA in water. The process was repeated 5 times each time with 24 h adsorption,

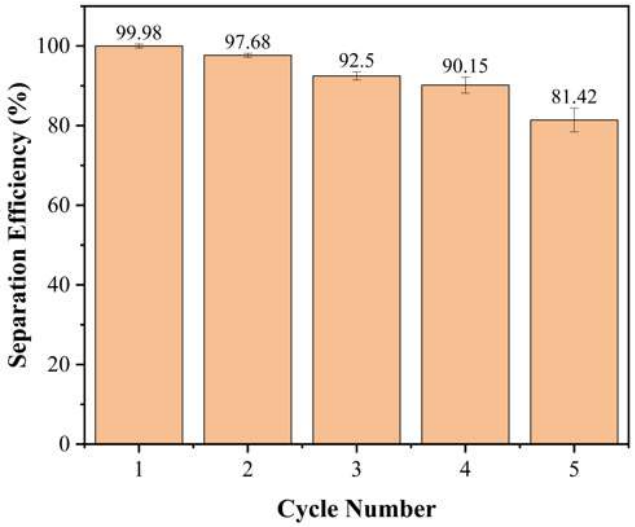


Figure 6.9 Stepwise separation efficiency of a single sPS gel in a five-step consecutive adsorption process. PFOA concentration was 1 μg/L in each step. sPS wet gel dimensions : diameter 1.5 ± 0.1 cm and height 0.85 ± 0.02 cm

and the separation efficiency of each step was calculated as shown in Figure 6.9. The stepwise efficiency gradually dropped and reduced to lower than 90 % after the 4$^{th}$ cycle. In the first 4 cycles,

the separation efficiency was 99.98, 97.98, 92.5 and 90.15 % respectively. This shows the ability of sPS gels to adsorb PFOA repeatedly even when the equilibrium adsorption ability of the gel was reached at the end of each step. In this context, conventional adsorbents would not have this ability unless they have extremely high adsorption capacities, which are a result of either a high pore volume or high specific surface areas, but adsorbents with such features are limited. Furthermore, to obtain the maximum adsorption capacity, generally high initial bulk concentrations of PFOA in water are taken (> 10-100 mg/L) and the maximum adsorption capacity is taken to be the adsorption value where the curve reaches a plateau in its adsorption performance. It should be noted, however, that the adsorption process is initial concentration dependent and hence, starting with a higher concentration would result in a larger number of molecules being adsorbed by the adsorbent. Such a test does not provide a complete picture of what transpires in a real-world situation where the sample is repeatedly subjected to $\leq$ 1 μg/L PFOA concentrations. In this regard, the repeated usability of sPS gel, in this study five times, before its separation efficiency dropped to below 90%, allows the adsorbent to be used for longer times without the need for frequent regenerations.

## 6.5 Conclusion

The data presented in this work established high separation performance of perfluorooctanoic acid from water at environmentally relevant concentrations using meso- and macro-porous syndiotactic polystyrene gels. The sPS gels can deplete the concentration of PFOA in water to levels below the EPA's 2023 health advisory limit of 4 ppt. The adsorption kinetics can easily be increased by increasing the pore volume and pore sizes, achieved in this work by varying the % solid content of the gel. A steep rise in the adsorption behavior for PFOA shown by sPS gels indicated aggregation of PFOA molecules at the solid-liquid interfaces or within the gel pores. In addition, the high surface area provided by the gel facilitated reuse of the gel multiple times with the separation efficiency > 90% unlike several low surface area adsorbents such as ion exchange

resins, β-cyclodextrin or microporous activated carbon. In summary, this chapter demonstrated a novel and promising adsorbent media for effective removal of PFAS molecules from water.

## 6.6 Acknowledgement

This work was partially supported by ACS Petroleum Research Fund under grant number PRF# 59000-ND7, U.S. National Science Foundation under grant number CMMI 1826030, NSF (DMR-2215940), and industrial members of Coalescence Filtration Nanofibers Consortium at The University of Akron

# CHAPTER VII

# SUMMARY AND RECOMMENDATIONS FOR FUTURE WORK

This thesis work dealt with development of porous polymer gel and aerogels for applications in the field of filtration and separation, specifically, towards oil-water emulsion separation and removal of PFAS molecules from water. In addition, an attempt was made in this work to understand the underlying science governing the separation processes which make polymer gels and aerogels better candidates for the above mentioned applications compared to conventionally used materials. A brief summary regarding the important findings of Chapter III, IV, V, and VI are presented below.

Chapter III aimed at developing an understanding of the adsorption behavior and the mechanism of non-ionic PEO-PPO-PEO block copolymer surfactants by three different surface energy porous polymer gels, namely syndiotactic polystyrene, polyimide, and polyurea. It was found that the surfactant adsorption performance was governed by the surface energy of the polymer gels with polystyrene adsorbing the highest amount of surfactant from water followed by polyimide and polyurea. It was inferred that the high hydrophobicity of the syndiotactic polystyrene surface was

responsible for driving the surfactant adsorption behavior. The syndiotactic polystyrene gel adsorbed ~ 2-3 g of surfactant /g of sPS, which is roughly an order of magnitude higher compared to traditional adsorbents. Two distinct surfactant adsorption behaviors were identified; below the CMC of the surfactant, the gels adsorbed as a monolayer onto the polymer strands whereas above the CMC, the surfactants were trapped as micelles within the pores of the polymer gel. The study reported for the first-time the adsorption behavior of the surfactant above its CMC value on a porous polymer substrate. The study also identified that the effective concentration of the surfactant within the gel were several folds the CMC value. The surfactant micelle size was also found to influence its adsorption performance.

Chapter IV focused on an understanding of the relationship between the high surfactant adsorption abilities of the polymer gels and the emulsion separation performance. The hypothesis behind this work was that the adsorption of surfactant molecules from an emulsion would lead to depletion of surfactants from the liquid-liquid, such as oil-water, interfaces. This in turnwould lead to destabilization of the emulsion followed by coalescence of the dispersed phase droplets into larger droplets and the eventual separation of oil and water phases by gravitational forces. It was found that the oil-water emulsion separation directly correlated with the surfactant adsorption abilities of the polymer gels. Syndiotactic polystyrene gels showed the best emulsion separation performance followed by polyimide, polyurea, and silica gels. In addition, it was reported that the syndiotactic polystyrene gels worked best in separating the oil-in-water emulsion stabilized by a short chain Pluronic L35 surfactant compared to a long chain Pluronic F127 surfactant. It was experimentally validated that the dependence of surfactant size/micelle size also influenced its oil-water emulsion separation performance by the sPS gel. It was observed that the dispersed phase oil droplets did not coalesce into larger droplets once the surfactant was adsorbed by the sPS gel, rather the oil droplets were absorbed by the sPS gel after displacement of water within the pores of the

sPS gel. This was attributed to the preference of the sPS surface to be wetted by an oil compared to water. Atomistic simulations of adsorption of the short chain Pluronic L35 and long chain Pluronic F127 surfactant on a sPS surface were performed to understand the structural configuration of the adsorbed surfactant, the surface area they occupy and whether the molecules aggregate into higher order structures at the sPS-water interface. It was found that both the PEO and PPO groups of the surfactant adsorbed on the sPS surface contrary to reports in literature suggesting only the hydrophobic PPO segment adsorbing on a hydrophobic solid surface and the PEO segment dangling in water. The PEO-PPO-PEO surfactant adsorbed on the sPS surface by having the oxygen group facing the water molecules to maximize its hydrogen bonding interactions, which was found to be true for both the short and long chain surfactant. The short chain surfactant aligned completely flat on the sPS surface whereas the PEO-segment of the long chain surfactant formed loops and coil-like structures on the sPS surface. When four chains of the short chain PEO-PPO-PEO surfactant were allowed to adsorb onto the sPS surface, it was observed that they all adsorbed at discrete points on the sPS surface but interacted with each other end-to-end.

Chapter V dealt with the development of an aerogel-glass fiber composite filter media for separation of emulsified water droplets from diesel fuel. This work combined the attributes of a glass fiber media and mesoporous aerogels of two different surface energy in a single filter media for separation of emulsified water droplets from diesel fuel in a continuous flow system. The glass fiber mats were impregnated with porous gels of syndiotactic polystyrene (sPS) and silica produced via dip coating in corresponding sol and sol gel transition. The resultant materials were supercritically dried to obtain aerogel-coated separation media. The pore sizes of the composite media were varied by changing the solid concentration of the polymer sol. The work elucidated the roles of size exclusion, surfactant adsorption, and coalescing filtration on overall separation

behavior and high efficiency. The presence of the high surface energy and hydrophilic silica aerogel led to adsorption of surfactant from the oil-water interfaces and effective attachment/coalescence of water droplets at the filter surface. It was found that the composite filter media was able to separate the water droplets from the emulsion with an efficiency of ~92 % compared to a traditionally used glass fiber media which showed an efficiency of ~ 30 %. The cooperative functioning of several filtration mechanisms in a single filter media led to such high separation efficiencies at low pressure drops resulting in a high quality factor media.

Chapter VI aimed at solving another pressing and emerging water contamination problem caused by per-and poly-fluoroalkyl substances (PFAS) using syndiotactic polystyrene gels. PFAS contamination has caught the attention of everyone due to the extremely toxic and negative effects of these molecules on the human body. In this work, we studied the adsorption performance of sPS gels for perfluorooctanoic acid (long chain PFAS) and perfluorobutanoic acid (short chain PFAS) at environmentally relevant concentrations from water (≤ 1 μg/L). Mass spectrometry was used as the tool to quantify the PFAS levels in water and using this technique we were able to quantify PFOA, PFBA amounts in water upto 0.01 ppt. The sPS gels were found to adsorb the PFOA molecules with extremely high efficiencies (90-99.98%, depending on the initial PFOA concentration) from water. The PFOA adsorption kinetic curve was obtained for times ranging from 10 mins to 24 h and it was found to take about 5 h to reach a separation efficiency of ~92 % and attained an efficiency of 99.98% in 24 h (initial concentration: 1 μg/L) using a sPS gel (0.06 g/mL solid concentration). The adsorption kinetics could be increased by using sPS gels with a more open pore network and larger pore volume obtained by reducing the sPS solid concentration from 0.06 g/mL to 0.02 g/mL. The sPS gel obtained with 0.02 g/mL solids concentration reached a separation efficiency of 99.98% in 5 h of contact time with PFOA-water solution (initial concentration: 1 μg/L). The reusability of the sPS gels without need for frequent generation was also studied in the

work. In addition, the performance of the sPS gel was also benchmarked against commercially used activated carbon and ion-exchange resin samples. The sPS gel was found to have a higher surface area, higher pore volume, and larger pore sizes compared to the two benchmarking materials which eventually led to its superior performance for PFAS adsorption.

There are several aspects of this thesis work which still require further investigation to understand the science behind the separation processes and lead to development of the polymer gels/ aerogels for the mentioned applications. The recommendations for future work are listed below.

1. The adsorption of non-ionic surfactants specifically, PEO-PPO-PEO triblock surfactants was addressed in Chapter III but other types of surfactants such as anionic, cationic, or other non-ionic surfactants should be studied to know the effect of surfactant charge, surfactant chain lengths, presence of different functionalities on the surfactant and the hydrophobic-lipophilic balance (HLB) values of the surfactant on their adsorption performance.
2. Using simulation approach in Chapter IV, the structural configuration of the adsorbed surfactant on a flat sPS surface was studied. However, the structures assumed by the surfactant within the meso- and macropores of the sPS gel still remain unknown. The effect of pore size on the structural organization of surfactant molecules can be studied using simulation approaches. In addition, the structure and adsorption of the surfactant on different surface energy polymers such as polyimide, polyurea, silica used in this work can be performed and a comparison can be made. In addition, the adsorption of a PEO-PPO-PEO surfactant micelle on a sPS surface or within a sPS pore can be studied using simulations. The question of whether a surfactant micelle can break to adsorb at a solid-

liquid interface and what role the mesopore confinement plays on surfactant adsorption still remains unanswered.

3. Chapter V dealt with the development of aerogel-glass fiber media for removal of emulsified water droplets from diesel fuel. Coalescence filtration was reported to be a dominant mechanism for removal of water droplets. It would be really helpful if we could visually observe the droplet attachment, droplet growth, and droplet detachment occurring at the filter media surface under continuous flow conditions. Since the droplets are approximately 10-50 μm in diameter, a high speed camera should be used along with an appropriate lens to look at such droplets. Further, glycerol monooleate was used as a surfactant to stabilize the emulsion in this work, but crude oil contains a mixture of several different surface active agents such as asphaltenes, naphthalenic acids, resins, etc, which have different functional groups and different interfacial tension reducing abilities. Therefore, using different model surfactants to stabilize the emulsion and observing the performance of the filter media would be useful to get a holistic performance of the fabricated filter.
4. Chapter VI aimed at removal of PFOA and PFBA molecules from water using meso- and macro-porous sPS gels. The experiments mentioned in this work were batch experiments with sPS gel monoliths being dipped in a 10 mL solution of the PFOA or PFBA in water for a desired time. However, the adsorbent materials are used in a packed bed column in a continuous flow setup for removal of the PFAS molecules. Therefore, we need to build a polymer aerogel loaded packed bed column and evaluate its performance for PFAS separation. The factors such as empty bed contact time of the adsorbent, bed volumes the adsorbent can treat before reaching its breakthrough, and the effect of adsorbent particle size on separation performance need to be obtained. Different polymer gel systems such as polyurea, polyurethane, polyimide, chitosan, cellulose with different surface energies and

different functional groups can be studied for their PFAS separation performance. PFAS is a large group of molecules, and all these molecules have different chain lengths, different functional groups and therefore would adsorb at a solid-liquid interface distinctly. We have narrowed down 5 additional PFAS molecules from a list of 76 PFAS chemicals released by the US EPA which need to be evaluated for their separation by the meso-macroporous polymer gels based on their relevance in industry and their presence in contaminated water sources. They are perfluorohexanesulphonic acid (PFHxS), perfluorononanoic acid (PFNA), perfluoro-3,6-dioxaheptanoic acid, 1H,1H,2H,2H-nonafluoro-1-hexanol and hexafluoropropylene dimer acid (Genx chemical). In addition, the performance of the adsorbent for removal of a mixture of PFAS molecules from liquids need to be evaluated. Further, the effect of the presence of other background water contaminants such as natural organic matter (NOM), salts on PFAS adsorption performance needs to be obtained.

5. Another fundamental question regarding PFAS adsorption that can be explored is the structural organization or self-assembly of adsorbed PFAS molecules within the pores of the polymer gels.

# REFERENCES

(1) Kistler, S. S. Coherent Expanded Aerogels and Jellies. *Nature* **1931**, *127* (3211), 741–741. https://doi.org/10.1038/127741a0.

(2) Teo, N.; Jana, S. C. Solvent Effects on Tuning Pore Structures in Polyimide Aerogels. *Langmuir* **2018**, *34* (29), 8581–8590. https://doi.org/10.1021/acs.langmuir.8b01513.

(3) Meador, M. A. B.; Malow, E. J.; Silva, R.; Wright, S.; Quade, D.; Vivod, S. L.; Guo, H.; Guo, J.; Cakmak, M. Mechanically Strong, Flexible Polyimide Aerogels Cross-Linked with Aromatic Triamine. *ACS Appl. Mater. Interfaces* **2012**, *4* (2), 536–544. https://doi.org/10.1021/am2014635.

(4) Tabata, M.; Adachi, I.; Ishii, Y.; Kawai, H.; Sumiyoshi, T.; Yokogawa, H. Development of Transparent Silica Aerogel over a Wide Range of Densities. *Nuclear Instruments and Methods in Physics Research Section A: Accelerators, Spectrometers, Detectors and Associated Equipment* **2010**, *623* (1), 339–341. https://doi.org/10.1016/j.nima.2010.02.241.

(5) Lee, J. K.; Gould, G. L.; Rhine, W. Polyurea Based Aerogel for a High Performance Thermal Insulation Material. *J Sol-Gel Sci Technol* **2009**, *49* (2), 209–220. https://doi.org/10.1007/s10971-008-1861-6.

(6) DeRossi, D.; Kajiwara, K.; Osada, Y.; Yamauchi, A. *Polymer Gels: Fundamentals and Biomedical Applications*; Springer Science & Business Media, 2012

(7) Teichner, S. J.; Nicolaon, G. A. Method of Preparing Inorganic Aerogels. US3672833A, June 27, 1972. https://patents.google.com/patent/US3672833A/en (accessed 2023-12-07).

(8) Tewari, P. H.; Hunt, A. J.; Lofftus, K. D. Ambient-Temperature Supercritical Drying of Transparent Silica Aerogels. *Materials Letters* **1985**, *3* (9), 363–367. https://doi.org/10.1016/0167-577X(85)90077-1. 178

(9) Bourdinaud, M.; Cheze, J. B.; Thevenin, J. C. Use of Silica Aerogel for Cherenkov Radiation Counter. *Nuclear Instruments and Methods* **1976**, *136* (1), 99–103. https://doi.org/10.1016/0029-554X(76)90401-8.

(10) Cohen, E. Thermal Properties of Advanced Aerogel Insulation. Thesis, Massachusetts Institute of Technology, 2011. https://dspace.mit.edu/handle/1721.1/67795 (accessed 2022-07-07).

(11) Kistler, S. S.; Caldwell, A. G. Thermal Conductivity of Silica Aërogel. *Ind. Eng. Chem.* **1934**, *26* (6), 658–662. https://doi.org/10.1021/ie50294a016.

(12) Cho, C.-C.; Smith, D. M.; Anderson, J. Low Dielectric-Constant Insulators for Electronics Applications. *Materials Chemistry and Physics* **1995**, *42* (2), 91–95. https://doi.org/10.1016/0254-0584(95)01569-8.

(13) Mary Joseph, A.; Nagendra, B.; Shaiju, P.; P. Surendran, K.; Bhoje Gowd, E. Aerogels of Hierarchically Porous Syndiotactic Polystyrene with a Dielectric Constant near to Air. *Journal of Materials Chemistry C* **2018**, *6* (2), 360–368. https://doi.org/10.1039/C7TC05102F.

(14) Yang, H.-S.; Choi, S.-Y.; Hyun, S.-H.; Park, H.-H.; Hong, J.-K. Ambient-Dried Low Dielectric SiO2 Aerogel Thin Film. *Journal of Non-Crystalline Solids* **1997**, *221* (2), 151–156. https://doi.org/10.1016/S0022-3093(97)00335-9.

(15) Baumann, T. F.; Worsley, M. A.; Han, T. Y.-J.; Satcher, J. H. High Surface Area Carbon Aerogel Monoliths with Hierarchical Porosity. *Journal of Non-Crystalline Solids* **2008**, *354* (29), 3513–3515. https://doi.org/10.1016/j.jnoncrysol.2008.03.006.

(16) Hasan, M. A.; Sangashetty, R.; Esther, A. C. M.; Patil, S. B.; Sherikar, B. N.; Dey, A. Prospect of Thermal Insulation by Silica Aerogel: A Brief Review. *J. Inst. Eng. India Ser. D* **2017**, *98* (2), 297–304. https://doi.org/10.1007/s40033-017-0136-1.

(17) Rotter, H.; Landau, M. V.; Carrera, M.; Goldfarb, D.; Herskowitz, M. High Surface Area Chromia Aerogel Efficient Catalyst and Catalyst Support for Ethylacetate Combustion. 179, *Applied Catalysis B: Environmental* **2004**, *47* (2), 111–126. https://doi.org/10.1016/j.apcatb.2003.08.006.

(18) Aghababaei Tafreshi, O.; Ghaffari-Mosanenzadeh, S.; Karamikamkar, S.; Saadatnia, Z.; Kiddell, S.; B. Park, C.; E. Naguib, H. Novel, Flexible, and Transparent Thin Film Polyimide Aerogels with Enhanced Thermal Insulation and High Service Temperature. *Journal of Materials Chemistry C* **2022**, *10* (13), 5088–5108. https://doi.org/10.1039/D1TC06122D.

(19) Ghaffari Mosanenzadeh, S.; Alshrah, M.; Saadatnia, Z.; Park, C. B.; Naguib, H. E. Double Dianhydride Backbone Polyimide Aerogels with Enhanced Thermal Insulation for High-Temperature Applications. *Macromolecular Materials and Engineering* **2020**, *305* (4), 1900777. https://doi.org/10.1002/mame.201900777.

(20) Tsou, P. Silica Aerogel Captures Cosmic Dust Intact. *Journal of Non-Crystalline Solids* **1995**, *186*, 415–427. https://doi.org/10.1016/0022-3093(95)00065-8.

(21) García-González, C. A.; Sosnik, A.; Kalmár, J.; De Marco, I.; Erkey, C.; Concheiro, A.; Alvarez-Lorenzo, C. Aerogels in Drug Delivery: From Design to Application. *Journal of Controlled Release* **2021**, *332*, 40–63. https://doi.org/10.1016/j.jconrel.2021.02.012.

(22) García-González, C. A.; Alnaief, M.; Smirnova, I. Polysaccharide-Based Aerogels - Promising Biodegradable Carriers for Drug Delivery Systems- Review Article. *Carbohydrate Polymers* **2011**, *86*, 1425–1438. https://doi.org/10.1016/j.carbpol.2011.06.066.

(23) Mao, J.; Iocozzia, J.; Huang, J.; Meng, K.; Lai, Y.; Lin, Z. Graphene Aerogels for Efficient Energy Storage and Conversion. *Energy Environ. Sci.* **2018**, *11* (4), 772–799. https://doi.org/10.1039/C7EE03031B.

(24) *Aerogel: The world's lightest solid*. New Atlas. https://newatlas.com/aerogel-the-worlds-lightest-solid/1740/ (accessed 2023-12-07). 180

(25) *Aerogel.org » The 2000's: New Possibilities and Commercialization*. https://www.aerogel.org/?p=829 (accessed 2023-12-07).

(26) Teo, N.; Joo, P.; Amis, E. J.; Jana, S. C. Development of Intricate Aerogel Articles Using Fused Filament Fabrication. 8.

(27) Li, Z.; Gong, L.; Cheng, X.; He, S.; Li, C.; Zhang, H. Flexible Silica Aerogel Composites Strengthened with Aramid Fibers and Their Thermal Behavior. *Materials & Design* **2016**, *99*, 349–355. https://doi.org/10.1016/j.matdes.2016.03.063.

(28) Joo, P.; Yao, Y.; Teo, N.; Jana, S. C. Modular Aerogel Brick Fabrication via 3D-Printed Molds. *Additive Manufacturing* **2021**, *46*, 102059. https://doi.org/10.1016/j.addma.2021.102059.

(29) Ishihara, N.; Seimiya, T.; Kuramoto, M.; Uoi, M. Crystalline Syndiotactic Polystyrene. *Macromolecules* **1986**, *19* (9), 2464–2465. https://doi.org/10.1021/ma00163a027.

(30) Ishihara, N.; Kuramoto, M.; Uoi, M. Stereospecific Polymerization of Styrene Giving the Syndiotactic Polymer. *Macromolecules* **1988**, *21* (12), 3356–3360. https://doi.org/10.1021/ma00190a003.

(31) Schellenberg, J. *Syndiotactic Polystyrene: Synthesis, Characterization, Processing, and Applications*; John Wiley & Sons, 2009.

(32) Park, J. Y. S. A. 109-1104. Syndiotactic Polystyrene Copolymer Resin Composition Having Macromonomer for Improving Impact Strength. EP1118639A2, July 25, 2001. https://patents.google.com/patent/EP1118639A2/en (accessed 2023-12-07).

(33) Albunia, A. R.; D'Aniello, C.; Guerra, G. Three Different Co-Crystalline Phases of Syndiotactic Polystyrene with a Nitroxide Radical. *CrystEngComm* **2010**, *12* (11), 3942–3949. https://doi.org/10.1039/C0CE00128G.

(34) Guerra, G.; Vitagliano, V. M.; De Rosa, C.; Petraccone, V.; Corradini, P. Polymorphism in Melt Crystallized Syndiotactic Polystyrene Samples. *Macromolecules* **1990**, *23* (5), 1539–1544. https://doi.org/10.1021/ma00207a050. 181

(35) Sobota, P. A Commentary on "Solvent-induced Polymorphism in Syndiotactic Polystyrene" by A. Immirzi, F. de Candia, P. Iannelli, A. Zambelli, V. Vittoria (Makromol. Chem., Rapid Commun. 1988, 9, 761–764). *Macromolecular Rapid Communications* **2005**, *26* (20), 1589.

(36) Chatani, Y.; Shimane, Y.; Inagaki, T.; Ijitsu, T.; Yukinari, T.; Shikuma, H. Structural Study on Syndiotactic Polystyrene: 2. Crystal Structure of Molecular Compound with Toluene. *Polymer* **1993**, *34* (8), 1620–1624. https://doi.org/10.1016/0032-3861(93)90318-5.

(37) Tarallo, O.; Petraccone, V. On the Crystal Structure of the Clathrate Forms of Syndiotactic Polystyrene Containing Carbon Disulfide and Iodine. *Macromolecular Chemistry and Physics* **2004**, *205* (10), 1351–1360. https://doi.org/10.1002/macp.200400118.

(38) Chatani, Y.; Inagaki, T.; Shimane, Y.; Shikuma, H. Structural Study on Syndiotactic Polystyrene: 4. Formation and Crystal Structure of Molecular Compound with Iodine. *Polymer* **1993**, *34* (23), 4841–4845. https://doi.org/10.1016/0032-3861(93)90007-W.

(39) Tarallo, O.; Petraccone, V. Syndiotactic Polystyrene Containing Ortho-Dichlorobenzene: Crystal Structure of the Clathrate Form. *Macromolecular Chemistry and Physics* **2005**, *206* (6), 672–679. https://doi.org/10.1002/macp.200400387.

(40) Daniel, C.; Guerra, G.; Musto, P. Clathrate Phase in Syndiotactic Polystyrene Gels. *Macromolecules* **2002**, *35* (6), 2243–2251. https://doi.org/10.1021/ma011531q.

(41) Daniel, C.; Menelle, A.; Brulet, A.; Guenet, J.-M. Thermoreversible Gelation of Syndiotactic Polystyrene in Toluene and Chloroform. *Polymer* **1997**, *38* (16), 4193–4199. https://doi.org/10.1016/S0032-3861(96)01005-1.

(42) Daniel, Ch.; Deluca, M. D.; Guenet, J.-M.; Brûlet, A.; Menelle, A. Thermoreversible Gelation of Syndiotactic Polystyrene in Benzene. *Polymer* **1996**, *37* (7), 1273–1280. https://doi.org/10.1016/0032-3861(96)80854-8. 182

(43) Daniel, C.; Avallone, A.; Guerra, G. Syndiotactic Polystyrene Physical Gels: Guest Influence on Structural Order in Molecular Complex Domains and Gel Transparency. *Macromolecules* **2006**, *39* (22), 7578–7582. https://doi.org/10.1021/ma061124k.

(44) Kobayashi, M.; Yoshioka, T.; Imai, M.; Itoh, Y. Structural Ordering on Physical Gelation of Syndiotactic Polystyrene Dispersed in Chloroform Studied by Time-Resolved Measurements of Small Angle Neutron Scattering (SANS) and Infrared Spectroscopy. *Macromolecules®* **1995**, *28* (22), 7376–7385. https://doi.org/10.1021/ma00126a015.

(45) Wang, X.; Jana, S. C. Synergistic Hybrid Organic–Inorganic Aerogels. *ACS Appl. Mater. Interfaces* **2013**, *5* (13), 6423–6429. https://doi.org/10.1021/am401717s.

(46) Wang, X.; Jana, S. C. Tailoring of Morphology and Surface Properties of Syndiotactic Polystyrene Aerogels. *Langmuir* **2013**, *29* (18), 5589–5598. https://doi.org/10.1021/la400492m.

(47) Wang, X.; Zhang, H.; Jana, S. Sulfonated Syndiotactic Polystyrene Aerogels: Properties and Applications. *J. Mater. Chem. A* **2013**, *1*. https://doi.org/10.1039/C3TA13099A.

(48) Venditto, V.; Pellegrino, M.; Califano, R.; Guerra, G.; Daniel, C.; Ambrosio, L.; Borriello, A. Monolithic Polymeric Aerogels with VOCs Sorbent Nanoporous Crystalline and Water Sorbent Amorphous Phases. *ACS Appl. Mater. Interfaces* **2015**, *7* (2), 1318–1326. https://doi.org/10.1021/am507116e.

(49) Kim, S. J.; Chase, G.; Jana, S. C. Polymer Aerogels for Efficient Removal of Airborne Nanoparticles. *Separation and Purification Technology* **2015**, *156*, 803–808. https://doi.org/10.1016/j.seppur.2015.11.005.

(50) Kulkarni, A.; Gotad, P.; Joo, P.; Agrawal, A.; Chase, G. C.; Jana, S. C. Water Separation from Diesel Fuel Using High Surface Area 3D-Printed Aerogel Constructs. *Separation and Purification Technology* **2024**, *328*, 125065. https://doi.org/10.1016/j.seppur.2023.125065. 183

(51) Mancuso, A.; Sacco, O.; Venditto, V.; Navarra, W.; Antico, P.; Daniel, C.; Vaiano, V. Selective Absorption of Aromatic Compounds by Syndiotactic Polystyrene Aerogels. *Macromolecular Symposia* **2023**, *408* (1), 2200062. https://doi.org/10.1002/masy.202200062.

(52) Mensitieri, G.; Vincenzo, V.; Guerra, G. Polymeric Sensing Films Absorbing Organic Guests into a Nanoporous Host Crystalline Phase. *Sensors and Actuators B: Chemical* **2003**, *92*, 255–261. https://doi.org/10.1016/S0925-4005(03)00273-9.

(53) Meador, M. A. Recent Advances in the Development of Processable High-Temperature Polymers. *Annual Review of Materials Science* **1998**, *28* (1), 599–630. https://doi.org/10.1146/annurev.matsci.28.1.599.

(54) Maier, G. Low Dielectric Constant Polymers for Microelectronics. *Progress in Polymer Science* **2001**, *26* (1), 3–65. https://doi.org/10.1016/S0079-6700(00)00043-5.

(55) Rhine, W.; Wang, J.; Begag, R. Polyimide Aerogels, Carbon Aerogels, and Metal Carbide Aerogels and Methods of Making Same. US7074880B2, July 11, 2006. https://patents.google.com/patent/US7074880B2/en (accessed 2021-06-28).

(56) Kawagishi, K.; Saito, H.; Furukawa, H.; Horie, K. Superior Nanoporous Polyimides via Supercritical CO2 Drying of Jungle-Gym-Type Polyimide Gels. *Macromolecular Rapid Communications* **2007**, *28* (1), 96–100. https://doi.org/10.1002/marc.200600587.

(57) Ghosh, M. K.; Mittal, K. L. *Polyimides: Fundamentals and Applications*; Plastics engineering (Marcel Dekker, Inc.); Marcel Dekker: New York, 1996.

(58) Guo, H.; Meador, M. A. B.; McCorkle, L.; Quade, D. J.; Guo, J.; Hamilton, B.; Cakmak, M.; Sprowl, G. Polyimide Aerogels Cross-Linked through Amine Functionalized Polyoligomeric Silsesquioxane. *ACS Appl Mater Interfaces* **2011**, *3* (2), 546–552. https://doi.org/10.1021/am101123h.

(59) Guo, H.; Meador, M. A. B.; McCorkle, L.; Quade, D. J.; Guo, J.; Hamilton, B.; Cakmak, M. Tailoring Properties of Cross-Linked Polyimide Aerogels for Better Moisture 184 Resistance, Flexibility, and Strength. *ACS Appl Mater Interfaces* **2012**, *4* (10), 5422–5429. https://doi.org/10.1021/am301347a.

(60) Guo, H.; Meador, M. A. B.; Cashman, J. L.; Tresp, D.; Dosa, B.; Scheiman, D. A.; McCorkle, L. S. Flexible Polyimide Aerogels with Dodecane Links in the Backbone Structure. *ACS Appl Mater Interfaces* **2020**, *12* (29), 33288–33296. https://doi.org/10.1021/acsami.0c09321.

(61) Shen, D.; Liu, J.; Yang, H.; Yang, S. Intrinsically Highly Hydrophobic Semi-Alicyclic Fluorinated Polyimide Aerogel with Ultralow Dielectric Constants. *Chem. Lett.* **2013**, *42* (10), 1230–1232. https://doi.org/10.1246/cl.130623.

(62) Meador, M. A. B.; Alemán, C. R.; Hanson, K.; Ramirez, N.; Vivod, S. L.; Wilmoth, N.; McCorkle, L. Polyimide Aerogels with Amide Cross-Links: A Low Cost Alternative for Mechanically Strong Polymer Aerogels. *ACS Appl. Mater. Interfaces* **2015**, *7* (2), 1240–1249. https://doi.org/10.1021/am507268c.

(63) Teo, N.; Jin, C.; Kulkarni, A.; Jana, S. C. Continuous Fabrication of Core-Shell Aerogel Microparticles Using Microfluidic Flows. *Journal of Colloid and Interface Science* **2020**, *561*, 772–781. https://doi.org/10.1016/j.jcis.2019.11.053.

(64) Jin, C.; Kulkarni, A.; Teo, N.; Jana, S. C. Fabrication of Pill-Shaped Polyimide Aerogel Particles Using Microfluidic Flows. *Ind. Eng. Chem. Res.* **2021**, *60* (1), 361–370. https://doi.org/10.1021/acs.iecr.0c05424.

(65) Agrawal, A.; Farrell, E.; Jana, S. C. Upcycling of Waste Fabrics into High-Efficiency Air Filters Using Flexible Polyimide Aerogel Coatings. *ACS Appl. Polym. Mater.* **2023**, *5* (11), 9317–9328. https://doi.org/10.1021/acsapm.3c01822.

(66) Farrell, E.; Jana, S. C. An Investigation on Morphology of Emulsion-Templated Polyimide Aerogel Foam Sheets. *ACS Appl. Polym. Mater.* **2023**, *5* (11), 9116–9127. https://doi.org/10.1021/acsapm.3c01623. 185

(67) Teo, N.; Gu, Z.; Jana, S. C. Polyimide-Based Aerogel Foams, via Emulsion-Templating. *Polymer* **2018**, *157*, 95–102. https://doi.org/10.1016/j.polymer.2018.10.030.

(68) Meador, M. A. B.; Wright, S.; Sandberg, A.; Nguyen, B. N.; Van Keuls, F. W.; Mueller, C. H.; Rodríguez-Solís, R.; Miranda, F. A. Low Dielectric Polyimide Aerogels As Substrates for Lightweight Patch Antennas. *ACS Appl. Mater. Interfaces* **2012**, *4* (11), 6346–6353. https://doi.org/10.1021/am301985s.

(69) Maleki, H.; Durães, L.; Portugal, A. An Overview on Silica Aerogels Synthesis and Different Mechanical Reinforcing Strategies. *Journal of Non-Crystalline Solids* **2014**, *385*, 55–74. https://doi.org/10.1016/j.jnoncrysol.2013.10.017.

(70) Soleimani Dorcheh, A.; Abbasi, M. H. Silica Aerogel; Synthesis, Properties and Characterization. *Journal of Materials Processing Technology* **2008**, *199* (1–3), 10–26. https://doi.org/10.1016/j.jmatprotec.2007.10.060.

(71) Brinker, C. J. Hydrolysis and Condensation of Silicates: Effects on Structure. *Journal of Non-Crystalline Solids* **1988**, *100* (1), 31–50. https://doi.org/10.1016/0022-3093(88)90005-1.

(72) Yang, X.; Sun, Y.; Shi, D.; Liu, J. Experimental Investigation on Mechanical Properties of a Fiber-Reinforced Silica Aerogel Composite. *Materials Science and Engineering: A* **2011**, *528* (13), 4830–4836. https://doi.org/10.1016/j.msea.2011.03.013.

(73) Duan, Y.; Jana, S. C.; Lama, B.; Espe, M. P. Reinforcement of Silica Aerogels Using Silane-End-Capped Polyurethanes. *Langmuir* **2013**, *29* (20), 6156–6165. https://doi.org/10.1021/la4007394.

(74) Zhang, G.; Dass, A.; Rawashdeh, A.-M. M.; Thomas, J.; Counsil, J. A.; Sotiriou-Leventis, C.; Fabrizio, E. F.; Ilhan, F.; Vassilaras, P.; Scheiman, D. A.; McCorkle, L.; Palczer, A.; Johnston, J. C.; Meador, M. A.; Leventis, N. Isocyanate-Crosslinked Silica Aerogel Monoliths: Preparation and Characterization. *Journal of Non-Crystalline Solids* **2004**, *350*, 152–164. https://doi.org/10.1016/j.jnoncrysol.2004.06.041. 186

(75) Meador, M. A. B.; Fabrizio, E. F.; Ilhan, F.; Dass, A.; Zhang, G.; Vassilaras, P.; Johnston, J. C.; Leventis, N. Cross-Linking Amine-Modified Silica Aerogels with Epoxies: Mechanically Strong Lightweight Porous Materials. *Chem. Mater.* **2005**, *17* (5), 1085–1098. https://doi.org/10.1021/cm048063u.

(76) Wang, J.; Kuhn, J.; Lu, X. Monolithic Silica Aerogel Insulation Doped with TiO2 Powder and Ceramic Fibers. *Journal of Non-Crystalline Solids* **1995**, *186*, 296–300. https://doi.org/10.1016/0022-3093(95)00068-2.

(77) Li, Z.; Gong, L.; Cheng, X.; He, S.; Li, C.; Zhang, H. Flexible Silica Aerogel Composites Strengthened with Aramid Fibers and Their Thermal Behavior. *Materials & Design* **2016**, *99*, 349–355. https://doi.org/10.1016/j.matdes.2016.03.063.

(78) Chakraborty, S.; Pisal, A. A.; Kothari, V. K.; Venkateswara Rao, A. Synthesis and Characterization of Fibre Reinforced Silica Aerogel Blankets for Thermal Protection. *Advances in Materials Science and Engineering* **2016**, *2016*, 1–8. https://doi.org/10.1155/2016/2495623.

(79) Wu, H.; Chen, Y.; Chen, Q.; Ding, Y.; Zhou, X.; Gao, H. Synthesis of Flexible Aerogel Composites Reinforced with Electrospun Nanofibers and Microparticles for Thermal Insulation. *Journal of Nanomaterials* **2013**, *2013*, e375093. https://doi.org/10.1155/2013/375093.

(80) Zhang, Z.; Shen, J.; Ni, X.; Wu, G.; Zhou, B.; Yang, M.; Gu, X.; Qian, M.; Wu, Y. Hydrophobic Silica Aerogels Strengthened with Nonwoven Fibers. *Journal of Macromolecular Science, Part A* **2006**, *43* (11), 1663–1670. https://doi.org/10.1080/10601320600934792.

(81) Yuan, B.; Ding, S.; Wang, D.; Wang, G.; Li, H. Heat Insulation Properties of Silica Aerogel/Glass Fiber Composites Fabricated by Press Forming. *Materials Letters* **2012**, *75*, 204–206. https://doi.org/10.1016/j.matlet.2012.01.114. 187

(82) Kim, S. J.; Raut, P.; Jana, S. C.; Chase, G. Electrostatically Active Polymer Hybrid Aerogels for Airborne Nanoparticle Filtration. *ACS Appl. Mater. Interfaces* **2017**, *9* (7), 6401–6410. https://doi.org/10.1021/acsami.6b14784.

(83) Biesmans, G.; Randall, D.; Francais, E.; Perrut, M. Polyurethane-Based Organic Aerogels' Thermal Performance. *Journal of Non-Crystalline Solids* **1998**, *225*, 36–40. https://doi.org/10.1016/S0022-3093(98)00103-3.

(84) Leventis, N.; Sotiriou-Leventis, C.; Chandrasekaran, N.; Mulik, S.; Larimore, Z. J.; Lu, H.; Churu, G.; Mang, J. T. Multifunctional Polyurea Aerogels from Isocyanates and Water. A Structure−Property Case Study. *Chem. Mater.* **2010**, *22* (24), 6692–6710. https://doi.org/10.1021/cm102891d.

(85) Shinko, A.; Jana, S. C.; Meador, M. A. Crosslinked Polyurea Aerogels with Controlled Porosity. *RSC Adv.* **2015**, *5* (127), 105329–105338. https://doi.org/10.1039/C5RA20788F.

(86) Shinko, A.; Jana, S. C.; Meador, M. A. Crosslinked Polyurea-Co-Polyurethane Aerogels with Hierarchical Structures and Low Stiffness. *Journal of Non-Crystalline Solids* **2018**, *487*, 19–27. https://doi.org/10.1016/j.jnoncrysol.2018.02.020.

(87) Jernelöv, A. The Threats from Oil Spills: Now, Then, and in the Future. *AMBIO* **2010**, *39* (5), 353–366. https://doi.org/10.1007/s13280-010-0085-5.

(88) Singh, H.; Bhardwaj, N.; Arya, S. K.; Khatri, M. Environmental Impacts of Oil Spills and Their Remediation by Magnetic Nanomaterials. *Environmental Nanotechnology, Monitoring & Management* **2020**, *14*, 100305. https://doi.org/10.1016/j.enmm.2020.100305.

(89) Kajitvichyanukul, P.; Hung, Y.-T.; Wang, L. K. Oil Water Separation. In *Advanced Physicochemical Treatment Processes*; Wang, L. K., Hung, Y.-T., Shammas, N. K., Eds.; Handbook of Environmental Engineering; Humana Press: Totowa, NJ, 2006; pp 521–548. https://doi.org/10.1007/978-1-59745-029-4_16. 188

(90) Mingyuan, L.; Christy, A. A.; Sjøblom, J. Water-in-Crude Oil Emulsions from the Norwegian Continental Shelf Part-VI — Diffuse Reflectance Fourier Transform Infrared Characterization of Interfacially Active Fractions from North Sea Crude Oil. In *Emulsions — A Fundamental and Practical Approach*; Sjöblom, J., Ed.; NATO ASI Series; Springer Netherlands: Dordrecht, 1992; pp 157–172. https://doi.org/10.1007/978-94-011-2460-7_11.

(91) Wilfong, D.; Dallas, A.; Yang, C.; Johnson, P.; Viswanathan, K.; Madsen, M.; Tucker, B.; Hacker, J. Emerging Challenges of Fuel Filtration. *Filtration* **2010**, *10*, 107–117.

(92) Stone, W.; Bessee, G.; Stanfel, C. Diesel Fuel/Water Separation Test Methods—Where We Are and Where We Are Going. *SAE International Journal of Fuels and Lubricants* **2009**, *2* (1), 317–323.

(93) Narayan, S.; Moravec, D. B.; Hauser, B. G.; Dallas, A. J.; Dutcher, C. S. Removing Water from Diesel Fuel: Understanding the Impact of Droplet Size on Dynamic Interfacial Tension of Water-in-Fuel Emulsions. *Energy Fuels* **2018**, *32* (7), 7326–7337. https://doi.org/10.1021/acs.energyfuels.8b00502.

(94) Tadros, T. F. Emulsions: Formation, Stability, Industrial Applications. In *Emulsions*; De Gruyter, 2016. https://doi.org/10.1515/9783110452242.

(95) Salager, J.-L. Phase Transformation and Emulsion Inversion on the Basis of Catastrophe Theory.

(96) Grahame, D. C. The Electrical Double Layer and the Theory of Electrocapillarity. *Chem. Rev.* **1947**, *41* (3), 441–501. https://doi.org/10.1021/cr60130a002.

(97) Wang, D.; Yang, D.; Huang, C.; Huang, Y.; Yang, D.; Zhang, H.; Liu, Q.; Tang, T.; Gamal El-Din, M.; Kemppi, T.; Perdicakis, B.; Zeng, H. Stabilization Mechanism and Chemical Demulsification of Water-in-Oil and Oil-in-Water Emulsions in Petroleum Industry: A Review. *Fuel* **2021**, *286*, 119390. https://doi.org/10.1016/j.fuel.2020.119390. 189

(98) Bai, L.; Huan, S.; Rojas, O. J.; McClements, D. J. Recent Innovations in Emulsion Science and Technology for Food Applications. *J. Agric. Food Chem.* **2021**, *69* (32), 8944–8963. https://doi.org/10.1021/acs.jafc.1c01877.

(99) Marti-Mestres, G.; Nielloud, F. Emulsions in Health Care Applications—An Overview. *Journal of Dispersion Science and Technology - J DISPER SCI TECH* **2002**, *23*, 419–439. https://doi.org/10.1080/01932690208984214.

(100) Chappat, M. Some Applications of Emulsions. *Colloids and Surfaces A: Physicochemical and Engineering Aspects* **1994**, *91*, 57–77. https://doi.org/10.1016/0927-7757(94)02976-8.

(101) Rosen, M. J.; Kunjappu, J. T. *Surfactants and Interfacial Phenomena*; John Wiley & Sons, 2012.

(102) *Pendant drop method for surface tension measurements*. https://www.biolinscientific.com/blog/pendant-drop-method-for-surface-tension-measurements (accessed 2023-12-15).

(103) Yu, Y.; Shi, X.; Liu, L.; Yao, J. Highly Compressible and Durable Superhydrophobic Cellulose Aerogels for Oil/Water Emulsion Separation with High Flux. *J Mater Sci* **2021**, *56* (3), 2763–2776. https://doi.org/10.1007/s10853-020-05441-5.

(104) Zhou, S.; You, T.; Zhang, X.; Xu, F. Superhydrophobic Cellulose Nanofiber-Assembled Aerogels for Highly Efficient Water-in-Oil Emulsions Separation. *ACS Appl. Nano Mater.* **2018**, *1* (5), 2095–2103. https://doi.org/10.1021/acsanm.8b00079.

(105) Li, Y.; Zhang, G.; Gao, A.; Cui, J.; Zhao, S.; Yan, Y. Robust Graphene/Poly(Vinyl Alcohol) Janus Aerogels with a Hierarchical Architecture for Highly Efficient Switchable Separation of Oil/Water Emulsions. *ACS Appl. Mater. Interfaces* **2019**, *11* (40), 36638–36648. https://doi.org/10.1021/acsami.9b11277.

(106) Jiang, G.; Ge, J.; Jia, Y.; Ye, X.; Jin, L.; Zhang, J.; Zhao, Z.; Yang, G.; Xue, L.; Xie, S. Coaxial Electrospun Nanofibrous Aerogels for Effective Removal of Oils and Separation 190 of Water-in-Oil Emulsions. *Separation and Purification Technology* **2021**, *270*, 118740. https://doi.org/10.1016/j.seppur.2021.118740.

(107) Shen, Y.; Li, D.; Wang, L.; Zhou, Y.; Liu, F.; Wu, H.; Deng, B.; Liu, Q. Superelastic Polyimide Nanofiber-Based Aerogels Modified with Silicone Nanofilaments for Ultrafast Oil/Water Separation. *ACS Appl. Mater. Interfaces* **2021**, *13* (17), 20489–20500. https://doi.org/10.1021/acsami.1c01136.

(108) Kim, J. F.; Kim, J. H.; Lee, Y. M.; Drioli, E. Thermally Induced Phase Separation and Electrospinning Methods for Emerging Membrane Applications: A Review. *AIChE Journal* **2016**, *62* (2), 461–490. https://doi.org/10.1002/aic.15076.

(109) Venault, A.; Chang, Y.; Wang, D.-M.; Bouyer, D. A Review on Polymeric Membranes and Hydrogels Prepared by Vapor-Induced Phase Separation Process. *Polymer Reviews* **2013**, *53* (4), 568–626. https://doi.org/10.1080/15583724.2013.828750.

(110) Ismail, N.; Venault, A.; Mikkola, J.-P.; Bouyer, D.; Drioli, E.; Tavajohi Hassan Kiadeh, N. Investigating the Potential of Membranes Formed by the Vapor Induced Phase Separation Process. *Journal of Membrane Science* **2020**, *597*, 117601. https://doi.org/10.1016/j.memsci.2019.117601.

(111) Guillen, G. R.; Pan, Y.; Li, M.; Hoek, E. M. V. Preparation and Characterization of Membranes Formed by Nonsolvent Induced Phase Separation: A Review. *Ind. Eng. Chem. Res.* **2011**, *50* (7), 3798–3817. https://doi.org/10.1021/ie101928r.

(112) Dmitrieva, E. S.; Anokhina, T. S.; Novitsky, E. G.; Volkov, V. V.; Borisov, I. L.; Volkov, A. V. Polymeric Membranes for Oil-Water Separation: A Review. *Polymers* **2022**, *14* (5), 980. https://doi.org/10.3390/polym14050980.

(113) Guillotin, M.; Lemoyne, C.; Noel, C.; Monnerie, L. Physicochemical Processes Occurring during the Formation of Cellulose Diacetate Membranes. Research of Criteria for Optimizing Membrane Performance. IV. Cellulose Diacetate-Acetone-Organic Additive 191 Casting Solutions. *Desalination* **1977**, *21* (2), 165–181. https://doi.org/10.1016/S0011-9164(00)80314-8.

(114) Wang, S.; Li, Y.; Fei, X.; Sun, M.; Zhang, C.; Li, Y.; Yang, Q.; Hong, X. Preparation of a Durable Superhydrophobic Membrane by Electrospinning Poly (Vinylidene Fluoride) (PVDF) Mixed with Epoxy–Siloxane Modified SiO2 Nanoparticles: A Possible Route to Superhydrophobic Surfaces with Low Water Sliding Angle and High Water Contact Angle. *Journal of Colloid and Interface Science* **2011**, *359* (2), 380–388. https://doi.org/10.1016/j.jcis.2011.04.004.

(115) Bormashenko, E.; Pogreb, R.; Whyman, G.; Bormashenko, Y.; Jager, R.; Stein, T.; Schechter, A.; Aurbach, D. The Reversible Giant Change in the Contact Angle on the Polysulfone and Polyethersulfone Films Exposed to UV Irradiation. *Langmuir* **2008**, *24* (12), 5977–5980. https://doi.org/10.1021/la800527q.

(116) Mansourizadeh, A.; Javadi Azad, A. Preparation of Blend Polyethersulfone/Cellulose Acetate/Polyethylene Glycol Asymmetric Membranes for Oil–Water Separation. *J Polym Res* **2014**, *21* (3), 375. https://doi.org/10.1007/s10965-014-0375-x.

(117) Xu, Z.-L.; Chung, T.-S.; Loh, K.-C.; Lim, B. C. Polymeric Asymmetric Membranes Made from Polyetherimide/Polybenzimidazole/Poly(Ethylene Glycol) (PEI/PBI/PEG) for Oil–Surfactant–Water Separation. *Journal of Membrane Science* **1999**, *158* (1), 41–53. https://doi.org/10.1016/S0376-7388(99)00030-7.

(118) Ghandashtani, M. B.; Zokaee Ashtiani, F.; Karimi, M.; Fouladitajar, A. A Novel Approach to Fabricate High Performance Nano-SiO2 Embedded PES Membranes for Microfiltration of Oil-in-Water Emulsion. *Applied Surface Science* **2015**, *349*, 393–402. https://doi.org/10.1016/j.apsusc.2015.05.037.

(119) Meng, H.; Xu, T.; Gao, M.; Bai, J.; Li, C. An Oil-Contamination-Resistant PVP/PAN Electrospinning Membrane for High-Efficient Oil–Water Mixture and Emulsion 192 Separation. *Journal of Applied Polymer Science* **2021**, *138* (11), 50043. https://doi.org/10.1002/app.50043.

(120) Hazlett, R. N. *Fibrous Bed Coalescence of Water. Steps in the Coalescence Process*. https://doi.org/10.1021/i160032a005.

(121) Singh, C. J.; Mukhopadhyay, S.; Rengasamy, R. S. Fibrous Coalescence Filtration in Treating Oily Wastewater: A Review. *Journal of Industrial Textiles* **2022**, *51* (3_suppl), 3648S-3682S. https://doi.org/10.1177/15280837211040863.

(122) VINSON, C. G. The Coalescence of Micron-Size Drops in Liquid-Liquid Dispersions in Flowpast Fine-Mesh Screen. Ph.D., University of Michigan, United States -- Michigan, 1965. https://www.proquest.com/docview/302143551/citation/E2DC1A4B7F304439PQ/1 (accessed 2023-12-21).

(123) Varghese, B. K.; Cleveland, T. G. Kenaf as a Deep-Bed Filter Medium to Remove Oil from Oil-in-Water Emulsions. *Separation Science and Technology* **1998**, *33* (14), 2197–2220. https://doi.org/10.1080/01496399808545723.

(124) Li, J.; Gu, Y. Coalescence of Oil-in-Water Emulsions in Fibrous and Granular Beds. *Separation and Purification Technology* **2005**, *42* (1), 1–13. https://doi.org/10.1016/j.seppur.2004.05.006.

(125) Wahi, R.; Chuah, L. A.; Choong, T. S. Y.; Ngaini, Z.; Nourouzi, M. M. Oil Removal from Aqueous State by Natural Fibrous Sorbent: An Overview. *Separation and Purification Technology* **2013**, *113*, 51–63. https://doi.org/10.1016/j.seppur.2013.04.015.

(126) Kulkarni, P. S.; Patel, S. U.; Chase, G. G. Layered Hydrophilic/Hydrophobic Fiber Media for Water-in-Oil Coalescence. *Separation and Purification Technology* **2012**, *85*, 157–164. https://doi.org/10.1016/j.seppur.2011.10.004.

(127) Kulkarni, P. S.; Patel, S. U.; Patel, S. U.; Chase, G. G. Coalescence Filtration Performance of Blended Microglass and Electrospun Polypropylene Fiber Filter Media. *Separation and Purification Technology* **2014**, *124*, 1–8. https://doi.org/10.1016/j.seppur.2013.12.014. 193

(128) Moorthy, K. EFFECT OF SURFACE ENERGY OF FIBERS ON COALESCENCE FILTRATION, University of Akron, 2007. https://etd.ohiolink.edu/apexprod/rws_olink/r/1501/10?clear=10&p10_accession_num=akron1185554340 (accessed 2023-01-10).

(129) Rajgarhia, S. S.; Jana, S. C.; Chase, G. G. Separation of Water from Ultralow Sulfur Diesel Using Novel Polymer Nanofiber-Coated Glass Fiber Media. *ACS Appl. Mater. Interfaces* **2016**, *8* (33), 21683–21690. https://doi.org/10.1021/acsami.6b07364.

(130) Bokka, S.; Li, Y.; Reneker, D. H.; Chase, G. G. Achievement of High Surface Charge in Poly(Vinylidene Fluoride) Fiber Yarns through Dipole Orientation during Fabrication. *Journal of Applied Polymer Science* **2023**, *140* (1), e53265. https://doi.org/10.1002/app.53265.

(131) Shin, C. Filtration Application from Recycled Expanded Polystyrene. *Journal of Colloid and Interface Science* **2006**, *302* (1), 267–271. https://doi.org/10.1016/j.jcis.2006.05.058.

(132) Yue, Y.; Hara, M.; Mukai, Y. Continuous Coalescence and Separation of Oil-in-Water Emulsion via Polyacrylonitrile Nanofibrous Membrane Coalescer. *Colloids and Surfaces A: Physicochemical and Engineering Aspects* **2023**, *657*, 130626. https://doi.org/10.1016/j.colsurfa.2022.130626.

(133) Sareen, S. S.; Rose, P. M.; Gudesen, R. C.; Kintner, R. C. Coalescence in Fibrous Beds. *AIChE Journal* **1966**, *12* (6), 1045–1050. https://doi.org/10.1002/aic.690120603.

(134) Khan, E.; Virojnagud, W.; Ratpukdi, T. Use of Biomass Sorbents for Oil Removal from Gas Station Runoff. *Chemosphere* **2004**, *57* (7), 681–689. https://doi.org/10.1016/j.chemosphere.2004.06.028.

(135) Langevin, D.; Argillier, J.-F. Interfacial Behavior of Asphaltenes. *Advances in Colloid and Interface Science* **2016**, *233*, 83–93. https://doi.org/10.1016/j.cis.2015.10.005. 194

(136) Jian, C.; Poopari, M. R.; Liu, Q.; Zerpa, N.; Zeng, H.; Tang, T. Reduction of Water/Oil Interfacial Tension by Model Asphaltenes: The Governing Role of Surface Concentration. *J. Phys. Chem. B* **2016**, *120* (25), 5646–5654. https://doi.org/10.1021/acs.jpcb.6b03691

(137) Kilpatrick, P. K. Water-in-Crude Oil Emulsion Stabilization: Review and Unanswered Questions. *Energy Fuels* **2012**, *26* (7), 4017–4026. https://doi.org/10.1021/ef3003262.

(138) Zeng, H.; Song, Y.-Q.; Johnson, D. L.; Mullins, O. C. Critical Nanoaggregate Concentration of Asphaltenes by Direct-Current (DC) Electrical Conductivity. *Energy Fuels* **2009**, *23* (3), 1201–1208. https://doi.org/10.1021/ef800781a.

(139) Liu, J.; Cui, X.; Huang, J.; Xie, L.; Tan, X.; Liu, Q.; Zeng, H. Understanding the Stabilization Mechanism of Bitumen-Coated Fine Solids in Organic Media from Non-Aqueous Extraction of Oil Sands. *Fuel* **2019**, *242*, 255–264. https://doi.org/10.1016/j.fuel.2019.01.029.

(140) Liu, D.; Li, C.; Zhang, X.; Yang, F.; Sun, G.; Yao, B.; Zhang, H. Polarity Effects of Asphaltene Subfractions on the Stability and Interfacial Properties of Water-in-Model Oil Emulsions. *Fuel* **2020**, *269*, 117450. https://doi.org/10.1016/j.fuel.2020.117450.

(141) Wu, J.; Xu, Y.; Dabros, T.; Hamza, H. Effect of EO and PO Positions in Nonionic Surfactants on Surfactant Properties and Demulsification Performance. *Colloids and Surfaces A: Physicochemical and Engineering Aspects* **2005**, *252* (1), 79–85. https://doi.org/10.1016/j.colsurfa.2004.09.034.

(142) Cendejas, G.; Arreguín, F.; Castro, L. V.; Flores, E. A.; Vazquez, F. Demulsifying Super-Heavy Crude Oil with Bifunctionalized Block Copolymers. *Fuel* **2013**, *103*, 356–363. https://doi.org/10.1016/j.fuel.2012.08.029.

(143) Atta, A. M.; Abdullah, M. M. S.; Al-Lohedan, H. A.; Ezzat, A. O. Demulsification of Heavy Crude Oil Using New Nonionic Cardanol Surfactants. *Journal of Molecular Liquids* **2018**, *252*, 311–320. https://doi.org/10.1016/j.molliq.2017.12.154. 195

(144) Nikkhah, M.; Tohidian, T.; Rahimpour, M. R.; Jahanmiri, A. Efficient Demulsification of Water-in-Oil Emulsion by a Novel Nano-Titania Modified Chemical Demulsifier. *Chemical Engineering Research and Design* **2015**, *94*, 164–172. https://doi.org/10.1016/j.cherd.2014.07.021.

(145) Abullah, M. M. S.; Al-Lohedan, H. A.; Attah, A. M. Synthesis and Application of Amphiphilic Ionic Liquid Based on Acrylate Copolymers as Demulsifier and Oil Spill Dispersant. *Journal of Molecular Liquids* **2016**, *219*, 54–62. https://doi.org/10.1016/j.molliq.2016.03.011.

(146) Bhardwaj, A.; Hartland, S. Dynamics of Emulsification and Demulsification of Water in Crude Oil Emulsions. *Ind. Eng. Chem. Res.* **1994**, *33* (5), 1271–1279. https://doi.org/10.1021/ie00029a025.

(147) Mansur, C. R. E.; Lechuga, F. C.; Mauro, A. C.; González, G.; Lucas, E. F. Behavior of Mixtures of Nonionic Polyoxide-Based Surfactants and Their Application in the Destabilization of Oil Emulsions. *Journal of Applied Polymer Science* **2007**, *106* (5), 2947–2954. https://doi.org/10.1002/app.26747.

(148) Mansur, C. R. E.; Barboza, S. P.; González, G.; Lucas, E. F. PLURONIC × TETRONIC Polyols: Study of Their Properties and Performance in the Destabilization of Emulsions Formed in the Petroleum Industry. *Journal of Colloid and Interface Science* **2004**, *271* (1), 232–240. https://doi.org/10.1016/j.jcis.2003.11.034.

(149) Fan, Y.; Simon, S.; Sjöblom, J. Chemical Destabilization of Crude Oil Emulsions: Effect of Nonionic Surfactants as Emulsion Inhibitors. *Energy Fuels* **2009**, *23* (9), 4575–4583. https://doi.org/10.1021/ef900355d.

(150) Dalmazzone, C.; Noïk, C.; Komunjer, L. Mechanism of Crude-Oil/Water Interface Destabilization by Silicone Demulsifiers. *SPE Journal* **2005**, *10* (01), 44–53. https://doi.org/10.2118/80241-PA. 196

(151) Yang, F.; Tchoukov, P.; Qiao, P.; Ma, X.; Pensini, E.; Dabros, T.; Czarnecki, J.; Xu, Z. Studying Demulsification Mechanisms of Water-in-Crude Oil Emulsions Using a Modified Thin Liquid Film Technique. *Colloids and Surfaces A: Physicochemical and Engineering Aspects* **2018**, *540*, 215–223. https://doi.org/10.1016/j.colsurfa.2017.12.056.

(152) Owsik, I. A.; Little, V. T. Reverse Emulsion Breaker Polymers. US10072217B2, September 11, 2018. https://patents.google.com/patent/US10072217B2/en (accessed 2021-01-26).

(153) Sun, H.; Wang, Q.; Li, X.; He, X. Novel Polyether-Polyquaternium Copolymer as an Effective Reverse Demulsifier for O/W Emulsions: Demulsification Performance and Mechanism. *Fuel* **2020**, *263*, 116770. https://doi.org/10.1016/j.fuel.2019.116770.

(154) Zhang, L.; Ying, H.; Yan, S.; Zhan, N.; Guo, Y.; Fang, W. Hyperbranched Poly(Amido Amine) Demulsifiers with Ethylenediamine/1,3-Propanediamine as an Initiator for Oil-in-Water Emulsions with Microdroplets. *Fuel* **2018**, *226*, 381–388. https://doi.org/10.1016/j.fuel.2018.03.196.

(155) Nguyen, D.; Sadeghi, N.; Houston, C. Chemical Interactions and Demulsifier Characteristics for Enhanced Oil Recovery Applications. *Energy Fuels* **2012**, *26* (5), 2742–2750. https://doi.org/10.1021/ef201800b.

(156) Hao, L.; Jiang, B.; Zhang, L.; Yang, H.; Sun, Y.; Wang, B.; Yang, N. Efficient Demulsification of Diesel-in-Water Emulsions by Different Structural Dendrimer-Based

Demulsifiers. *Ind. Eng. Chem. Res.* **2016**, *55* (6), 1748–1759. https://doi.org/10.1021/acs.iecr.5b04401.

(157) Ezzat, A. O.; Atta, A. M.; Al-Lohedan, H. A.; Abdullah, M. M. S.; Hashem, A. I. Synthesis and Application of Poly(Ionic Liquid) Based on Cardanol as Demulsifier for Heavy Crude Oil Water Emulsions. *Energy Fuels* **2018**, *32* (1), 214–225. https://doi.org/10.1021/acs.energyfuels.7b02955. 197

(158) Katepalli, H.; Bose, A.; Hatton, T. A.; Blankschtein, D. Destabilization of Oil-in-Water Emulsions Stabilized by Non-Ionic Surfactants: Effect of Particle Hydrophilicity. *Langmuir* **2016**, *32* (41), 10694–10698. https://doi.org/10.1021/acs.langmuir.6b03289.

(159) Zhu, B.-Y.; Gu, T. Surfactant Adsorption at Solid-Liquid Interfaces. *Advances in Colloid and Interface Science* **1991**, *37* (1), 1–32. https://doi.org/10.1016/0001-8686(91)80037-K.

(160) Parfitt, G. D.; Rochester, C. H. *Adsorption from Solution at the Solid/Liquid Interface / Edited by G.D. Parfitt and C.H. Rochester.*; Academic Press, 1983.

(161) Shar, J. A.; Obey, T. M.; Cosgrove, T. Adsorption Studies of Polyethers Part 1. Adsorption onto Hydrophobic Surfaces. *Colloids and Surfaces A: Physicochemical and Engineering Aspects* **1998**, *136* (1), 21–33. https://doi.org/10.1016/S0927-7757(97)00182-9.

(162) Partyka, S.; Zaini, S.; Lindheimer, M.; Brun, B. The Adsorption of Non-Ionic Surfactants on a Silica Gel. *Colloids and Surfaces* **1984**, *12*, 255–270. https://doi.org/10.1016/0166-6622(84)80104-3.

(163) Müter, D.; Rother, G.; Bock, H.; Schoen, M.; Findenegg, G. H. Adsorption and Depletion Regimes of a Nonionic Surfactant in Hydrophilic Mesopores: An Experimental and Simulation Study. *Langmuir* **2017**, *33* (42), 11406–11416. https://doi.org/10.1021/acs.langmuir.7b02262.

(164) Tiberg, F. Physical Characterization of Non-Ionic Surfactant Layers Adsorbed at Hydrophilic and Hydrophobic Solid Surfaces by Time-Resolved Ellipsometry. *Faraday Trans.* **1996**, *92* (4), 531. https://doi.org/10.1039/ft9969200531.

(165) Shin, T. G.; Müter, D.; Meissner, J.; Paris, O.; Findenegg, G. H. Structural Characterization of Surfactant Aggregates Adsorbed in Cylindrical Silica Nanopores. *Langmuir* **2011**, *27* (9), 5252–5263. https://doi.org/10.1021/la200333q.

(166) US EPA, O. *EPA and Partners Describe a Chemical Category Prioritization Approach to Select 75 PFAS for Testing using New Approach Methods*. 198 https://www.epa.gov/sciencematters/epa-and-partners-describe-chemical-category-prioritization-approach-select-75-pfas (accessed 2023-08-06).

(167) US EPA, O. *PFAS Chemical Lists and Tiered Testing Methods Descriptions*. https://www.epa.gov/chemical-research/pfas-chemical-lists-and-tiered-testing-methods-descriptions (accessed 2023-08-06).

(168) Abbasian Chaleshtari, Z.; Foudazi, R. A Review on Per- and Polyfluoroalkyl Substances (PFAS) Remediation: Separation Mechanisms and Molecular Interactions. *ACS EST Water* **2022**, *2* (12), 2258–2272. https://doi.org/10.1021/acsestwater.2c00271.

(169) Xiao, L.; Ling, Y.; Alsbaiee, A.; Li, C.; Helbling, D. E.; Dichtel, W. R. β-Cyclodextrin Polymer Network Sequesters Perfluorooctanoic Acid at Environmentally Relevant Concentrations. *J. Am. Chem. Soc.* **2017**, *139* (23), 7689–7692. https://doi.org/10.1021/jacs.7b02381.

(170) *Report: Up to 110 Million Americans Could Have PFAS-Contaminated Drinking Water | EWG*. https://www.ewg.org/research/report-110-million-americans-could-have-pfas-contaminated-drinking-water (accessed 2023-08-06).

(171) Panieri, E.; Baralic, K.; Djukic-Cosic, D.; Buha Djordjevic, A.; Saso, L. PFAS Molecules: A Major Concern for the Human Health and the Environment. *Toxics* **2022**, *10* (2), 44. https://doi.org/10.3390/toxics10020044.

(172) *PFAS chemicals overview | ATSDR*. https://www.atsdr.cdc.gov/pfas/health-effects/overview.html (accessed 2024-01-03).

(173) History and Use of Per- and Polyfluoroalkyl Substances (PFAS) Found in the Environment.

(174) Bruton, T. A.; Sedlak, D. L. Treatment of Aqueous Film-Forming Foam by Heat-Activated Persulfate Under Conditions Representative of In Situ Chemical Oxidation. *Environ. Sci. Technol.* **2017**, *51* (23), 13878–13885. https://doi.org/10.1021/acs.est.7b03969. 199

(175) Smith, S. J.; Wiberg, K.; McCleaf, P.; Ahrens, L. Pilot-Scale Continuous Foam Fractionation for the Removal of Per- and Polyfluoroalkyl Substances (PFAS) from Landfill Leachate. *ACS EST Water* **2022**, *2* (5), 841–851. https://doi.org/10.1021/acsestwater.2c00032.

(176) McGregor, R. In Situ Treatment of PFAS-impacted Groundwater Using Colloidal Activated Carbon. *Remediation Journal* **2018**, *28*, 33–41. https://doi.org/10.1002/rem.21558.

(177) Xiao, F.; Simcik, M. F.; Gulliver, J. S. Mechanisms for Removal of Perfluorooctane Sulfonate (PFOS) and Perfluorooctanoate (PFOA) from Drinking Water by Conventional and Enhanced Coagulation. *Water Research* **2013**, *47* (1), 49–56. https://doi.org/10.1016/j.watres.2012.09.024.

(178) Hubert, M.; Meyn, T.; Hansen, M. C.; Hale, S. E.; Arp, H. P. H. Per- and Polyfluoroalkyl Substance (PFAS) Removal from Soil Washing Water by Coagulation and Flocculation. *Water Research* **2024**, *249*, 120888. https://doi.org/10.1016/j.watres.2023.120888.

(179) Gagliano, E.; Sgroi, M.; Falciglia, P. P.; Vagliasindi, F. G. A.; Roccaro, P. Removal of Poly- and Perfluoroalkyl Substances (PFAS) from Water by Adsorption: Role of PFAS Chain Length, Effect of Organic Matter and Challenges in Adsorbent Regeneration. *Water Research* **2020**, *171*, 115381. https://doi.org/10.1016/j.watres.2019.115381.

(180) Cantoni, B.; Turolla, A.; Wellmitz, J.; Ruhl, A. S.; Antonelli, M. Perfluoroalkyl Substances (PFAS) Adsorption in Drinking Water by Granular Activated Carbon: Influence of Activated Carbon and PFAS Characteristics. *Science of The Total Environment* **2021**, *795*, 148821. https://doi.org/10.1016/j.scitotenv.2021.148821.

(181) Karbassiyazdi, E.; Kasula, M.; Modak, S.; Pala, J.; Kalantari, M.; Altaee, A.; Esfahani, M. R.; Razmjou, A. A Juxtaposed Review on Adsorptive Removal of PFAS by Metal-Organic Frameworks (MOFs) with Carbon-Based Materials, Ion Exchange Resins, and Polymer 200 Adsorbents. *Chemosphere* **2023**, *311*, 136933. https://doi.org/10.1016/j.chemosphere.2022.136933.

(182) Lee, T.; Speth, T. F.; Nadagouda, M. N. High-Pressure Membrane Filtration Processes for Separation of Per- and Polyfluoroalkyl Substances (PFAS). *Chemical Engineering Journal* **2022**, *431*, 134023. https://doi.org/10.1016/j.cej.2021.134023.

(183) Johnson, J. K.; Hoffman, C. M. Jr.; Smith, D. A.; Xia, Z. Advanced Filtration Membranes for the Removal of Perfluoroalkyl Species from Water. *ACS Omega* **2019**, *4* (5), 8001–8006. https://doi.org/10.1021/acsomega.9b00314.

(184) Li, R.; Xintong, J.; Youshuang, Z.; Yuran, Z.; Jing, G. Precipitation of Proteins from Soybean Whey Wastewater by Successive Foaming and Defoaming. *Chemical Engineering and Processing - Process Intensification* **2018**, *128*, 124–131. https://doi.org/10.1016/j.cep.2018.04.012.

(185) Tabibi, S.; Moussavi, M.; Adlo, H. Cobalt Removal from an Industrial Effluent by Foam Fractionation. *Environmental Challenges* **2021**, *4*, 100135. https://doi.org/10.1016/j.envc.2021.100135.

(186) de Jesus Gregersen, K. J.; Pedersen, L.-F.; Pedersen, P. B.; Syropoulou, E.; Dalsgaard, J. Foam Fractionation and Ozonation in Freshwater Recirculation Aquaculture Systems. *Aquacultural Engineering* **2021**, *95*, 102195. https://doi.org/10.1016/j.aquaeng.2021.102195.

(187) Goto, Y.; Nema, Y.; Matsuoka, K. Foam Separation of Dyes Using Anionic, Cationic, and Amphoteric Surfactants. *Journal of Oleo Science* **2020**, *69* (6), 549–555. https://doi.org/10.5650/jos.ess20004.

(188) Burns, D. J.; Stevenson, P.; Murphy, P. J. C. PFAS Removal from Groundwaters Using Surface-Active Foam Fractionation. *Remediation Journal* **2021**, *31* (4), 19–33. https://doi.org/10.1002/rem.21694. 201

(189) Meng, P.; Deng, S.; Maimaiti, A.; Wang, B.; Huang, J.; Wang, Y.; Cousins, I. T.; Yu, G. Efficient Removal of Perfluorooctane Sulfonate from Aqueous Film-Forming Foam Solution by Aeration-Foam Collection. *Chemosphere* **2018**, *203*, 263–270. https://doi.org/10.1016/j.chemosphere.2018.03.183.

(190) Buckley, T.; Xu, X.; Rudolph, V.; Firouzi, M.; Shukla, P. Review of Foam Fractionation as a Water Treatment Technology. *Separation Science and Technology* **2022**, *57* (6), 929–958. https://doi.org/10.1080/01496395.2021.1946698.

(191) Lee, Y.-C.; Wang, P.-Y.; Lo, S.-L.; Huang, C. P. Recovery of Perfluorooctane Sulfonate (PFOS) and Perfluorooctanoate (PFOA) from Dilute Water Solution by Foam Flotation. *Separation and Purification Technology* **2017**, *173*, 280–285. https://doi.org/10.1016/j.seppur.2016.09.012.

(192) Oraby, A.; Weickardt, I.; Zibek, S. Foam Fractionation Methods in Aerobic Fermentation Processes. *Biotechnology and Bioengineering* **2022**, *119* (7), 1697–1711. https://doi.org/10.1002/bit.28102.

(193) Wang, Y.; Ji, Y.; Tishchenko, V.; Huang, Q. Removing Per- and Polyfluoroalkyl Substances (PFAS) in Water by Foam Fractionation. *Chemosphere* **2023**, *311*, 137004. https://doi.org/10.1016/j.chemosphere.2022.137004.

(194) Boonyasuwat, S.; Chavadej, S.; Malakul, P.; Scamehorn, J. F. Anionic and Cationic Surfactant Recovery from Water Using a Multistage Foam Fractionator. *Chemical Engineering Journal* **2003**, *93* (3), 241–252. https://doi.org/10.1016/S1385-8947(03)00043-3.

(195) Chuyingsakultip, N.; Chavadej, S.; Malakul, P.; Scamehorn, J. F. Surfactant Recovery from Aqueous Phase Using Multi-Stage Foam Fractionation. アジア・太平洋化学工学会議発表論文要旨集 **2004**, *2004*, 186–186. https://doi.org/10.11491/apcche.2004.0.186.0. 202

(196) Morrison, A. L.; Strezov, V.; Niven, R. K.; Taylor, M. P.; Wilson, S. P.; Wang, J.; Burns, D. J.; Murphy, P. J. C. Impact of Salinity and Temperature on Removal of PFAS Species from Water by Aeration in the Absence of Additional Surfactants: A Novel Application of Green Chemistry Using Adsorptive Bubble Fractionation. *Ind. Eng. Chem. Res.* **2023**, *62* (13), 5635–5645. https://doi.org/10.1021/acs.iecr.3c00150.

(197) Oyetade, O. A.; Varadwaj, G. B. B.; Nyamori, V. O.; Jonnalagadda, S. B.; Martincigh, B. S. A Critical Review of the Occurrence of Perfluoroalkyl Acids in Aqueous Environments and Their Removal by Adsorption onto Carbon Nanotubes. *Rev Environ Sci Biotechnol* **2018**, *17* (4), 603–635. https://doi.org/10.1007/s11157-018-9479-9.

(198) Pabon, M.; Corpart, J. M. Fluorinated Surfactants: Synthesis, Properties, Effluent Treatment. *Journal of Fluorine Chemistry* **2002**, *114* (2), 149–156. https://doi.org/10.1016/S0022-1139(02)00038-6.

(199) Xiao, X.; Ulrich, B. A.; Chen, B.; Higgins, C. P. Sorption of Poly- and Perfluoroalkyl Substances (PFASs) Relevant to Aqueous Film-Forming Foam (AFFF)-Impacted Groundwater by Biochars and Activated Carbon. *Environ. Sci. Technol.* **2017**, *51* (11), 6342–6351. https://doi.org/10.1021/acs.est.7b00970.

(200) Park, M.; Wu, S.; Lopez, I. J.; Chang, J. Y.; Karanfil, T.; Snyder, S. A. Adsorption of Perfluoroalkyl Substances (PFAS) in Groundwater by Granular Activated Carbons: Roles of Hydrophobicity of PFAS and Carbon Characteristics. *Water Research* **2020**, *170*, 115364. https://doi.org/10.1016/j.watres.2019.115364.

(201) Forrester, E. R. Removal of Short Chain PFAS via GAC Adsorption. *Journal of the New England Water Works Association* **2019**, *133* (2), 81–84.

(202) Woodard, S.; Berry, J.; Newman, B. Ion Exchange Resin for PFAS Removal and Pilot Test Comparison to GAC: WOODARD et Al. *Remediation* **2017**, *27* (3), 19–27. https://doi.org/10.1002/rem.21515. 203

(203) Lino Conte; Luigi Falletti; Alessandro Zaggia; Marco Milan. Polyfluorinated Organic Micropollutants Removal from Water by Ion Exchange and Adsorption. *Chemical Engineering Transactions* **2015**, *43*, 2257–2262. https://doi.org/10.3303/CET1543377.

(204) *Cyclopure | Targeting PFAS Everywhere to Make Water Safe*. Cyclopure. https://cyclopure.com/ (accessed 2024-01-08).

(205) Ateia, M.; Attia, M. F.; Maroli, A.; Tharayil, N.; Alexis, F.; Whitehead, D. C.; Karanfil, T. Rapid Removal of Poly- and Perfluorinated Alkyl Substances by Poly(Ethylenimine)-Functionalized Cellulose Microcrystals at Environmentally Relevant Conditions. *Environmental Science & Technology Letters* **2018**. https://doi.org/10.1021/acs.estlett.8b00556.

(206) Wang, W.; Maimaiti, A.; Shi, H.; Wu, R.; Wang, R.; Li, Z.; Qi, D.; Yu, G.; Deng, S. Adsorption Behavior and Mechanism of Emerging Perfluoro-2-Propoxypropanoic Acid (GenX) on Activated Carbons and Resins. *Chemical Engineering Journal* **2019**, *364*, 132–138. https://doi.org/10.1016/j.cej.2019.01.153.

(207) Kawano, S.; Kida, T.; Takemine, S.; Matsumura, C.; Nakano, T.; Kuramitsu, M.; Adachi, K.; Akashi, M. Efficient Removal and Recovery of Perfluorinated Compounds from Water by Surface-Tethered β-Cyclodextrins on Polystyrene Particles. *Chemistry Letters* **2013**, *42* (4), 392–394. https://doi.org/10.1246/cl.121239.

(208) Alsbaiee, A.; Smith, B. J.; Xiao, L.; Ling, Y.; Helbling, D. E.; Dichtel, W. R. Rapid Removal of Organic Micropollutants from Water by a Porous β-Cyclodextrin Polymer. *Nature* **2016**, *529* (7585), 190–194. https://doi.org/10.1038/nature16185.

(209) Ching, C.; Klemes, M. J.; Trang, B.; Dichtel, W. R.; Helbling, D. E. β-Cyclodextrin Polymers with Different Cross-Linkers and Ion-Exchange Resins Exhibit Variable Adsorption of Anionic, Zwitterionic, and Nonionic PFASs. *Environ. Sci. Technol.* **2020**, *54* (19), 12693–12702. https://doi.org/10.1021/acs.est.0c04028. 204

(210) Appleman, T. D.; Higgins, C. P.; Quiñones, O.; Vanderford, B. J.; Kolstad, C.; Zeigler-Holady, J. C.; Dickenson, E. R. V. Treatment of Poly- and Perfluoroalkyl Substances in U.S. Full-Scale Water Treatment Systems. *Water Research* **2014**, *51*, 246–255. https://doi.org/10.1016/j.watres.2013.10.067.

(211) Kucharzyk, K. H.; Darlington, R.; Benotti, M.; Deeb, R.; Hawley, E. Novel Treatment Technologies for PFAS Compounds: A Critical Review. *Journal of Environmental Management* **2017**, *204*, 757–764. https://doi.org/10.1016/j.jenvman.2017.08.016.

(212) Wang, J.; Wang, L.; Xu, C.; Zhi, R.; Miao, R.; Liang, T.; Yue, X.; Lv, Y.; Liu, T. Perfluorooctane Sulfonate and Perfluorobutane Sulfonate Removal from Water by Nanofiltration Membrane: The Roles of Solute Concentration, Ionic Strength, and Macromolecular Organic Foulants. *Chemical Engineering Journal* **2018**, *332*, 787–797. https://doi.org/10.1016/j.cej.2017.09.061.

(213) Tang, C. Y.; Fu, Q. S.; Criddle, C. S.; Leckie, J. O. Effect of Flux (Transmembrane Pressure) and Membrane Properties on Fouling and Rejection of Reverse Osmosis and Nanofiltration Membranes Treating Perfluorooctane Sulfonate Containing Wastewater. *Environ. Sci. Technol.* **2007**, *41* (6), 2008–2014. https://doi.org/10.1021/es062052f.

(214) Xu, P.; Bellona, C.; Drewes, J. E. Fouling of Nanofiltration and Reverse Osmosis Membranes during Municipal Wastewater Reclamation: Membrane Autopsy Results from Pilot-Scale Investigations. *Journal of Membrane Science* **2010**, *353* (1), 111–121. https://doi.org/10.1016/j.memsci.2010.02.037.

(215) Qin, D.; Liu, Z.; Bai, H.; Sun, D. D.; Song, X. A New Nano-Engineered Hierarchical Membrane for Concurrent Removal of Surfactant and Oil from Oil-in-Water Nanoemulsion. *Sci Rep* **2016**, *6* (1), 24365. https://doi.org/10.1038/srep24365.

(216) Wang, D.; McLaughlin, E.; Pfeffer, R.; Lin, Y. S. Adsorption of Oils from Pure Liquid and Oil–Water Emulsion on Hydrophobic Silica Aerogels. *Separation and Purification Technology* **2012**, *99*, 28–35. https://doi.org/10.1016/j.seppur.2012.08.001. 205

(217) Lee, J. H.; Kopecek, J.; Andrade, J. D. Protein-Resistant Surfaces Prepared by PEO-Containing Block Copolymer Surfactants. *Journal of Biomedical Materials Research* **1989**, *23* (3), 351–368. https://doi.org/10.1002/jbm.820230306.

(218) Zhang, R.; Somasundaran, P. Advances in Adsorption of Surfactants and Their Mixtures at Solid/Solution Interfaces. *Advances in Colloid and Interface Science* **2006**, *123–126*, 213–229. https://doi.org/10.1016/j.cis.2006.07.004.

(219) *Micellar Liquid Chromatography | Taylor & Francis Group*. Taylor & Francis. https://www.taylorfrancis.com/https://www.taylorfrancis.com/books/edit/10.1201/9781482273816/micellar-liquid-chromatography-alain-berthod-celia-garcia-alvarez-coque (accessed 2021-05-24).

(220) Schwarze, M. Micellar-Enhanced Ultrafiltration (MEUF) – State of the Art. *Environ. Sci.: Water Res. Technol.* **2017**, *3* (4), 598–624. https://doi.org/10.1039/C6EW00324A.

(221) Xu, S.-L.; Wang, C.; Zeng, Q.-D.; Wu, P.; Wang, Z.-G.; Yan, H.-K.; Bai, C.-L. Self-Assembly of Cationic Surfactants on a Graphite Surface Studied by STM. *Langmuir* **2002**, *18* (3), 657–660. https://doi.org/10.1021/la0111506.

(222) Lugo, D.; Oberdisse, J.; Karg, M.; Schweins, R.; Findenegg, G. H. Surface Aggregate Structure of Nonionic Surfactants on Silica Nanoparticles. *Soft Matter* **2009**, *5* (15), 2928–2936. https://doi.org/10.1039/B903024G.

(223) Lugo, D. M.; Oberdisse, J.; Lapp, A.; Findenegg, G. H. Effect of Nanoparticle Size on the Morphology of Adsorbed Surfactant Layers. *J. Phys. Chem. B* **2010**, *114* (12), 4183–4191. https://doi.org/10.1021/jp911400j.

(224) Brumaru, C.; Geng, M. L. Interaction of Surfactants with Hydrophobic Surfaces in Nanopores. *Langmuir* **2010**, *26* (24), 19091–19099. https://doi.org/10.1021/la1031009.

(225) Giordano, F.; Denoyel, R.; Rouquerol, J. Influence of Porosity on the Adsorption of a Non-Ionic Surfactant on Silica. *Colloids and Surfaces A: Physicochemical and* 206 *Engineering Aspects* **1993**, *71* (3), 293–298. https://doi.org/10.1016/0927-7757(93)80044-F.

(226) Müter, D.; Shin, T.; Demé, B.; Fratzl, P.; Paris, O.; Findenegg, G. H. Surfactant Self-Assembly in Cylindrical Silica Nanopores. *J. Phys. Chem. Lett.* **2010**, *1* (9), 1442–1446. https://doi.org/10.1021/jz100279y.

(227) Wanless, E. J.; Ducker, W. A. Organization of Sodium Dodecyl Sulfate at the Graphite−Solution Interface. *J. Phys. Chem.* **1996**, *100* (8), 3207–3214. https://doi.org/10.1021/jp952439x.

(228) Zhu, B.-Y.; Gu, T. Surfactant Adsorption at Solid-Liquid Interfaces. *Advances in Colloid and Interface Science* **1991**, *37* (1), 1–32. https://doi.org/10.1016/0001-8686(91)80037-K.

(229) Lin, W.-H.; Jana, S. C. Analysis of Porous Structures of Cellulose Aerogel Monoliths and Microparticles. *Microporous and Mesoporous Materials* **2021**, *310*, 110625. https://doi.org/10.1016/j.micromeso.2020.110625.

(230) Kulkarni, A.; Jana, S. C. Surfactant-Free Syndiotactic Polystyrene Aerogel Foams via Pickering Emulsion. *Polymer* **2021**, *212*, 123125. https://doi.org/10.1016/j.polymer.2020.123125.

(231) Teo, N.; Jana, S. C. Solvent Effects on Tuning Pore Structures in Polyimide Aerogels. *Langmuir* **2018**, *34* (29), 8581–8590. https://doi.org/10.1021/acs.langmuir.8b01513.

(232) Mawhinney, K.; Jana, S. C. Design Of Emulsion-Templated Mesoporous–Macroporous Polyurea Gels and Aerogels. *ACS Appl. Polym. Mater.* **2019**, *1* (11), 3115–3129. https://doi.org/10.1021/acsapm.9b00762.

(233) Daniel, C.; Giudice, S.; Guerra, G. Syndiotatic Polystyrene Aerogels with β, γ, and ε Crystalline Phases. *Chem. Mater.* **2009**, *21* (6), 1028–1034. https://doi.org/10.1021/cm802537g.

(234) *Polyurethane-Based Aerogels for Use as Environmentally Acceptable Super Insulants in the Future Appliance Market - G. Biesmans, D. Randall, E. Francais, M. Perrut, 1998*. 207 https://journals.sagepub.com/doi/abs/10.1177/0021955X9803400502 (accessed 2021-06-28).

(235) Teo, N.; Jana, S. C. Open Cell Aerogel Foams via Emulsion Templating. *Langmuir* **2017**, *33* (44), 12729–12738. https://doi.org/10.1021/acs.langmuir.7b03139.

(236) Mosanenzadeh, S. G.; Alshrah, M.; Saadatnia, Z.; Park, C. B.; Naguib, H. E. Double Dianhydride Backbone Polyimide Aerogels with Enhanced Thermal Insulation for High-Temperature Applications. *Macromolecular Materials and Engineering* **2020**, *305* (4), 1900777. https://doi.org/10.1002/mame.201900777.

(237) Daniel, C.; Alfano, D.; Venditto, V.; Cardea, S.; Reverchon, E.; Larobina, D.; Mensitieri, G.; Guerra, G. Aerogels with a Microporous Crystalline Host Phase. *Advanced Materials* **2005**, *17* (12), 1515–1518. https://doi.org/10.1002/adma.200401762.

(238) Daniel, C.; Dammer, C.; Guenet, J.-M. On the Definition of Thermoreversible Gels: The Case of Syndiotactic Polystyrene. *Polymer* **1994**, *35* (19), 4243–4246. https://doi.org/10.1016/0032-3861(94)90604-1.

(239) *Superior Nanoporous Polyimides via Supercritical CO2 Drying of Jungle-Gym-Type Polyimide Gels - Kawagishi - 2007 - Macromolecular Rapid Communications - Wiley Online Library*. https://onlinelibrary.wiley.com/doi/full/10.1002/marc.200600587 (accessed 2021-06-28).

(240) *US5484818A - Organic aerogels - Google Patents*. https://patents.google.com/patent/US5484818A/en (accessed 2021-06-28).

(241) Gu, S.; Jana, S. C. Open Cell Aerogel Foams with Hierarchical Pore Structures. *Polymer* **2017**, *125*, 1–9. https://doi.org/10.1016/j.polymer.2017.07.085.

(242) *Multifunctional Polyurea Aerogels from Isocyanates and Water. A Structure−Property Case Study | Chemistry of Materials*. https://pubs.acs.org/doi/10.1021/cm102891d (accessed 2021-06-28). 208

(243) Singh, V.; Khullar, P.; Dave, P. N.; Kaur, N. Micelles, Mixed Micelles, and Applications of Polyoxypropylene (PPO)-Polyoxyethylene (PEO)-Polyoxypropylene (PPO) Triblock Polymers. *Int J Ind Chem* **2013**, *4* (1), 12. https://doi.org/10.1186/2228-5547-4-12.

(244) Wu, S. Calculation of Interfacial Tension in Polymer Systems. *Journal of Polymer Science Part C: Polymer Symposia* **1971**, *34* (1), 19–30. https://doi.org/10.1002/polc.5070340105.

(245) Myers, D. *Surfactant Science and Technology*; John Wiley & Sons, 2020.

(246) KRUPKA, T. M.; EXNER, A. A. Structural Parameters Governing Activity of Pluronic Triblock Copolymers in Hyperthermia Cancer Therapy. *Int J Hyperthermia* **2011**, *27* (7), 663–671. https://doi.org/10.3109/02656736.2011.599828.

(247) Davies, J. T. *Interfacial Phenomena*; Elsevier, 2012.

(248) Somasundaran, P.; Shrotri, S.; Huang, L. Thermodynamics of Adsorption of Surfactants at Solid-Liquid Interface. *Pure and Applied Chemistry* **1998**, *70* (3), 621–626. https://doi.org/10.1351/pac199870030621.

(249) Vijayendran, B. R. Polymer Polarity and Surfactant Adsorption. *Journal of Applied Polymer Science* **1979**, *23* (3), 733–742. https://doi.org/10.1002/app.1979.070230308.

(250) Samiey, B.; Golestan, S. Adsorption of Triton X-100 on Silica Gel: Effects of Temperature and Alcohols. *cent.eur.j.chem.* **2010**, *8* (2), 361–369. https://doi.org/10.2478/s11532-009-0135-7.

(251) Somasundaran, P.; Fuerstenau, D. W. Mechanisms of Alkyl Sulfonate Adsorption at the Alumina-Water Interface 1. *J. Phys. Chem.* **1966**, *70* (1), 90–96. https://doi.org/10.1021/j100873a014.

(252) Malmsten, M.; Linse, P.; Cosgrove, T. Adsorption of PEO-PPO-PEO Block Copolymers at Silica. **1992**, *25* (9), 8.

(253) Levitz, P. Aggregative Adsorption of Nonionic Surfactants onto Hydrophilic Solid/Water Interface. Relation with Bulk Micellization. *Langmuir* **1991**, *7* (8), 1595–1608. https://doi.org/10.1021/la00056a010. 209

(254) Schönhoff, M.; Larsson, A.; Welzel, P. B.; Kuckling, D. Thermoreversible Polymers Adsorbed to Colloidal Silica: A 1H NMR and DSC Study of the Phase Transition in Confined Geometry. *J. Phys. Chem. B* **2002**, *106* (32), 7800–7808. https://doi.org/10.1021/jp015538l.

(255) Ma, J.; Guo, C.; Tang, Y.; Liu, H. 1H NMR Spectroscopic Investigations on the Micellization and Gelation of PEO−PPO−PEO Block Copolymers in Aqueous Solutions. *Langmuir* **2007**, *23* (19), 9596–9605. https://doi.org/10.1021/la701221f.

(256) Alexandridis, P.; Alan Hatton, T. Poly(Ethylene Oxide)poly(Propylene Oxide)poly(Ethylene Oxide) Block Copolymer Surfactants in Aqueous Solutions and at Interfaces: Thermodynamics, Structure, Dynamics, and Modeling. *Colloids and Surfaces A: Physicochemical and Engineering Aspects* **1995**, *96* (1), 1–46. https://doi.org/10.1016/0927-7757(94)03028-X.

(257) Bharatiya, B.; Ghosh, G.; Bahadur, P.; Mata, J. The Effects of Salts and Ionic Surfactants on the Micellar Structure of Tri-Block Copolymer PEO-PPO-PEO in Aqueous Solution. *Journal of Dispersion Science and Technology* **2008**, *29* (5), 696–701. https://doi.org/10.1080/01932690701751876.

(258) Pérez-Sánchez, G.; Vicente, F. A.; Schaeffer, N.; Cardoso, I. S.; Jorge, M.; Coutinho, J. A. P. Rationalizing the Phase Behavior of Triblock- Copolymers through Experiments and Molecular Simulations. 51.

(259) Su, Y.; Liu, H. Temperature-Dependent Solubilization of PEO-PPO-PEO Block Copolymers and Their Application for Extraction Trace Organics from Aqueous Solutions. *Korean J. Chem. Eng.* **2003**, *20* (2), 343–346. https://doi.org/10.1007/BF02697250.

(260) Yonguep, E.; Kapiamba, K. F.; Kabamba, K. J.; Chowdhury, M. Formation, Stabilization and Chemical Demulsification of Crude Oil-in-Water Emulsions: A Review. *Petroleum Research* **2022**, *7* (4), 459–472. https://doi.org/10.1016/j.ptlrs.2022.01.007. 210

(261) Liang, H.; Esmaeili, H. Application of Nanomaterials for Demulsification of Oily Wastewater: A Review Study. *Environmental Technology & Innovation* **2021**, *22*, 101498. https://doi.org/10.1016/j.eti.2021.101498.

(262) Wang, D.; Yang, D.; Huang, C.; Huang, Y.; Yang, D.; Zhang, H.; Liu, Q.; Tang, T.; Gamal El-Din, M.; Kemppi, T.; Perdicakis, B.; Zeng, H. Stabilization Mechanism and Chemical Demulsification of Water-in-Oil and Oil-in-Water Emulsions in Petroleum Industry: A Review. *Fuel* **2021**, *286*, 119390. https://doi.org/10.1016/j.fuel.2020.119390.

(263) Shehzad, F.; Hussein, I. A.; Kamal, M. S.; Ahmad, W.; Sultan, A. S.; Nasser, M. S. Polymeric Surfactants and Emerging Alternatives Used in the Demulsification of Produced Water: A Review. *Polymer Reviews* **2018**, *58* (1), 63–101. https://doi.org/10.1080/15583724.2017.1340308.

(264) Martínez-Palou, R.; Cerón-Camacho, R.; Chávez, B.; Vallejo, A. A.; Villanueva-Negrete, D.; Castellanos, J.; Karamath, J.; Reyes, J.; Aburto, J. Demulsification of Heavy Crude Oil-in-Water Emulsions: A Comparative Study between Microwave and Thermal Heating. *Fuel* **2013**, *113*, 407–414. https://doi.org/10.1016/j.fuel.2013.05.094.

(265) Xia, L.; Lu, S.; Cao, G. Stability and Demulsification of Emulsions Stabilized by Asphaltenes or Resins. *Journal of Colloid and Interface Science* **2004**, *271* (2), 504–506. https://doi.org/10.1016/j.jcis.2003.11.027.

(266) Binner, E. R.; Robinson, J. P.; Silvester, S. A.; Kingman, S. W.; Lester, E. H. Investigation into the Mechanisms by Which Microwave Heating Enhances Separation of Water-in-Oil Emulsions. *Fuel* **2014**, *116*, 516–521. https://doi.org/10.1016/j.fuel.2013.08.042.

(267) Kocherginsky, N. M.; Tan, C. L.; Lu, W. F. Demulsification of Water-in-Oil Emulsions via Filtration through a Hydrophilic Polymer Membrane. *Journal of Membrane Science* **2003**, *220* (1), 117–128. https://doi.org/10.1016/S0376-7388(03)00223-0. 211

(268) Hu, J.; Chen, J.; Zhang, X.; Xiao, J.; An, S.; Luan, Z.; Liu, F.; Zhang, B. Dynamic Demulsification of Oil-in-Water Emulsions with Electrocoalescence: Diameter Distribution of Oil Droplets. *Separation and Purification Technology* **2021**, *254*, 117631. https://doi.org/10.1016/j.seppur.2020.117631.

(269) Luo, X.; Gong, H.; Yin, H.; He, Z.; He, L. Optimization of Acoustic Parameters for Ultrasonic Separation of Emulsions with Different Physical Properties. *Ultrasonics Sonochemistry* **2020**, *68*, 105221. https://doi.org/10.1016/j.ultsonch.2020.105221.

(270) Gotad, P. S.; Kafle, N.; Miyoshi, T.; Jana, S. C. Meso- and Macroporous Polymer Gels for Efficient Adsorption of Block Copolymer Surfactants. *Langmuir* **2022**, *38* (44), 13558–13568. https://doi.org/10.1021/acs.langmuir.2c02198.

(271) Gotad, P. S.; Jana, S. C. Aerogel-Glass Fiber Composite Filter Media for Effective Separation of Emulsified Water Droplets from Diesel Fuel. *Separation and Purification Technology* **2024**, *332*, 125705. https://doi.org/10.1016/j.seppur.2023.125705.

(272) Le Follotec, A.; Pezron, I.; Noik, C.; Dalmazzone, C.; Metlas-Komunjer, L. Triblock Copolymers as Destabilizers of Water-in-Crude Oil Emulsions. *Colloids and Surfaces A:*

*Physicochemical and Engineering Aspects* **2010**, *365* (1), 162–170. https://doi.org/10.1016/j.colsurfa.2010.02.025.

(273) Liu, J.; Li, X.; Jia, W.; Li, Z.; Zhao, Y.; Ren, S. Demulsification of Crude Oil-in-Water Emulsions Driven by Graphene Oxide Nanosheets. *Energy Fuels* **2015**, *29* (7), 4644–4653. https://doi.org/10.1021/acs.energyfuels.5b00966.

(274) *Synthesis of a novel copolymer of block polyether macromonomer and diallyldimethylammonium chloride and its reverse demulsification performance | Elsevier Enhanced Reader*. https://doi.org/10.1016/j.petrol.2018.12.059.

(275) Lemos, R. C. B.; da Silva, E. B.; dos Santos, A.; Guimarães, R. C. L.; Ferreira, B. M. S.; Guarnieri, R. A.; Dariva, C.; Franceschi, E.; Santos, A. F.; Fortuny, M. Demulsification of 212 Water-in-Crude Oil Emulsions Using Ionic Liquids and Microwave Irradiation. *Energy Fuels* **2010**, *24* (8), 4439–4444. https://doi.org/10.1021/ef100425v.

(276) Silva, E. B.; Santos, D.; Alves, D. R. M.; Barbosa, M. S.; Guimarães, R. C. L.; Ferreira, B. M. S.; Guarnieri, R. A.; Franceschi, E.; Dariva, C.; Santos, A. F.; Fortuny, M. Demulsification of Heavy Crude Oil Emulsions Using Ionic Liquids. *Energy Fuels* **2013**, *27* (10), 6311–6315. https://doi.org/10.1021/ef302008d.

(277) Daniel, C.; Dammer, C.; Guenet, J.-M. On the Definition of Thermoreversible Gels: The Case of Syndiotactic Polystyrene. *Polymer* **1994**, *35* (19), 4243–4246. https://doi.org/10.1016/0032-3861(94)90604-1.

(278) Daniel, C.; Menelle, A.; Brulet, A.; Guenet, J. m. Thermoreversible Gelation of Syndiotactic Polystyrene: Effect of Solvent Type. *Macromolecular Symposia* **1997**, *114* (1), 159–164. https://doi.org/10.1002/masy.19971140119.

(279) Long, L.-Y.; Weng, Y.-X.; Wang, Y.-Z. Cellulose Aerogels: Synthesis, Applications, and Prospects. *Polymers* **2018**, *10* (6), 623. https://doi.org/10.3390/polym10060623.

(280) Paria, S.; Manohar, C.; Khilar, K. C. Adsorption of Anionic and Non-Ionic Surfactants on a Cellulosic Surface. *Colloids and Surfaces A: Physicochemical and Engineering Aspects* **2005**, *252* (2–3), 221–229. https://doi.org/10.1016/j.colsurfa.2004.09.022.

(281) Abbott, L. J.; Hart, K. E.; Colina, C. M. Polymatic: A Generalized Simulated Polymerization Algorithm for Amorphous Polymers. *Theor Chem Acc* **2013**, *132* (3), 1334. https://doi.org/10.1007/s00214-013-1334-z.

(282) Thompson, A. P.; Aktulga, H. M.; Berger, R.; Bolintineanu, D. S.; Brown, W. M.; Crozier, P. S.; in 't Veld, P. J.; Kohlmeyer, A.; Moore, S. G.; Nguyen, T. D.; Shan, R.; Stevens, M. J.; Tranchida, J.; Trott, C.; Plimpton, S. J. LAMMPS - a Flexible Simulation Tool for Particle-Based Materials Modeling at the Atomic, Meso, and Continuum Scales. *Computer Physics Communications* **2022**, *271*, 108171. https://doi.org/10.1016/j.cpc.2021.108171. 213

(283) Berendsen, H. J. C.; Grigera, J. R.; Straatsma, T. P. The Missing Term in Effective Pair Potentials. *J. Phys. Chem.* **1987**, *91* (24), 6269–6271. https://doi.org/10.1021/j100308a038.

(284) Ileri Ercan, N.; Stroeve, P.; Tringe, J. W.; Faller, R. Understanding the Interaction of Pluronics L61 and L64 with a DOPC Lipid Bilayer: An Atomistic Molecular Dynamics Study. *Langmuir* **2016**, *32* (39), 10026–10033. https://doi.org/10.1021/acs.langmuir.6b02360.

(285) Bekele, S.; Tsige, M. Interfacial Properties of Oxidized Polystyrene and Its Interaction with Water. *Langmuir* **2013**, *29* (43), 13230–13238. https://doi.org/10.1021/la403099e.

(286) Watkins, E. K.; Jorgensen, W. L. Perfluoroalkanes: Conformational Analysis and Liquid-State Properties from Ab Initio and Monte Carlo Calculations. *J. Phys. Chem. A* **2001**, *105* (16), 4118–4125. https://doi.org/10.1021/jp004071w.

(287) Baker, J. A.; Berg, J. C. Investigation of the Adsorption Configuration of Polyethylene Oxide and Its Copolymers with Polypropylene Oxide on Model Polystyrene Latex Dispersions. *Langmuir* **1988**, *4* (4), 1055–1061. https://doi.org/10.1021/la00082a042.

(288) Bekele, S.; Tsige, M. Effect of Polymer/Solid and Polymer/Vapor Instantaneous Interfaces on the Interfacial Structure and Dynamics of Polymer Melt Systems. *Langmuir* **2016**, *32* (28), 7151–7158. https://doi.org/10.1021/acs.langmuir.6b01554.

(289) Shandiz, S. A.; Leuty, G. M.; Guo, H.; Mokarizadeh, A. H.; Maia, J. M.; Tsige, M. Structure and Thermodynamics of Linear, Ring, and Catenane Polymers in Solutions and at Liquid–Liquid Interfaces. *Langmuir* **2023**, *39* (20), 7154–7166. https://doi.org/10.1021/acs.langmuir.3c00589.

(290) Domínguez, H. Self-Aggregation of the SDS Surfactant at a Solid−Liquid Interface. *J. Phys. Chem. B* **2007**, *111* (16), 4054–4059. https://doi.org/10.1021/jp067768b. 214

(291) Király, Z.; Börner, R. H. K.; Findenegg, G. H. Adsorption and Aggregation of C8E4 and C8G1 Nonionic Surfactants on Hydrophilic Silica Studied by Calorimetry. *Langmuir* **1997**, *13* (13), 3308–3315. https://doi.org/10.1021/la9620768.

(292) Brown, R.; Wines, T. Improve Suspended Water Removal from Fuels. *Hydrocarbon Processing - HYDROCARB PROCESS* **1993**, *72*, 95–100. https://doi.org/10.1007/978-1-4757-1209-4_14.

(293) *Diesel Engine Emissions and Their Control*. technology.matthey.com. https://technology.matthey.com/journal (accessed 2023-01-10).

(294) Wang, J.; Ponting, M.; Zhang, C.; Olah, A.; Baer, E. Fuel Filtration Properties and Mechanism of a Novel Fibrous Filter Produced by a Melt-Process. *Journal of Membrane Science* **2017**, *526*, 229–241. https://doi.org/10.1016/j.memsci.2016.12.040.

(295) McLean, J. D.; Kilpatrick, P. K. Effects of Asphaltene Solvency on Stability of Water-in-Crude-Oil Emulsions. *Journal of Colloid and Interface Science* **1997**, *189* (2), 242–253. https://doi.org/10.1006/jcis.1997.4807.

(296) Kumar Gupta, R.; J. Dunderdale, G.; W. England, M.; Hozumi, A. Oil/Water Separation Techniques: A Review of Recent Progresses and Future Directions. *Journal of Materials Chemistry A* **2017**, *5* (31), 16025–16058. https://doi.org/10.1039/C7TA02070H.

(297) Shin, C.; Chase, G. G. Water-in-Oil Coalescence in Micro-Nanofiber Composite Filters. *AIChE Journal* **2004**, *50* (2), 343–350. https://doi.org/10.1002/aic.10031.

(298) Shin, C.; Chase, G. G. Separation of Water-in-Oil Emulsions Using Glass Fiber Media Augmented with Polymer Nanofibers. *Journal of Dispersion Science and Technology* **2006**, *27* (4), 517–522. https://doi.org/10.1080/01932690500374276.

(299) Hazlett, R. N. Fibrous Bed Coalescence of Water. Steps in the Coalescence Process. *Ind. Eng. Chem. Fund.* **1969**, *8* (4), 625–632. https://doi.org/10.1021/i160032a005.

(300) Patel, S. U.; Patel, S. U.; Chase, G. G. Electrospun Superhydrophobic Poly(Vinylidene Fluoride-Co-Hexafluoropropylene) Fibrous Membranes for the Separation of Dispersed 215 Water from Ultralow Sulfur Diesel. *Energy Fuels* **2013**, *27* (5), 2458–2464. https://doi.org/10.1021/ef400248c.

(301) Rajgarhia, S. S.; Benavides, R. E.; Jana, S. C. Morphology Control of Bi-Component Polymer Nanofibers Produced by Gas Jet Process. *Polymer* **2016**, *93*, 142–151. https://doi.org/10.1016/j.polymer.2016.04.018.

(302) Zhang, X.; Lu, Y. Centrifugal Spinning: An Alternative Approach to Fabricate Nanofibers at High Speed and Low Cost. *Polymer Reviews* **2014**, *54* (4), 677–701. https://doi.org/10.1080/15583724.2014.935858.

(303) Patel, S. U.; Kulkarni, P. S.; Patel, S. U.; Chase, G. G. The Effect of Surface Energy of Woven Drainage Channels in Coalescing Filters. *Separation and Purification Technology* **2012**, *87*, 54–61. https://doi.org/10.1016/j.seppur.2011.11.021.

(304) Brown, R. C. *Air Filtration: An Integrated Approach to the Theory and Applications of Fibrous Filters*; Pergamon Press: Oxford; New York, 1993.

(305) Wang, H.; Hu, X.; Ke, Z.; Du, C. Z.; Zheng, L.; Wang, C.; Yuan, Z. Review: Porous Metal Filters and Membranes for Oil–Water Separation. *Nanoscale Res Lett* **2018**, *13* (1), 284. https://doi.org/10.1186/s11671-018-2693-0.

(306) Zhou, X.; Zhang, Z.; Xu, X.; Guo, F.; Zhu, X.; Men, X.; Ge, B. Robust and Durable Superhydrophobic Cotton Fabrics for Oil/Water Separation. *ACS Appl Mater Interfaces* **2013**, *5* (15), 7208–7214. https://doi.org/10.1021/am4015346.

(307) Fu, C.; Gu, L.; Zeng, Z.; Xue, Q. One-Step Transformation of Metal Meshes to Robust Superhydrophobic and Superoleophilic Meshes for Highly Efficient Oil Spill Cleanup and Oil/Water Separation. *ACS Appl. Mater. Interfaces* **2020**, *12* (1), 1850–1857. https://doi.org/10.1021/acsami.9b17052.

(308) Lv, W.; Mei, Q.; Xiao, J.; Du, M.; Zheng, Q. 3D Multiscale Superhydrophilic Sponges with Delicately Designed Pore Size for Ultrafast Oil/Water Separation. *Advanced Functional Materials* **2017**, *27* (48), 1704293. https://doi.org/10.1002/adfm.201704293. 216

(309) Si, Y.; Fu, Q.; Wang, X.; Zhu, J.; Yu, J.; Sun, G.; Ding, B. Superelastic and Superhydrophobic Nanofiber-Assembled Cellular Aerogels for Effective Separation of Oil/Water Emulsions. *ACS Nano* **2015**, *9* (4), 3791–3799. https://doi.org/10.1021/nn506633b

(310) Cao, Y.; Zhang, X.; Tao, L.; Li, K.; Xue, Z.; Feng, L.; Wei, Y. Mussel-Inspired Chemistry and Michael Addition Reaction for Efficient Oil/Water Separation. *ACS Appl. Mater. Interfaces* **2013**, *5* (10), 4438–4442. https://doi.org/10.1021/am4008598.

(311) Alazab, A. A.; Saleh, T. A. Magnetic Hydrophobic Cellulose-Modified Polyurethane Filter for Efficient Oil-Water Separation in a Complex Water Environment. *Journal of Water Process Engineering* **2022**, *50*, 103125. https://doi.org/10.1016/j.jwpe.2022.103125.

(312) Huang, Z.; Shen, L.; Lin, H.; Li, B.; Chen, C.; Xu, Y.; Li, R.; Zhang, M.; Zhao, D. Fabrication of Fibrous MXene Nanoribbons (MNRs) Membrane with Efficient Performance for

Oil-Water Separation. *Journal of Membrane Science* **2022**, *661*, 120949. https://doi.org/10.1016/j.memsci.2022.120949.

(313) Fan, Q.; Yi, M.; Chai, C.; Li, W.; Qi, P.; Wang, J.; Hao, J. Oxidation Stability Enhanced MXene-Based Porous Materials Derived from Water-in-Ionic Liquid Pickering Emulsions for Wearable Piezoresistive Sensor and Oil/Water Separation Applications. *Journal of Colloid and Interface Science* **2022**, *618*, 311–321. https://doi.org/10.1016/j.jcis.2022.03.073.

(314) Yu, H.; Wu, M.; Duan, G.; Gong, X. One-Step Fabrication of Eco-Friendly Superhydrophobic Fabrics for High-Efficiency Oil/Water Separation and Oil Spill Cleanup. *Nanoscale* **2022**, *14* (4), 1296–1309. https://doi.org/10.1039/D1NR07111D.

(315) Caps, R.; Fricke, J. Aerogels for Thermal Insulation. In *Sol-Gel Technologies for Glass Producers and Users*; Aegerter, M. A., Mennig, M., Eds.; Springer US: Boston, MA, 2004; pp 349–353. https://doi.org/10.1007/978-0-387-88953-5_46. 217

(316) Kim, S. J.; Raut, P.; Jana, S. C.; Chase, G. Electrostatically Active Polymer Hybrid Aerogels for Airborne Nanoparticle Filtration. *ACS Appl. Mater. Interfaces* **2017**, *9* (7), 6401–6410. https://doi.org/10.1021/acsami.6b14784.

(317) Zhai, C.; Jana, S. C. Tuning Porous Networks in Polyimide Aerogels for Airborne Nanoparticle Filtration. *ACS Appl. Mater. Interfaces* **2017**, *9* (35), 30074–30082. https://doi.org/10.1021/acsami.7b09345.

(318) Daniel, C.; Alfano, D.; Guerra, G.; Musto, P. Physical Gelation of Syndiotactic Polystyrene in the Presence of Large Molar Volume Solvents Induced by Volatile Guests of Clathrate Phases. *Macromolecules* **2003**, *36* (5), 1713–1716. https://doi.org/10.1021/ma021564l.

(319) Yang, X.; Wang, H.; Chase, G. G. Performance of Hydrophilic Glass Fiber Media to Separate Dispersed Water Drops from Ultra Low Sulfur Diesel Supplemented by Vibrations. *Separation and Purification Technology* **2015**, *156*, 665–672. https://doi.org/10.1016/j.seppur.2015.10.062.

(320) Lawson, G. B. Coalescence Behaviour of Liquid Drops at Plane Interfaces. Ph.D., The University of Manchester (United Kingdom), England. https://www.proquest.com/docview/2132036491/abstract/30CCBDFDDC7C4554PQ/1 (accessed 2023-01-11).

(321) Du, C.; Wang, J.; Chen, Z.; Chen, D. Durable Superhydrophobic and Superoleophilic Filter Paper for Oil–Water Separation Prepared by a Colloidal Deposition Method. *Applied Surface Science* **2014**, *313*, 304–310. https://doi.org/10.1016/j.apsusc.2014.05.207.

(322) Zhang, W.; Shi, Z.; Zhang, F.; Liu, X.; Jin, J.; Jiang, L. Superhydrophobic and Superoleophilic PVDF Membranes for Effective Separation of Water-in-Oil Emulsions with High Flux. *Advanced Materials* **2013**, *25* (14), 2071–2076. https://doi.org/10.1002/adma.201204520. 218

(323) Zhang, Q.; Li, L.; Li, Y.; Cao, L.; Yang, C. Surface Wetting-Driven Separation of Surfactant-Stabilized Water–Oil Emulsions. *Langmuir* **2018**, *34* (19), 5505–5516. https://doi.org/10.1021/acs.langmuir.7b04248.

(324) Clayfield, E. J.; Dixon, A. G.; Foulds, A. W.; Miller, R. J. L. The Coalescence of Secondary Dispersions: I. The Effect of Wettability and Surface Energy. *Journal of Colloid and Interface Science* **1985**, *104* (2), 500–511. https://doi.org/10.1016/0021-9797(85)90057-8.

(325) Avenue, 677 Huntington; Boston; Ma 02115. *Stricter federal guidelines on 'forever chemicals' in drinking water pose challenges*. News. https://www.hsph.harvard.edu/news/features/stricter-federal-guidelines-on-forever-chemicals-in-drinking-water-pose-challenges/ (accessed 2023-08-06).

(326) US EPA, O. *EPA Announces New Drinking Water Health Advisories for PFAS Chemicals, $1 Billion in Bipartisan Infrastructure Law Funding to Strengthen Health Protections*. https://www.epa.gov/newsreleases/epa-announces-new-drinking-water-health-advisories-pfas-chemicals-1-billion-bipartisan (accessed 2023-02-08).

(327) Barry, V.; Winquist, A.; Steenland, K. Perfluorooctanoic Acid (PFOA) Exposures and Incident Cancers among Adults Living near a Chemical Plant. *Environ Health Perspect* **2013**, *121* (11–12), 1313–1318. https://doi.org/10.1289/ehp.1306615.

(328) Worley, R. R.; Moore, S. M.; Tierney, B. C.; Ye, X.; Calafat, A. M.; Campbell, S.; Woudneh, M. B.; Fisher, J. Per- and Polyfluoroalkyl Substances in Human Serum and Urine Samples from a Residentially Exposed Community. *Environ Int* **2017**, *106*, 135–143. https://doi.org/10.1016/j.envint.2017.06.007.

(329) Nayak, S.; Sahoo, G.; Das, I. I.; Mohanty, A. K.; Kumar, R.; Sahoo, L.; Sundaray, J. K. Poly- and Perfluoroalkyl Substances (PFAS): Do They Matter to Aquatic Ecosystems? *Toxics* **2023**, *11* (6), 543. https://doi.org/10.3390/toxics11060543. 219

(330) *Emerging Contaminants and PFAS*. Brown and Caldwell. https://brownandcaldwell.com/services/emerging-contaminants-and-pfas/ (accessed 2023-08-06).

(331) *US EPA sets health advisory limits for 6 PFAS*. Chemical & Engineering News. https://cen.acs.org/environment/persistent-pollutants/US-EPA-sets-health-advisory-6-PFAS/100/i22 (accessed 2023-08-06).

(332) Podder, A.; Sadmani, A. H. M. A.; Reinhart, D.; Chang, N.-B.; Goel, R. Per and Poly-Fluoroalkyl Substances (PFAS) as a Contaminant of Emerging Concern in Surface Water: A Transboundary Review of Their Occurrences and Toxicity Effects. *Journal of Hazardous Materials* **2021**, *419*, 126361. https://doi.org/10.1016/j.jhazmat.2021.126361.

(333) US EPA, O. *Drinking Water Health Advisories for PFOA and PFOS*. https://www.epa.gov/sdwa/drinking-water-health-advisories-pfoa-and-pfos (accessed 2023-08-06).

(334) *In-Situ Treatment: Downhole Foam Fractionation (DFF)*. OPEC Systems. https://opecsystems.com/enviro/pfas-solutions/in-situ-treatment-downhole-foam-fractionation-dff/ (accessed 2023-08-07).

(335) Flores, C.; Ventura, F.; Martin-Alonso, J.; Caixach, J. Occurrence of Perfluorooctane Sulfonate (PFOS) and Perfluorooctanoate (PFOA) in N.E. Spanish Surface Waters and Their Removal in a Drinking Water Treatment Plant That Combines Conventional and Advanced Treatments in Parallel Lines. *Sci Total Environ* **2013**, *461–462*, 618–626. https://doi.org/10.1016/j.scitotenv.2013.05.026.

(336) Fagbayigbo, B. O.; Opeolu, B. O.; Fatoki, O. S.; Akenga, T. A.; Olatunji, O. S. Removal of PFOA and PFOS from Aqueous Solutions Using Activated Carbon Produced from Vitis Vinifera Leaf Litter. *Environ Sci Pollut Res* **2017**, *24* (14), 13107–13120. https://doi.org/10.1007/s11356-017-8912-x. 220

(337) Xu, J.; Liu, Z.; Zhao, D.; Gao, N.; Fu, X. Enhanced Adsorption of Perfluorooctanoic Acid (PFOA) from Water by Granular Activated Carbon Supported Magnetite Nanoparticles. *Science of The Total Environment* **2020**, *723*, 137757. https://doi.org/10.1016/j.scitotenv.2020.137757.

(338) Ateia, M.; Alsbaiee, A.; Karanfil, T.; Dichtel, W. Efficient PFAS Removal by Amine-Functionalized Sorbents: Critical Review of the Current Literature. *Environ. Sci. Technol. Lett.* **2019**, *6* (12), 688–695. https://doi.org/10.1021/acs.estlett.9b00659.

(339) Iswar, S.; Galmarini, S.; Bonanomi, L.; Wernery, J.; Roumeli, E.; Nimalshantha, S.; Ben Ishai, A. M.; Lattuada, M.; Koebel, M. M.; Malfait, W. J. Dense and Strong, but Superinsulating Silica Aerogel. *Acta Materialia* **2021**, *213*, 116959. https://doi.org/10.1016/j.actamat.2021.116959.

(340) Im, H.; Kim, T.; Song, H.; Choi, J.; Park, J. S.; Ovalle-Robles, R.; Yang, H. D.; Kihm, K. D.; Baughman, R. H.; Lee, H. H.; Kang, T. J.; Kim, Y. H. High-Efficiency Electrochemical Thermal Energy Harvester Using Carbon Nanotube Aerogel Sheet Electrodes. *Nat Commun* **2016**, *7* (1), 10600. https://doi.org/10.1038/ncomms10600.

(341) Lee, D.; Kim, J.; Kim, S.; Kim, G.; Roh, J.; Lee, S.; Han, H. Tunable Pore Size and Porosity of Spherical Polyimide Aerogel by Introducing Swelling Method Based on Spherulitic

Formation Mechanism. *Microporous and Mesoporous Materials* **2019**, *288*, 109546. https://doi.org/10.1016/j.micromeso.2019.06.008.

(342) Baetens, R.; Jelle, B. P.; Gustavsen, A. Aerogel Insulation for Building Applications: A State-of-the-Art Review. *Energy and Buildings* **2011**, *43* (4), 761–769. https://doi.org/10.1016/j.enbuild.2010.12.012.

(343) Xie, X.; Zheng, Z.; Wang, X.; Lee Kaplan, D. Low-Density Silk Nanofibrous Aerogels: Fabrication and Applications in Air Filtration and Oil/Water Purification. *ACS Nano* **2021**, *15* (1), 1048–1058. https://doi.org/10.1021/acsnano.0c07896. 221

(344) Liang, J.; Wang, Z.; Ye, Q.; Qiao, L.; Jiang, H.; Guo, Y.; Fan, Z. Pump-Inject Antimicrobial and Biodegradable Aerogel as Mask Intermediate Filter Layer for Medical Protection of Air Filtration. *Materials Today Sustainability* **2022**, *19*, 100211. https://doi.org/10.1016/j.mtsust.2022.100211.

(345) Lin, B.; Wang, Z.; Zhu, Q.; Hamzah, W. N. B.; Yao, Z.; Cao, K. Aerogels for the Separation of Asphalt-Containing Oil–Water Mixtures and the Effect of Asphalt Stabilizer. *RSC Adv.* **2020**, *10* (42), 24840–24846. https://doi.org/10.1039/D0RA00544D.

(346) Figueroa-Gerstenmaier, S.; Daniel, C.; Milano, G.; Vitillo, J. G.; Zavorotynska, O.; Spoto, G.; Guerra, G. Hydrogen Adsorption by δ and ε Crystalline Phases of Syndiotactic Polystyrene Aerogels. *Macromolecules* **2010**, *43* (20), 8594–8601. https://doi.org/10.1021/ma101218q.

(347) Joseph, A. M.; Nagendra, B.; Shaiju, P.; Surendran, K. P.; Gowd, E. B. Aerogels of Hierarchically Porous Syndiotactic Polystyrene with a Dielectric Constant near to Air. *J. Mater. Chem. C* **2018**, *6* (2), 360–368. https://doi.org/10.1039/C7TC05102F.

(348) Gu, T.; Huang, Z. Thermodynamics of Hemimicellization of Cetyltrimethylammonium Bromide at the Silica Gel/Water Interface. *Colloids and Surfaces* **1989**, *40*, 71–76. https://doi.org/10.1016/0166-6622(89)80007-1.

(349) Deng, S.; Zhang, Q.; Nie, Y.; Wei, H.; Wang, B.; Huang, J.; Yu, G.; Xing, B. Sorption Mechanisms of Perfluorinated Compounds on Carbon Nanotubes. *Environmental Pollution* **2012**, *168*, 138–144. https://doi.org/10.1016/j.envpol.2012.03.048.

(350) Klemes, M. J.; Ling, Y.; Ching, C.; Wu, C.; Xiao, L.; Helbling, D. E.; Dichtel, W. R. Reduction of a Tetrafluoroterephthalonitrile-β-Cyclodextrin Polymer to Remove Anionic Micropollutants and Perfluorinated Alkyl Substances from Water. *Angewandte Chemie International Edition* **2019**, *58* (35), 12049–12053. https://doi.org/10.1002/anie.201905142. 222

(351) Inyang, M.; Dickenson, E. R. V. The Use of Carbon Adsorbents for the Removal of Perfluoroalkyl Acids from Potable Reuse Systems. *Chemosphere* **2017**, *184*, 168–175. https://doi.org/10.1016/j.chemosphere.2017.05.161.

(352) Du, Z.; Deng, S.; Bei, Y.; Huang, Q.; Wang, B.; Huang, J.; Yu, G. Adsorption Behavior and Mechanism of Perfluorinated Compounds on Various Adsorbents—A Review. *Journal of Hazardous Materials* **2014**, *274*, 443–454. https://doi.org/10.1016/j.jhazmat.2014.04.038.

(353) Punyapalakul, P.; Suksomboon, K.; Prarat, P.; Khaodhiar, S. Effects of Surface Functional Groups and Porous Structures on Adsorption and Recovery of Perfluorinated Compounds by Inorganic Porous Silicas. *Separation Science and Technology* **2013**, *48*. https://doi.org/10.1080/01496395.2012.7